**Title**
Elucidating Nanoscale Dynamics of Matter and Energy Transport in Heterogeneous Systems Using Time-Resolved Spectroscopies and Microscopies



**Author**
Roberts, Trevor D

**Publication Date**
2022

Peer reviewed|Thesis/dissertation

# Elucidating Nanoscale Dynamics of Matter and Energy Transport in Heterogeneous Systems Using Time-Resolved Spectroscopies and Microscopies

by

Trevor D Roberts

A dissertation submitted in partial satisfaction of the

requirements for the degree of

Doctor of Philosophy

in

Chemistry

in the

Graduate Division

of the

University of California, Berkeley

Committee in charge:

Professor Naomi S. Ginsberg, Chair
Professor Stephen Leone
Professor Krishna Niyogi

Spring 2022

Elucidating Nanoscale Dynamics of Matter and Energy Transport in Heterogeneous Systems Using Time-Resolved Spectroscopies and Microscopies

Abstract

Elucidating Nanoscale Dynamics of Matter and Energy Transport in Heterogeneous Systems Using Time-Resolved Spectroscopies and Microscopies

by

Trevor D Roberts

Doctor of Philosophy in Chemistry

University of California, Berkeley

Professor Naomi S. Ginsberg, Chair

Solution processable materials offer a variety of exciting possibilities, owing to their low-cost and ease of tunability. Many next-generation electronic devices are being developed using solution processable materials, but their performance is typically hindered by the complex heterogeneous structures that result from their assembly or deposition. The characteristic length scales of this heterogeneity are typically nanometers and micrometers, and time scales of interest for material function can vary by many orders of magnitude (e.g., femtoseconds to minutes) depending on the context. In this dissertation, we employ a suite of time-resolved spectroscopies and microscopies to address material dynamics relevant for the transport of (excitation) energy and mass.

Chapter 2 describes measurements characterizing the excited state evolution of a protein-bound chromophore intended for a biomimetic photosynthetic light harvesting complex using transient absorption spectroscopy. These measurements employ a series of chromophore-protein chemical linking groups that vary in their length and rigidity, which enables control over the chromophore-protein coupling. The findings here inform design principles for biomimetic light harvesting systems as well as the underlying photophysics potentially employed in natural photosynthetic systems for efficient excitation transport.

Chapter 3 describes correlative widefield single-particle tracking and atomic force microscopy (AFM) phase imaging to determine how the nano- and microscale semicrystalline morphology in electrolytic poly(ethylene oxide) (PEO) thin films influences the motion of small particles. The findings here suggest that polymer crystallinity, if controlled well, need not necessarily be a detriment to the transport of small particle species despite this historically being a challenge for PEO solid-state electrolytes that are investigated as next-generation battery materials.

Chapter 4 gives an overview of time-resolved ultrafast STED (TRUSTED), an ultrafast trans-

formation of STED super-resolution microscopy to track exciton migration at the nanoscale in optoelectronically coupled materials. TRUSTED takes advantage of well-defined optical quenching boundaries such that exciton displacements, even over small distances, will register as a change in the number of excitons quenched. We describe the basics as well as the nuances in trying to apply this method to a series of electronically coupled materials.

Finally, Chapter 5 will discuss the ongoing investigation, at the time of this writing, of exciton transport in Tellurium doped CdSe/CdS core-shell quantum dot superlattices. We investigate exciton transport using TRUSTED as well as time-resolved emission spectroscopy (TRES) and single-particle emission spectroscopy to characterize how the energetic disorder imposed by dopants modulates exciton transport. Steps to finish this work are detailed, which involve reconciling the time-rate of exciton energy decay measured by TRES with the exciton diffusivity measured by TRUSTED.

Taken together, this dissertation illustrates specific examples of characterizing material structure-function relationships across a variety of different systems. To do so, it requires using a number of different characterization tools, and, in each case, reveals the importance of matching the scale of the experimental length and/or time resolution to the native length and time scales of material structural heterogeneities and dynamics, respectively.

To Mom, Dad, Taylor, and Grandma

# Contents

# List of Figures

# List of Tables

# Acknowledgments

I have a great many people to thank, as the work described in this dissertation and beyond would not have been possible without the collaboration, support, encouragement, and patience of others.

I would first like to thank my advisor, Professor Naomi Ginsberg, for her support over the years. Naomi, thank you for the many illuminating scientific conversations, for guiding my understanding of physical chemistry, for cultivating an environment in which learning is paramount, and for pushing me to continue onward even when I sometimes felt lost. I was in perpetual awe of your ability to juggle so many things simultaneously and yet still prioritize the well-being of your students.

Thank you to the very talented postdocs I have had the fortune to overlap with: Clarice Aiello, Milan Delor, Jon Raybin, James Utterback, and Rongfeng Yuan. Milan, thank you for your mentorship during the beginning of my graduate school experience, for introducing me to ultrafast spectroscopy, and for countless conversations about science. Rongfeng, thank you for your collaboration and guidance these past few years, for your hard work and creativity, and for your kindness.

Thank you to the wonderful graduate students I worked with, past and present, in the Ginsberg group: Rebecca Wai, Hannah Weaver, Jenna Tan, Leo Hamerlynck, Christian Tanner, Vivian Wall, Brendan Folie, Lucas Ginsberg, Connor Bischak, and Ben Cotts. Thank you all so much for all the help, conversations, humor, and comradery over the years. You all were my sunshine in the D-level.

I was lucky to work with many scientific collaborators over the years here at Berkeley and beyond. Thank you to Jing Dai, Amanda Bischoff, Julia Rogers, Samia Hamed, Prof. Phill Geissler, Prof. Jeff Neaton, Prof. Matt Francis, Ke Yang, Ravi Pokhrel, Pete Trefonas, Cam Li, Prof. Sean Roberts, Limin Xiang, Alex Choi, Prof. Ke Xu, Niklas Keller, Justin Ondry, Rafi Brinn, and Prof. Paul Alivisatos.

Thank you to the TRUSTED predecessors for their work on developing the apparatus. Thanks to Sam Penwell for his thorough notes and logs and thanks to Lucas Ginsberg for getting me acquainted with the operation of the set-up.

Thank you to those that help the Berkeley machine run smoothly, especially to Jessie Woodcock, Carl Lamey, Joel Adlen, and Negest Williams.

Thank you to the friends I made during my time at Berkeley. Catherine Saladrigas and Hannah Kenagy, thank you for being an amazing study group first year and for your continued friendship afterwards. Thank you to Cindy Hong, Eugene Kapustin, and Helge Berneaud for the many fun weekends, and thank you to John Lee for acting as an honorary roommate as well as hosting many times in Pacifica.

Thank you to my dear friends/roommates that helped keep me sane over the years as we navigated the Berkeley grad school experience together. Ed Miller, thanks for your spontaneity and willingness to go do random things, like escape rooms and floating rivers in 100 degree heat, as well as your various idiosyncracies that made playing board games with you a waking nightmare. Danny Thach, thank you for your passionate approach to

everything and fierce loyalty, for willing to help me at any point even if it means ripping your pants, for your humor in any situation, for making it feel like you bring home wherever you go, and for reminding me that life is too short and splurging sometimes is ok. Jeff Derrick, thanks for agreeing to be roommates for six years after we happened to be paired up on visitation weekend, for the multitude of sanity checks and advice over the years, for preserving the health of our group's glovebox, for including me in your plans so I didn't become a complete recluse, for consuming an incalculable amount of television together, and for allowing me to be Erwin and Nigel's favorite.

Thank you to the network of people from The University of Chicago that propelled me to where I am now. Thank you to Julie Feder and Professor Sean Crosson for their support in the Beckman Scholars program. Thank you to Preston Scrape, my graduate student mentor while I was in the Butler group, for fielding so many questions and graciously working with me on his project. Thank you to Professor Laurie Butler, for introducing me to physical chemistry, for demonstrating what academic rigor is, for always being available to chat with an anxious undergrad, and for proving to me that I am capable of doing science.

Thank you to my wonderful friends from home. Thank you to Seth, Riley, Brandon, Eric, and others from Stanwood for always keeping in touch, for the many adventures, for the laughs when I needed them most, and for grounding me in the more important things in life.

Finally, thank you to my family. Dave, thank you for your advice and stimulating conversations throughout my life. Taylor, thank you for your support and optimism as well as your kinship growing up together, which helped shape many of my passions. Grandma, thank you for always being there, for all the treats, unyielding encouragement, and for living a life that inspires me to persevere in the face of adversity. Mom and Dad, I owe everything to you. Thank you for supporting my education, for teaching me what hard work is, and for never once pushing me to be anything other than what I want to be.

# Chapter 1

# Introduction

## 1.1 Solution Processable Materials for Energy Applications

Solution processable materials offer a variety of exciting possibilities. They are materials that can form solid-state structures or devices by first depositing the dissolved material as a solution and then removing its solvent (otherwise known as a "wet" processing method). Numerous solution processable polymers[1–5], organic semiconductors[6, 7], self-assembling nanomaterials[8–10], and more are promising for energy harvesting and storage applications, given their low-cost and ease of tunability. Owing to their "printable" nature, one can pattern the deposition of these materials in a controllable manner, and one popular form-factor is the thin film. Thin films can be flexible as well as easily integrated into device architectures and even biological media (e.g. skin-like electronics[5]). Some examples of this are solid-state polymer electrolytes for safer Li-ion batteries[11, 12], efficient organic electronics[13, 14], and quantum dot displays and solar cells[9, 15]. Beyond these applications, they afford researchers an excellent platform for the development of model systems to better understand fundamental questions, like how natural photosynthetic systems achieve such remarkable excitation transport efficiency.

Despite these potentially lucrative features, many solution processable materials suffer performance losses due to morphological heterogeneities present over nanometer to micrometer length scales. It is therefore imperative to characterize material dynamics over length and time scales relevant to transport through and in the vicinity of such morphological heterogeneities. But to achieve such characterization in numerous different materials, we must reconcile the challenge of disparate time and length scales. Transport processes of interest for this dissertation can occur on time scales ranging from 10s of femtoseconds to minutes and length scales ranging from 10s of nanometers to 100s of micrometers. In order to address such varied processes, we leverage in this dissertation a suite of spatially- and temporally-resolved characterization tools - some correlatively, and even some that we ourselves developed.

## 1.2 Chromophore and Semiconductor Photophysics

For each project discussed in this dissertation, the optical excitation of chromophores plays a central role. Whether we wish to better understand how these excitations are perturbed by (or couple to) their environment (Chapters 2, 4, 5), how these excitations migrate through and within their surroundings (Chapters 4 and 5), or to use these excitations as a probe to learn more about a material that is itself not optically active (Chapter 3), it is necessary to understand the essential photophysics that ensue after light absorption.

A chromophore is a light absorbing moiety in a compound responsible for determining the material's color. The optical excitation of a chromophore promotes an electron from the ground electronic state to an electronic excited state. When considering semiconductor systems, the language of an "exciton" is used to describe this phenomenon. In a semiconductor, after the electron is promoted from the valence band to the conduction band, it leaves behind a positive vacancy referred to as a "hole." The electron and hole are Coulombically attracted to one another and the bound electron-hole pair is the overall charge neutral quasi-particle known as the exciton. The extent to which the electron and hole are coupled to one another, or the exciton binding energy, is contingent on the dielectric constant of the surrounding medium[16] because it affects the screening between the two charges.

Figure 1.1, from Ref [16], provides a schematic overview of the relative differences in nature of the excitons for a variety of semiconducting systems. The two materials in particular that are relevant for this dissertation are organic semiconductors and quantum dot solids. The degree of localization for excitons in organic semiconductors can vary, but they generally possess higher exciton binding energies than those found in quantum dot nanocrystals. The exciton binding energy determines the amount of energy required to separate the electron and hole species into free charge carriers. An additional consideration is the exciton Böhr radius (i.e. the electron-hole separation distance). In quantum dot systems, the Böhr radius generally exceeds the size of the nanocrystal itself, and as a result the exciton experiences quantum confinement[17]. This is what leads to the exquisite tunability of their optical bandgap by virtue of changing the nanocrystal size, and they exhibit properties in between those of a bulk semiconductor and individual molecules.

Despite the difference in the nature of the exciton species in each system in this thesis (molecules, molecular aggregates, quantum dots), there are a number of processes that are generally relevant to consider following photoexcitation. Figure 1.2a provides a schematic energy level diagram of the relevant relaxation pathways and excited states pertinent to molecular and organic semiconductor systems. Figure 1.2b provides a complementary energy level diagram that considers the valence and conduction band of a quantum dot nanocrystal. Below I will briefly describe the most salient excitation relaxation processes of a hypothetical exciton in the context of both diagrams.

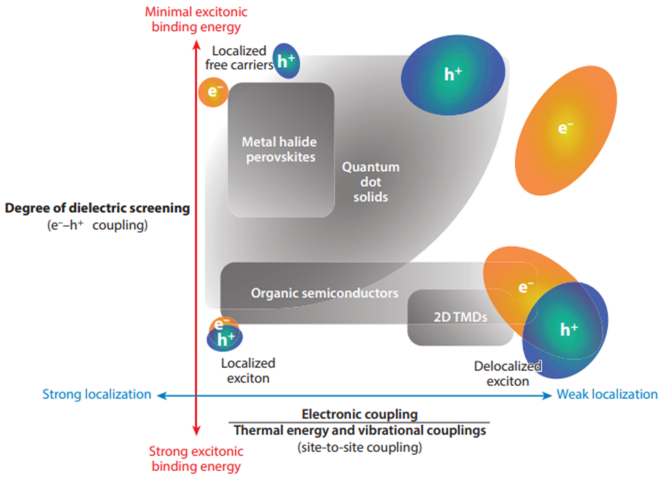


Figure 1.1: Chart of the various properties of the photoexcited species in semiconductors as a consequence of their localization and dielectric screening. Reprinted from Ref [16] with permission.

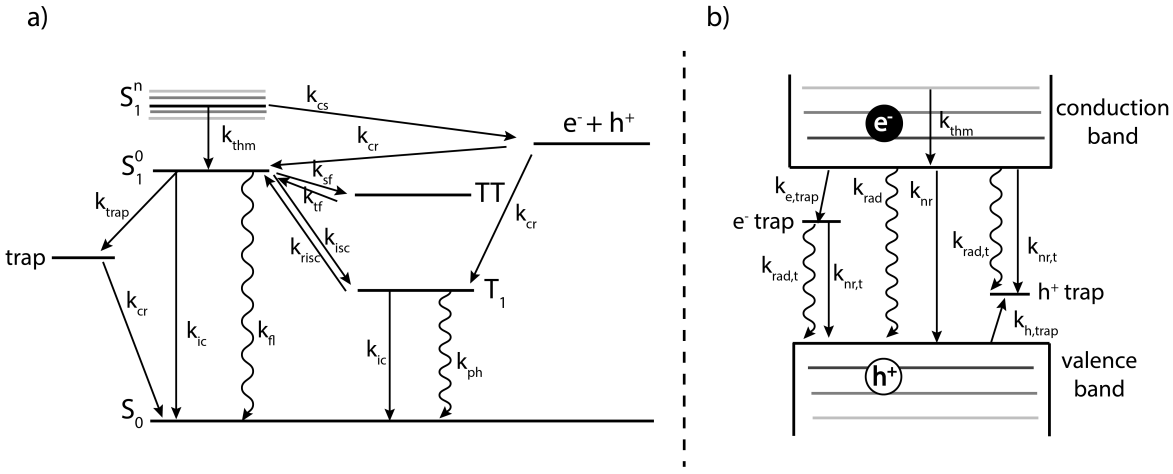


Figure 1.2: Schematic of the various states (horizontal lines) and processes (arrows) important for this dissertation. (a) Typical picture of states and processes associated with molecular and organic semiconducting systems. (b) Typical picture of bands, states and processes associated with semiconductor nanoparticles.

### 1.2.1 Thermalization and vibrational relaxation

A molecule or semiconductor may be excited from its electronic ground state to a higher lying excited state manifold, $S_1^n$ and will then proceed to relax to the lower lying excited state, $S_1^0$.

In quantum dots, this manifests as the electron relaxing from an energy level from one of its discrete "atomic-like" states higher up in the conduction band to the band edge. When an exciton possesses this excess energy it is often referred to as "hot." This energy is typically lost as rapid electron and hole thermalization followed by transfer as heat to the surrounding environment (e.g. molecules transferring heat to solvent via vibrational relaxation, excitons coupling to phonon modes in the lattice), where the exciton will thermalize via a rate, $k_{\text{thm}}$. The timescales for thermalization are on the order of tens of femtoseconds to a few picoseconds for semiconductors [18, 19] and a few ps to 10s of ps for molecular systems [20].

### 1.2.2 Charge separation

Excitons may undergo charge separation and dissociate into free carriers($k_{\text{cs}}$). And similarly, an electron and hole species may recombine back into the exciton species($k_{\text{cr}}$). This process may occur more readily in systems where the exciton binding energy is comparatively low. If the exciton is initially created with enough excess energy above its bandgap or first excited state, it could directly lead to a charge separation event provided the separation rate can outcompete the rapid thermalization ($k_{\text{thm}}$) rate.

Charge separation can occur at donor-acceptor (i.e. the donor "donates" its energy to the acceptor) interfaces, where either the electron or hole species can transfer from a donor to an acceptor. For example, CdSe quantum dots can transfer electrons photogenerated to a metal oxide, like $TiO_2$[21], or charge transfer events can be driven with donor-acceptor polymer blends in organic solar cells[22, 23].

### 1.2.3 Intersystem Crossing

Intersystem crossing ($k_{\text{isc}}$) is the conversion of a singlet to a triplet exciton through an electron spin flip, and reverse intersystem crossing ($k_{\text{risc}}$) is the just the opposite process of this. Direct population of the triplet state is unlikely given that it is an optically forbidden transition, so intersystem crossing is the primary means to populate the triplet state. Although triplets are much longer lived species than singlets on average, their mobilities in semiconductors is mostly much lower.

#### Singlet Fission

Singlet fission ($k_{\text{sf}}$) is a special circumstance in some semiconductors where if the triplet energy is close to half that of the singlet, the singlet exciton can split into two unique triplets. This occurs in two steps, with the creation of a correlated triplet pair prior to triplet separation to two individual triplets. The opposite of singlet fission is triplet fusion ($k_{\text{tf}}$). I only mention this process because the perylene diimide (PDI) samples discussed in Chapter 4 exhibit this unique property[24], but since we are using fluorescence as our measurement we are primarily concerned with the singlet species.

### 1.2.4 Nonradiative relaxation

Nonradiative relaxation ($k_{\mathrm{nr}}$) is the process by which an exciton sheds its excitation energy in a way that does not result in the emisssion of a photon.

Excitons that relax nonradiatively in molecular and organic systems do so through a process known as internal conversion ($k_{\mathrm{ic}}$), where the excitation energy is redistributed throughout the solvent/lattice environment in vibrational and phonon modes rather than through the emission of a photon. This can vary significantly from system to system for a number of reasons, but molecular systems that are more rigid tend to have a lower internal conversion rate[25], owing to their comparatively lower ability to adopt configurations amenable for this energy redistribution. In organic semiconductors, nonradiative recombination/relaxation can also be facilitated by carrier trap-states (see Section 1.2.6).

In inorganic systems like nanocrystals, nonradiative relaxations can occur if the exciton couples to the phonon modes of the crystal lattice[26] and can similarly nonradiatively recombine at lattice defect sites, often located at the surface of the nanocrystal[9, 27] (see Section 1.2.6).

### 1.2.5 Fluorescence/Photoluminescence

The relaxation of an optical excitation back to the chromophore's electronic ground state can result in the radiative emission of a photon. This is what is referred to as fluorescence ($k_{\mathrm{fl}}$), when the wavelength of the emitted light is of a different wavelength than the absorbed light. The difference in energy between the absorbed photon and the emitted photon is the Stokes shift. Photoluminescence ($k_{\mathrm{rad}}$) more generally describes the situation in which the chromophore may emit a photon either through fluorescence or phosphorescence, and it is used when discussing direct band gap semiconductors.

#### Photoluminescence Quantum Yield

The photoluminscence quantum yield (PLQY) is a very useful metric that establishes the relative extent radiative and nonradiative relaxation pathways manifest for a given chromophore. The PLQY is the ratio of the number of photons emitted to the number absorbed[28]. If we sum all of the rate constants that correspond to processes that lead to the relaxation of the exciton back to the ground state (or irreversible charge separation) without an emission of a photon, this is the nonradiative rate, or $k_{\mathrm{nr}}$. The PLQY is formally defined as:

$$\mathrm{PLQY} = \frac{k_{\mathrm{rad}}}{k_{\mathrm{rad}} + k_{\mathrm{nr}}}, \tag{1.1}$$

where $k_{rad}$ is the rate of all emissive processes. Improvements in a system's quantum yield usually target removal of nonradiative decay pathways, for example, passivation techniques that eliminate charge trapping sites. It is important to point out that the PLQY concerns

the *relative* rates between radiative and nonradiative relaxation. There can exist systems with high PLQY and relatively fast or relatively slow radiative rates, provided $k_{\mathrm{rad}} >> k_{\mathrm{nr}}$.

**Exciton Lifetime**

The lifetime of an emissive exciton is frequently characterized by measuring the time-resolved photoluminescence of the chromophore in question. The lifetime of a chromophore is:

$$\tau = \frac{1}{k_{\mathrm{rad}} + k_{\mathrm{nr}}} \tag{1.2}$$

Time-resolved photoluminescence measurements involve recording the photoluminescence intensity as a function of time after excitation ($I(t)$), which is proportional to the number of excitons. The plot of the intensity vs time appears as a decaying exponential (in the simplest case), and an exponential fit to the curve yields the exciton lifetime[28]. To rationalize this characterization, let us consider the simplest rate of exciton relaxation:

$$\frac{\partial n(t)}{\partial t} = (k_{\mathrm{rad}} + k_{\mathrm{nr}})n(t), \tag{1.3}$$

where the number of excitons, $n(t)$ is proportional to $I(t)$. The solution to Equation 1.3 in terms of intensity is:

$$I(t) = I_o e^{-t/(k_{\mathrm{rad}}+k_{\mathrm{nr}})}, \tag{1.4}$$

and we recover Equation 1.2 for the time constant. This time constant is the average time an exciton spends in the excited state, although care must be taken with this interpretation when the system photophysics are not so straightforward (e.g. multi-exponential decays).

### 1.2.6 Trap States

The notion of a trap state can be somewhat nebulous depending on the context, but it is generally a lattice imperfection state at a lower energy level that localizes a charge (electron or hole, $k_{\mathrm{e,trap}}$ and $k_{\mathrm{h,trap}}$ respectively) to be spatially distributed at the site of the imperfection and energetically placed within the band gap of the semiconductor[29]. These trap states can either be "shallow" or "deep," where the energy difference between the trap and band edge is on the order of, or much greater than, $k_{\mathrm{B}}T$, respectively. Relaxation from these trap states can occur both radiatively and non-radiatively, depending on the circumstance. In organic semiconductors, electron trap states generally hinder device efficiency - in organic light emitting diodes (OLEDs), trap states lead to a reduction in the emission efficiency[29] and similarly in organic solar cells the localization of the charge reduces its overall mobility.

In inorganic semiconductors, surface defects[27] and dopants[30] can play a role in trapping either the electron or hole species of an exciton. Radiative recombination can occur from these trap states[31, 32], or the defects may serve to more readily facilitate nonradiative charge recombination.

## 1.3 Fluorescence Microscopy

Fluorescence microscopy is a potent and ever-developing tool used for imaging an incredibly diverse array of systems, and it is paramount for the work detailed in Chapters 3, 4, 5. Fluorescence microscopy applications can range from routine use for characterization of biological samples[33, 34] to characterizing optically addressable quantum emitters [35, 36] to resolving complex questions in neuroscience [37, 38] to imaging energy flow in optoelectronically coupled materials[39], just to reference a very sparse subset.

The essential components of a simple fluorescence microscope are shown in Figure 1.3. The idea is to excite a sample with a light source and then collect the photons emitted from the sample via fluorescence, while simultaneously rejecting photons at the excitation wavelength(s). The excitation source is typically first filtered by an excitation filter, which is particularly useful for selecting a certain spectral region of broadband sources (e.g. lamps). The excitation light is of a wavelength sufficiently short such that the dichroic mirror reflects the light towards the microscope objective. The objective is responsible for both introducing the excitation light to the sample as well as collecting the sample's emitted light. The sample's emission is of a wavelength sufficiently long that it transmits through the dichroic filter (due to the fluorophore's Stokes shift). The emission is transmitted through an additional emission filter to select a particular spectral region, and then collected on a detector. Detectors can range from cameras, photodiodes, or other devices, depending on the measurement purpose.

Omitted from this simple picture are the optical elements responsible for determining the particular type of fluorescent microscope, which for the purposes of this discussion will focus on widefield fluorescence microscopy and confocal fluorescence microscopy.

### 1.3.1 Widefield Fluorescence Microscopy

In a widefield geometry, the excitation source is focused on the back focal plane of the microscope. This results in the light transmitting through the objective as a collimated (or very close to collimated) beam that homogeneously illuminates an entire region of the sample at once. The fluorescence from the sample at any given time is detected as a 2D image, typically on a camera or array based detector. Charge coupled devices (CCDs) are cameras frequently employed in widefield setups and relatively recent (2001) EM-CCDs (electron multiplying charge coupled device) have enabled profound sensitivity to sample fluorescence, down to the single-molecule level[40]. Figure 1.4 conceptually demonstrates such a widefield layout, where we note that multiple individual fluorescent targets in the sample plane are illuminated and fluoresce at the same time.

In Chapter 3, we employ a widefield microscope to track the motion of individual fluorescent probes in a polymer matrix, capturing multiple particle trajectories simultaneously.

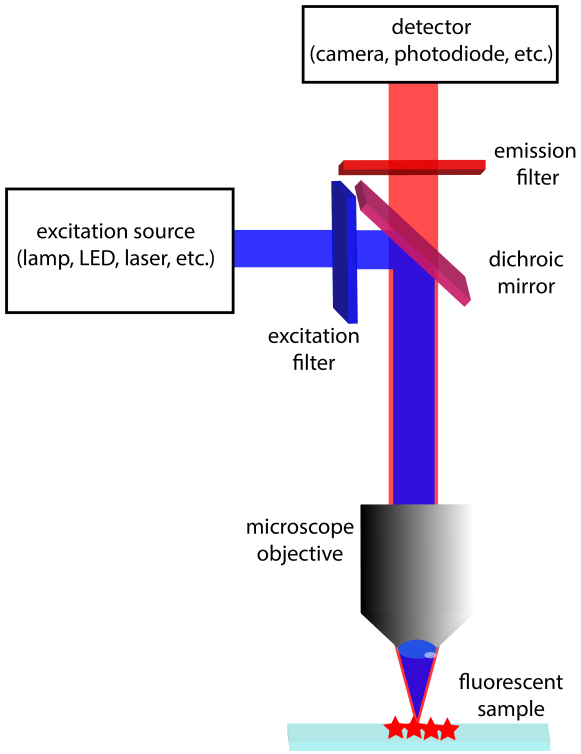


Figure 1.3: Essential components of fluorescence microscope.

### 1.3.2 Scanning Fluorescence Microscopy

In scanning fluorescence microscopy, point illumination is used, where the excitation beam is first expanded in order to over-fill the back aperture of the microscope objective. This results in the excitation light transmitting through the objective such that it is focused within the sample plane. The illumination spot size is thus significantly smaller than in widefield microscopy and, provided the set-up is optimized, the light may be focused to a spot as tight as the optical diffraction limit will allow. Given the spot size is so small, in order to render an image, either the excitation beam must be raster scanned in across the sample (via servo-controlled oscillating mirrors) or the sample stage must translate relative to the excitation beam (with a piezoelectric sample stage, for instance). Figure 1.5 conceptually demonstrates a confocal geometry, where the excitation source is first expanded prior to meeting the objective, and the light emerges at a focus within the sample plane. The region of the sample illuminated is comparatively much smaller than Fig 1.4.

In scanning confocal fluorescence microscopy, a pinhole placed at the focal plane of the telescope just in front of the detector helps eliminate out-of-focus emission and stray/scattered light. Whether confocal or not, the emitted light is usually detected on a sensitive detector like a PMT (photomultiplier tube) or avalanche photodiode (APD). These detectors are not

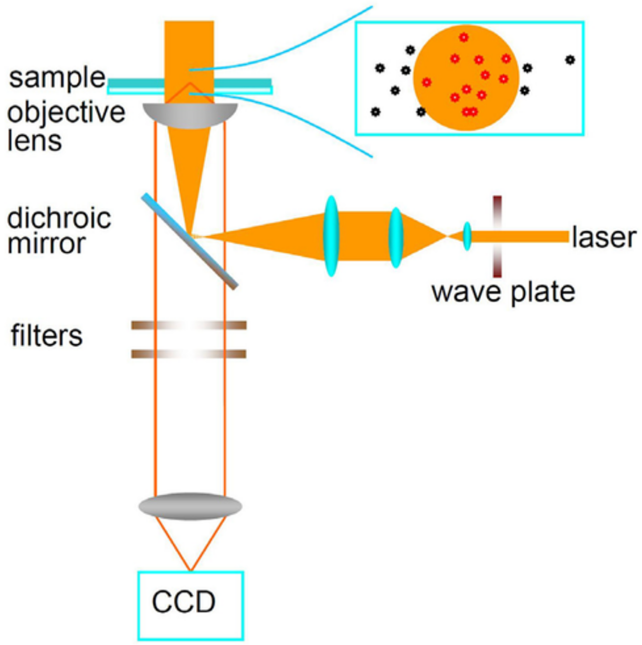


Figure 1.4: Schematic of a widefield fluorescence microscopy set-up. Adapted with permission from Ref [41].

composed of many pixels, like the CCDs used for widefield microscopy, but, rather, are single-element. An image is built pixel-by-pixel, where the emission intensity is recorded for each point the laser (or sample stage) is scanned. Care must be taken when trying to employ such a raster scanning method to observe dynamics - the rate of the raster scan should be much faster than the dynamics being observed. These single-element detectors now usually come equipped with the capability to perform TCSPC (time-correlated single-photon counting), which enables measuring the fluorescence lifetime of target fluorophores/chromophores as a function of their location within the sample of interest. This is referred to as fluorescence lifetime imaging microscopy (FLIM), a technique that leverages a molecule's fluorescence lifetime as a sensitive readout of environmental variations within a sample, like viscosity, pH, or proximity to quenching sites[42, 43].

In Chapters 4,5, we make use of a scanning microscopy geometry reminiscent of the confocal set-up, but without any confocal pinhole. Moreover, our detector is a single-photon avalanche diode (SPAD), capable of TCSPC as well as *gated-detection*, a critically important feature that is described in detail in Chapter 4.

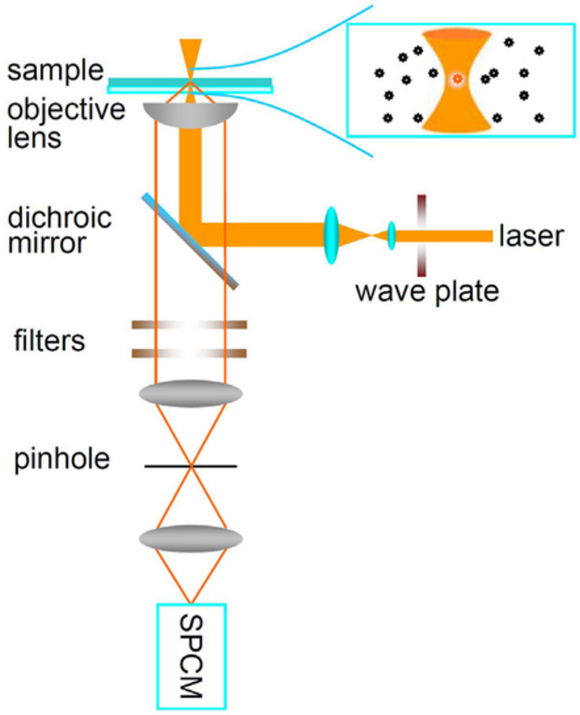


Figure 1.5: Schematic of a confocal fluorescence microscopy set-up. Adapted with permission from Ref [41].

### 1.3.3 Optical Diffraction Limit and Super-Resolution

As a consequence of the wave-like nature of light, fluorescence microscopes (and indeed, all optical microscopes) must contend with the diffraction limit, which hinders the ability of a microscope from distinguishing individual features of spatially separated distances on the order of the wavelength of light. Put forth by Abbé[44], the constructive and destructive interference of light will render the lateral image of an isotropic point emitter as a spot of a finite intensity volume with a series of concentric rings of decreasing intensity (known as an Airy disk). In most fluorescence applications, the signal-to-noise ratio and/or detector sensitivity precludes observing this Airy pattern, and it instead appears as a Gaussian. The image of this pattern is what is referred to as the microscope's point-spread function (PSF).

The size of this spot depends on the wavelength of light used to report on the emitter ($\lambda$) and the numerical aperture (NA) of the microscope:

$$D = \frac{\lambda}{2NA} = \frac{\lambda}{2n\sin\theta}, \tag{1.5}$$

where $NA$ is defined as $n \sin\theta$, with $n$ being the refractive index of the imaging medium and $\theta$ the aperture angle of the microscope objective. The achievable resolution can therefore be improved by changing the $NA$ - through changing the refractive index of the medium between the objective and the sample coverslip (for example, oil has $n \sim 1.5$ instead of $\sim$1.0 for air) or increasing the aperture angle of the objective, or one can decrease the wavelength of light used in the measurement. State-of-the-art microscope objectives nowadays can possess numerical apertures higher than 1[45] (e.g., the $NA = 1.4$ oil immersion lenses used in Chapters 3, 4, 5, so the diffraction limited spot size of an optimized microscope can be a bit better than $\lambda/2$. Note that Equation 1.5 refers to the lateral resolution; in the axial direction the resolution is $D_{axial} = \dfrac{2\lambda}{2NA^2}$.

While the ability to distinguish features as close as $\sim$200 nm is sufficient for many applications, there are a variety of extraordinarily critical processes that occur on length scales much smaller than 100s of nm. For example, exciton migration in photosynthetic membranes[46], chemical transport across synaptic clefts in synapse cells[37], the self-assembly dynamics of emerging supramolecular systems[47], and many more. The ability to visualize structures responsible for these processes is necessary to elucidate a more complete mechanistic understanding. The aforementioned systems are generally not amenable to electron microscopies, which, although capable of achieving 10s of nm resolution with comparative ease, damage organic materials during image acquisition. Optical microscopies, on the other hand, are comparatively much less invasive. Moreover, if the processes of interest are a consequence of optical excitation, then it behooves us to be able to both trigger and observe these excitation events below the diffraction limit on length scales commensurate with the size of the key structures.

Super-resolution fluorescence microscopy enables surmounting the optical diffraction limit, which, for much of the 20th century, remained an obstacle. This development has profoundly transformed our ability to visualize structures in numerous contexts, so much so that it was recognized with the 2014 Nobel prize in Chemistry[48]. Here I will only briefly touch on this topic, as Chapters 3, 4, 5 go into more explicit detail. While there are a number of super-resolution imaging techniques, and more variations and developments are still emerging, the far-field super-resolving techniques relevant for this dissertation are PALM/STORM and STED.

Photo-activated localization microscopy (PALM) and stochastic optical reconstruction microscopy (STORM) are very similar in spirit to one another. Both techniques rely on building a super-resolution image via the switching of fluorophores between an active "ON" state to and an inactive "OFF" state. The idea is to assume that each diffraction limited emission spot represents the probability distribution of the location of an individual fluorophore, and furthermore, to only image, at any given time, a sparse subset of individual emitters. Each emitter PSF is fit with a 2D Gaussian function, where the centroid of the Gaussian represents the emitter location, and the precision of this assignment scales with the number of photons detected (i.e. brighter emitters leads to more precise fits). This is referred to as *super-localization*. PSF localizations on the order of 10s of nm are common,

which is vastly superior to the $\sim$ 200 nm diffraction limit. The key to achieving super-resolution, however, is to introduce/engineer temporal emission sparsity. In doing so, the issue of multiple overlapping PSFs is circumvented, which would otherwise preclude single-emitter localization. A series of images are collected, each containing a small subset of the total number of emitters present in the region of interest, and each image is analyzed via super-localization. By generating an image which is the accumulation of all emitter PSF localizations, we achieve a super-resolved image.

Stimulated emission depletion (STED) microscopy, on the other hand, is a different far-field super-resolution technique that does not rely on post-processing analysis of a series of images, but rather uses a donut-shaped depletion beam coaligned with the excitation source to narrow the microscope PSF in real-time via stimulated emission. The image is constructed by raster scanning these two beams together over the target sample. Figure 1.6 schematically demonstrates these two different classes of super-resolution.

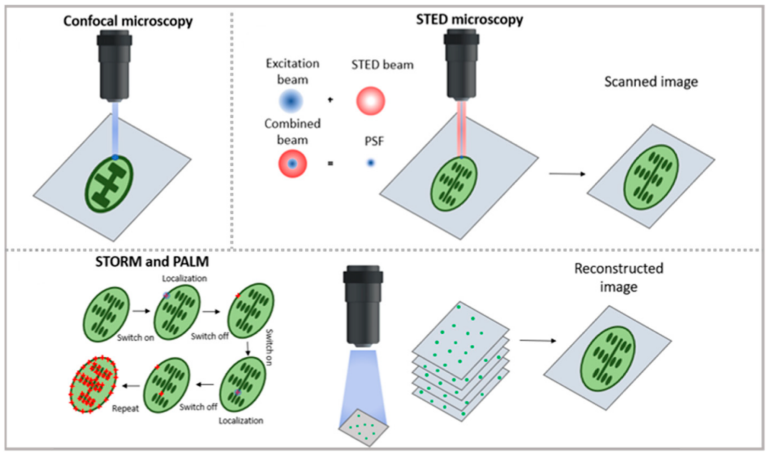


Figure 1.6: Schematic demonstrating the differences between STED super-resolution microscopy and PALM/STORM. Adapted from Ref [49] with permission.

In Chapter 3, we employ the super-localization post-processing used in PALM and STORM to localize the position of individual fluorescent probes well below the diffraction

limit. While we are not super-resolving any given structure per se, we are able to observe particle displacement on the order of 10s of nm. In Chapters 4 and 5, we employ a highly modular transformation of STED microscopy to not only image optoelectronically coupled materials below the diffraction limit, but to observe the migration of sub-diffraction limted volumes of excitons.

## 1.4 Diffusion

Much of the work in this dissertation concerns the characterization of the migration of particles or quasi-particles in heterogeneous media. Diffusion is the random migration of particles as a consequence of their motion due to thermal energy[50] and leads to spreading from areas of high concentration to areas of low concentration. One cannot overstate the importance of diffusion in the function of biological, chemical, and material systems.

It is useful to first consider a microscopic treatment of diffusion, as Chapter 3 concerns the study of the motion of individual fluorescent probes in a polymer matrix, and then to build to a macroscopic treatment, as Chapters 4 and 5 rely on characterizing the diffusion of excitons via the spatiotemporal evolution of a distribution profile.

### 1.4.1 Random Walks

Brownian motion is used to describe the random motion of particles suspended in a medium, and the particles that participate in this motion have a limited memory of their past (i.e. a Markovian process) owing to the frequent collisions within their environment[51]. The equations that describe this diffusive motion can be developed by considering a random walk in one dimension.

Let's assume we have a random walker starting at position $x = 0$. For each step with probability, $p$, the walker moves $+l$, and similarly with each step with probability, $q$, the walker moves -$l$. Each step occurs with the same time, $\tau$. Let's define $n_+$ to be the number of steps in the $+x$ direction, $n_-$ to be the number of steps in the -$x$ direction, and finally $N$ to be the total number of steps such that $N = n_+ + n_-$. As they are probabilities, we have the condition:

$$p + q = 1, \tag{1.6}$$

and if we are in an "unbiased" random walk regime, we assert:

$$p = q = \frac{1}{2}. \tag{1.7}$$

Figure 1.7 depicts examples of 1D random walk trajectories within this framework.

Let's consider a random trajectory for our walker. Let's say it moves with a sequence $+l$, $+l$, -$l$, -$l$, $+l$, -$l$, -$l$, $+l$, $+l$, $+l$. We note that $n_+ = 6$, $n_- = 4$, and the total steps are $N = 10$. To estimate the probability of this particular trajectory is then:

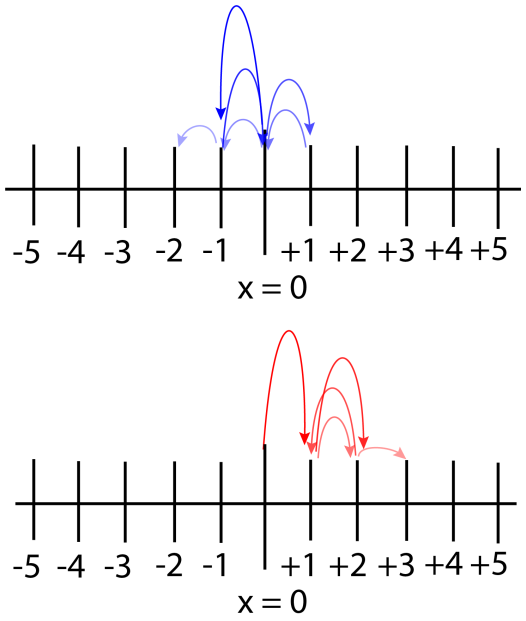


Figure 1.7: Cartoon schematic of random walk trajectories in 1D.

$$(p)^{n_+}(q)^{n_-} = \left(\frac{1}{2}\right)^6 \left(\frac{1}{2}\right)^4 \tag{1.8}$$

Here let's now consider the notion of displacement, which is the distance from the initial starting point. The displacement, $x$, is defined as:

$$x = (n_+ - n_-)l = (2n_+ - N)l, \tag{1.9}$$

which for this case is $x = +2l$. To more generally assess the likelihood of a given displacement, we turn to the binomial probability distribution:

$$P(n_+, N) = \left(\frac{N!}{n_+!n_-!}\right) p^{n_+} q^{n_-}, \tag{1.10}$$

which describes the probability of achieving $n_+$ out of $N$ total steps (i.e. the displacement via Equation 1.9.)

Figure 1.8 represents the probability distribution of a walker's displacement for a series of random walks with a different numbers of steps. A few key points are illustrated by comparing these distributions. First, regardless of the number of steps, the most likely displacement from the origin is net zero. Second, as we allow a walker to take a greater number of steps, the relative spread in the displacement increases only modestly - it does not increase linearly with the number of steps taken. These observations are captured in the mean displacement and root-mean-square displacement.

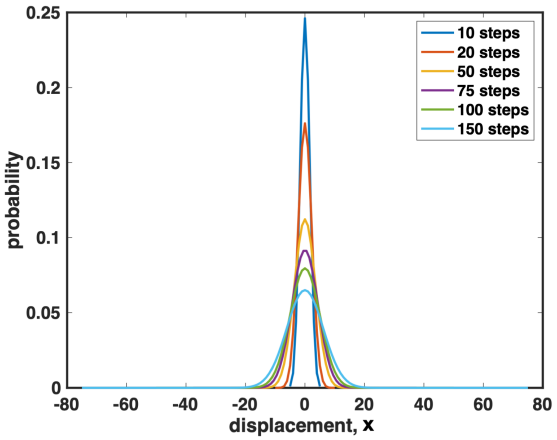


Figure 1.8: Binomial probability distributions of the displacement from the origin for different numbers of steps.

The mean displacement is:

$$\langle x_N \rangle = (2\langle n_+ \rangle - N)l \tag{1.11}$$

$\langle n_+ \rangle$ is the probability weighted average of $n_+$ for all $N$.

$$\langle n_+ \rangle = \sum_{n_+=0}^{N} n_+ P(n_+, N) = \sum_{n_+=0}^{N} \left( \frac{n_+ N!}{n_+! n_-!} \right) p^{n_+} q^{n_-} \tag{1.12}$$

To simplify, the term for $n_+ = 0$ is just $0, \frac{n_+}{n_+!}$ is $\frac{1}{(n_+ - 1)!}$, and if we pull out a $pN$ from the summation, the mean steps in the $+x$ direction is:

$$\langle n_+ \rangle = pN \sum_{n_+=0}^{N} \left( \frac{(N-1)!}{(n_+ - 1)! n_-!} \right) p^{n_+ - 1} q^{n_-} \tag{1.13}$$

If we substitute $\alpha$ for $(N-1)$ and $\beta$ for $n_+ - 1$, then:

$$\langle n_+ \rangle = pN \sum_{\beta=0}^{\alpha} \left( \frac{\alpha!}{(\beta)! n_-!} \right) p^{\beta} q^{\alpha - \beta} \tag{1.14}$$

The expression in the summation is reminiscent of our original binomial distribution, and the sum is equal to 1. Therefore, $\langle n_+ \rangle = pN$. Returning to Equation 1.11, we have:

$$\langle x_N \rangle = (2\frac{N}{2} - N)l = 0. \tag{1.15}$$

If we were to consider a number of walkers, characterizing the spread in their collective motion can be described by the root-mean-squared displacement. Because walker displacement is symmetric about the origin with positive and negative values, squaring the displacement serves to provide a finite positive value. The mean-squared displacement is then:

$$\begin{aligned} \langle x_N^2 \rangle &= \langle [(2n_+ - N)l]^2 \rangle \\ \langle x_N^2 \rangle &= (4\langle n_+^2 \rangle - 4\langle n_+ \rangle N + N^2)l^2 \end{aligned} \tag{1.16}$$

Here $\langle n_+^2 \rangle = (pN)^2 + pqN = N^2/4 + N/4$ (determined using the same treatment as Equation 1.12). And so we arrive at:

$$\langle x_N^2 \rangle = Nl^2, \tag{1.17}$$

which makes the root-mean-squared:

$$\sqrt{\langle x_N^2 \rangle} = \sqrt{Nl^2}. \tag{1.18}$$

Recall that in this picture each step takes the same amount of time, $\tau$, which is to say that $N$ steps occur within a time $N\tau$. The root-mean-square displacement thus scales in time as $\sqrt{N\tau}$. In other words, diffusion (over great distances) is slow!

Translating a random walk from 1D to 2D and 3D is straightforward given the assertion that motions along $x$, $y$, and $z$ coordinates are statistically independent from one another. Figure 1.9 depicts the path taken from a random walk in 2D for a simulated walker, where each step along the $x$ and $y$ coordinates was generated randomly and independent from the others.

### Diffusion coefficient

Now, how do different kinds of particles in different environments and different conditions diffuse? Thus far, the treatment has been agnostic to these concerns and would suggest all particles are displaced by the same distances at the same rate. This is of course, not true, and the variability among different diffusing species (or the same species but in different environments) is in part captured in the diffusion coefficient, $D$. As we'll soon see, the diffusion coefficient is sensitive to particle size, characteristics of the surrounding medium, and the temperature, among other factors.

We can define a diffusion coefficient as:

$$D = \frac{l^2}{2\tau}. \tag{1.19}$$

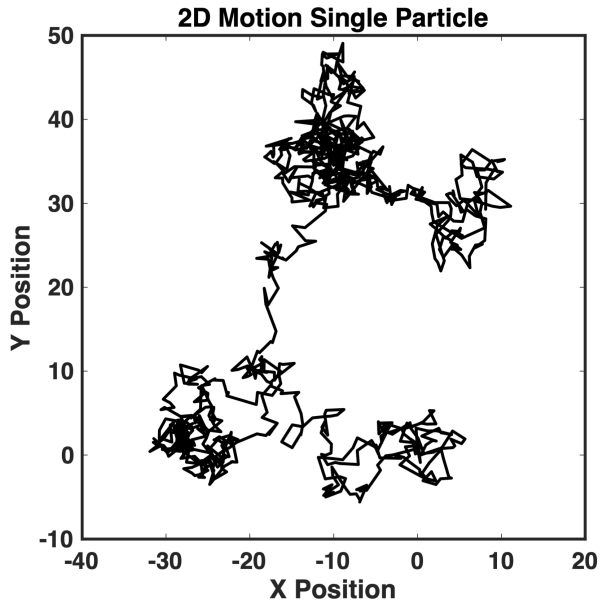


Figure 1.9: Simulation of a 2D random walk.

Recall $l$ is our displacement distance and $\tau$ is the time for a given step. If a system were to have a higher diffusion coefficient, this would suggest a greater displacement distance, $l$, can be achieved within the same time window, $\tau$, for a given particle's motion. We now rework our mean-squared displacement from equation 1.17 and introduce a general time, $t$, which is equivalent to $N\tau$, and arrive at:

$$\langle x^2 \rangle = \frac{l^2 t}{\tau} = 2Dt \tag{1.20}$$

For 2 dimensions, we have our mean-square displacement, $\langle r^2 \rangle$, defined as:

$$\langle r^2 \rangle = \langle x^2 \rangle + \langle y^2 \rangle = 2Dt + 2Dt = 4Dt \tag{1.21}$$

and for 3 dimensions, we have $6Dt$. Equation 1.20 is significant, given it states that the randomly governed displacements in a particle's position, or fluctuations, are expressly related to the diffusion coefficient. One of the most powerful results of statistical mechanics is the fluctuation-dissipation theorem, wherein thermodynamic fluctuations in a physical quantity can predict the response to a system perturbation, and vice versa[52].

An outcome of the fluctuation-dissipation theorem is the Stokes-Einstein relationship, which defines a diffusion coefficient as the ratio of thermal movement against the resistance to movement due to the viscosity of a solvent:

$$D = \frac{k_B T}{6\pi\eta R_H}, \tag{1.22}$$

where $T$ is absolute temperature, $\eta$ is the solvent viscosity, and $R_H$ is the hydrodynamic radius of the particle. This relationship enables characterizing local material properties as a function of particle mobility. For example, in cellular systems, particles with identical characteristics may exhibit differences in their diffusion coefficients as a function of their occupancy within particular cellular compartments. Such differences reveal important information about the relative viscosity in various cell locations[53, 54], which plays a critical role in regulating chemical transport[55] and providing structural support[56].

### 1.4.2 Fick's Law and the Diffusion Equation

Our approach to the macroscopic description of diffusion will rely on Fick's law as well as how a given density of particles changes due to a flux.

Figure 1.10 demonstrates a discretized grid with each cell containing many particles, initially all isolated on the left side of the space via a dividing barrier. If the volume of each grid voxel is $l^3$, then we can define the particle density on the left and right sides of the barrier as:

$$\begin{aligned} \Phi_L &= \frac{n_L}{l^3} \text{ and} \\ \Phi_R &= \frac{n_R}{l^3} \end{aligned} \tag{1.23}$$

where $n_L$ and $n_R$ are the left- and right-hand number of particles.
The gradient of the total particle density in 1D is:

$$\nabla\Phi = \frac{\Phi_R - \Phi_L}{l} \tag{1.24}$$

For each of the cells closest to the dividing barrier for the left and right sides, $n_L/2$ particles will cross from the left to right, and $n_R/2$ particles will cross from right to left. We define the net flux, $j$, to be the net number of particles crossing the dividing surface per unit time and unit area:

$$j = \frac{1}{\tau l^2}\left(\frac{n_L}{2} - \frac{n_R}{2}\right) = \frac{l^3}{\tau l^2}\left(\frac{\Phi_L - \Phi_R}{2}\right) = \frac{l^2}{2\tau}\left(\frac{\Phi_L - \Phi_R}{l}\right) \tag{1.25}$$

From equation 1.19, $\frac{l^2}{2\tau}$ is our diffusion coefficient, $D$, and $\left(\frac{\Phi_L - \Phi_R}{l}\right)$ is the negative of Equation 1.24. We now arrive at Fick's law:

$$j = -D\nabla\Phi. \tag{1.26}$$

To characterize how the particle density changes in a given time interval, we essentially need to account for the change in the flux in all directions (i.e. a continuity equation):

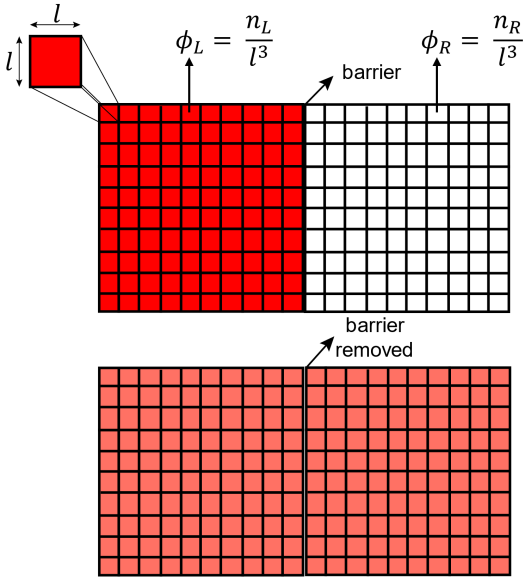


Figure 1.10: Schematic representation of a density of particles readjusting after a dividing barrier between the left and right is removed.

$$\frac{\partial \Phi(r,t)}{\partial t} = -\vec{\nabla} \cdot \vec{j} \tag{1.27}$$

and finally, combining Equations 1.26 and 1.27, we arrive at the diffusion equation:

$$\frac{\partial \Phi(r,t)}{\partial t} = D\nabla^2 \Phi(r,t). \tag{1.28}$$

Equation 1.28 states that provided we know the diffusion coefficient for our system and the density profile of our particles, we can describe the spatial evolution of the density at every point in time! Furthermore, the time-rate of change is related to the gradient in the distribution profile, such that distributions with sharper gradients will change more dramatically over a given duration of time. This concept is illustrated in Figure 1.8, where the change in the probability distribution from 10 steps to 50 steps is much more prominent than the change in the distribution from 50 steps to 100 steps. We'll discuss this phenomenon in more detail in Chapter 4, as diffusion of quasi-particles follows the same formalism as diffusion of actual particles, though on extremely disparate timescales.

## 1.5 Remaining Chapters Overview

Chapter 2 describes measurements characterizing the excited state evolution of a protein-bound chromophore using transient absorption spectroscopy. These measurements are conducted using a series of chromophore-protein chemical linking groups that vary in their length and rigidity, which enables control over the degree of coupling between the chromophore its protein/solvent environment. The findings here inform design principles for biomimetic light harvesting systems as well as the underlying photophysics potentially employed in natural systems for efficient excitation transport.

Chapter 3 describes a measurement that leverages correlative widefield single-particle tracking and AFM phase imaging to determine how the nano- and microscale semicrystalline morphology in electrolytic poly(ethylene oxide) (PEO) thin films influences the motion of small particles. The findings here not only emphasize the power of correlative imaging, but suggest that polymer crystallinity, if controlled well, need not necessarily be a detriment to the transport of small particle species despite this historically being a challenge for PEO solid-state electrolytes.

Chapter 4 provides an overview of time-resolved ultrafast STED (TRUSTED), an ultrafast transformation of STED super-resolution microscopy to track exciton migration at the nanoscale in optoelectronically coupled materials. TRUSTED takes advantage of well-defined optical quenching boundaries such that exciton displacements, even over small distances, will register as a change in the number of excitons quenched. I will describe the basics as well as the nuances I came to discover in trying to apply this method to a series of electronically coupled materials.

Chapter 5 will discuss the ongoing investigation, at the time of this writing, of exciton transport in Tellurium doped CdSe/CdS core-shell quantum dot superlattices. We investigate exciton transport using TRUSTED and complement this measurement with time-resolved emission spectroscopy and single-particle emission spectroscopy to characterize how the energetic disorder imposed by dopants modulates exciton transport. I will present our hypotheses regarding the role dopants play in perturbing the spatioenergetic landscape of the superlattices and will discuss the challenge in applying any single conventional model of energy transport to model our data.

# Chapter 2

# Controlling ultrafast photoinduced dynamics via linker engineering in a biomimetic light harvesting platform

*Portions of this chapter are adapted or reprinted with permission from Delor et al., "Exploiting Chromophore–Protein Interactions through Linker Engineering To Tune Photoinduced Dynamics in a Biomimetic Light-Harvesting Platform,"* J. Am. Chem. Soc. ***2018**, 140 (20), 6278–6287* 

This chapter discusses a highly collaborative work involving multiple research groups here at Berkeley. I'll begin by first introducing the motivation behind synthetically emulating natural photosynthetic systems and their remarkable excitation energy transport properties, and, then, describe the circular permutant of the tobacco mosaic virus (cpTMV), which serves as our biomimetic platform to systematically investigate structural paradigms critical to light harvesting. We use ultrafast transient absorption (TA) spectroscopy to measure the excited state dynamics of sulforhodamine B (SRB) bioconjugated to cpTMV with a prototypical series of chemical linking groups varying in length and rigidity. We find that the timescales of the excited state evolution reported by TA measurements are related to the degree of chromophore-protein-solvent coupling induced by the different chemical linkers. I will then show how these findings are strongly supported by molecular dynamics simulations. Finally, I will detail how our study not only demonstrates that more rigid chromophore-protein chemical linking groups could benefit biomimetic light harvesters, but also suggest design principles possibly employed by natural photosynthetic systems for long range excitation energy transport.

## 2.1 Introduction

One of the "holy grails" of science is elucidating the precise mechanism(s) by which natural photosynthetic systems harvest solar energy and transfer electronic excitation energy to

redox reaction centers. Natural systems can approach near-perfect quantum efficiencies[46] in this regard, a feat we have yet to accomplish with state-of-the-art organic and inorganic light harvesting materials alike.[1] This is all the more remarkable when considering the relative complexity of photosynthetic machinery, as natural light harvesters are often composed of highly intricate networks of solvated protein-pigment complexes. Furthermore, determining how photosynthetic organisms achieve electronic energy transport with such fidelity in warm, wet, "biologically noisy" environments[58] in particular remains an intensely researched (and sometimes controversial) topic. In many typical inorganic semiconductors, like monocrystalline silicon, material homogeneity and structural order is paramount for the efficient transport of excitons or conduction of charge, but nature's design principles do not necessarily follow this rule to a T. The way in which the electronically active pigments couple to their protein-solvent environments, or bath, is critical to understanding how photosynthetic systems overcome and even harness dynamical fluctuations for efficient transport.

Figure 2.1 shows the crystal structures of *Rhodopseudomonas palustris* (purple bacteria) light harvesting complex 1 (LH1, central ring) and light harvesting complex 2 (LH2, peripheral rings), a system this chapter will continue to make reference and comparison to.[59, 60] Bacteriochlorophylls are shown in green, and the proteins are silver helices. The central yellow and red structures are the reaction center. Note that many other components of this system, like carotenoid structures, are omitted for clarity. Bacteriochlorophylls on peripheral LH2 units absorb photons and transfer the resulting electronic excitation energy via excited-state energy transfer throughout the network of other bacteriochlorophylls in LH2, as well as those found in LH1. This excited-state eventually results in a charge separation, which is used to drive biochemistry in the reaction center. The bacteriochlorophylls in LH2 form what are referred to as the B800 and B850 rings, as these chromophores primarily absorb at $\sim$ 800 nm and $\sim$ 850 nm, respectively. Similarly, bacteriochlorophyll in LH1 form a B875 ring, absorbing predominantly at $\sim$ 875 nm.[60, 61] As the LH1 complex absorbs at a lower energy than LH2, there is an energy gradient formed where excitations occuring within LH2 complexes are funneled to LH1 and the reaction center. Depending on the incident photon flux, purple bacteria can actually control the relative production and nature of LH2 complexes[62] to balance the overall absorbing ability of the organism with excess energy mediation. Although much appears to be known about purple bacteria, attempts to synthetically emulate this and other natural systems' long range excited-state energy transfer have proven challenging, suggesting there are more subtle design principles at play involving the substituent chromophores, proteins, and solvent all working in concert.

[1]Note, "efficiency" in this context is defined as the probability of converting an absorbed photon into a charge separated state[57]. The efficiency of generating chemical fuel defined as the probability per photon absorption event is another matter.

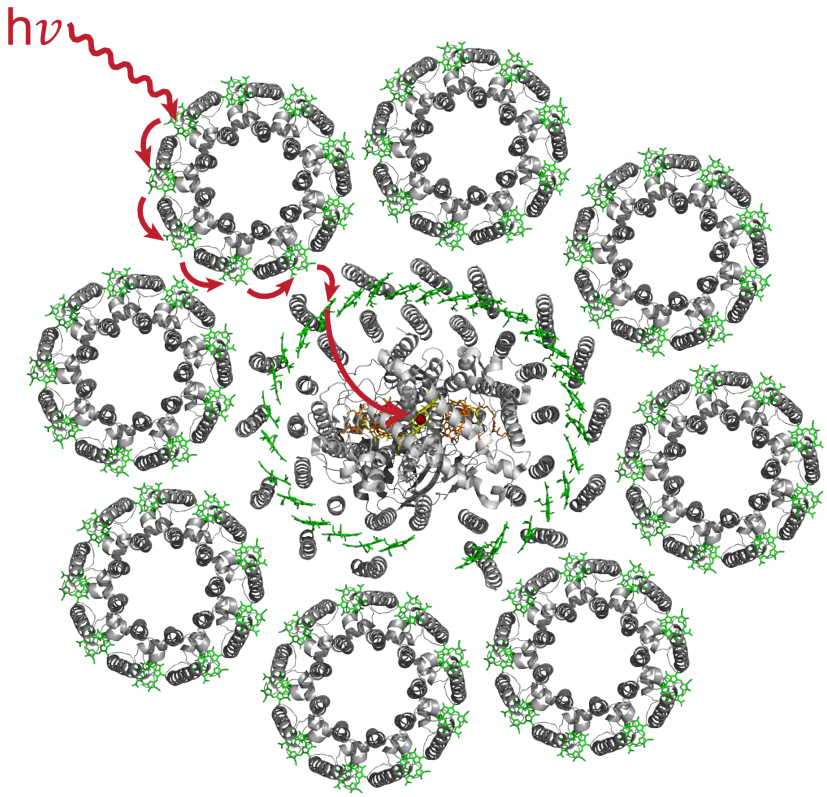


Figure 2.1: Crystal structures of the light harvesting complexes 1 and 2 (LH1 and LH2, respectively) of purple bacteria. Figure adapted with permission from [59].

### 2.1.1 Biomimetic approaches to understanding natural photosynthesis

Much has yet to be learned by systematically elucidating the factors governing natural photosynthetic systems' exceptional properties; unfortunately, perturbing the intricate configurations of photosynthetic organisms by removing chromophores or mutating protein residues often destabilizes the overall molecular architecture or alters multiple variables at a time. The resulting difficulty in performing controlled experiments obfuscates how function emerges from such complex structures.

One alternative strategy to learn about nature is to create biomimetic light-harvesting assemblies using modular scaffolds that enable the systematic changing of one structural variable at a time. These scaffolds can range from all-molecular constructs [63–65] to protein-chromophore supramolecular structures.[10, 20, 66–71] With regard to protein-chromophore

assemblies, viral coat proteins in particular have proven to be fertile model systems. One example is shown in Figure 2.2 from Ref. [68], in which Belcher and co-workers use the coat protein of the M13 virus and genetically modified it in such a way to create clusterings of chromophore attachment sites with demonstrably enhanced energy transport properties.

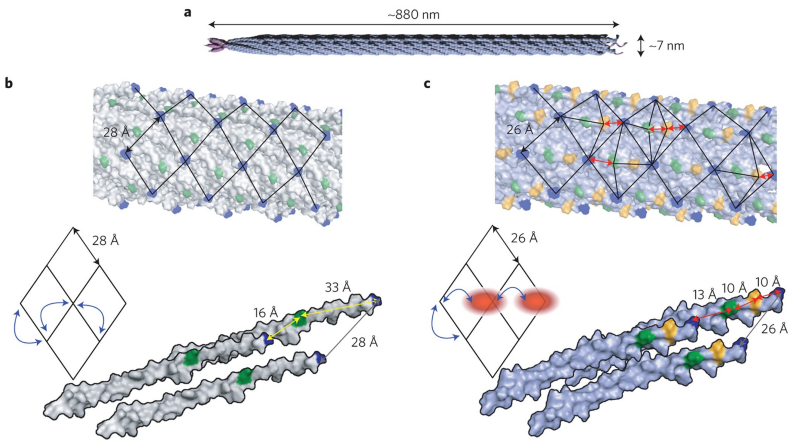


Figure 2.2: Example of using engineered M13 viral coat proteins as a scaffold for energy transfer. Adapted with permission from Ref. [68].

Another example of a modular viral coat protein is the Tobacco Mosaic Virus (TMV) coat protein (Fig 2.3), in which functionalized monomer protein subunits self-assemble into higher order structures, like double-disks or longer micron scale rods, depending on the preparation conditions[10]. By labelling monomer units via bio-conjugation with either donor or acceptor chromophores, this relatively rigid TMV scaffold facilitates proximal placement of chromophores to enable the transfer of excitation energy between adjacent chromophores.

Unfortunately in practice the energy collection and transfer efficiencies over nanometer-to-micron length-scales achieved in nature are extremely difficult to reproduce in artificial systems. This challenge is largely due to the requirement that synthetic platforms both accommodate large chromophore densities and establish the precise positioning and energetic properties that protect fragile electronic excitations and optimize excitation energy transfer.[72–77]

### 2.1.2 Long and flexible protein-chromophore linkers preclude facile control over chromophore position and orientation

Although much progress has been made on biomimetic light-harvesting scaffolds, control of the specific configuration of chromophores relative to one another and relative to the protein itself has been lacking and has differed substantially from natural light-harvesting

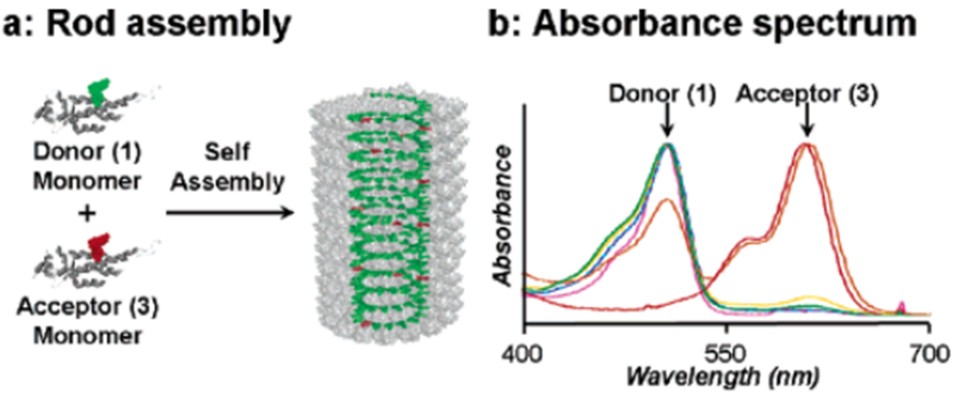


Figure 2.3: TMV protein monomers labelled with either donor or acceptor chromophores will self assemble into higher-order rod structures. The rigid protein scaffold enables chromophores to be placed within the requisite proximity to one another for excited-state energy transfer. Donor chromophores absorb significantly bluer than the acceptor chromophores, making them ideal donor-acceptor pairs. Figure adapted from Ref [10] with permission.

complexes, where bound chromophores often fit tightly into protein pockets.[78–81] Most biomimetic attempts employ dyes used in fluorescent bioimaging, where long and flexible tethers connecting the chromophore to the protein scaffold are common.[10, 66, 67] Such bioconjugation schemes often preclude precise control over positioning and orientation, as the chromophores can sample large and random conformational volumes. An example of a typical chromophore used for biological labelling, Alexa Fluor 488, is shown in Figure 2.4, where the Alexa Fluor 488 is maleimide functionalized with a 5-carbon alkane linking group. Maleimide has proven to react successfully with activated cysteine residues on target proteins to covalently anchor fluorescent dyes. The 5-carbon alkane linker is comparatively long and flexible in light of the Alexa Fluor 488's size and rigidity such that the Alexa Fluor can presumably freely sample the protein-solvent interface.

The orientational mismatch between chromophores in light harvesting assemblies has a pronounced effect on the energy transfer rate. When the interchromophore coupling is within the "weak-coupling" regime (often when chromophores are arranged in such a way that there isn't pronounced molecular orbital overlap between adjacent chromophores) Förster resonance energy transfer, or FRET, is typically invoked. The rate of energy transfer described by FRET is:

$$k_{FRET} = \frac{1}{\tau_D}\left(\frac{R_o}{R}\right)^6 \tag{2.1}$$

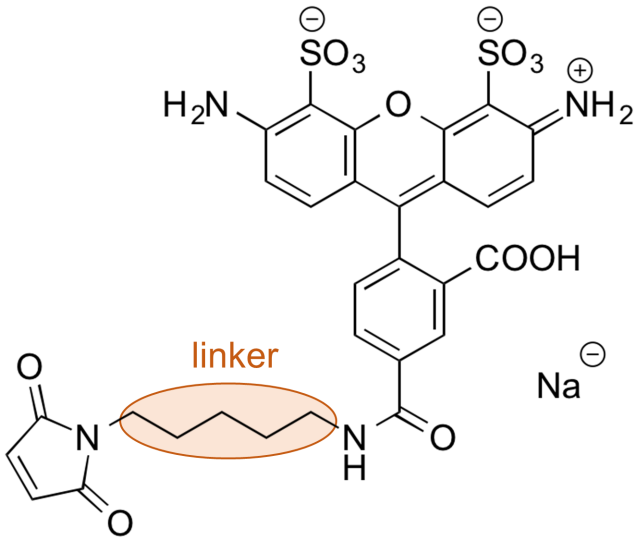


Figure 2.4: Commercially available maleimide-functionalized Alexa 488 for use in bioconjugation. 5-carbon alkyl linker between maleimide and Alexa Fluor 488 is highlighted in orange.

where $\tau_D$ is the lifetime of the donor chromophore, and $R$ is the interchromophore distance (or more specifically, the distance between the centers of the two point-dipoles used as approximations of the chromophore's charge redistribution from ground to excited states). Here,

$$R_o^6 \propto \Phi_D \kappa^2 J(\lambda), \quad \text{and} \tag{2.2}$$

$$\kappa^2 = (\cos\theta_T - 3\cos\theta_A \cos\theta_D)^2 = (\sin\theta_A \sin\theta_D \cos\Phi - 2\cos\theta_A \cos\theta_D)^2 , \tag{2.3}$$

where $\Phi_D$ is donor quantum yield, $J(\lambda)$ is the spectral overlap between the absorption of the acceptor chromophore and the emission of the donor chromophore, and $\kappa^2$ describes the orientation of the transition dipole moments of the donor and acceptor chromophore. A graphical representation of the angles formed between two transition dipoles used to calculate $\kappa$ in Equation 2.3 are shown in Fig 2.5.

In nature, where chromophores are often held in place inside protein pockets with little orientational freedom, the $\kappa^2$ parameter could in principle be significantly greater than if chromophore transition dipoles in the ensemble were isotropically distributed over the length and time scales commensurate with energy transfer. Isotropically distributed dipoles have a

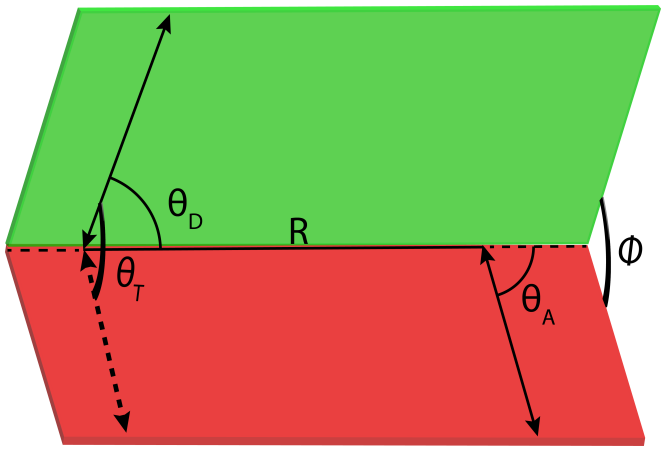


Figure 2.5: Orientational dependence of dipole-dipole coupling. $\theta_A$ and $\theta_D$ are the angles formed between the donor and acceptor dipoles with the line connecting the donor and acceptor, $\theta_T$ is the angle formed between the donor and acceptor dipoles, and $\Phi$ is the angle formed between the planes containing the donor and acceptor dipoles

$\langle\kappa^2\rangle$ of 2/3, but per Equation 2.3, $\langle\kappa^2\rangle$ can range from 0 to 4, where 4 represents the most strongly coupled relative orientation of transition dipoles.

A clear need therefore exists for crafting chromophore–protein linkers that can establish and maintain interchromophore orientations and separations through conformational restrictions.

## 2.2 cpTMV as a biomimetic light harvesting scaffold

As mentioned previously, the self-assembled structures of the TMV coat protein have proven to be exceptionally versatile platforms for the study of light-harvesting[10, 20, 71, 82–84]. In this chapter, we'll focus on the use of the circular permutant of TMV (cpTMV), which self-assembles into an 18 nm-wide $C_2$ symmetric double-ring structure. By introducing a uniquely reactive cysteine residue, we are able to attach chromophores covalently at specific locations on the protein monomers, which can then self-assemble in different supramolecular configurations depending on the pH and ionic strength conditions. The assembly consists of 34 monomers (17 per ring) with a hydrated cavity extending radially outward from the central pore.

### 2.2.1 Light harvesting toolkit

The cpTMV platform is combined with chromophore–protein linker engineering to conduct a systematic study of the effects of conformational constriction and attachment orientation

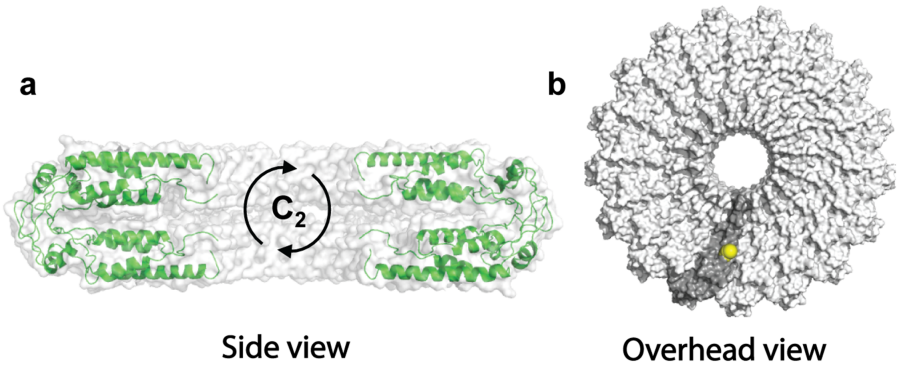


Figure 2.6: Structure of cpTMV, (a) side view and (b) overhead view. A single monomer unit of the cpTMV disk is shaded in grey in (b), with an example chromophore labelling site in yellow.

on chromophore photophysics. Because a major aim is to mimic environmentally protected photosynthetic chromophores, this chapter will primarily focus on systems where only *one* chromophore is present per cpTMV assembly, thus allowing detailed characterization of the chromophore–protein interactions, free of complicating factors such as interchromophore interactions. Investigations of fully-labelled assemblies of cpTMV, where each of 34 monomers are labelled with a chromophore, were performed, but, at the time of this study, it became clear that modified future experimental approaches would be needed in order to accurately deconvolve various photophysics on the fully-labeled assemblies. My colleague **Leo Hamerlynck**, however, has more recently studied fully-labelled cpTMV assemblies using transient absorption anisotropy, and I suggest the reader consult his work!

### Protein labelling sites

We use one of two labelling sites to explore distinct environments: the protein-water interface ("outstide" labeling site S23C) and the nanoscale hydrated protein cavity ("inside" labeling site Q101C). Figure 2.7 shows these labelling sites on top-bottom monomer pairs of TMV, with a chromophore conjugated for scale. The chromophore is highlighted in yellow for outside labelling, and blue for inside labelling, a color-scheme used throughout. Previous studies measured the excited state dynamics of cpTMV bound chromophores at both the inside and outside labelling sites[20], but here we extend this work by introducing variable chemical linking groups instead of the 5-carbon chemical linkers used previously.

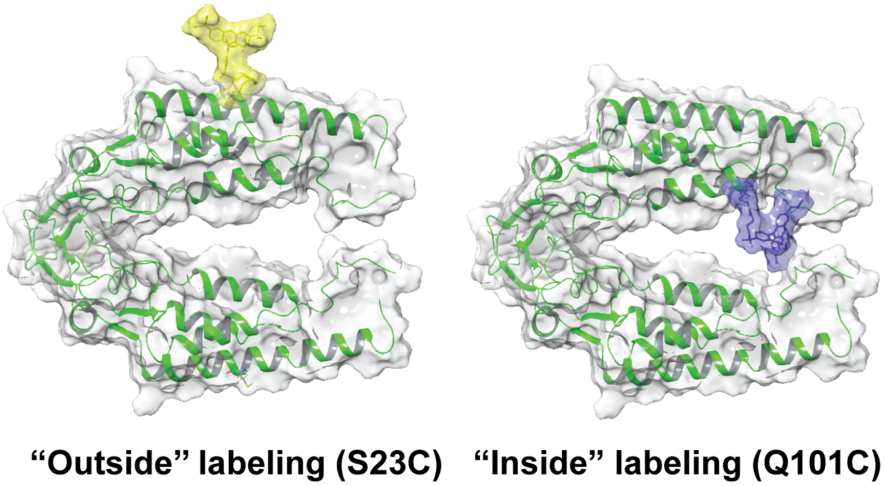


Figure 2.7: Outside and inside labelling sites of cpTMV.

### Chromophore and linkers

The chromophore in question is Sulforhodamine B (SRB), chosen for its high visible light absorption cross-section ($\epsilon_{570}$ nm 83 000 $M^{-1}$ $cm^{-1}$ in water) and relative rigidity due to few rotational degrees of freedom in the electronically active moieties (see Section 2.4.1). Figure 2.8 shows the series of linkers used to control the distance of the chromophores from the protein surface and their conformational volume. In all cases, these linkers are shorter and more rigid than in typical bioimaging labels, which use pentyl or longer alkyl chain linkers. In this series, changing from a 4-carbon butyl (Bu) to a 2-carbon ethyl (Et) moiety straightforwardly shortens the linker. Allylic 1,3-strain when using cyclohexyl (Cyc) moieties further reduces conformational freedom compared to alkyl chains. The chiral center of these linkers provides an additional degree of control, as the two enantiomers (Cyc-SS and Cyc-RR) are expected to lead to different attachment orientations on the protein surface.

Altogether 12 systems are investigated: SRB attached to two separate positions (S23C and Q101C, Figure 2.7) on cpTMV via four different linkers (Bu, Et, Cyc-SS, Cyc-RR, Figure 2.8b), along with control experiments using free maleimide-functionalized chromophores after reaction with the sodium salt of 2-mercaptoethanesulfonate in buffer. All experiments are performed in solution using a sodium phosphate buffer. These 12 systems form a series with systematically varied chromophore–bath couplings, enabling extraction of detailed information about how the protein environment affects the nuclear-electronic dynamics of each assembly. At the time of this study, **Jing Dai** in the Francis group performed all protein expression and dye/linker synthesis.

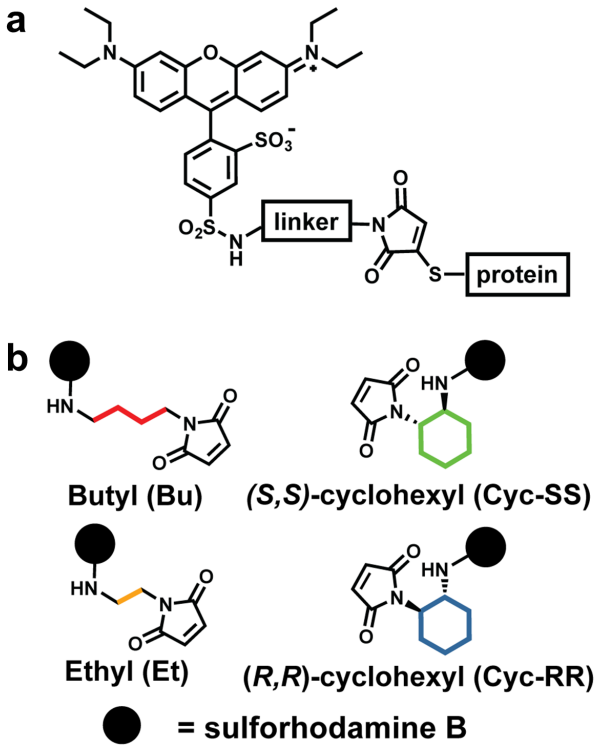


Figure 2.8: Chromophore-linker system. (a) Sulforhodamine b (SRB) bioconjugated to a protein residue via a maleimide functionalized with a variable linker. (b) 4 different linkers between SRB and maleimide: Butyl, Ethyl, *(S,S)*-cyclohexyl, and *(R,R)*-cyclohexyl

.

## 2.3 Transient absorption spectroscopy probes excited-state evolution of chromophores

Transient absorption (TA) is a powerful non-linear optical spectroscopy used to study a tremendous number and variety of systems[85]. TA has been used extensively to study energy transfer processes in photosynthetic systems[86], but also a range of organic and inorganic semiconductors and their photophysics[87, 88], charge separation in photo-catalysts[89, 90], and even fundamental molecular reactions like electrocyclic ring-openings[91]. The time resolution of TA can range from nanoseconds to recently as fast as attoseconds[92].

What follows is by no means an exhaustive overview of transient absorption spectroscopy, but merely the requisite concepts to follow our interpretation of TA measurements on the 12 SRB systems outlined previously. The TA results presented in this chapter were collected and analyzed by both myself and **Milan Delor**.

### 2.3.1 TA as an ultrafast pump-probe technique

TA is a 2 laser pulse "pump-probe" technique, in which the first laser pulse "pumps", or promotes, the sample into an excited state. TA is certainly not limited to the study of electronic transitions, but for the work outlined in this chapter we are pumping SRB from its electronic ground state to an electronic excited state. After excitation by the pump, the system is allowed to evolve in time for a controllable duration, $\tau$, before being introduced to the second laser pulse, the "probe." The probe arrives at the same region of the sample that was excited. After passing through the sample, the pump pulse is blocked while the probe pulse is sent to a detector. Figure 2.9 shows a schematic of such a TA experiment. The probe pulse here is a broad UV-to-NIR white light continuum, and so an additional step in the detection of the probe is to disperse the spectrum before detection, typically with some kind of spectrometer. The probe in TA need not be as spectrally broad as this case, but there are certain advantages to simultaneously measuring the transient change in a sample's absorption across an entire spectrum.

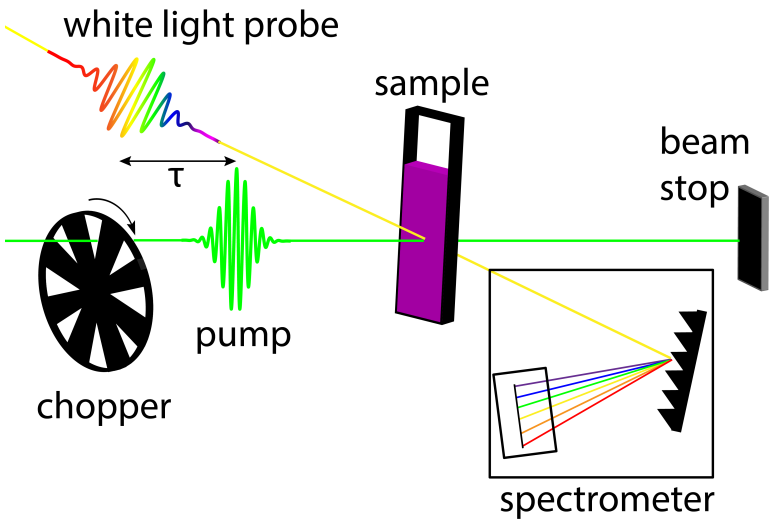


Figure 2.9: Schematic of white light TA experiment.

In order to isolate the differential change in a sample's absorption as a consequence of interacting with the pump pulse, we employ the use of a chopper wheel in the pump path. By intermittently blocking the pulse train of the pump line, we can effectively achieve a $pump_{\text{on}}$ and a $pump_{\text{off}}$ measurement, which is the probe's transmission intensity with and without the pump ($T_{\text{on}}$ and $T_{\text{off}}$). By placing a chopper wheel into the pump path to modulate the excitation at a relatively high frequency (e.g. 500 Hz), we can relate $T_{\text{on}}$ and $T_{\text{off}}$ signals frequently enough such that their differential signal can, to an extent, remain agnostic to experimental fluctuations like variation in the white light spectrum for our probe.

The difference between $T_{on}$ and $T_{off}$ represents the sample's response to the pump pulse, and this value is typically normalized to $T_{off}$ such that our observable is $\frac{\Delta T}{T} = \frac{T_{on} - T_{off}}{T_{off}}$. $\frac{\Delta T}{T}$ may also be represented as the change in the sample's optical density (OD), as often is assumed that $\frac{\Delta T}{T} \approx -\Delta OD$ provided $|\Delta OD| << 1$, which is typical in most TA experiments. $\Delta OD$ will be the unit of choice for the remainder of this chapter.

The time resolution of a TA experiment is determined by the temporal width (pulse duration) of the pump and probe pulses. This means TA in the visible region is typically capable of measuring dynamics that occur on 10's of femtosecond timescales (hence *ultrafast*). Care must be taken, however, to ensure that the optical elements along the laser beam's path prior to the sample do not introduce substantial dispersion that can temporally stretch the pulses and effectively lower the time resolution. In many cases, the use of a prism compressor (see Figure 2.10) is helpful to compensate for the dispersive elements in an optical path.

### 2.3.2 Optical set-up used for white-light TA experiments

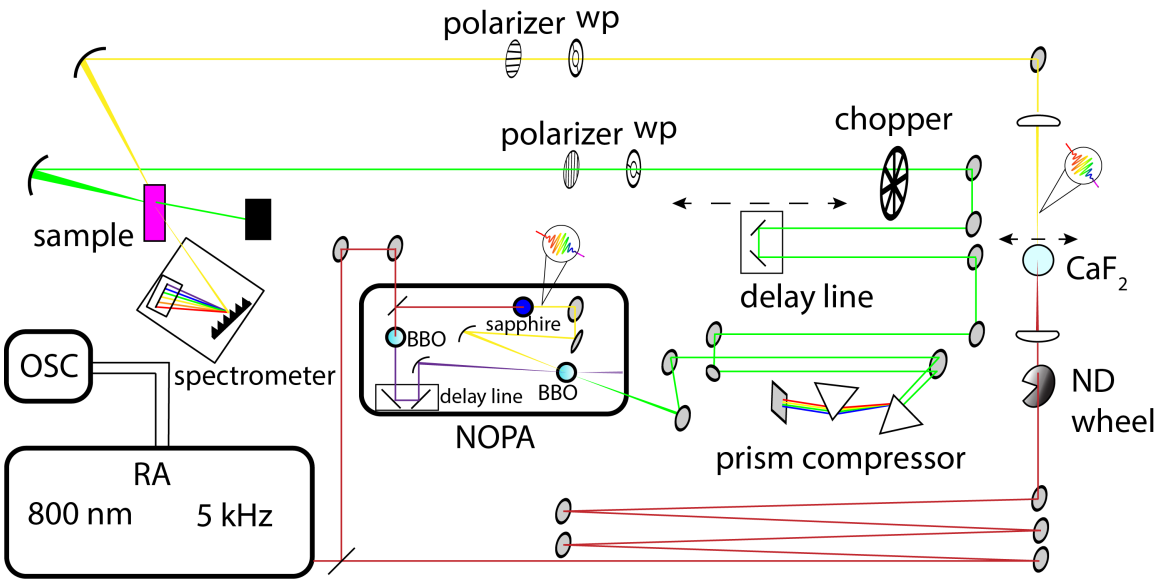


Figure 2.10: Schematic of the optical table used for white light TA experiments.

Figure 2.10 provides a schematic of the optical table layout of the TA setup used for the experiments detailed in this chapter. A commercial oscillator (OSC) generates ultrafast laser pulses at 800 nm and seeds the regenerative amplifer (RA) to amplify the pulses. The

RA outputs 800 nm pulses at a 5 kHz repetition rate and is sent through a beam splitter to generate our "pump arm" (green) and "probe arm" (yellow).

Along the pump arm, the 800 nm beam is coupled into a home-built non-colinear optical parametric amplifier (NOPA) in order to tune the excitation source for the sample across the visible spectrum. The 800 nm beam is sent through a beam splitter, where one arm is frequency doubled to 400 nm via a $\beta$-barium borate (BBO) crystal. The other arm focuses the 800 nm beam onto a sapphire crystal to generate a white-light continuum. The 400 nm NOPA "pump" (note this is NOT the pump beam we refer to as part of the "pump-probe" combination at the sample, which is admittedly confusing) and white-light "signal" beams are focused together at a particular crossing angle onto a BBO crystal for parametric amplification[93], wherein the energy of the NOPA pump beam is converted to the white-light signal beam of the NOPA. By varying the delay between pump and signal, we can selectively amplify specific spectral regions of the white light, thus enabling a tunable spectral output.

For our experiments, we tune the NOPA output to a peak wavelength of $\sim$570 nm. We then temporally compress the pulses via a folded prism compressor and couple the pump into an opto-mechanical delay line, which is used to control the arrival time of the pump pulse at the sample relative to the probe pulse. A chopper wheel "chops" the pump beam at a 500 Hz frequency. The pump is then sent through a half-waveplate and polarizer to attenuate its power just before being focused into the sample-containing cuvette via a curved mirror.

Along the probe arm, we send the 800 nm beam for a "walk" by passing it between multiple silver mirrors in order to roughly match the path length of the pump arm. Afterwards, the 800 nm beam is attenuated by a neutral density wheel and then focused into a $CaF_2$ crystal to generate a UV-to-NIR white light continuum. We continuously raster the motion of the $CaF_2$ to avoid thermal damage on a given spot. The white light is collimated on an off-axis parabolic mirror and sent through a half-waveplate and polarizer. The probe polarizer's angle is set to be $54.7^o$ relative to the pump polarizer, which is the "magic angle" required to avoid anisotropic contrubtions to the signal. The probe is then focused onto the sample-containing cuvette in the same position as the pump via a curved mirror, and the transmission of the probe through the sample is collected on an Ocean optics spectrometer.

### 2.3.3 Origins of various signals in spectrally-resolved TA

Transient changes in a sample's absorption spectrum due to pump excitation can occur by various photophysical mechanisms, and the distinct spectral signatures of these changes provide useful information about the nature of the relative populations of a chromophore's excited-state evolution. Three such signatures discussed here are: ground state bleach (GSB), excited state absorption (ESA), and stimulated emission (SE). These mechanisms are typical for small organic molecules in TA, but by no means are they the exclusive framework with which to consider all materials and their respective excited-states.

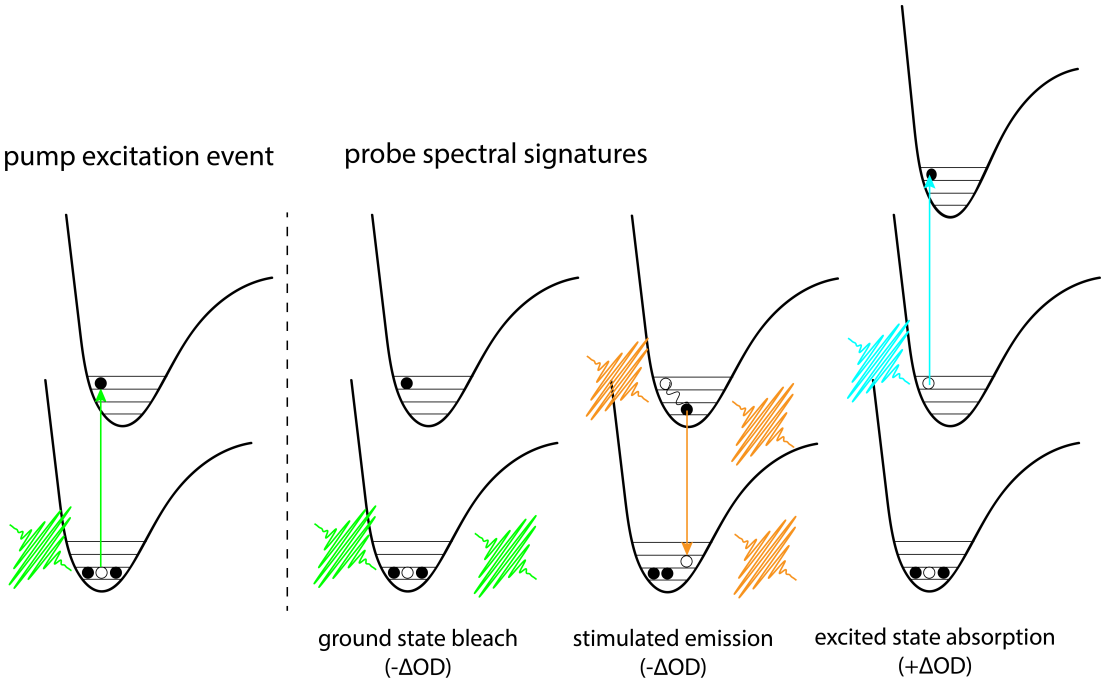


Figure 2.11: Schematic of various spectral signatures in TA signal.

### Ground State Bleach

The **ground state bleach** signature occurs because the pump excites the sample system from the ground state to an excited state. This leads to a corresponding decrease in the overall population in the ground state compared to when the system is not already photoexcited by the pump, so when probing in the region that energetically corresponds to this ground-to-excited state transition, there are fewer absorption events. Thus, the probe will transmit more in the event with the pump than without the pump, leading to an overall negative value in $\Delta OD$. In Figure 2.11 this is represented by the probe pulse being introduced to the sample (left side of potential surface) and then "passing" through (right side of potential surface) as no absorption event occurs. For our experiments, the GSB provides the strongest signal (i.e. largest $|\Delta OD|$), and the rate at which the GSB signature disappears typically corresponds to the excited-state lifetime of the chromophore in question.

### Stimulated Emission

The **stimulated emission** signature occurs when probing at wavelengths corresponding to the optical transition that couples the excited state to the ground state. Figure 2.11 represents this as probing an electronic transition back to the ground state that is redder in energy than the initial excitation (left side of potential surface), and due to stimulated emission,

the sample will emit a photon of the same wavelength and phase as the probe (right side of surface). While normally the probe would pass through the sample at this wavelength, due to the action of the pump pulse exciting the sample and subsequent vibrational relaxation within the electronic state surface, we generate an additional photon due to SE which yields an overall higher transmission intensity compared to when the system is not already photoexcited by the pump and a negative $\Delta OD$. The SE signature is usually very close in energy to and overlaps with the GSB, but if the sample in question has a dynamic Stokes shift, the rate at which the peak of the SE signature redshifts is typically a reflection of the sample's excited state vibrational relaxation.

#### Excited State Absorption

The **excited state absorption** signature occurs when probing at wavelengths corresponding to optical transitions that couple the chromophore already in an excited state to an energetically higher excited state. This is shown in Figure 2.11 as probing an electronic transition from the initial excited electronic surface to a higher one, where the energy difference between the two excited electronic states is even greater than that of the ground-to-initial excited state. The ESA signature is not required to be a transition that is higher in energy than the initial excitation, it can be (and often is) a lower energy transition as well, but for our data it happens to be at higher energy (shorter) wavelengths. While the probe would normally transmit through the sample at these wavelengths if the system were not first photoexcited by the pump, because of the pump pulse excites the chromophore to the initial excited electronic surface, the probe can now be absorbed, leading to a decrease in the probe transmission intensity relative to the unpumped system and a positive $\Delta OD$.

### 2.3.4 Analyzing TA data

TA data is collected by recording the probe's transmission at a series of ultrafast time delays between the pump and probe. For a single spectral component of the probe, an example TA dataset is shown in Figure 2.12 (note these datasets are sometimes referred to as "kinetic traces" or "transients"), where the change in optical density is recorded at each pump-probe time delay. The simplest physical model to describe TA data is to assume that the system is evolving from one state to another at a constant rate and that the population profile can be described by a system of linear differential equations (first-order kinetics). If this is the case, the data can be modelled using a sum of exponentials as the solution to the first order rate equations.

For simplicity, let's assume our system after excitation relaxes from an excited state to the ground state with some time constant $\tau_1$ (a rate-constant $k_1 = \frac{1}{\tau_1}$). The decaying component of our signal can then be fit with:

$$\Delta OD(t) = A_1 e^{-t/\tau_1}. \tag{2.4}$$

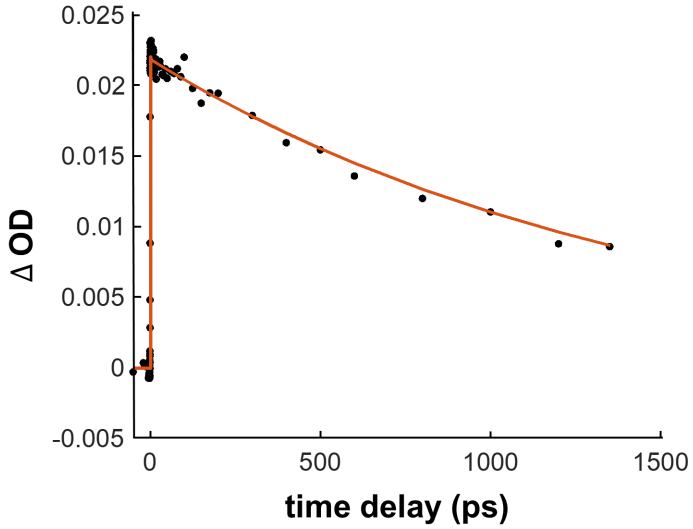


Figure 2.12: Example kinetic trace and fit to TA data of SRB in solution

To account for the rising component of the TA signal, we need to consider the instrument response function (IRF), which is the convolution of the shape of our excitation pulse and the detector response in time[94]. In principle, if the target dynamics we care to extract from our experiments are significantly longer (e.g., nanoseconds) than the time duration of the IRF, then it is not entirely necessary to account for it, but here we're interested in timescales on the order of a few picoseconds. The instrument response function, $IRF(t)$ is well described by a Gaussian with center $t_0$ (often referred to as time-zero in experiments) and standard deviation $\sigma_{IRF}$:

$$IRF(t) = \frac{1}{\sigma_{IRF}\sqrt{2\pi}} e^{\frac{-(t-t_0)}{2\sigma_{IRF}^2}}. \tag{2.5}$$

The fit to our data is a convolution of Equations 2.4 and 2.5, such that:

$$\Delta OD(t) = \int_0^\infty \frac{1}{\sigma_{IRF}\sqrt{2\pi}} e^{\frac{-(\tau-t_0)}{2\sigma_{IRF}^2}} A_1 e^{(\tau-t)/\tau_1} d\tau, \tag{2.6}$$

which from a computational perspective thankfully has an analytical solution:

$$\Delta OD(t) = \frac{1}{2} A_1 e^{-(t-t_0)/\tau_1} e^{\frac{1}{2}\left(\frac{\sigma_{IRF}}{\tau_1}\right)^2} \left[1 + \text{erf}\left(\frac{t - (t_0 + \frac{\sigma_{IRF}^2}{\tau_1})}{\sqrt{2}\sigma_{IRF}}\right)\right] \tag{2.7}$$

Now when fitting the data with Equation 2.7, $\tau_1$, $\sigma_{IRF}$, $A_1$, and $t_0$ are all free parameters. $\sigma_{IRF}$ should be quite close in value to the pump pulse width, which can be measured separately from the experiment (for example, with an autocorrelator), as a good secondary check.

The above picture considers the case of a single spectral component and a single exponential decay, but in our experiment we are using a white-light continuum probe and the dynamic evolution of the SRB chromophore requires at least two exponentials to be adequately captured. The sign and magnitude of certain parameter values depend on where we are spectrally probing our sample and are therefore wavelength dependent. So our model (pre-IRF convolution) would more appropriately be:

$$\Delta OD(t, \lambda) = A_1(\lambda)e^{-t/\tau_1} + A_2(\lambda)e^{-t/\tau_2}. \tag{2.8}$$

Note here that with the convolution of the IRF, our time-zero parameter is also wavelength dependent, $t_0 \rightarrow t_0(\lambda)$! This is because different spectral components of the white light probe pulse travel at different speeds (i.e. there is "chirp" in the probe pulse) due to the wavelength dependence of the refractive index of transmissive optics. As a consequence, the experimental "clock" starts at different times depending on which wavelength of the probe we are analyzing.

Shown in Figure 2.13a is an example of TA spectra at a number of pump-probe time delays ranging from 1 ps to 1200 ps, where we can clearly see that the amplitude of the data varies with the detected wavelength. If we were to fit the time series of each spectral component (here we actually bin the data to $\sim$80 spectral components, both to smooth out noise in the spectra and to reduce the computational overhead), we can generate a plot like Figure 2.14, which superimposes all the kinetic traces and obtains a resulting global fit to each trace.

Here, a global fit represents fitting each kinetic trace with a set of wavelength-dependent parameters, $A_1, A_2, t_0$, and wavelength-independent parameters $\tau_1$, $\tau_2$. That is to say, while each kinetic trace may have its own unique set of $A_1, A_2, t_0$, all traces must share the same $\tau_1$, $\tau_2$. One advantage to this approach is the statistical constraints it places on the shared time constants, which is not achieved in single-color probe TA.

Finally, it can be very useful to plot the amplitudes, $A_1(\lambda)$ and $A_2(\lambda)$, of the global fit as a function of wavelength. An example of these resulting spectra, referred to as Decay Associated Spectra (DAS), are shown in Figure 2.13b. DAS help distill the essential changes in the spectral evolution of the system as it evolves between states. For example, a subtle blue- or redshift of a spectral peak can more clearly be represented by a characteristic dispersive lineshape in the DAS of the corresponding time constant.

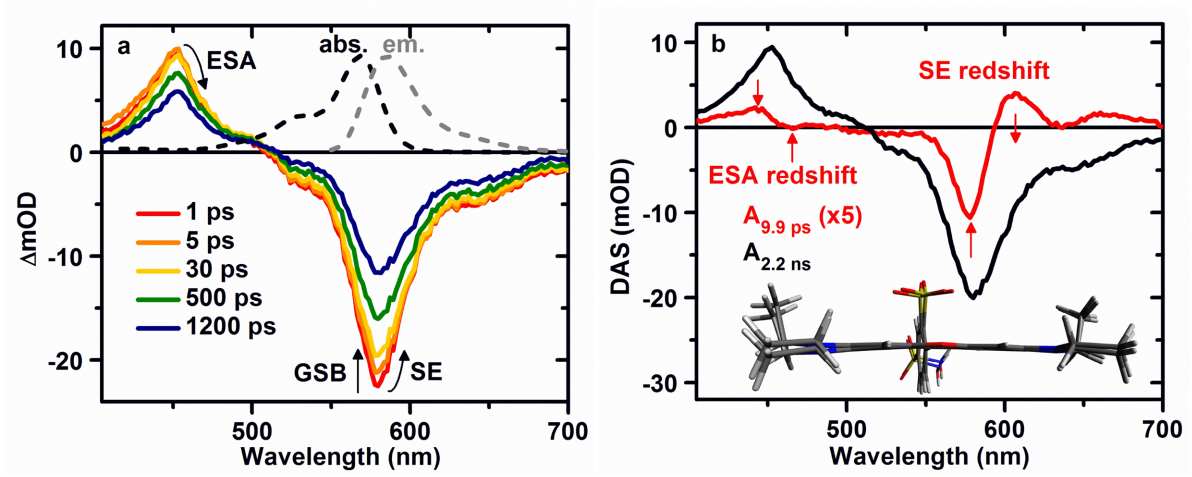


Figure 2.13: TA data and analysis of SRB-Cyc-SS attached at S23C (outside) site of cpTMV. (a) TA spectra at representative delay times from 1 to 1200 ps. The steady-state absorption and emission spectra are dashed curves. (b) Decay associated spectra corresponding to the two time components of the bi-exponential global fit of the data in (a). Inset below is SRB in its ground electronic state overlain on top of SRB's bright electronic excited state, demonstrating a very subtle buckling of the xanthene core.

## 2.4 Protein-chromophore linkers enable control over the timescales of SRB's excited state evolution

Here we address the need for well-defined chromophore configurations by comparing the ultrafast TA time scales and results from molecular dynamics (MD) simulations of chromophores bound to supramolecular protein assemblies derived from the TMV coat protein via a series of increasingly constricting linkers.

Figure 2.13 displays the TA spectra of SRB-Cyc-SS attached at the outside S23C site of cpTMV at representative delay times following light excitation at 570 nm, the lowest allowed electronic transition. The spectra display excited state absorption (ESA) around 450 nm and a band convolving ground state bleaching (GSB) and stimulated emission (SE) centered at 580 nm. The TA spectra for all 12 systems follow very similar spectral profiles. The datasets of the 12 different systems are shown in Figures 2.15, 2.16, and 2.17, where each figure are the datasets of our 4 linkers corresponding to one of the three labeling environments. In every case, the kinetics across the visible spectrum are well fit by a biexponential function, with a short component on the order of a few picoseconds and a longer component on the order of a few nanoseconds. Although the spectral evolution is equivalent across systems, indicating the protein environment does not change the nature of the populated excited states, the time scales for these processes are vastly different, providing a useful handle on

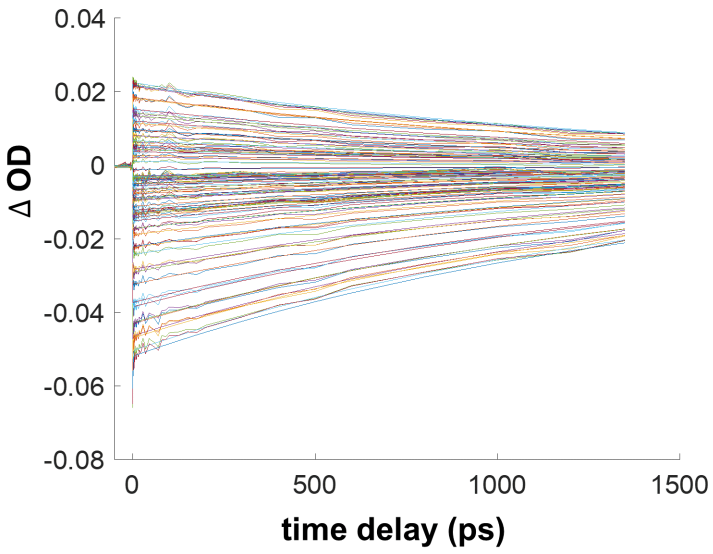


Figure 2.14: Example kinetic traces extracted from entire TA spectrum and their global fits.

the influence of the biomolecular environment on chromophore-bath dynamics.

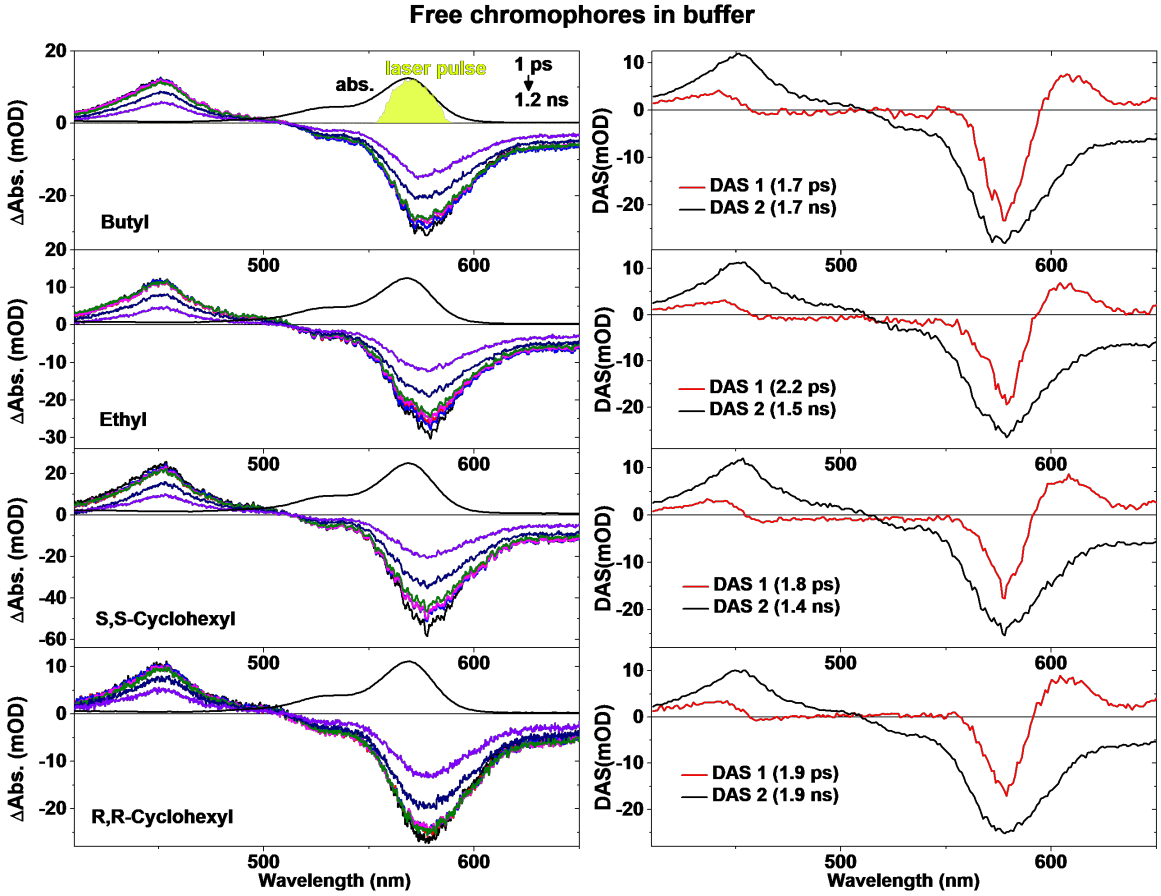


Figure 2.15: All representative TA data and Decay Associated Spectra for SRB with the 4 different linkers in buffer.

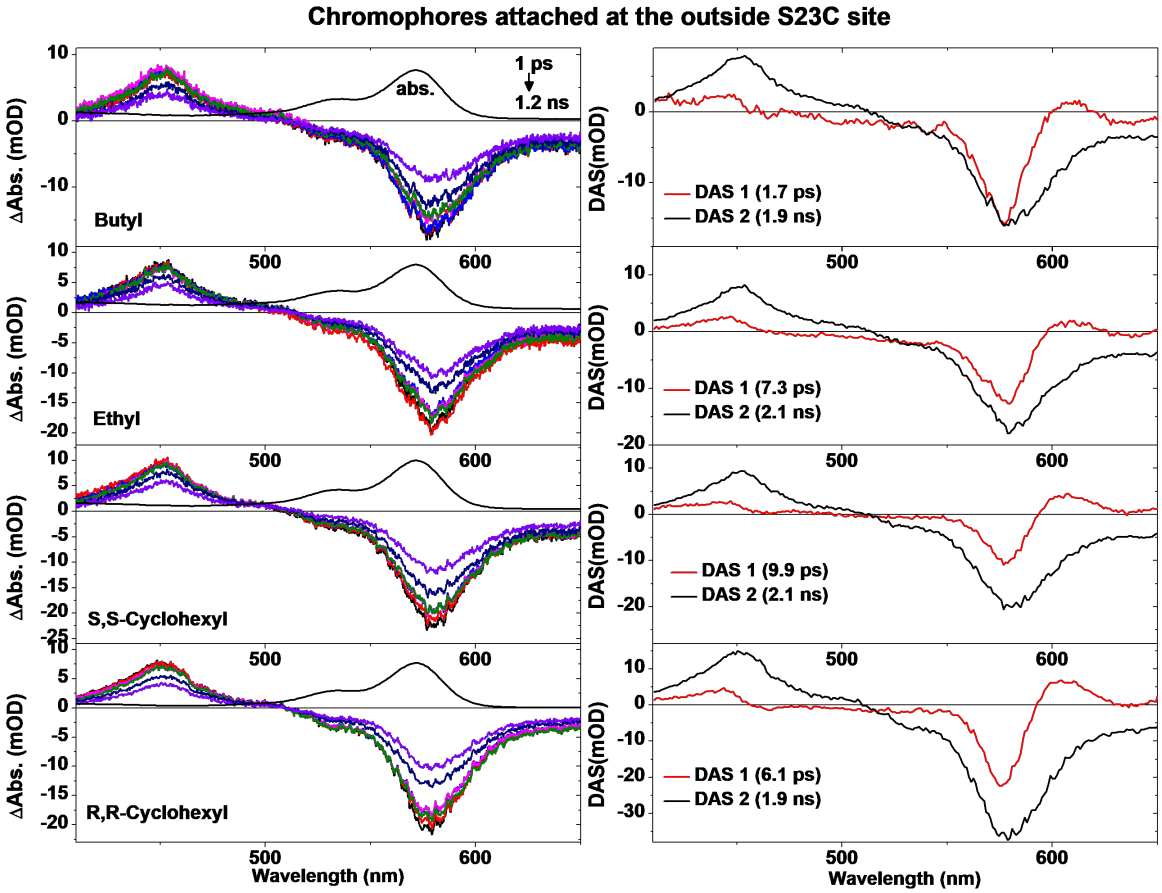


Figure 2.16: All representative TA data and Decay Associated Spectra for SRB attached at the outside labeling site S23C with the 4 different linkers.

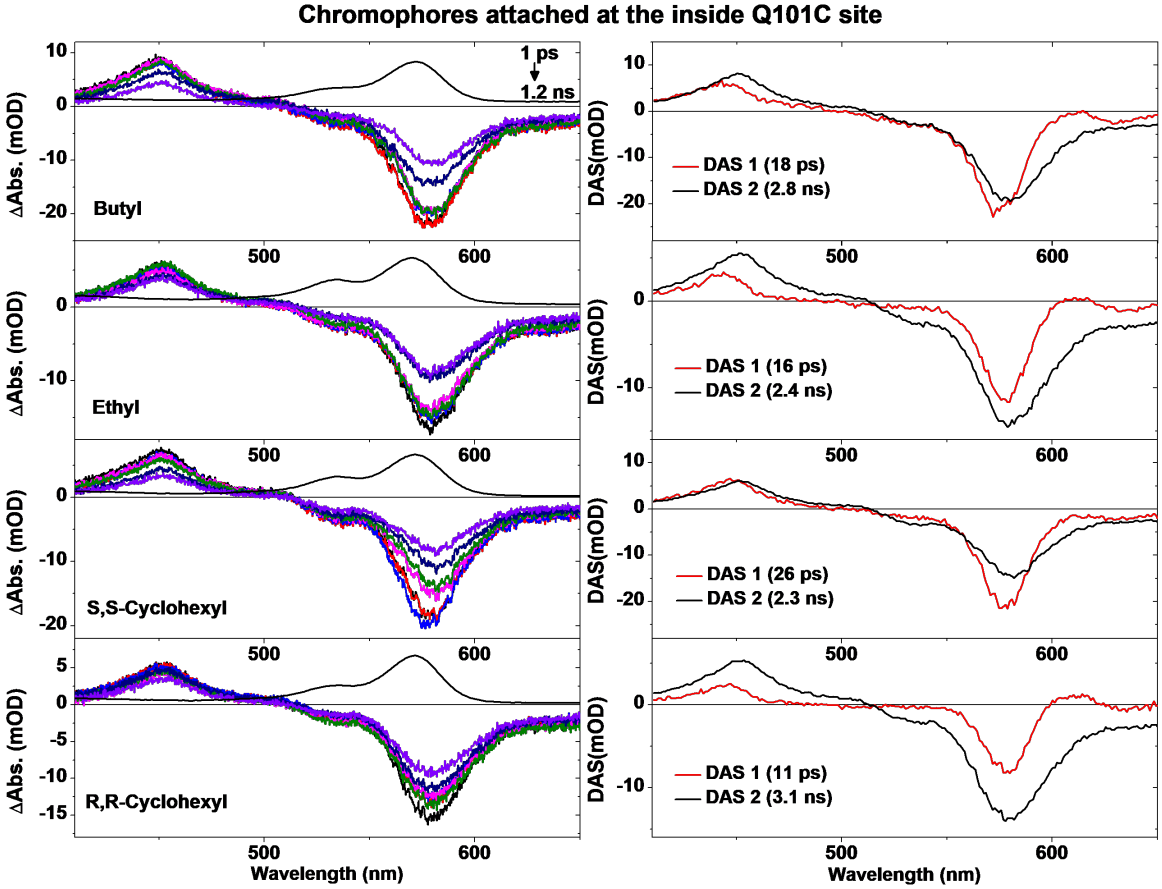


Figure 2.17: All representative TA data and Decay Associated Spectra for SRB attached at the inside labeling site Q101C with the 4 different linkers.

### 2.4.1 Excited state dynamics of SRB

Before comparing results across the 12 different compounds, we provide a brief interpretation of the observed chromophore dynamics themselves, using time-dependent density functional theory (TD-DFT) to support our excited state assignments. The TD-DFT calculations were performed by **Samia Hamed** of the Neaton group at the time of this study.

Although the excited state dynamics of rhodamine dyes are well-studied, the excited state processes can depend on the specific molecular details of both the phenyl and xanthene moieties[95–100]. Solvent and intramolecular structural reorganization are expected to occur within the first few picoseconds after photoexcitation. Intramolecular reorganization in rhodamines is not yet fully characterized, but involves some combination of the following: rotation of the dialkylamino groups and/or C–N bond order reduction, rotation of the initially orthogonal phenyl ring with respect to the xanthene core, and/or buckling of the xanthene moiety [95, 96, 98] This reorganization can facilitate electron delocalization in the excited state. Previous TD-DFT calculations on Rhodamine B, a close analogue to SRB with a carboxylate moiety replacing the $SO_3^-$ group on the phenyl ring, identified a dark, low-lying charge transfer (CT) state that may be responsible for partial quenching of the lowest-lying bright state[98].

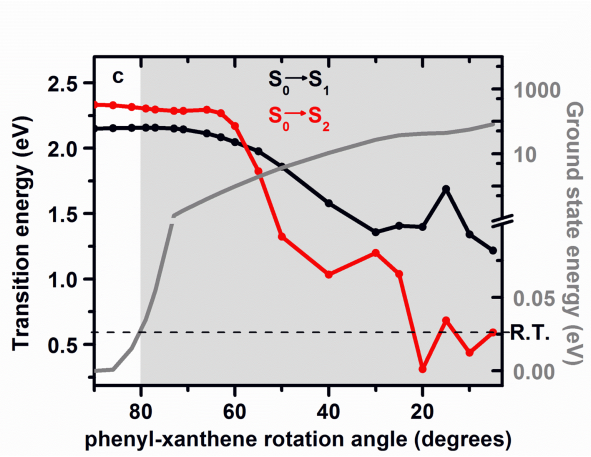


Figure 2.18: Plot of vertical transition energies, calculated from TD-DFT at the PBE0/6-31+g* level, from the ground to bright $S_1$ and ground to dark $S_2$ states as a function of phenyl-xanthene rotation angle.

The TD-DFT calculations corroborate the existence of a lower-lying CT state when the phenyl-xanthene dihedral approaches a planar configuration in SRB. Accessing this CT state would, however, necessitate rotation of the phenyl ring with respect to the xanthene core towards a quasi-planar geometry, representing an energetic barrier of ∼2 eV on the

excited state potential energy surface from the initially orthogonal geometry (Figure 2.18). This barrier arises due to severe steric constraints imposed by the $SO_3^-$ group, rendering this quenching pathway unfeasible at room temperature without large excess energy in the excitation pulse. Instead, the only major intramolecular nuclear relaxation pathway involves subtle buckling of the xanthene core and slight rotation of the dialkylamino groups (Figure 2.13, inset).

From these TD-DFT calculations we deduce that the short lifetime component in the TA of SRB is primarily a result of nuclear relaxation along the intramolecular and solvent reaction coordinates, rather than internal conversion between different excited states. The spectral changes accompanying these processes are: a redshift of the stimulated emission between 580 and 610 nm, seen as a dispersive differential profile (negative-to-positive) in the short-time component DAS (red curve, figure 2.13b) and a slight redshift of the excited state absorption (ESA) at 450 nm, seen again as a dispersive differential profile, but is positive-to-negative as the $\Delta OD$ sign is the opposite of the SE. The population in the $S_1$ excited state then decays back to the ground state on nanosecond time scales.

### 2.4.2 Trends in the rate of SRB's excited state evolution amongst chromophore-linker configurations

We observe several revealing trends in the rate of excited state evolution that clearly demonstrate the importance of chromophore–protein linker configuration and positioning in biomimetic light-harvesting systems. Figure 2.19a and Table 1 display the lifetimes associated with the picosecond solvation and intramolecular reorganization process for all systems. The nanosecond relaxation component lifetimes are also shown in Table 1 and Figure 2.19b and follow approximately similar trends, albeit less prominently.

The most dominant features immediately observed from Figure 2.19a are the up to 5-fold slowing of solvation and structural rearrangement when the chromophores are attached to cpTMV at outer surface site S23C, and up to 14-fold slowing when attached at intracavity site Q101C, when compared to chromophores in buffer. The fact that dynamic retardation is clearly present even at the outside S23C site for the more rigid linkers (all except butyl) suggests that the chromophores are close enough to the protein–solvent interface to be directly affected by it. Interestingly, however, SRB-Bu, which has the longest and most flexible linker, does not exhibit dynamic retardation at the outside position, instead displaying the same time scales as for the free chromophore in solution. This result indicates that even if the chromophore is covalently attached to the protein, provided the linker is long and flexible enough, it remains unaffected by the latter and only samples the bulk solvent environment far away from the protein surface. Inside the protein cavity, SRB-Bu is slowed down by an amount similar to other complexes. At this attachment site, confinement by the top and bottom protein surfaces, separated by $\sim$2 nm[20], precludes the presence of a bulk-like environment, leading to much more constrained dynamics irrespective of the linker used.

Another surprising feature in Figure 2.19a is that the greatest retardation is experienced

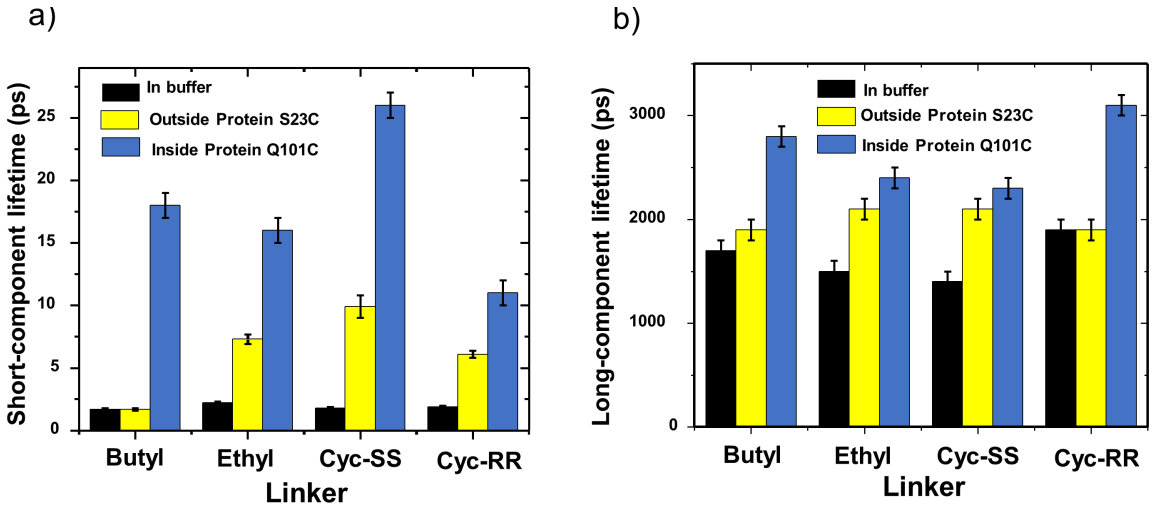


Figure 2.19: Time-constants from global analysis of TA data. (a) Short-component lifetimes resulting from fits of TA data on SRB with 4 different linkers in 3 different labeling sites. (b)Long-component lifetimes.

Table 2.1: Short and long lifetime components as well as the corresponding ratios between protein labeling sites and buffer

| linker | $\tau$ component | buffer | S23C | Q101C | S23C/buffer | Q101C/buffer |
|---|---|---|---|---|---|---|
| Butyl | short(ps) | 1.7 | 1.7 | 18 | 1.0 | 11 |
| | long(ns) | 1.7 | 1.9 | 2.8 | 1.1 | 1.6 |
| Ethyl | short(ps) | 2.2 | 7.3 | 16 | 3.3 | 7.3 |
| | long(ns) | 1.5 | 2.1 | 2.4 | 1.4 | 1.6 |
| Cyc-SS | short(ps) | 1.8 | 9.9 | 26 | 5.5 | 14 |
| | long(ns) | 1.4 | 2.1 | 2.3 | 1.5 | 1.6 |
| Cyc-RR | short(ps) | 1.9 | 6.1 | 11 | 3.2 | 5.8 |
| | long(ns) | 1.9 | 1.9 | 3.1 | 1.0 | 1.6 |

by SRB-Cyc-SS both inside and outside of the cavity. This difference is especially salient when comparing the enantiomers Cyc-SS and Cyc-RR, with the former slowing by a factor greater than the latter by 1.7 times at the outside position and by 2.5 times inside the cavity. Thus, a chiral modification of the chromophore linker translates into major changes in the excited state dynamics of the system. This finding suggests that enantiomers can be selected for purposes of generating slow excited state dynamics that approximate the environmental protection of chromophore electronic excitations in natural photosynthesis. Overall, in line with the previous findings in earlier studies of this system using generic linkers[20], the inte-

rior protein cavity can be used to constrain both chromophores and water molecules and, in this way, substantially slow relaxation along the electronic excited state potential energy surface. Yet, going beyond our previous findings relating to confinement[20], we also learn here that purpose-specific linkers enable dynamic retardation at the protein surface, which would be absent using the long tethers typical for commercial bioimaging dyes, and provide far better control over the extent to which chromophore–protein interactions tune the excited state dynamics both inside and outside the protein cavity. These compounds therefore facilitate a much more systematic and precise way to study the role of chromophore–protein–solvent interactions in light-harvesting systems.

### 2.4.3 Molecular dynamic simulations corroborate TA results

To obtain a molecular-level understanding of the trends in excited state dynamics observed for the four chromophore-linker systems attached to the surface site of cpTMV, we investigate how each linker alters the orientation and positioning of the chromophore on the protein surface using MD simulations performed with GROMACS. These simulations were constructed and carried out by **Julia Rogers** in the Geissler group, and any plots or graphics related to the MD simulations found in this chapter were similarly generated by Julia.

#### Model system used for simulations

For computational tractability, a reduced system consisting of surface helices 1 and 2 of a cpTMV monomer, along with helix 2 of an adjacent monomer is simulated. The chromophore is attached to S23C on helix 1. A close analogue of SRB, AlexaFluor 488, is used since accurate force field parameters for AlexaFluor 488 have been developed to reproduce experimental data[101], whereas parameters have not yet been developed for SRB. The MD simulations not only confirm an intuitive picture of cyclohexyl-linked chromophores being constrained closer to the protein surface, but also reveal a detailed and subtle picture of chromophore–protein–water interactions that successfully explains the observed trends in excited state dynamics.

#### Simulating chromophore surface localization with different linkers

More specifically, we consider how each linker determines the extent to which the chromophore is localized at the protein surface. The increased length and flexibility of the butyl and ethyl linkers allow the chromophore to sample many different configurations that reach far from the protein surface. In contrast, the Cyc-RR and Cyc-SS constrain the chromophore in specific configurations relative to the protein surface. In Figure 2.20a, the distribution of the minimum distance between any carbon atom of the chromophore's xanthene core and a heavy protein atom is plotted. For all four systems, the chromophore can specifically interact with protein side chains, resulting in the peak at at a distance of $\sim$0.35 nm. The distributions for the butyl and ethyl systems exhibit a broad second peak centered at $\sim$1.2 nm and

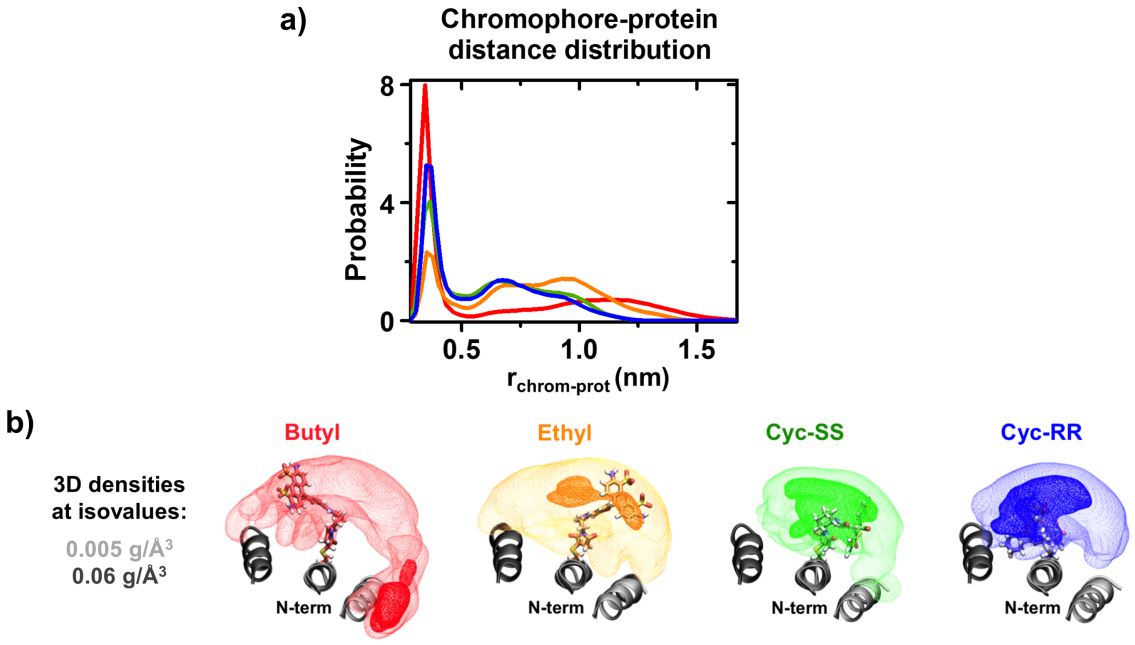


Figure 2.20: Molecular dynamic simulations of chromophore-protein system with all 4 linkers. (a) Chromphore-protein distance distribution for all 4 linkers. (b) 3D density plots of chromophore locations averaged over 500 ns at low and high isovalues for all 4 linkers.

~1 nm, respectively, whereas the distributions for the cyclohexyl systems both exhibit a second peak centered at ~0.7 nm. The 3D density plots of the xanthene heavy atoms of the chromophore (Figure 2.20b), averaged over the last 500 ns of the MD simulations, provide further insight into common chromophore conformations on the protein surface. Plots at a low density isovalue (0.005 g/Å$^3$) show all possible locations where the chromophore can be found during the simulations. Consistent with the distance distributions, the chromophore samples the largest expanse of space when attached via butyl and ethyl linkers, as compared to Cyc-RR or Cyc-SS. Plots at a more stringent isovalue (0.06 g/Å$^3$) help to identify the most common conformations of the chromophore on the protein surface. Since the butyl and ethyl linkers are quite flexible, the butyl- and ethyl-linked chromophores adopt many different conformations and reside in multiple regions on the protein surface with densities less than 0.06 g/Å$^3$. As a result, large, significant regions at this density isovalue are not observed. In contrast, the Cyc-RR- and Cyc-SS-linked chromophores adopt only a few, very specific conformations on the protein such that significant regions of density are observed

at the more stringent isovalue. These results support the conclusion that chromophores attached via either butyl or ethyl sample more regions of space farther from the protein surface than those attached via the cyclohexyl groups, which remain within the biomolecular hydration shells[102].

### 2.4.4 MD simulations reveal Cyclohexyl linkers preserve dipole orientation

An additional consequence of restricting chromophore conformational sampling via cyclohexyl linkers is the ability to preserve orientational correlations for longer. In Figure 2.20c, the transition dipole moment orientational correlation function of the chromophore is plotted for all systems, showing that rotational reorientation is considerably slower for Cyc-SS- and Cyc-RR-linked chromophores compared to ethyl- and butyl-linked complexes. The cyclohexyl linkers retain orientational correlations over several nanoseconds, i.e., over the full excited state lifetimes of the chromophores. In light-harvesting assemblies, the ability to retain orientational correlations between adjacent chromophores throughout the exciton lifetime allows for direct optimization of nonradiative energy transfer. Such control is necessary to reproduce the directional and efficient energy transport over long distances that is achieved in natural systems.

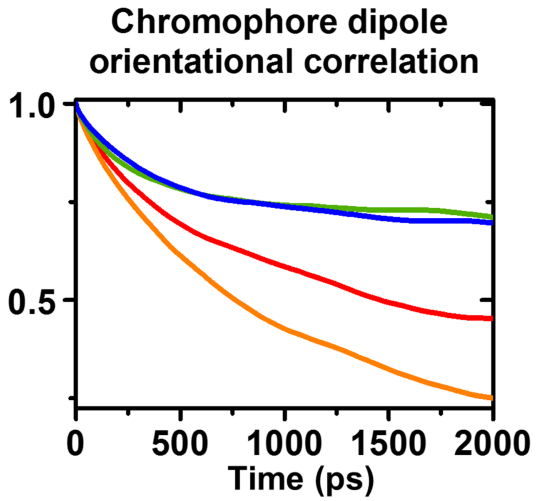


Figure 2.21: Chromophore dipole orientational correlation function with each of linking group.

These simulations suggest that the cyclohexyl linkers are ideal chromophore-protein linkers for biomimetic light harvesting, but experimental evidence proving that the dipole orientation is preserved over the lifetime of the SRB exciton necessitates some kind of measure

of the system's anisotropy, which are measurements we did not perform at the time of this study. Furthermore, even if the cyclohexyl linkers can indeed preserve the orientation of a given SRB's transition dipole, the *relative* orientations between proximal SRB chromophores must still be in optimal configurations for efficient energy transfer. In other words, despite mitigating potential dynamic fluctuations that can disrupt optimal dipole-dipole couplings, the cyclohexly linked chromophores must still be attached to the cpTMV assembly in statically optimal configurations as well. But cyclohexyl linkers are certainly a step in the right direction!

I'd like to point out that **Leo Hamerlynck** in the Ginsberg group has taken tremendous strides to better understand these concepts and much more by studying fully-labelled cpTMV assemblies with transient absorption anisotropy and nuanced simulations of energy transfer, described in a manuscript in preparation at the time of this writing.

### 2.4.5 Reconciling differences between excited state dynamics of Cyc-SS and Cyc-RR linkers

To explain the differences between the excited state dynamics of Cyc-RR and Cyc-SS-linked chromophores, we investigated the dynamics of water molecules around the chromophore and the protein surface. The molecular interpretation of chromophore dynamic retardation due to slowed water molecules near biomolecular surfaces has been studied in depth by a wide range of experimental and computational techniques and remains somewhat controversial[102–111]. Mounting evidence suggests that water dynamics near protein surfaces are not affected as much as previously thought, typically only slowing by a factor of 2–3 over the first hydration shells, with the effect rapidly dropping off radially toward bulk water[102, 110]. As a result, the commonly observed order-of-magnitude retardation in the excited state dynamics of chromophores located in the first few hydration shells is often attributed to slow biomolecular motion affecting both water and chromophore dynamics in its heterogeneous dielectric environment[102, 108, 112–114].

Figure 2.22 displays the rotational time correlation function of the water dipole moments for molecules in the bulk (far away from the protein surface) compared to those within 5 Å of any of the chromophores' xanthene heavy atoms in our cpTMV system. These simulations show that the water dynamics near the chromophores are slowed by a factor of $\sim$2, corroborating the aforementioned studies, but with the largest retardation occurring around the Cyc-SS linker. The difference in water dynamics around Cyc-RR- and Cyc-SS-linked chromophores is a priori surprising given that they reside a similar distance away from the protein surface. The dissimilarity suggests that a mechanism based on specific chromophore–protein–solvent interactions is responsible for the observed dynamic differences.

A closer look at the different chromophore orientations for the Cyc-SS and Cyc-RR complexes in Figure 2.20b and Figure 2.23 reveals that the chromophore attached via Cyc-SS resides primarily above the two helices of the same monomer, where a high density of hydrophobic amino acid residues are located, whereas the chromophore attached via Cyc-RR

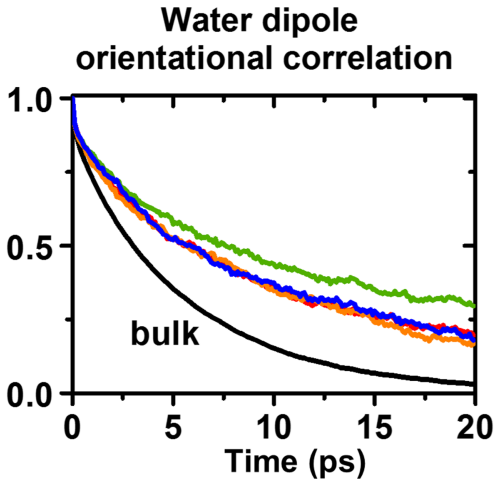


Figure 2.22: Simulations of the water dipole moment rotational time correlation functions of water molecules near chromophores and far from chromophores (bulk).

resides above a less dense region between adjacent monomers (Figure 2.23). To determine a more detailed picture of slowed water dynamics, and whether it can be attributed to the protein residues alone or to both the protein and chromophore, the dynamics of waters within 5 Å of each protein side chain were analyzed for the model cpTMV system with and without a chromophore (Figure 2.23). The water diffusion coefficients are plotted in false color scale around the protein surface, with blue representing the greatest retardation in water dynamics. Without the chromophore present (left), it is already apparent that water dynamics are slowest around densely packed areas of the protein, such as the area between the helices of a cpTMV monomer, and within deeper pockets or grooves along the protein surface.

Strikingly, when the chromophore is present, the water dynamics around specific residues are further slowed, suggesting that the chromophore also impacts the solvent dynamics. This retardation is particularly noticeable for the Cyc-SS complex, which is constrained just above a dense region of the protein surface. These observations suggest that water molecules are effectively sandwiched between the chromophore and the protein surface, leading to retardation near the surface that is a factor of $\sim$1.5 greater than in the absence of the chromophore. For the ethyl complex, which mainly resides in a similar but more distant region, water molecules near the surface are slightly slowed by a factor of $\sim$1.1 compared to without the chromophore. Finally, the Cyc-RR complex, which primarily resides above the more recessed and sparser groove between adjacent monomers, has a negligible effect on water dynamics in the already fairly dynamically constrained groove compared to the system without the chromophore.

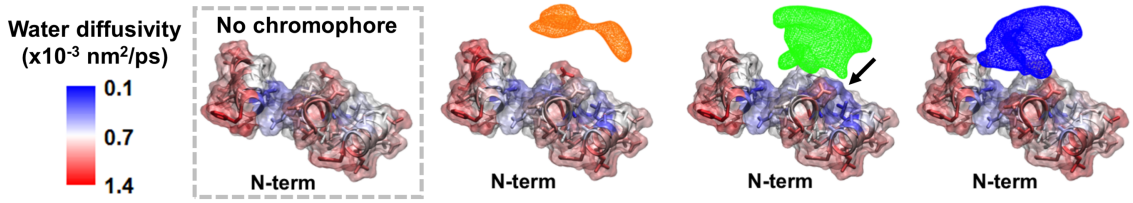


Figure 2.23: Simulations of water diffusivity on the protein surface with and without the presence of chromophores with various linkers.

### 2.4.6 Hydration dynamics and protein motion is responsible for dynamic retardation of chromphore dynamics

The differences in water dynamics correlate with the retardation trends observed experimentally between Ethyl-, Cyc-SS- and Cyc-RR-linked complexes at S23C (yellow bars in Figure 2.19) remarkably well. In the TA, the intramolecular and solvent dynamics for Et-, Cyc-SS, and Cyc-RR-linked chromophores are slowed by factors of 3.3, 5.5, and 3.2, respectively (Table 2.1). In the simulations, the compounded retardation of water molecules between the protein and chromophore are by factors of ∼4.8, 6.4, and 4.6, respectively. These results show that explicit inclusion of the chromophore in simulations is paramount to accurately determine the system dynamics, and that in certain cases, the strong interaction between chromophore, protein, and solvent leads to a supracomplex with intricately coupled dynamics. We therefore believe that a combination of slowed hydration dynamics and protein motion, the latter being particularly effective at intracavity labeling sites where chromophores are surrounded by protein residues, are responsible for the up to 14-fold retardation (for Cyc-SS linked to inner cavity site Q101C) in solvent-chromophore dynamics in our experiments. By engineering the distance from the protein surface and the volumes sampled by chromophores in relation to specific protein residues, solvent–solute interactions can be finely and predictively tuned. The complex interplay between protein, water, and chromophore motions and dielectric interactions thus provides an exceptionally rich and system-specific platform to control the excited state properties of biomimetic assemblies.

## 2.5 Conclusion

Toward developing biomimetic light harvesting assemblies, we have combined a highly tunable protein scaffold based on the tobacco mosaic virus coat protein with a library of chromophore–protein linkers. This combination enabled us to systematically study the molecular dynamics of chromophore–protein–solvent interactions and their effect on the ultrafast ex-

cited state dynamics of the chromophores. Small modifications to the position, mobility, and attachment orientation of the chromophores on the protein surface, achieved through alkyl chain shortening or switching the chiral configurations of the linkers, suffice to control the nuclear relaxation dynamics of the system considerably. These results therefore highlight the often-overlooked importance of purpose-specific linker engineering in combination with judicious attachment positioning to tune the properties of artificial light-harvesting systems.

On the basis of these findings, we describe below how our assemblies enable a modular approach to tune the balance between chromophore–protein and interchromophore couplings, and how such fine-tuning will permit further understanding of how nature has optimized its complex photosynthetic environment for light harvesting.

### 2.5.1 Shorter and more rigid linking groups enable stronger chromophore-protein-solvent couplings and leads to slower excited state evolution

First, at the level of chromophore–protein interactions, we found that minor modifications to chromophore–protein linker length and rigidity transform into pronounced differences in the chromophore properties when bound to the protein assembly. For example, shortening the butyl linker by just two bonds to ethyl reins in the chromophore closer to the protein surface and into a region prone to chromophore–protein interactions. This shortening changes the chromophore environment from being completely bulk-like to the more heterogeneous protein–solvent interface. Consequently, a greater than 4-fold slowing of the Stokes shift time scale occurs at the outside labeling position between butyl-linked and ethyl-linked chromophores. Further rigidifying the chromophore to cyclohexyl-based linkers enhances the retardation up to 6-fold. This strategy to tune the optical properties of chromophores and preserve electronic excitations in the system by coupling the chromophore and protein may be a crucial photosynthetic design principle, where chromophores are tightly bound within protein pockets and thus necessarily interact with their biomolecular environment.

These considerations invite a more explicit comparison of our biomimetic light harvesting platform with the natural ones that it seeks to emulate. In light-harvesting systems where interchromophore energy transfer between identical chromophores is present, retarding Stokes shift dynamics could enable a larger number of resonant energy hops to proceed well out-of-equilibrium within the lifetime of an excitation. These energy hops can be more efficient than those initiated from structurally relaxed chromophores due to the larger spectral overlap between adjacent chromophores prior to nuclear relaxation, thus aiding long-range energy transport. A schematic of this potential scenario is shown in Figure 2.24, where a protein-confined chromophore has relatively lower and higher rate constants, $k_{\mathrm{rel}}$ and $k_{\mathrm{hop}}$, for vibrational relaxation and hopping, respectively, than in the free chromphore case. Furthermore, the preservation of excess energy within the system can help overcome unwanted trapping in low-energy states that are inevitable in disordered environments.

While individual chromophore dynamics in natural light-harvesting systems are unknown

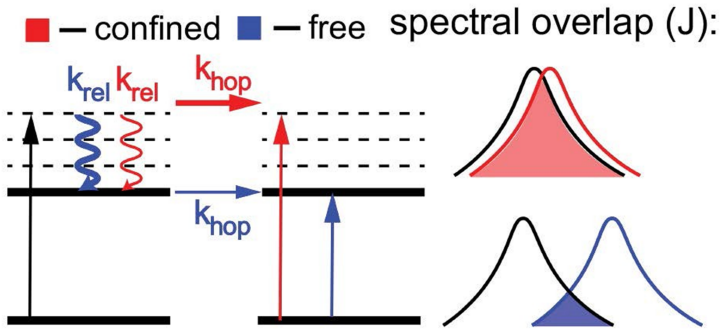


Figure 2.24: Schematic energy diagram of a free chromophore and a protein bound chromophore. In this hypothetical scenario, the protein bound chromophore has a comparatively faster hopping rate and slower vibrational relaxation rate, leading to more efficient energy transport while preserving higher energies.

due to our inability to study them in the absence of interchromophore coupling, their degree of confinement, range of motion and distance from protein surfaces in complexes such as the LH2 of purple bacteria or the FMO of green sulfur bacteria are on the same order as for our cyclohexyl-based complexes[78, 115]. Chromophores in these natural systems are thus likely subject to similar or greater dynamic retardation of their individual Stokes shift dynamics. Our highly tunable scaffold will facilitate a bottom-up approach to test our hypotheses on the role of relaxation retardation on light-harvesting and provide direct insight into whether these mechanisms are also likely to be operative in photosynthetic organisms.

### 2.5.2 Chirality of linking groups enables more precise chromophore-protein-solvent couplings

Second, looking toward the control of interchromophore interactions, we have shown that further constraints on chromophore environments can be readily applied by locking the chromophore into specific positions on the protein surface. To that end, we found that linker chirality can be exploited: despite no major difference in length or rigidity, changing the linker from (*R,R*)- to (*S,S*)-cyclohexyl leads to considerably slower excited state dynamics due to different attachment positions. These different configurations lead to distinct chromophore–protein bath interactions, including sandwiching water molecules in a tight space between chromophore and protein. Furthermore, both cyclohexyl-linked chromophores exhibit much longer orientational decorrelation times than the more flexible alkyl linkers. Over the full course of the chromophores' excited state lifetimes, this constraint enables greater

control of the relative orientations of the chromophores with respect to each other and the protein surface—a crucial feature to achieve long-range energy transport. The ability to manipulate the relative position and orientation of adjacent chromophores in easily configurable artificial light harvesting constructs presents the further possibility to mimic and test the characteristics of specific interchromophore motifs found in nature.

### 2.5.3 Towards the future of using a bottom-up design to learn about photosynthesis

Having refined chromophore–protein interactions through our studies performed in the absence of interchromophore interactions, we are now poised to reintroduce these interactions via saturating labeling densities to form complete biomimetic light harvesters. A key challenge will be to obtain the right balance between interchromophore and chromophore–protein coupling for a range of energy transport regimes found in nature, from long-range dipole–dipole to short-range excitonic processes, while maintaining systems free of contact quenching. The degree of control over chromophore–protein interactions that we have demonstrated in our bottom-up approach, and the flexibility over attachment positioning and hence interchromophore distance afforded by our synthetic scaffold, will prove essential in finding the tuning range over which energy transfer proceeds efficiently for different transport regimes. Examining the role of chromophore–solvent–protein interactions over the entirety of this tuning range will enable testing and refining our current models seeking to explain the high quantum efficiencies and vast diversity of photosynthetic organisms.

To mimic nature even further, the construction of extended arrays of cpTMV rings, analogous to the arrays of natural light harvesting complexes packed into lipid membranes, could allow the exploration of longer range biomimetic energy transfer using recently developed spatially resolved approaches[116, 117]. A schematic of such a system we have envisioned for the cpTMV system is shown in Figure 2.25. Once the synthetic capabilities to asymmetrically couple cpTMV disks of varying chromophore identities are developed, we could try and arrange cpTMV "donor" rings peripherally around cpTMV "acceptor" ring, in much the same way LH2 complexes are arranged around LH1 complex in purple bacterial antenna systems.

Ultimately, the fine level of control over linker properties achievable through well-known synthetic procedures, along with high-throughput screening of candidate linkers using computational modeling, represents a highly effective strategy to design purpose-specific biomimetic tools to more easily test hypotheses regarding the molecular mechanisms of natural photosynthetic light harvesting. In particular, since nuclear-electronic coupling often dictates the fate of molecular excited states following light absorption, harnessing chromophore–bath couplings to affect the structural motion of electronically coupled arrays of chromophores[118–121] could prove paramount to achieving long-range energy transport as efficiently as in natural photosynthetic systems. Such an achievement would help elucidate the molecular and intermolecular origin of the unparalleled efficiency of photosynthetic light harvesting.

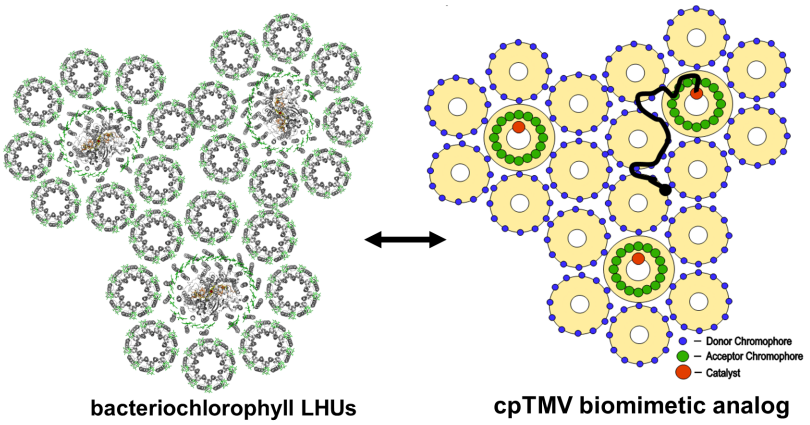


Figure 2.25: Schematic of mesoscales cpTMV assembly emulating the bacteriochlorophyll-containing light harvesting units found in nature

.

# Chapter 3

# Correlative AFM Phase Imaging and Widefield Single-Particle Tracking in PEO thin films

*Portions of this chapter are adapted or reprinted with permission from Roberts et al., "Direct Correlation of Single-Particle Motion to Amorphous Microstructural Components of Semicrystalline Poly(ethylene oxide) Electrolytic Films,"* J. Phys. Chem. Lett. ***2020**, 11 (12), 4849–4858 Copyright 2020 American Chemical Society.*

## 3.1 Introduction

Semicrystalline polymers constitute some of the most widely used materials in the world, and their functional properties are intimately connected to their structure on a range of length scales. Many of these properties depend on the micro- and nanoscale heterogeneous distribution of crystalline and amorphous phases, but this renders the interpretation of ensemble averaged measurements challenging. In this chapter, we use superlocalized widefield single-particle tracking in conjunction with AFM phase imaging to correlate the crystalline morphology of lithium-triflate-doped poly(ethylene oxide) thin films to the motion of individual fluorescent probes at the nanoscale. The results demonstrate that probe motion is intrinsically isotropic in amorphous regions and that, without altering this intrinsic diffusivity, closely spaced, often parallel, crystallite fibers anisotropically constrain probe motion along intercalating amorphous channels. This constraint is emphasized by the agreement between crystallite and anisotropic probe trajectory orientations. This constraint is also emphasized by the extent of the trajectory confinement correlated to the width of the measured gaps between adjacent crystallites. This study illustrates with direct nanoscale correlations how controlled and periodic arrangement of crystalline domains is a promising design principle for mass transport in semicrystalline polymer materials without compromising their mechanical stability.

### 3.1.1 Semicrystalline polymers

Solution processable semicrystalline polymers, such as polyethylene and its derivatives[122] as well as numerous nylons and rubbers[123], are an important class of materials and constitute one of the largest groups of commercially useful polymers. Intimately connected to the polymer's functional properties are the morphologies[124–127] resulting from various means of preparation, wherein the distribution of crystalline and amorphous material is inhomogeneous on a wide variety of length scales[128–130]. Crystallinity in such materials typically corresponds to greater mechanical strength but renders the material more brittle, and more amorphous character corresponds to greater flexibility at the cost of mechanical strength[131]. It is well known that the polymer material is more fluid in its amorphous state and more rigid in the crystalline state, as lamellar crystallites form when polymer chains tightly fold upon themselves, which increases local material density and reduces free volume[132–134]. A common procedure to create polymer films is to begin with a solution of the polymer dissolved in a solvent and then to "cast" the polymer into a solid film by rapid removal of the solvent via spincoating or dropcasting. Shown in Figure 3.1 is a schematic overview of a semicrystalline polymer film, where the solution-cast film is composed of both regions of highly ordered polymer chains (crystallites) and randomly distributed polymer chains (amorphous polymer). Semicrystalline polymer films are intensely studied for a number of promising applications, like prolonged drug elution[135], charge transport in organic semiconductors[3], and ion conduction [11], among others.

Polymer crystallinity can be very hierarchical. When polymer chains fold together into local ordered lamellae, these lamellae can further assemble into larger superstructures, like spherulites [136], where crystalline fibrils radially extend from a nucleus and the remaining space is filled with amorphous polymer. Such superstructures can easily exceed diameters 100s of microns in length, and understanding how to leverage such macroscopic semicrystalline polymer superstructures for device applications (like semiconducting electronics) is an active area of research [137]. Figure 3.2 shows a schematic detailing the hierarchy of the crystalline and amorphous polymer material in spherulites as well as a polarized optical microscopy (POM) image of a poly(ethylene oxide) spincoated thin film revealing numerous spherulitic structures (indicated by the characteristic Maltese cross pattern) of various sizes. It is important to reiterate that regardless of the size of these polymer superstructures, the arrangement or separation of crystalline and amorphous regions can range from angstroms to hundreds of nanometers [138] and ultimately the macroscopic properties of the polymer are critically associated with the polymer's morphology on these length scales.

### 3.1.2 Poly(ethylene oxide) as a solid-state electrolyte matrix

Poly(ethylene oxide) (PEO) is a particularly well studied semicrystalline polymer with applications for solid-state electrolytes, for example, in batteries[11]. The polar ether backbone of PEO is amenable to solvating ions, like $Li^+$, allowing deposits of PEO to behave as an electrolyte component in devices. Solid-state electrolytes are an attractive alternative to

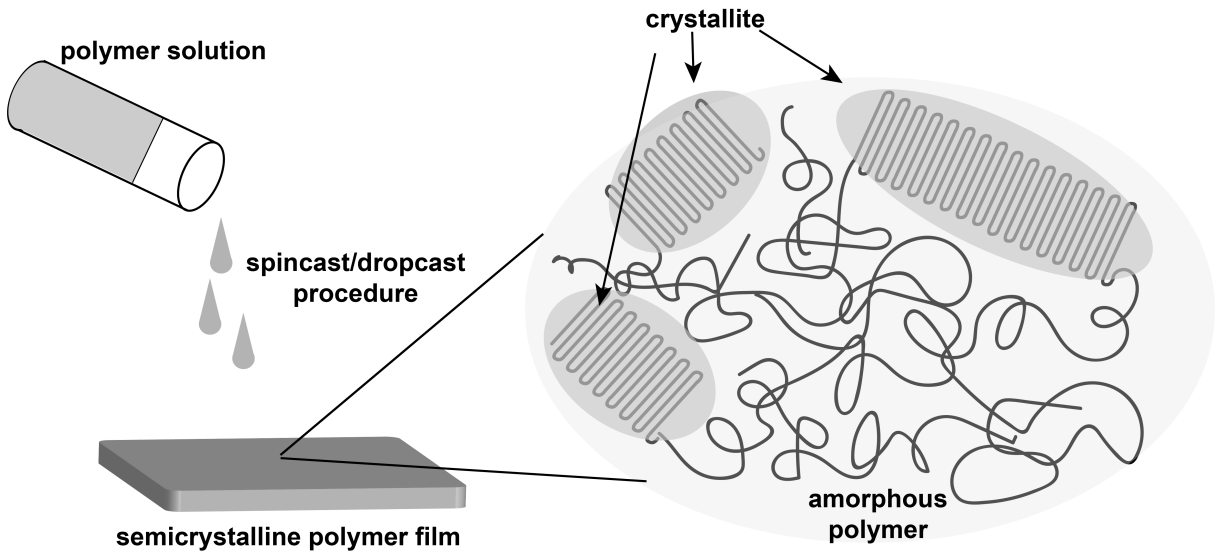


Figure 3.1: Schematic of a semicrystalline polymer film prepared via a spincasting/dropcasting procedure. Crystallites are highlighted as regions where polymer chains are in a folded order, and amorphous polymer shown as polymer chains adopting random configurations.

liquid electrolytes due to their promise of increased safety by removing flammable solvents as well as supressing the growth of Lithium dendrites across electrode surfaces, which can result in dangerous short-circuiting of battery cells [139]. As ambient temperature is between the range of PEO's glass transition temperatures ($\sim$ -67 to -28° C), and melting temperatures ($\sim$ 55 to 65°) it offers desirable transport properties for ions as well as desirable structural integrity for incorporation in devices. While the precise mechanism is still under investigation, the conductivity, or movement, of $Li^+$ ions in a PEO network is thought to be facilitated by the polymer chain flexibility in the amorphous state, where the continuous segmental rearrangement can allow lithium ions to migrate greater distances (Figure 3.3b).

Room temperature ion conductivity remains to be improved, however, and strategies to improve conductivity often involve suppressing crystallinity, which is typically monitored as a fractional composition in bulk[140–143]. It is generally believed that crystallites behave as impermeable boundaries for the transport of ions, molecules, and other dopants in the amorphous state[144–147]. Additionally, when doped with ionic salts, some polymers can form ordered polymer-ion crystalline complexes, where the polymer chain backbone tightly coordinates around charged ions, as has been demonstrated for PEO[148–154]. Such crystalline material may also serve to impede the transport of small particles.

Unfortunately, despite the heterogeneous morphology of semicrystalline polymer materials like PEO, most measurements of material parameters are made in bulk[11, 148, 153, 155–160], making it challenging to associate specific elements of the morphology with func-

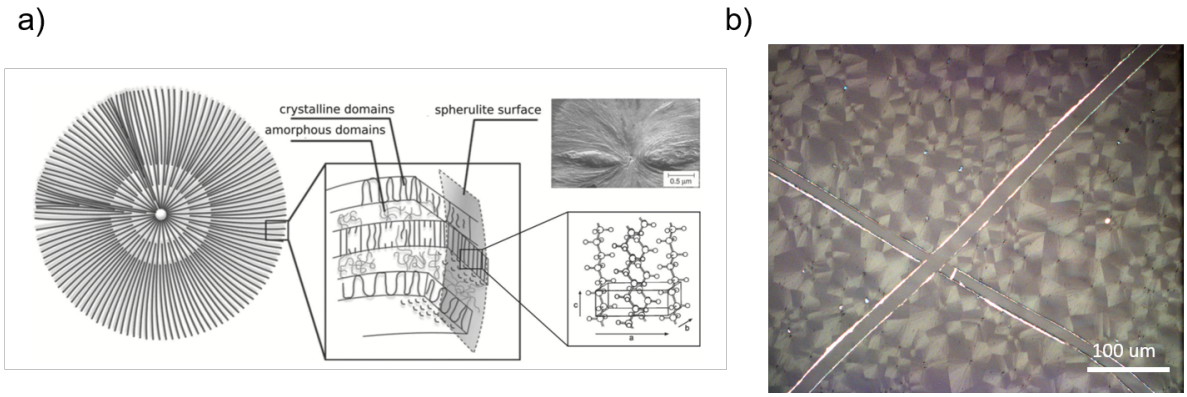


Figure 3.2: Polymer spherulite schematic and optical microscopy image of spherulites. (a) Schematic demonstrating how the fibers of a spherulite are composed of crystalline polymer domains, and that these domains are intercalated by disordered amorphous polymer material. Adapted with permission from Ref [137]. (b) Example POM (polarized optical microscopy) image of a spherulitic poly(ethylene oxide) thin film produced via spincoating. Spherulites can often be distinguished in brightfield microscopy by a characteristic Maltese cross pattern of alternating bright and dark contrast under polarized illumination and orthogonal polarized detection. Spherulites shown here are as large as $\sim 100$ $\mu$m in diameter.

tional attributes. For example, bulk conductivity measurements average the motion of ions over length scales orders of magnitude larger than the separation between crystalline and amorphous phases. A more explicit measurement of how small species – whether charged or neutral - move as a function of the film microstructural components could help to more explicitly identify optimal morphologies that balance mechanical and transport properties. By characterizing the motion of a neutral probe specifically as a function of nanoscale spatial coordinates and morphological composition, we stand to gain more insight into precisely how crystallites influence transport. Furthermore, a nanoscale mapped correspondence between morphological composition and motion of a probe would demonstrate whether probe motion in amorphous regions is affected by region size and proximity to crystallites.

## 3.2 Experimental Method: Imaging methods employed and the model system

We correlate the mechanical and morphological spatial map of a semicrystalline polymer via atomic force microscopy (AFM) phase imaging with single-particle localization and dynamic tracking (SPT) to map the motion of a probe in films as a function of composition and resulting morphology. Previous studies correlating AFM with fluorescence imaging demonstrate

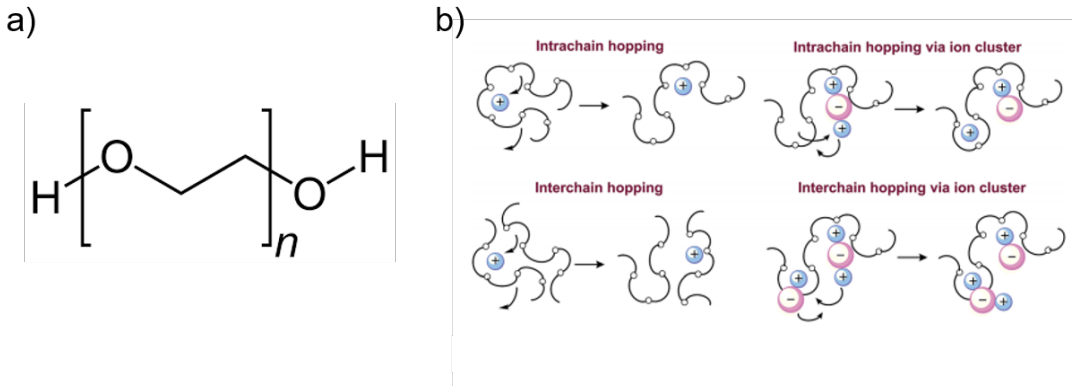


Figure 3.3: PEO and ion solvation. (a) Chemical structure of PEO. (b) Proposed mechanisms for ion transport throughout a PEO network, where ions can hop from site-to-site along the PEO chains in various ways. Adapted with permission from ref [11].

how the two characterizations can complement one another[161, 162] and even elucidate discrepancies[163] between the two imaging modalities. We use a ternary system of PEO, lithium triflate (LiOTf) and fluorescent Coumarin 6 (C6) to measure the nanoscale motion of fluorescent C6 complexes at 40 nm precision and correlate it to film morphology obtained via AFM phase imaging.

The nanoscale resolution of polymer morphology provided by AFM and the nanoscale dynamics of probe particles provided by SPT enables explicit correlations to be drawn between polymer structure and function over **relevant** length scales. A description of each imaging technique, as well as the model system investigated, follows.

### 3.2.1 AFM phase imaging of semicrystalline polymers

Tapping-mode AFM imaging is a widely used technique to characterize sample surfaces with exquisite detail and resolutions substantially smaller than conventional optical microscopies. Briefly, the essential components of common AFM set-ups are: a sharp tip (usually $< 10$ nm in radius), a microcantilever, a laser, a cantilever deflection sensor, a piezoelectric positioner, and an electronic feedback mechanism between deflection sensor and piezoelectric positioner [164]. The laser is focused on the cantilever and is reflected onto a detector like a photodiode. Upon interaction between the sample and tip, the cantilever's motion is perturbed, which is registered by consequently deflecting the focused laser into a slightly different position on the photodiode. By registering how the laser deflection changes as a function of scanning the tip over a sample, one builds an image where various physical properties are encoded into the tip's spatially-dependent response, like the height variation of a sample's surface, for example.

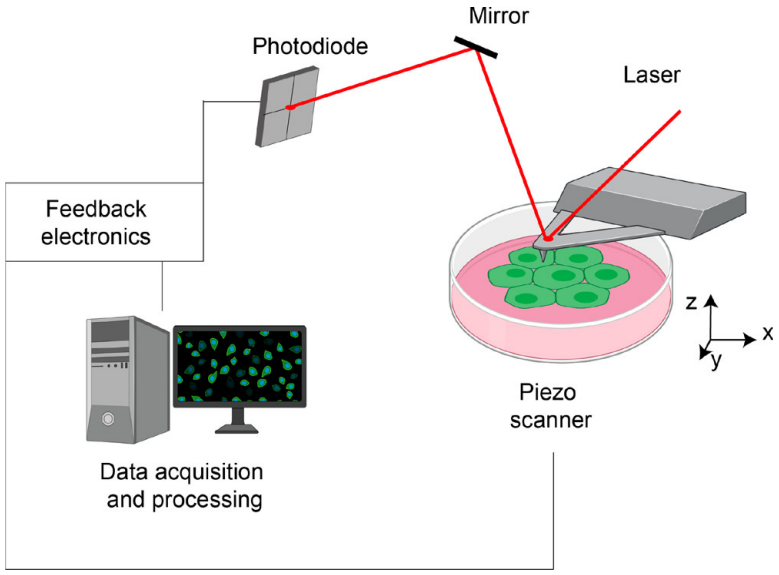


Figure 3.4: Basic components of common AFM set-ups. Reproduced with permission from [164].

In tapping-mode, the cantilever is made to resonate at a high frequency (in other words, driven) prior to material interaction, and when brought into contact with the sample surface, it will intermittently contact or "tap" the sample. The differences in both oscillation amplitude and frequency of the signal upon interaction with a sample surface report on material surface variability. Certain sample properties, like adhesive and viscoelastic properties[165] or surface wetting[166, 167], can prevent the AFM tip from moving up and down at the exact same time as the input signal, which induces an effective "lag" in the tip's motion that is registered as a phase shift[168].

In the case of semicrystalline polymers, the dramatic difference between the viscoelastic properties of a polymer in the crystalline phase versus the amorphous phase yields excellent contrast when comparing the relative phase shifts in tapping-mode AFM imaging. This is particularly useful for characterizing a semicrystalline polymer film, where intricate morphologies resulting from the distribution of the crystalline and amorphous polymer phases may show little-to-no variability in the film's height. Figure 3.6 demonstrates the clarity AFM phase imaging provides in determining regions of crystallinity and amorphous polymer in lithium triflate doped PEO thin films. Rod-like features that correspond to crystallites do not register as clearly in the height images, but in the phase images there is an almost binary distinction between crystallites (white, rod- or fiber-like features) and amorphous polymer (relatively featureless blue regions).

Notably, the phase images from tapping-mode AFM provide sufficient resolution to image the spatial separation between crystallites on the order of 10s of nm. Such sensitive spatial

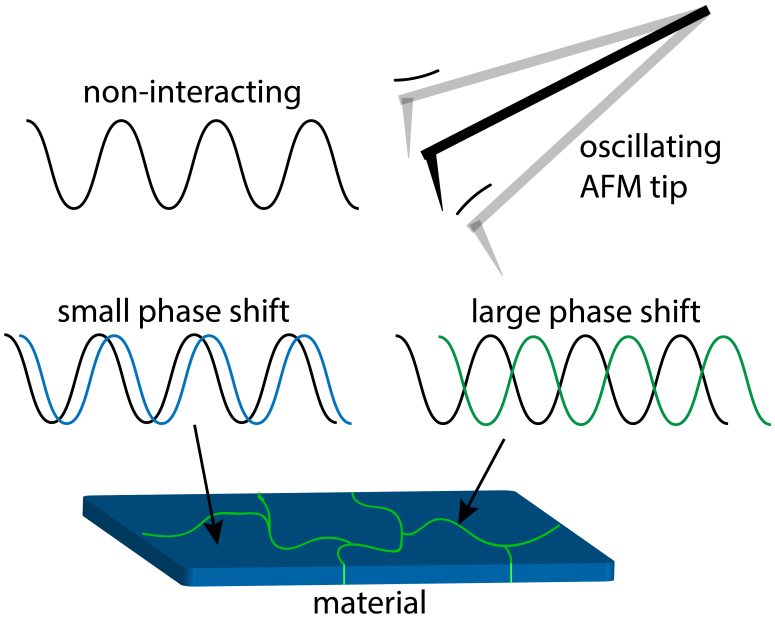


Figure 3.5: Cartoon depiction of AFM phase imaging. AFM cantilever oscillates at a resonate frequency prior to contact with the sample. Differences in material properties, like those of the blue and green regions, will impart different phase shifts into the AFM cantilever's oscillatory motion.

mapping is a key factor to determining the nature of how and the extent to which crystallites influence small particle transport.

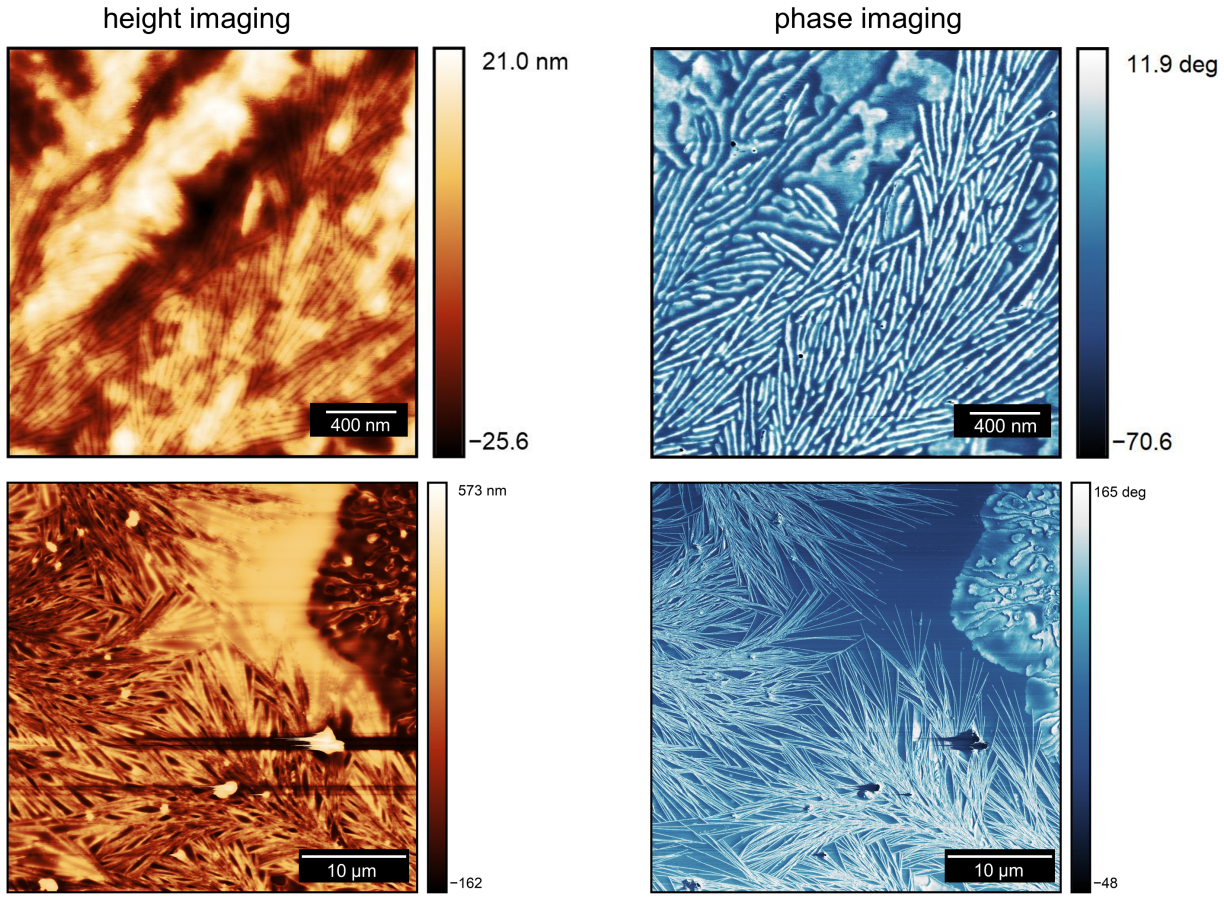


Figure 3.6: Tapping-mode AFM imaging of semicrystalline PEO thin films. Shown are AFM height images and corresponding phase images of two different fields of view of a semicrsystalline PEO thin film. Rod-like features that register as darker signal (and therefore lower height) are difficult to discern in the height images, but become unambiguous in the phase images, where the higher phase values correspond to regions of crystallinity (white) and the lower phase values correspond to regions of amorphous polymer (blue).

### 3.2.2 Widefield single-particle tracking

We use widefield single-particle tracking (SPT) to explain how morphological heterogeneities on the order of tens of nm influence probe motion, which has also proven to be useful in deducing nanoscale behavior in a variety of biological[169–171], polymer[172–178], and other material[179] systems.

SPT enables one to monitor the spatial evolution of individual fluorescent probes as a

function of time by recording consecutive images of the same field of view (i.e. a movie) over a specified period of time and monitoring the spatial coordinates of a given probe within each frame. The temporal resolution is determined by the overall time between the beginning of one frame and the beginning of the consecutive frame, which includes both the acquisition/exposure time of a given frame as well as the time-lag between ending one frame's acquisition, storing the data, and beginning the consecutive frame's acquisition. The signal-to-noise ratio is related to the frame rate, where longer acquisition times enable collecting more fluorescent photons but at the expense of averaging dynamics out over longer periods of time. For typical SPT measurements, the frame rate can range from 1 - 1000 ms in order to observe particle dynamics on seconds to hours timescales.

SPT can naturally incorporate a post-processing analysis known as super-localization, which is used extensively in the field of super-resolution fluorescence microscopy[180]. When imaging fluorescent emitters in a conventional imaging system, like a wide-field epi-fluorescence microscope, the resolution is ultimately limited by the optical diffraction limit ($D = \frac{\lambda}{2NA}$, where $\lambda$ is the wavelength of the detected photons and $NA$ is the numerical aperture of the microscope objective) irrespective of whether the actual size of an emitter in question is substantially smaller. That is, each individual emitter (typically 1 - 10 nm) will yield an image with an effective microscope point-spread function (PSF) possessing a width (often defined as the full-width at half-maximum, FWHM) that corresponds to the diffraction limit (typically 150 - 250 nm). Super-localization is a clever analysis of emitter PSFs, which can be explained using the equations provided by Carl Zeiss Microscopy Online Campus[181]. The procedure involves first fitting individual profiles with a 2D Gaussian function:

$$I(x,y) = I_o \exp\left(-\frac{(x-x_o)^2 + (y-y_o)^2}{2s^2}\right) \tag{3.1}$$

The centroid of this 2D Gaussian fit is the most probable location of the emitter within the imaged PSF. The certainty, or precision, with which one can confidently localize the emitter scales with number of detected photons:

$$\sigma_{x,y}^2 = \frac{\left(s^2 + \frac{q^2}{12}\right)}{N} + \frac{8\pi s^4 b^2}{q^2 N^2} \tag{3.2}$$

where $\sigma_{x,y}$ is the localization precision in X,Y dimensions, s is the standard deviation of the 2D Gaussian fit to the emitter PSF, N is the total number of detected photons, q is the pixel size, and b is the background noise. Critically, Equation 3.2 demonstrates that $\sigma_{x,y} \approx \frac{s^2}{N}$, and therefore the localization precision becomes more certain (i.e. smaller) as the number of detected photons increases. Provided the fluorescent emitters are bright enough under the imaging conditions, localization precisions of 10's of nm can be achieved. A technically more rigorous approach would be to fit each emitter PSF to an Airy function, which is more physically representative of a truly diffraction limited PSF, but Gaussians

are computationally much less demanding and still yield sufficiently similar results to Airy functions.

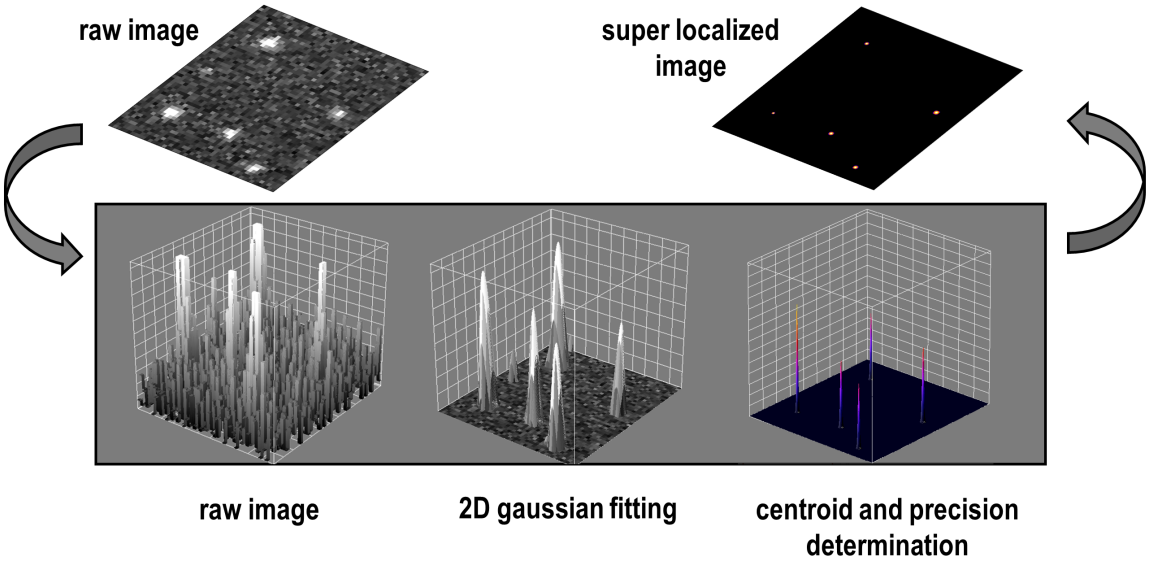


Figure 3.7: Super-localization analysis workflow. The raw image is a pixelated recording of individual fluorescent probes. The point-spread functions, shown as the raw image's surface plot, are fit by 2D Gaussian functions. The centroids of the Gaussian fits are determined, as well as the localization precision described by Equation 3.2. This information is rendered into a new super-localized image, where each spot's location is the estimate of the emitter's location, and the width of each spot is the precision from the fit.

The motion of a given emitter can therefore be characterized with 10s of nm precision by monitoring its location in a time-series of consecutive images and super-localizing its PSF in each image. Using the microscope setup in Fig 3.8, we acquire movies with 100 ms exposure ($\sim$ 130 ms frame-to-frame time) on an electron multiplying charge coupled device (EM-CCD) camera with micromanager software[182] using continuous wave (CW) 532 nm illumination.

Individual probes can then be followed over an average of 24 frames in order to learn how they explore the film morphology. Probe super-localization is performed using the ImageJ GDSC SMLM plug-in[183], and trajectories are reconstructed using MATLAB scripts. The average localization precision of particles is $\sim$ 40 nm, and the distribution of particles and corresponding measured signal is shown in Fig 3.9. There is a correlated increase with the localization precision as the signal count is higher, as expected from Equation 3.2.

With regards to trajectory reconstruction, we chose to write our own analysis script in

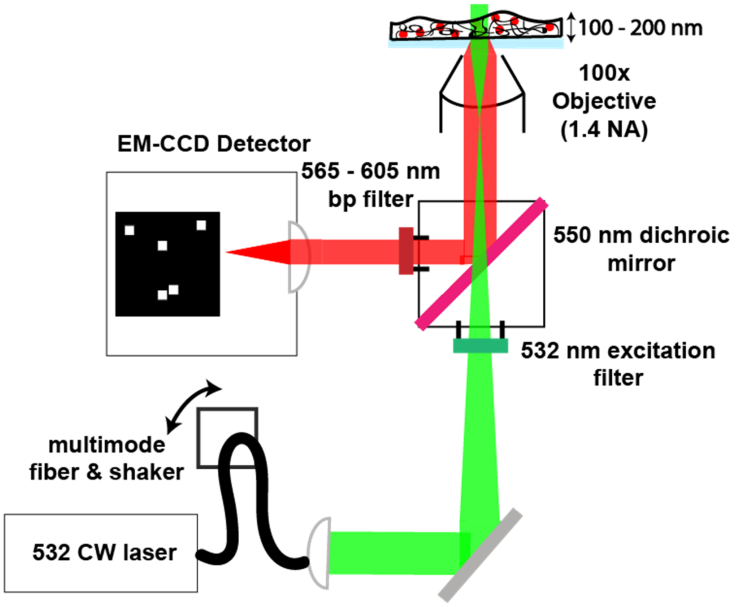


Figure 3.8: Schematic of single-particle fluorescence imaging, with 532 nm continuous wave excitation of thin-film sample and emission detection between 565 and 605 nm. The laser output is coupled through a multimode fiber to scramble its polarization and is shaken at a sufficient frequency to spatially average the intensity pattern in each frame. The 532 nm is then passed through a 532 nm excitation filter and 550 nm dichroic before arriving at the objective.

part because various ImageJ plug-ins would, in one way or another, fail visual inspections of the acquired movies. For instance, variability in signal intensity over the course of a probe's trajectory would yield erroneous fragmentation of trajectories or misassign particle positions. While the more sophisticated nature of the algorithms used in ImageJ in principle enable superior trajectory reconstruction for various circumstances, such as low signal-to-noise, high particle density, systematic drift, or even temporary disappearance of particles (i.e. "blinking")[184], such analysis plug-ins are "black boxes" in some ways that prevents us from easily determining the various input parameters required for successful trajectory reconstruction. Given that most of our data have a sufficiently high signal-to-noise and that the emitter density in any given frame is sufficiently low to accurately localize positions, we felt confident in using our relatively more simplified scripts. To this end, we employ

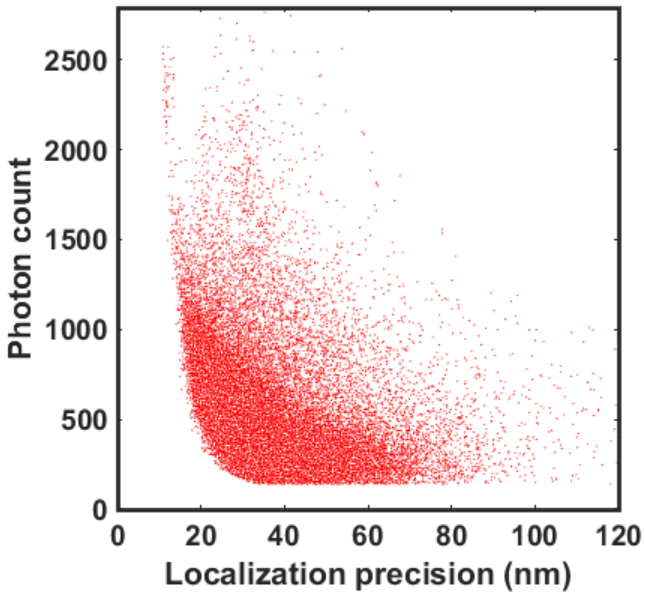


Figure 3.9: Precision and corresponding signal value of every emitter localized in a representative data set. Fits assume an aberration free, two-dimensional Gaussian point spread function.

a number of thresholding criteria to reconstruct trajectories accurately, some of which are shown in Fig 3.10.

A representative super-localization image in Fig 3.18a is generated by fitting each emitter in each frame to a 2D gaussian and then superimposing the collection of all gaussian fits. The width of each spot represents the localization error, and the intensity represents the density of distinct emitters found within the spot. The mean squared displacement (MSD) of each reconstructed trajectory thus identified is obtained using a two-dimensional Brownian diffusion model:

$$MSD(n\delta t) = \frac{1}{N-1-n}\sum_{i=1}^{N-1-n}\left\langle (x_{i+n}-x_i)^2 + (y_{i+n}-y_i)^2 \right\rangle = 4Dn\delta t \tag{3.3}$$

where $N$ represents the total number of frames in a given trajectory, $n$ is the given frame from the initial frame, and $n\delta t$ is the corresponding time at which the MSD is calculated. As we increase the time point by 1, the number of available data points for the MSD decreases by 1. As a consequence, the effective uncertainty of MSD estimates grow with each step and so we only fit the first 1/4 of the time points to avoid statistically unreliable data points.

We characterize the anisotropy of probe trajectories using a principal component analysis (PCA) on vectors that represent each step and are repositioned to originate at the origin of

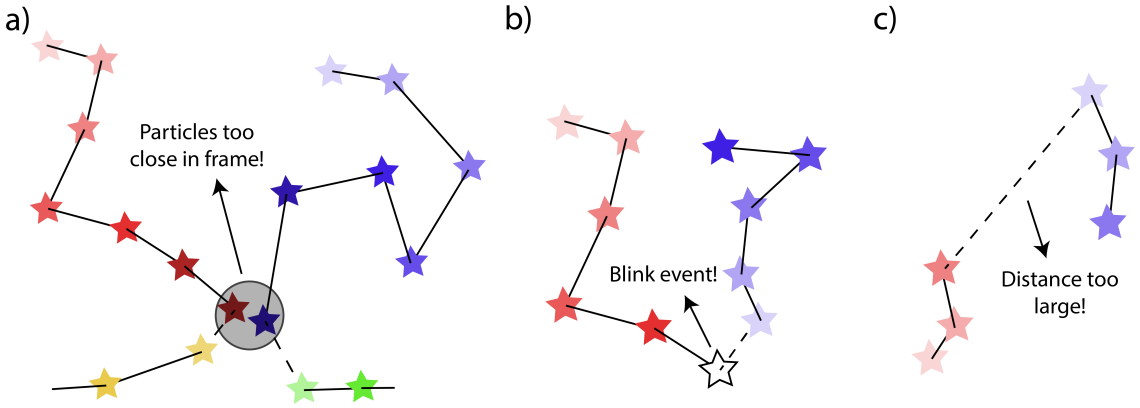


Figure 3.10: Circumstances that terminate trajectory formation. Different colors represent different trajectories. (a) Trajectories of two particles that become too close in space to be distinguished. (b) The emission of a particle "blinks" off for a frame. (c) The nearest neighbor between consecutive frames is too great a distance to be physically reasonable.

the coordinate system. Major and minor axes, along with their respective variances, $\mathcal{L}_{max}$ and $\mathcal{L}_{min}$, are extracted. We define the anisotropy parameter of a trajectory to be ($\mathcal{L}_{max}$ - $\mathcal{L}_{min}$)/ ($\mathcal{L}_{max}$ + $\mathcal{L}_{min}$) (Fig 3.11). In our analysis, we consider only trajectories of probes that we take to be mobile, i.e. whose diffusion coefficients are above a threshold of 0.0075 $\mu m^2/s$.

### 3.2.3 Ternary system of PEO, Lithium Triflate, and Coumarin 6 aggregates as model system

To investigate the role crystallinity plays in dictating probe motion, we prepare spin-coated thin films ( 100 nm) consisting of 600,000 Mw PEO, lithium triflate (LiOTf), and Coumarin 6 (C6). These samples serve as model semi-crystalline polymer systems, as the LiOTf is present at relevant millimolar (mM) concentrations, and C6 is present at much lower nM concentrations (Fig 3.12, and see below).

#### Degree and nature of crystallinity in PEO films

LiOTf is a common lithium salt used in Li-ion battery research[11], and we use the doping concentration of LiOTf to tune the relative crystallinity and corresponding morphology of the system at room temperature. According to the phase diagram describing the PEO-LiOTf system[140, 154, 185], at 15 mM LiOTf doping, crystallites are likely PEO:LiOTf crystalline complexes, and a significant amorphous component is also present possibly due to incomplete crystallization[158], a likely outcome due in part to the spincoating procedure. In this study we examine films prepared with a number of LiOTf co-doping concentrations between 1 to 15

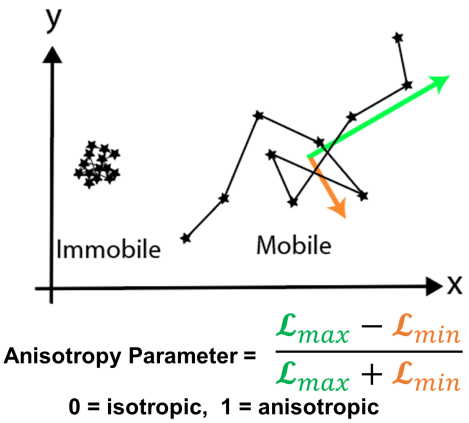


Figure 3.11: Schematic of immobile and mobile particle trajectories, with the major principal component of the mobile trajectory shown in green and the minor principal component shown in orange. The anisotropy parameter is defined as the difference between the maximum eigenvalue and minimum eigenvalue divided by the sum of the maximum and minimum eigenvalues generated by principal component analysis.

mM LiOTf, and these values are highlighted on the PEO:LiOTf phase diagram from Vallee et al.[154] (Figure 3.13).

### Determining the identity of our probes to be Coumarin 6 aggregates

Determining the nature of our fluorescent probes was not trivial. C6 is a versatile fluorescent dye, with notable applications for sensing changes in a material's pH due to its solvatochromaticity. Upon protonation, both the absorption and emission spectra of C6 substantially redshift[186, 187]. It was actually this unique property we initially sought to leverage in order to track $Li^+$ ions, as we hypothesized that $Li^+$ could potentially interact with C6 in much the same way $H^+$ does. Furthermore, we had developed the experimental workflow and infrastructure required to monitor C6 in its protonated state in polymer systems from work involving photoacid generators. By exciting the sample at 532 nm and detecting emission between 565 to 605 nm (Fig 3.8), we exclusively monitor emission from C6 that has been redshifted in some way. A control measurement involving PEO thin films doped with C6 and $H_2SO_4$ however revealed that single protonated C6 molecules in PEO were comparatively much dimmer and more susceptible to photobleaching under the same imaging conditions used to measure PEO films with LiOTf and C6. Figure 3.14 shows not only a markedly

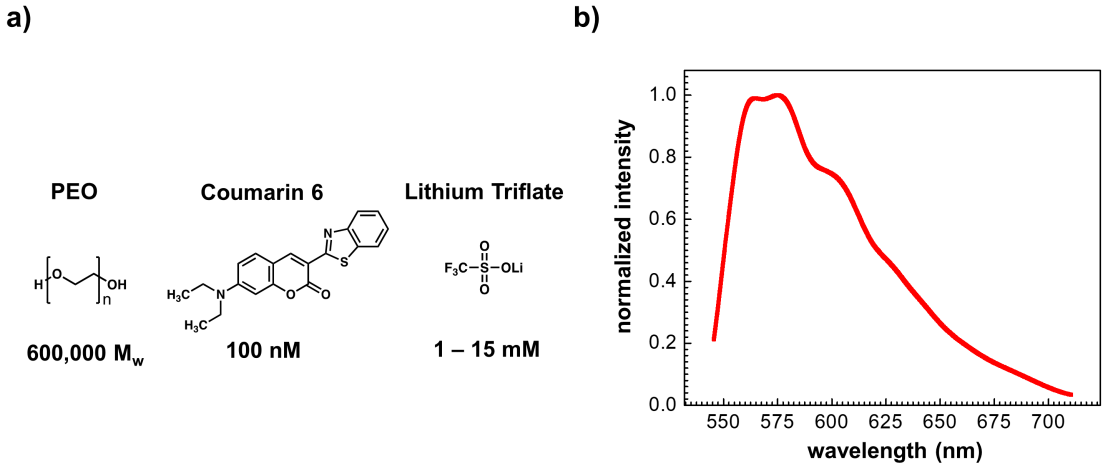


Figure 3.12: Ternary system used for SPT and AFM measurements. (a) 600 000 Mw PEO is dissolved along with 100 nM Coumarin 6 and 1 - 15 mM LiOTf. (b) Average of over 200,000 single-particle spectra of 10 mM LiOTf and 100 nM C6 co-doped PEO thin film, using 532 nm excitation. Spectrum acquired on separate, spectrally-resolved single-molecule fluorescence microscope.

higher density of emitters in PEO films with C6 and LiOTF, but the relative brightness of these emitters is ∼2x higher. It is worth noting that the background signal is higher in the case of the $H_2SO_4$, and one possible explanation for this is that the density of emitters (in this case, individual protonated C6 molecules) is actually quite high - so much so that individual emitters are spatially indistinguishable, yet their overall brightness is comparatively much lower.

C6 is hydrophobic, and so it may also form fluorescent aggregates with red-shifted absorption and emission spectra in polar media[188, 189]. Both the polar ether backbone of PEO as well as the ionic environment via the inclusion of LiOTf may instigate the formation of such aggregates.

Additional spectrally resolved single-molecule fluorescence microscopy measurements[190, 191] (Fig 3.12b), conducted in collaboration with the Xu group at Berkeley, confirm that the probes in films also containing LiOTf are not individual C6 molecules redshifted as a consequence of direct proton interaction, as initially hypothesized, but are likely C6 aggregates (Fig 3.15). The nature of the probe is further substantiated by the averaged single-particle spectrum, which shows much broader features than unprotonated or protonated individual C6 molecules, which can be seen in Fig 3.15e.

Furthermore, the average probe emission spectrum is not correlated to particle mobility and does not depend on the identity of the salt cation. Single-molecule displacement

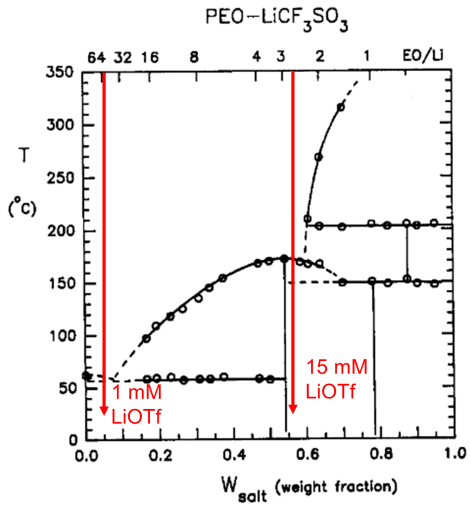


Figure 3.13: Phase diagram of PEO:LiOTF with 1 mM and 15 mM LiOTf co-doping concentrations highlighted. Figure adapted with permission from [154].

mapping (smDM) imaging[54], developed by our collaborators in the Xu group, is another way of measuring particle diffusion - rather than follow a single particle's trajectory over multiple frames, this technique measures local statistics of the instantaneous displacements of diffusing single particles. Higher frame-to-frame displacements correspond to higher diffusivity. We use this method and analysis, in tandem with spectrally resolved single-particle emission detection, to verify if there are correlations between particle mobility and spectra. Both Figure 3.15a and 3.15b demonstrate that the emission spectrum does not vary with the size of the frame-to-frame probe displacement, and therefore the emission spectrum does not vary with probe diffusivity. Since spectral shifts are often used as a proxy for aggregate size and are not apparent in our measurements of the probe spectra corresponding to different diffusivities, we posit that the fluorescent aggregates that we track have an approximately uniform size distribution to within the sensitivity of our measurements, such that the dynamics of different C6 complexes can be directly compared. To substantiate the notion that the polar ionic environment is responsible for the formation of C6 aggregates independent of directly interacting with $Li^+$ ions, we prepared films of PEO and C6 but replaced LiOTf with triphenysulfonium triflate (TPS-OTf). The triflate anion is the same, but the $Li^+$ cation is replaced by a more sterically bulky TPS cation which should in principle frustrate direct interactions with individual C6 molecules. We find that the averaged single-particle emission spectra at different salt concentrations in Figures 3.15c (LiOTf) and 3.15d (TPS-OTf) appear similar. Together, these data suggest that the probe emission scarcely depends on both the salt concentration and identity.

The averaged probe spectrum shows a minor, if any, dependence on the concentration of

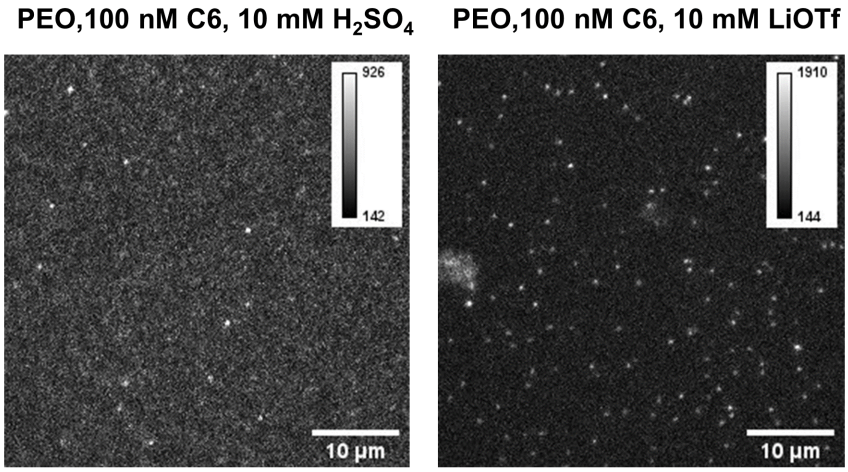


Figure 3.14: Comparison of fluorescence imaging between PEO films doped with 100 nM C6 and 10 mM $H_2SO_4$ and PEO films doped with 100 nM C6 and 10 mM LiOTf.

salt, yet increasing the LiOTf concentration markedly increases the C6 aggregate fluorescence from a film. Figure 3.16 shows films both without (a) and with (b) LiOTf that are illuminated with 532 nm continuous wave widefield excitation with a laser intensity of $\sim$75 W/cm$^2$. The emission intensity increases with the addition of LiOTf to the PEO films doped with 10 $\mu$M C6, suggesting the presence of a fluorescent species that is sparingly or not at all present in the C6-only films.

To this end, we find that for a fixed C6 concentration, the number of single fluorescent aggregate particles detected per imaging frame is linearly proportional to the salt concentration. Figure 3.17a plots the average number of emitters detected in PEO thin films prepared with different loading concentrations of LiOTf (but the loading concentration of C6 in every film is 100 nM) shown as grey data points. We note that the average number of emitters detected per film increases with the LiOTf concentration ranging from 0.5 to 10 mM. Importantly, a control film prepared with *only* 10 mM LiOTf (red data point) shows very few emitters (possibly trace fluorescent impurities intrinsic to the PEO and/or LiOTf materials) and suggests that only the combination of C6 and LiOTf is what results in the comparatively higher density of emitters. We also find that although increasing the LiOTf loading concentration results in a higher density of emitters, the average integrated signal of the individual emitters remains constant within experimental error, shown in Figure 3.17b. Taken together, the data presented in these two plots recapitulate our observations from the spectrally-resolved single-particle measurements: that LiOTf plays a role in inducing the generation of these fluorescent species, but the identity of this species remains roughly the same for different LiOTf loading concentrations.

Overall, the numerous above findings strongly support the assertion that the fluorescent

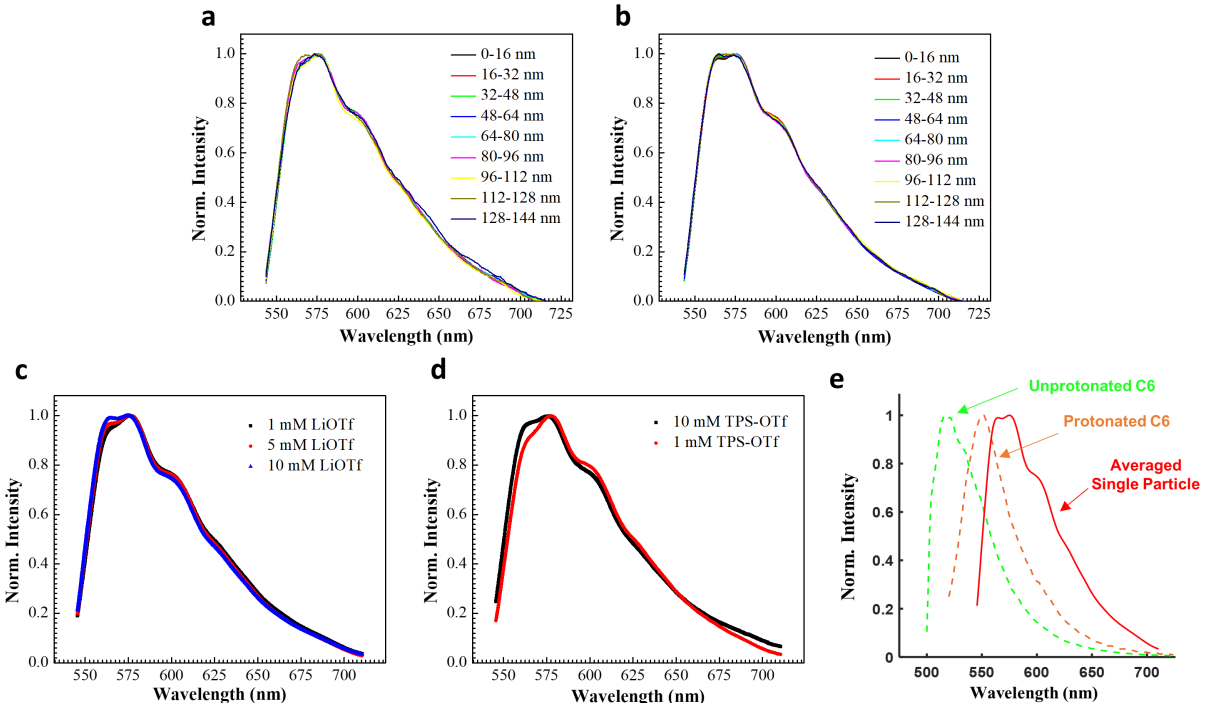


Figure 3.15: Spectrally-resolved single-particle imaging shows that the probes that are imaged consist of spectrally uniform Coumarin 6 aggregates. (a) Average emission spectrum of probes in spin-cast PEO films with 1mM LiOTf and 100 nM C6. Each curve corresponds to a different range in the size of the probe displacement between two consecutive frames. (b) Similar results from PEO films with a higher 10 mM concentration of LiOTf. (c) Averaged single-particle emission spectra at 3 different LiOTf concentrations show a weak, if any, dependence, on LiOTf concentration. (d) Averaged single-particle spectra in PEO films doped with triphenylsulfonium trifluoromethanesulfonate (TPS-OTf) also show weak, if any, dependence on salt concentration. (e) Normalized bulk emission spectra from unprotonated and protonated Coumarin 6 in a PEO thin film (dashed green and orange curves, respectively) compared to the averaged single-particle spectrum of a PEO thin film with 100 nM C6 and 10 mM LiOTf (solid red curve). The unprotonated and protonated C6 emission spectra peak near 515 and 550 nm, respectively; the averaged single-particle spectrum peaks near 580 nm. In addition, the averaged single-particle spectrum shows an additional shoulder around 610 nm not present in the protonated C6 spectrum. This comparison shows that the fluorescent probes that we track are not single protonated C6 molecules.

probes in this study are LiOTf-induced C6 aggregates of roughly similar sizes. Peculiarly, despite other reports that microscale aggregates or crystals of C6 result in dramatic decreases in the fluorescence quantum yield [189], we find the nanoscale aggregates in this study to be

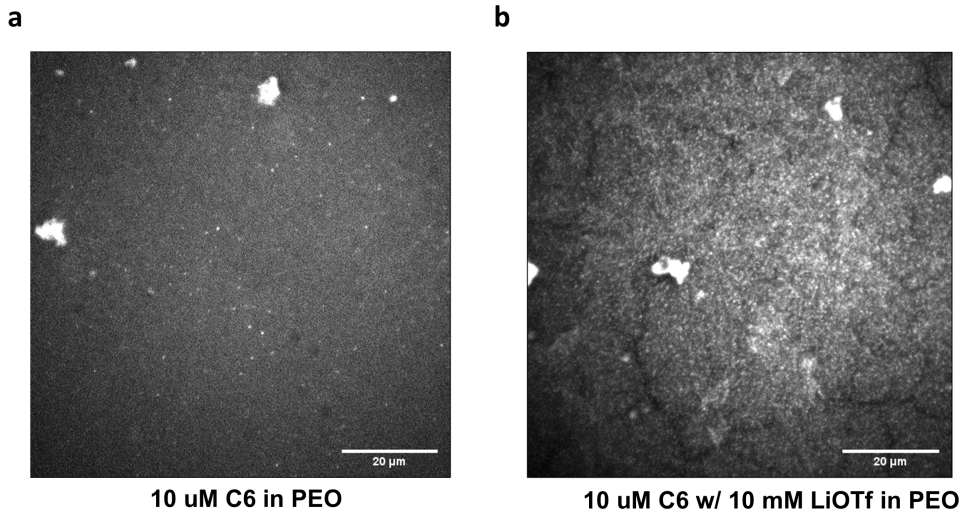


Figure 3.16: LiOTf enhances C6 complex fluorescence in PEO thin films. (a) PEO thin film doped with 10 $\mu$M Coumarin 6 (C6) and (b) PEO thin film prepared with 10 $\mu$M C6 and 10 mM LiOTf.

comparatively bright and robust emitters that suitably enable multi-frame tracking for SPT measurements.

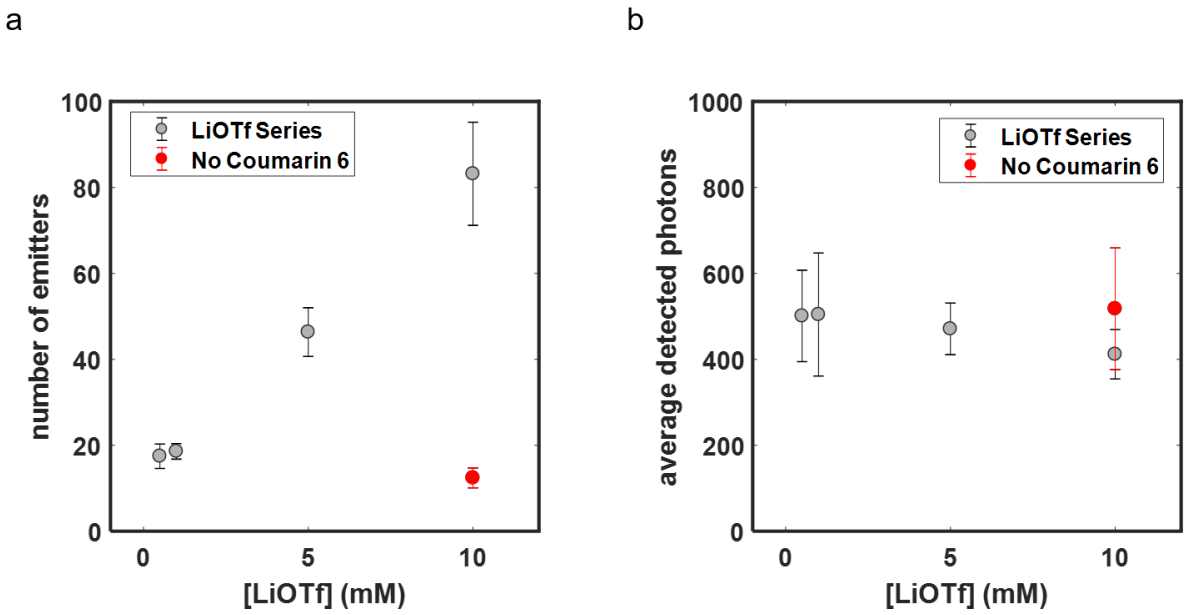


Figure 3.17: Average number of emitters detected and average single-particle signal strength as a function of LiOTf concentration. (a) Plot of the average number of single-particle emitters detected in PEO thin films prepared with different LiOTf loading concentrations. For each black point, a different PEO thin film was prepared with 100 nM Coumarin 6 and a different LiOTf loading concentration ranging from 0.5 to 10 mM. The red point represents a PEO thin film prepared with 10 mM LiOTf without any Coumarin 6. The number of emitters detected is averaged over 10 fields of view. Each field-of-view is sampled for at least 30 frames and the number of distinct emitters detected is averaged. (b) Plot of the average integrated signal of single-particle 2D gaussian fits of the same PEO thin films plotted in (a).

## 3.3 Correlative imaging enables *explicit* observation of structure-function properties in semicrystalline PEO films

### 3.3.1 Directly comparing AFM phase images with dynamical maps from SPT

Comparing dynamical and structural information within the same field of view enables a variety of important correlations to be established. The super-localized fluorescence image of the SPT data (Fig 3.18a) provides a representation of trajectories obtained in a given movie recording, where the false color intensity indicates the emitter density. There is a

higher density of emitters in the top left as compared to the bottom left of the frame. Furthermore, thin, elongated patterns can be identified on the right-hand side of the image, whereas no such patterns are apparent in the top left of the frame. The AFM height map used to prepare Fig 3.18b has an original height range of -78 to 523 nm, and this large range is due to some very tall continuous structures identified with red overlay. Upon thresholding to remove these structures, the image height variation becomes limited to -31 to 32 nm. The AFM phase image in Fig 3.18d has a range of 82 degrees and is marked by a series of thin, rod-like shapes at lower phase angle (darker) than the uniform background (lighter), and these shapes agree with other AFM phase images of semicrystalline PEO[192–195]. Fig 3.18c plots the trajectories of fluorescent probe centroids obtained from Fig 3.18a, color-coded by the anisotropy parameter defined in Fig 1d. Blue colors represent the most isotropic trajectories (approaching 0), yellow colors represent the most anisotropic trajectories (approaching 1), and green colors represent intermediate values of the anisotropy parameter. Only trajectories of emitters that fluoresced for at least 15 consecutive frames and for which the diffusion coefficient $D > 0.0075$ $\mu m^2/s$ are shown. Like in Fig 3.18a, the trajectories in the bottom right in this representation also show more rod-like shapes.

We next relate the AFM and SPT data in Fig 3.18 to compare and contrast crystallite rich and amorphous rich regions. The bottom right corner of the ROI in Fig 3.18a-d, corresponds to a PEO crystallite-rich region where anisotropic probe trajectories are most common. The directionality of the crystallites appears to be imprinted onto the probe trajectories as well. In contrast, the top left corner of the region of interest (ROI) is primarily composed of amorphous material, and probe trajectories there are mostly isotropic in nature. Even within regions of dense crystallites, $\sim$1-2 $\mu m^2$ pockets of amorphous polymer yield isotropic trajectories (more isolated blue spots in Fig 3.18c).

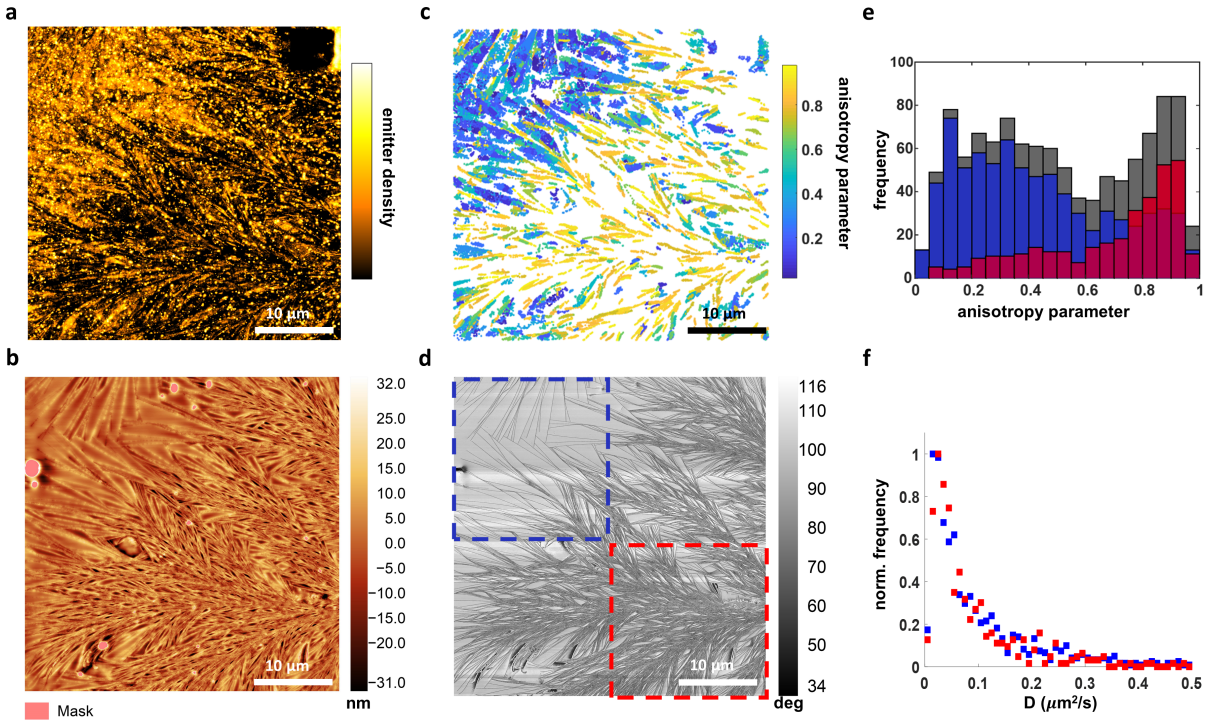


Figure 3.18: Correlative single-particle tracking and AFM imaging. (a) Superlocalized fluorescence image with superimposed 2D Gaussian fits to individual Coumarin 6 aggregates integrated over 8000 frames with 100 ms of exposure per frame. (b) Tapping-mode AFM height image in same region of interest as (a). (c) Plot of trajectories, which are color-coded by anisotropy parameter. (d) Tapping-mode AFM phase image of same ROI as (b).(e) Distribution of anisotropy parameters of mobile trajectories corresponding to red and blue squares in (d). (f) Normalized distribution of 1D diffusion coefficients along the major axes of trajectories.

### 3.3.2 Comparison of anisotropy and diffusivity in crystallite rich and amorphous rich regions

The dynamical data can be further represented by statistically characterizing the distributions of anisotropy parameters and diffusion coefficients associated with each trajectory within various subregions of the region of interest (ROI) in Fig 3.18a-d. The grey histogram in Fig 3.18e shows the total distribution of anisotropy parameters for all trajectories found in both boxed regions in Fig 3.18d. The red distribution presented over the top of it includes the anisotropy parameters for trajectories only in the red box in Fig 3.18d, and the blue distribution includes the anisotropy parameters for trajectories only in blue box. The red distribution is skewed much more toward high anisotropy parameter, peaking at 0.95, and

the blue distribution is broadly isotropic, peaking at 0.15. In Fig 3.18f we also compare distributions of trajectory diffusion coefficients for each of the boxed regions in Fig 2d. To obtain each of the diffusion coefficients, each step of a trajectory is first projected along the major axis of motion determined by PCA, and a diffusion coefficient is computed by equating the mean squared displacement of these projected steps to $2Dt$, for diffusion coefficient $D$ and trajectory duration $t$. This procedure is employed for both isotropic and anisotropic trajectories in order to compare them using a common metric. Interestingly, both the data from the blue and red regions in Fig 3.18d have similar distributions of diffusion coefficients. Both distributions peak near 0.03 $\mu m^2/s$ and tail off at 0.4 $\mu m^2/s$.

### 3.3.3 Correlative AFM and SPT findings are reproducible in separate films

We find similar results upon repeating the correlative AFM and SPT experiments in additional films independently prepared with the same composition. Figure 3.19 demonstrates the reproducibility of our experimental findings, wherein regions of dense crystallites, shown as darker contrast, thin fibers (Fig 3.19d), correspond to more anisotropic trajectories (Fig 3.19c), and similarly regions of amorphous polymer (lighter contrast, featureless) correspond to more isotropic trajcectories. Interestingly, in this experiment the AFM tip used to mark a fiducial did not fully remove the polymer in the square seen in the top right of Fig 3.19c. Before carving the fiducial, AFM images (3.19 b and d) demonstrate crystalline properties. In this particular case, carving the fiducial destroyed the crystalline fibers in the top right corner of the ROI, as seen in panels 3.19a and 3.19c. As a consequence, we note that the trajectories therein are isotropic in nature!

### 3.3.4 Spread in distributions of anisotropy parameters is likely due to finite sampling

The distribution of major axis diffusion coefficients for both primarily amorphous and primarily crystalline regions are very similar, suggesting that probe trajectories in crystallite rich regions are unhindered along the direction of crystalline fibers. In addition to the peak anisotropy parameter values, the blue and red distributions in Fig 3.18e each have a substantial spread. To further explore the origin of the spreads in each of the two distributions, we simulated isotropic and anisotropic random walks of various trajectory step lengths. 2D random walk simulations were performed using a diffusion coefficient of 0.15 $\mu m^2/s$ and 0.1 s step size in order to emulate our experimental observations. Further, every position generated in the simulation is modified by a random number generated by a Gaussian distribution whose standard deviation is 40 nm, which is the average precision of the single-molecule localizations. Figure 3.20a and b show histograms of the anisotropy parameters resulting from PCA of 1000 simulated trajectories, each with 30 steps, with the notable difference that the simulations in 3.20b had avoided boundaries of 50 nm width on one of the two dimensions

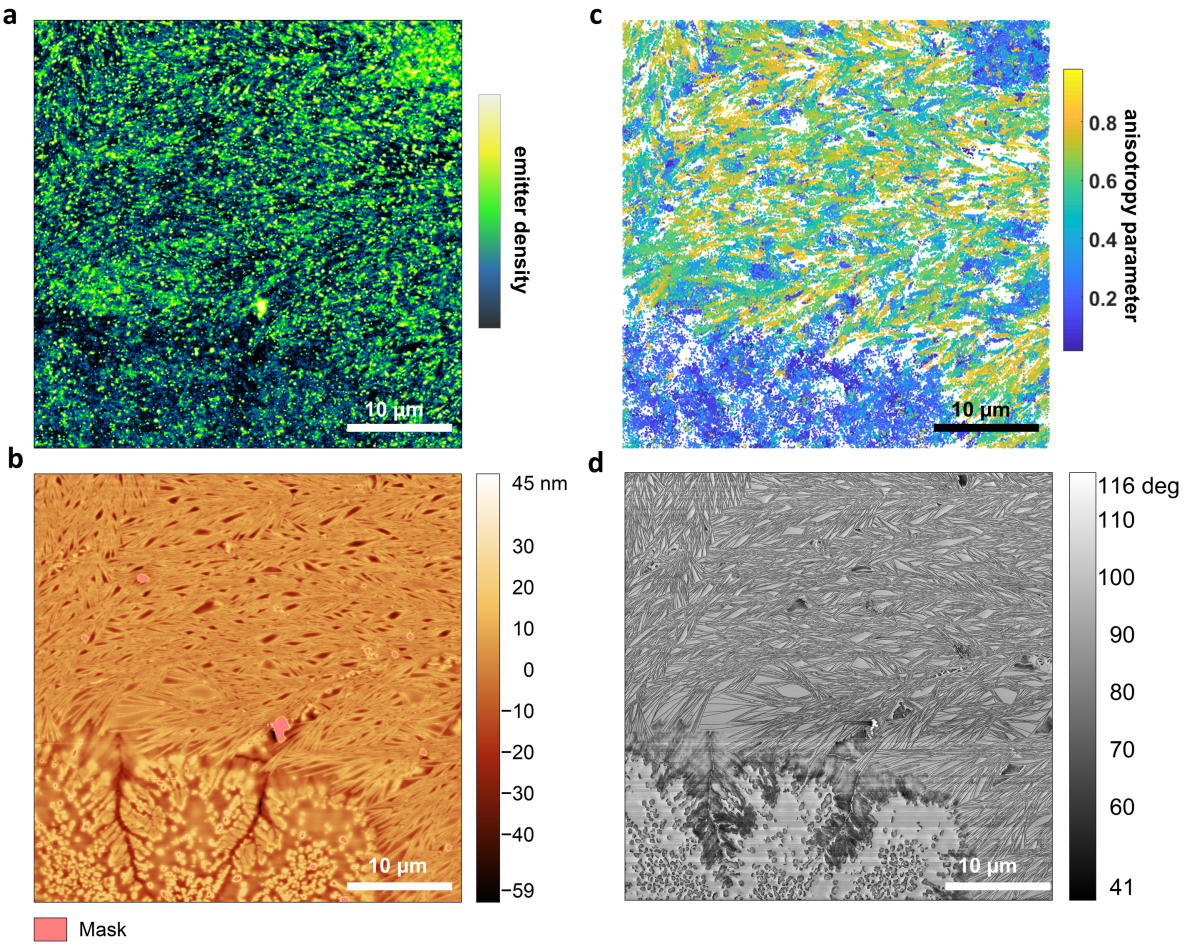


Figure 3.19: Correlative AFM and single-particle tracking of another PEO film prepared with 15 mM LiOTf. (a) The super-localized fluorescence image. (b) The tapping mode AFM height image. (c) Trajectories color coded by their anisotropy parameters. (d) The AFM phase image corresponding to the height image in (b).

to simulate confined diffusion. The widths of the distribution appear similar to those of Fig 3.18e, yet if we simulate the same conditions of Fig 3.20a and b with 1000 steps instead of 30, shown in Fig 3.20c and d for free and confined diffusion, respectively, we note a significant narrowing of the distributions. Thus, the spread in our observed distributions of the anisotropy parameter are primarily a consequence of finite trajectory length, suggesting the values at which the distributions each peak are more representative of the probe motion than the spreads.

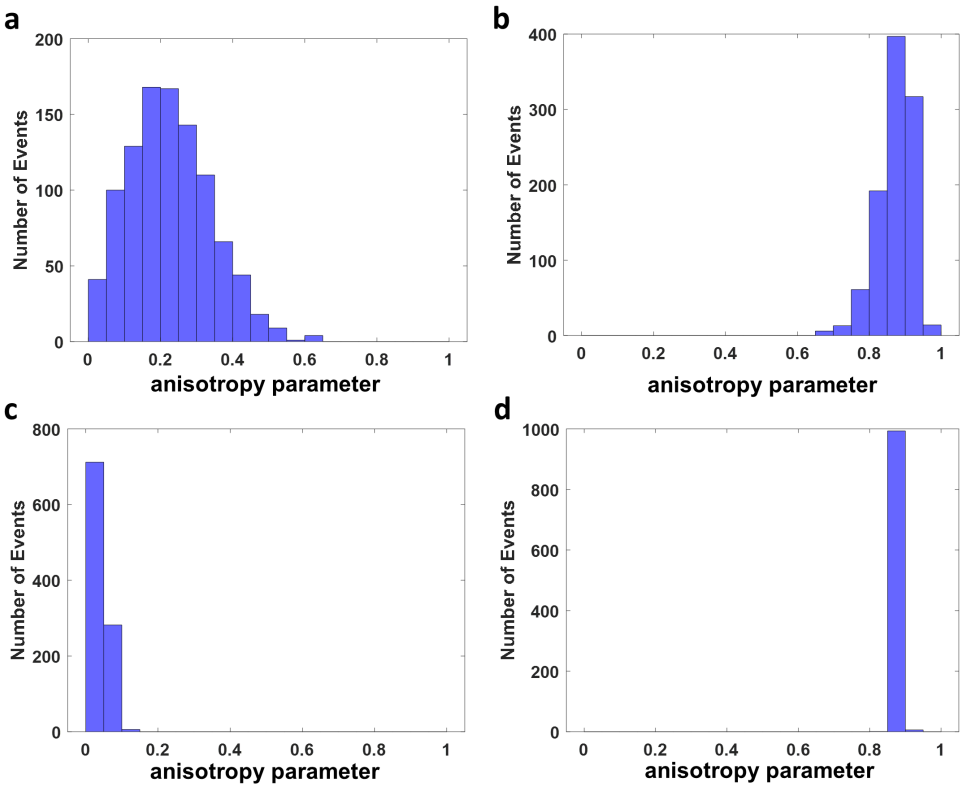


Figure 3.20: Simulations with various degrees of probe confinement to show the effect of trajectory length (number of frames) on expected distribution of the anisotropy parameter. (a) The distribution of anisotropy parameter from the simulation of a two-dimensional free random walk, with 30 steps. (b) Anisotropy parameter distribution upon applying avoided boundaries (50 nm width) on one of the two dimensions to simulate confined diffusion, with 30 steps. (c) Same conditions as (a), but with 1000 steps. (d) Same conditions as (b), but with 1000 steps.

### 3.3.5 Visually and quantitatively demonstrating crystallite orientation is imprinted upon probe trajectories

To compare SPT trajectories and AFM-derived morphology more directly we overlaid the data for Fig 3.18c and Fig 3.18d in Fig 3.21a,b. The overlay shows that the majority of locations where the probes are observed fall within lighter contrast regions of the AFM data, which we take to represent amorphous PEO. In fact, the trajectories generally conform to the boundaries delineated by crystalline fibers, even when these fibers are curved. Generally,

trajectories residing in more narrow channels between crystalline fibers are more anisotropic (yellow), and trajectories residing in larger pockets of amorphous material between crystallites are more isotropic (bluer). Exceptions to these categorizations could be due to out-of-plane amorphous channels crossing beneath the surface structure that we primarily map with AFM, though these exceptions are a small minority. Based on the similarity of the amorphous channel depth (up to 60 nm, Figure 3.18b) and film thickness ($\sim$100 nm), the similarity of major axis probe diffusivities measured in confined amorphous PEO and in unconfined regions as well as the comparable diffusivities observed in annealed PEO films (see Fig 3.25 and discussion in Section 3.4.1), we infer that the probes diffuse within, as opposed to on the surface of, the amorphous PEO. In any case, the absence of isotropic trajectories in the crystallite-rich region remains as strong evidence for the structural/dynamical correlation.

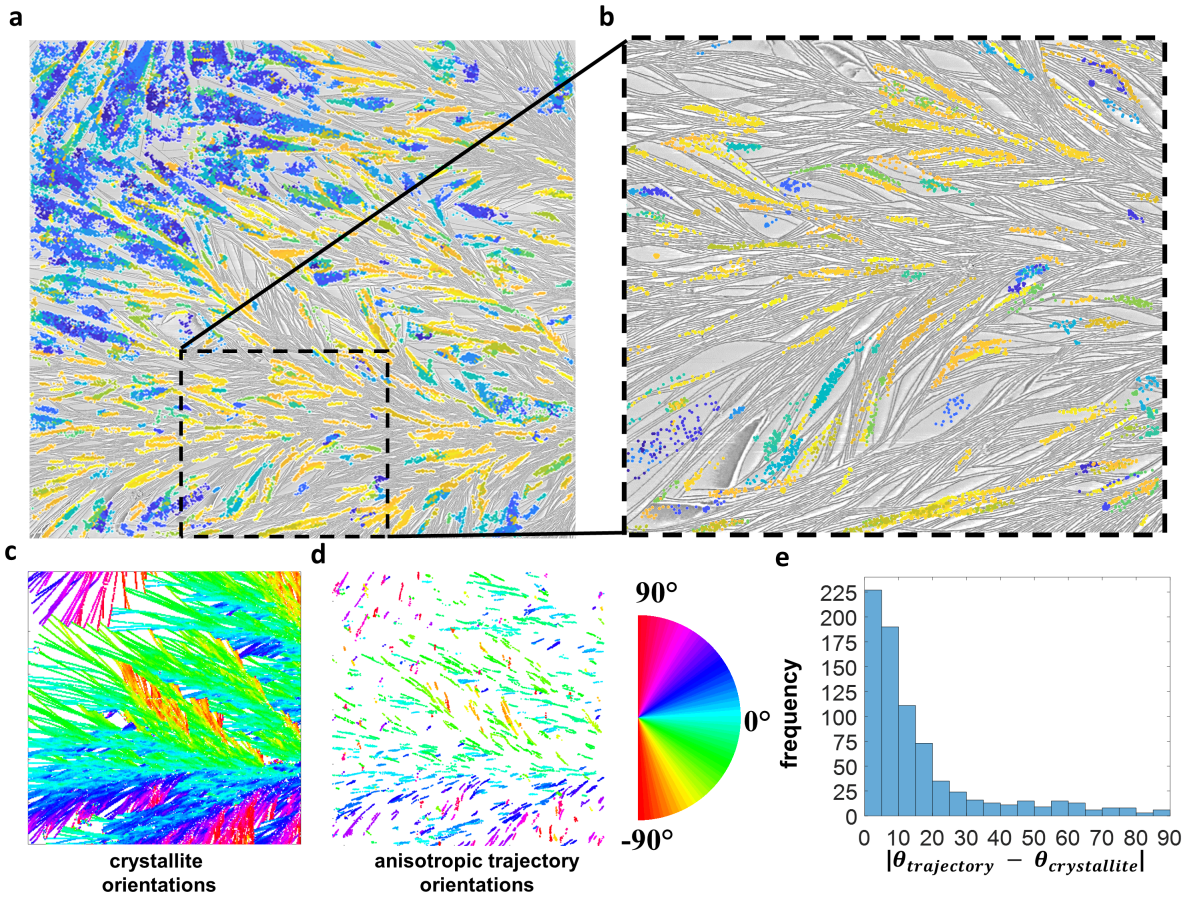


Figure 3.21: Overlay of mobile trajectories color-coded by anisotropy parameter with AFM phase image. (a) Full, 40 × 40 $\mu$m$^2$, field of view of Figure 3.18c,d. (b) Magnification of 15 × 15 $\mu$m$^2$ dashed box in (a). (c) Pixel-binned and binarized 40 × 40 $\mu$m$^2$ AFM phase image from Figure 3.18d, where each pixel is color-coded according to the semicircle inset and corresponds to the average orientation of crystallites relative to the lab frame horizontal. (d) Probe trajectories from the same 40 × 40 $\mu$m$^2$ ROI as (c) possessing an anisotropy parameter greater than 0.75 with each step of each trajectory color-coded by the orientation of a trajectory's major axis relative to the lab frame horizontal. (e) Distribution of values corresponding to the difference between a trajectory's major axis orientation and the crystallite orientation in the location of the trajectory's average position.

Additional information regarding the extent to which crystalline fibers constrain probe motion can be obtained by further quantitating the degree of correlation between crystallite boundary orientation and the major axes of nearby probe trajectories, which we do in Fig 3.21c-e. Fig 3.21c shows a color-coded map of crystallite orientation obtained by thresholding and binarizing the AFM phase image shown in Figures 3.18d and 3.21a. Shown in Fig

3.22 is a schematic demonstrating how the image in Fig 3.21c is rendered. We begin with a small ROI extracted from the binarized AFM image in black and white, where white represents crystallites and black represents amorphous material. We use the bwlabel function in MATLAB to determine connected groups (4 in the example, each filled with a random color to the right of the binarized black and white image) and their angles relative to the lab frame horizontal axis. The average orientation of crystallites for this 16×16 pixel bin is reported as one consolidated color (yellow in this case, to the right of the arrow) according to the orientation map in the semicircle inset (Fig 3.21d). The spatial bin is scanned over the binarized image in steps of 8 pixels, where each pixel is 15.6 nm long on a side, until we have rendered a new image corresponding to the orientation of the crystallites color-coded by their orientation relative to the lab frame horizontal axis.

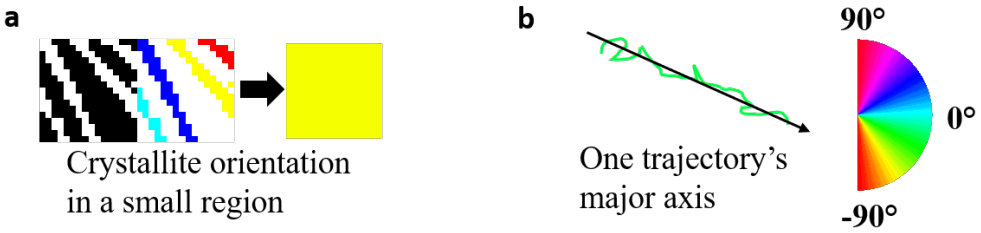


Figure 3.22: Workflow for generating AFM and trajectory orientation maps. (a) Schematic representing the analysis to generate a pixel in Fig 3.21c. The pixel is actually a small ROI of the original AFM phase image binarized, and the pixel value is the average orientation of crystallites within the ROI. (b) Schematic of a trajectory color-coded by the angle its major axis forms with the lab frame horizontal axis.

Similarly, Fig 3.21d shows a map using the same orientational color-coding for the major axis of tracked probe trajectories shown in Figures 3.18c and 3.21a possessing an anisotropy parameter greater than 0.75. A schematic of such is shown in Fig 3.22b. Visually, there is a high degree of spatial correlation between the structural and dynamical orientational maps in Fig 3.21c and Fig 3.21d. To further quantify this correlation, Fig 3.21e shows the distribution of orientational mismatch between proximal crystallites and anisotropic probe trajectory major axis orientations, $|\Theta_{trajectory} - \Theta_{crystallite}|$. The distribution is peaked around zero mismatch with a half-width of ∼15 degrees. This half-width is within the error of the average crystallite spacing calculated in Fig 3.23.

### 3.3.6 Comparison between probe trajectory widths and crystallite spacing

In addition to quantitating the orientational correlation between structural and dynamical information, we investigate the correlations of spatial scales in our two types of measurements

that relate to the apparent confinement of dynamical trajectories within narrow channels between crystalline fibers (Fig 3.23). To do so we first perform a 2D fast Fourier transform (FFT) on the same thresholded and binarized AFM phase image as in our orientational analysis (Fig 3.22). Each pixel in Fig 3.23a is color-coded to represent the local period of, or spacing between, adjacent crystalline fibers, as calculated using the Fourier transform. To create this map, the 2D FFT is performed in spatial bins of 33×33 pixels, and the spatial bin is scanned over the thresholded, binarized image in steps of 16 pixels (Fig 3.23b). The distribution of spacings in Fig 3.23a is shown in Fig 3.23d (black) and ranges from 40 to 150 nm, peaking at 50-55 nm. Spatial periods larger than 150 nm are not reported on account of the size of spatial bins in the 2D FFT.

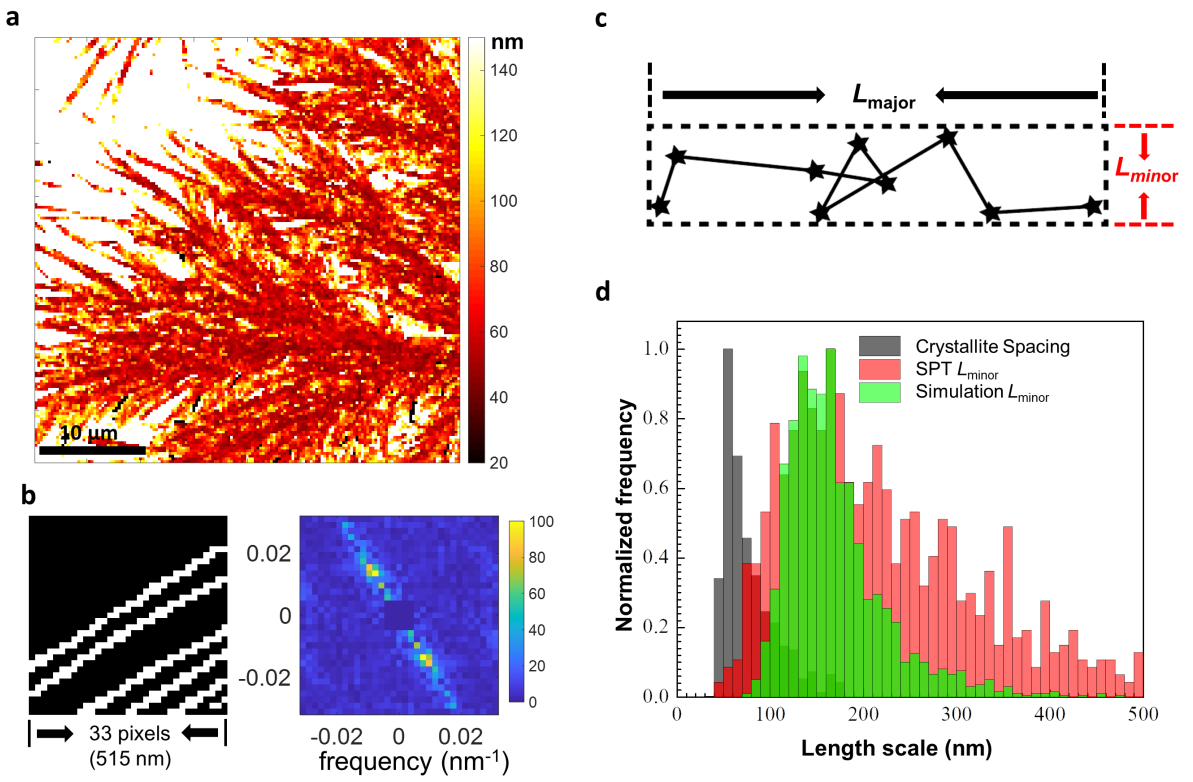


Figure 3.23: Comparison of crystallite spacing to trajectory width. (a) A heat map of crystallite spacing extracted from the AFM phase image using a 2D FFT. The method is illustrated in (b). The left black and white image is a cropped, binarized AFM phase image, in which the black and white regions correspond to amorphous and crystallite regions, respectively. Its 2D FFT generates the heat map of spatial frequency (at right). (c) Schematic to illustrate definition of the minor axis width (red) of a trajectory (black stars connected by solid black lines), as compared to the major axis width (black). (d) The distribution of crystallite spacing obtained from 2D FFT analysis is shown in black. The distribution of trajectory widths on the minor axis for anisotropic trajectories (anisotropy parameter ¿ 0.75) is shown in red. The distribution of trajectory widths of simulated trajectories that sample confinement from the black distribution of crystallite spacings and a localization error from a 40 nm Gaussian distribution is shown in green.

We next relate the spacings between crystallite fibers to the spatial extent of confined probe trajectories measured via SPT. For each trajectory possessing an anisotropy parameter value greater than 0.75, we consider the greatest distance between trajectory particle positions along the minor axis, as reported by PCA (schematic shown in Fig 3.23c). This minor axis width distribution peaks at 150 nm (Fig 3.23d, red).

To reconcile this difference between the distribution of crystallite spacings reported by the 2D FFT analysis of the AFM phase image and the distribution of trajectory widths along the minor axis, we numerically simulate confined random walk trajectories. Each simulated trajectory is 29 frames long (median number of frames for anisotropic trajectories), and the degree of confinement for a given trajectory is drawn from the distribution of crystallite spacings extracted from AFM (Fig 3.23d, black). Furthermore, a random error drawn from a Gaussian distribution ($\sigma$ = 40 nm) is added to each position of a given trajectory to incorporate the effect of the 40 nm experimental localization error. The minor axis width distribution of these simulated trajectories is shown in Fig 3.23d in green and peaks at 150 nm. These simulations suggest that to within the 40 nm localization uncertainty of our SPT measurements, the peak trajectory minor axis width of 150 nm is consistent with the crystallite fiber spacing of 50-55 nm determined via FFT analysis.

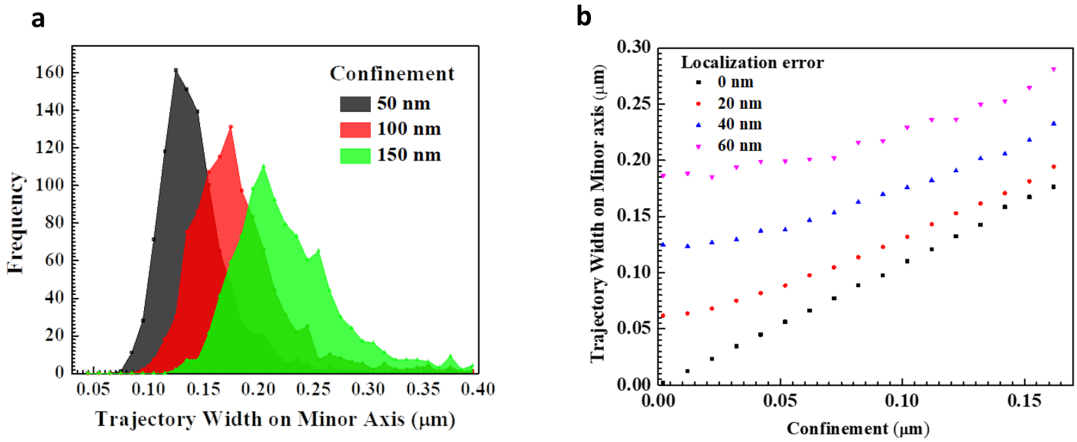


Figure 3.24: Simulated two-dimensional random walks to determine the effect of confinement convolved with localization precision error. (a) Distributions of the minor axis width extracted from trajectories simulated with varying degrees of confinement along one dimension convolved with a 40 nm localization error. (b) Plot of the median minor axis width extracted from simulated trajectories as a function of confinement. Different colored data represent a series of simulations with varying localization error.

Additional confined random walk simulations recapitulate the assertion that at least within our localization uncertainty there is agreement between trajectory width and crys-

tallite spacing. Fig 3.24a show distributions of the minor axis widths of simulated random walks, where each distribution represents a different confinement value along one dimension. The distributions are effectively convolved with the localization uncertainty of 40 nm (by using a similar practice as the simulations in Fig 3.20). With this localization error, one can distinguish 50 nm and 150 nm confinement by comparing minor axis trajectory widths, but smaller differences between crystalline fiber spacings would be difficult to discern. While we note that as the confinement decreases the distributions broaden and shift to higher mean values as one would expect, there is a systematic overestimation of the actual confinement value via the simulated trajectory width distributions. Fig 3.24b reports the median of 1000 simulated minor axis trajectory widths as a function of confinement for a series of different localization uncertainties. With 0 nm localization uncertainty, the simulated trajectory widths perfectly recover the confinement value, but as the localization uncertainty increases the simulated minor axis widths disagreement correspondingly increases.

## 3.4 Potential design principles for semicrystalline polymers

The above results present an opportunity to further establish relationships between probe motion within semicrystalline PEO and its structural features. The discussion below focuses on the influence of the configuration and shape of crystallites on probe motion and on suggestions for how these findings serve as design principles for controlling crystalline growth within semicrystalline polymers. We consider the collection of our observations and analysis of location, orientation, and length scale correlations between the semicrystalline morphology map obtained by AFM and the probe motion within this morphology obtained by SPT.

### 3.4.1 Anisotropy of particle motion is a faithful reporter of film crystallinity

Comparing the locations where the probes are observed to the locations of crystalline and amorphous components of the PEO film microstructure in the overlays in Figure 3.21 allowed us to similarly establish that the probes are forced out of crystalline regions. This segregation is a probable result of the crystallization process, as crystallization often purifies the material composition, forcing out impurities, such as the fluorescent probes. We also learned that the motion of the fluorescent probes within the amorphous PEO where they reside is isotropic, provided that the extent of the amorphous region exceeds a typical diffusion length of the probe. If, however, the extent of an amorphous region is smaller than the intrinsic diffusion length of the probes along a given axis, then the probe motion is confined along that axis, generating anisotropy in the probe trajectory.

Incidentally, we also found that measuring single-particle trajectories in a given film before and after removing its crystalline microstructure via thermal annealing shifts the

original anisotropy parameter distribution to become substantially more isotropic, while preserving the value of the unconfined diffusion coefficient. Figure 3.25 shows the distribution of the anisotropy parameters and diffucsion coefficients along the major axis for probes in PEO films co-doped with 1, 10, and 15 mM LiOTf (black border). As we increase the LiOTf co-doping concentration, the relative amorphous component of the films increase due to frustrated crystallization of pure PEO cyrstals[154], and we note a relative increase of more isotropic valued trajectories in the anisotropy distributions. The distributions of diffusion coefficients along the major axis of travel appear similar.

When the films are annealed, however, we note that the distributions of the anisotropy parameters in each of the 1, 10, and 15 mM LiOTf doped films shift significantly towards the isotropic values. Annealing was accomplished by placing samples on a 100 $^{o}$C hotplate to melt the polymer and temporarily destroy the crystalline structure. Again, the distributions of the diffusion coefficients along the major axis appear similar between the different loading concentrations and importantly appear similar to the distributions in the pre-annealing case. Given these distributions appear similar in different LiOTf concentrations as well as before and after annealing reinforce the notion that crystallites anisotropically constrain the motion of probes but do not affect their diffusivity.

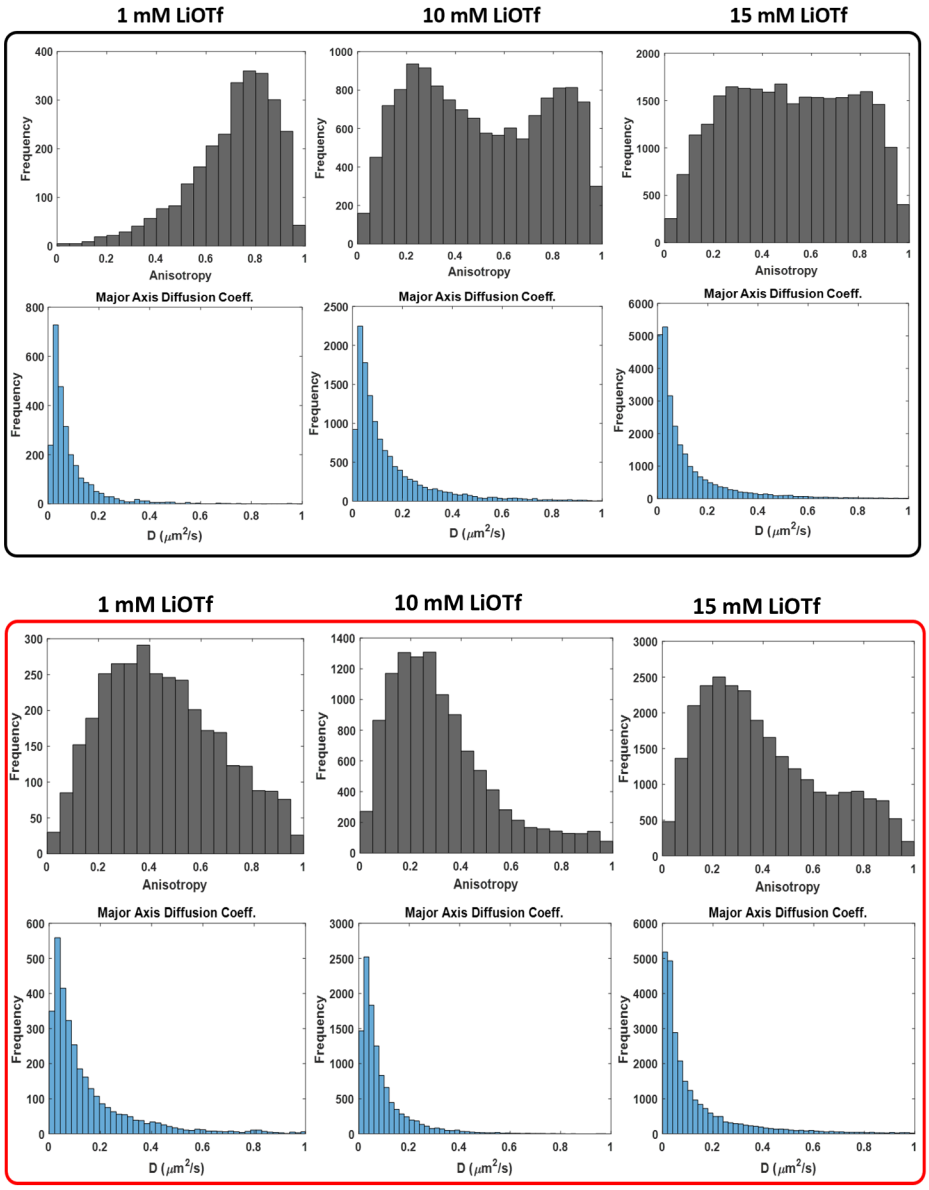


Figure 3.25: Anisotropy parameter and major axis diffusion coefficient distributions before (black box) vs after (red box) annealing of 1, 10, 15 mM LiOTf films.

The *orientation* of these anisotropic trajectories correlates strongly to the orientation of the crystalline boundaries, and the *extent* of this anisotropy is directly correlated to the extent of confinement between adjacent crystallites, which are often parallel to one another. Furthermore, the width of probe trajectories on the minor axis and its nearby crystallite spacing agree in size to within the uncertainty of our measurements. Though quantitatively correlating the extent of confined probe trajectories and the widths of amorphous channels beneath the SPT localization uncertainty of 40 nm is not currently possible, the degree of probe trajectory anisotropy is able to report on the specific spatial configurations of crystallites in the film morphology. In fact, the most extreme case of anisotropic probe motion is achieved by lowering the LiOTf concentration from 15 to 1 mM, which creates more densely packed, presumably pure PEO, crystallites configured in a spherulitic morphology, as compared to ones we primarily study in this work composed of a PEO–salt complex[185]. While PEO–salt crystallites and pure PEO crystallites differ in height, width, and spacing, it is interesting to note that both appear to behave functionally as impermeable barriers that geometrically confine the probe transport.

Figure 3.26a shows an AFM height image of a 1 mM LiOTf doped PEO thin film in a $25\times25$ $\mu$m$^2$ field of view. The distinguished dark lines represent the boundaries between two spherulite superstructures, which typically result as a consequence of impinging on one another over the course of growth. A zoomed in height (b) and phase (c) image of the spherulite's structure in a $1\times1$ $\mu$m$^2$ reveal amorphous channels to be even thinner than in the case we explored in detail with 15 mM LiOTf loading concentrations. Beyond the severely anisotropic nature of the probe motion in these spherulites, the orientation of trajectories relative to a given spherulite's nucleus match one's expectations (see schematic in Fig 3.26d. This is quantitavely supported by the distribution of angle mismatches between a trajectory's orientation and the angle relative to the nucleus, which peaks near 0.

Our findings therefore suggest that the degree of anisotropy observed in fluorescent probe motion in SPT is an excellent reporter for lamellar crystallinity and that the semicrystalline microstructures observed in AFM phase images also report well on each of the location, confinement, and trajectory orientation of particle motion. This deduction is also well-supported by bulk conductivity measurements reported by Li and co-workers[145] that show ions preferentially travel parallel, and not perpendicular, to crystalline plates of PEO.

### 3.4.2 Controlled arrangement of crystallites for deterministic mass transport

Furthermore, our findings indicate that pursuit of a controlled arrangement of crystallites could be quite worthwhile for material design. Interestingly, such design strategies have been discussed in the context of semicrystalline semiconducting polymers, wherein charge transport actually occurs predominantly in crystalline domains, and intercrystallite transport can behave as a bottleneck[3, 196]. In the case of ion motion in solid-state electrolytes, suppressing crystallinity has historically been the strategy to improve ion mobility, with

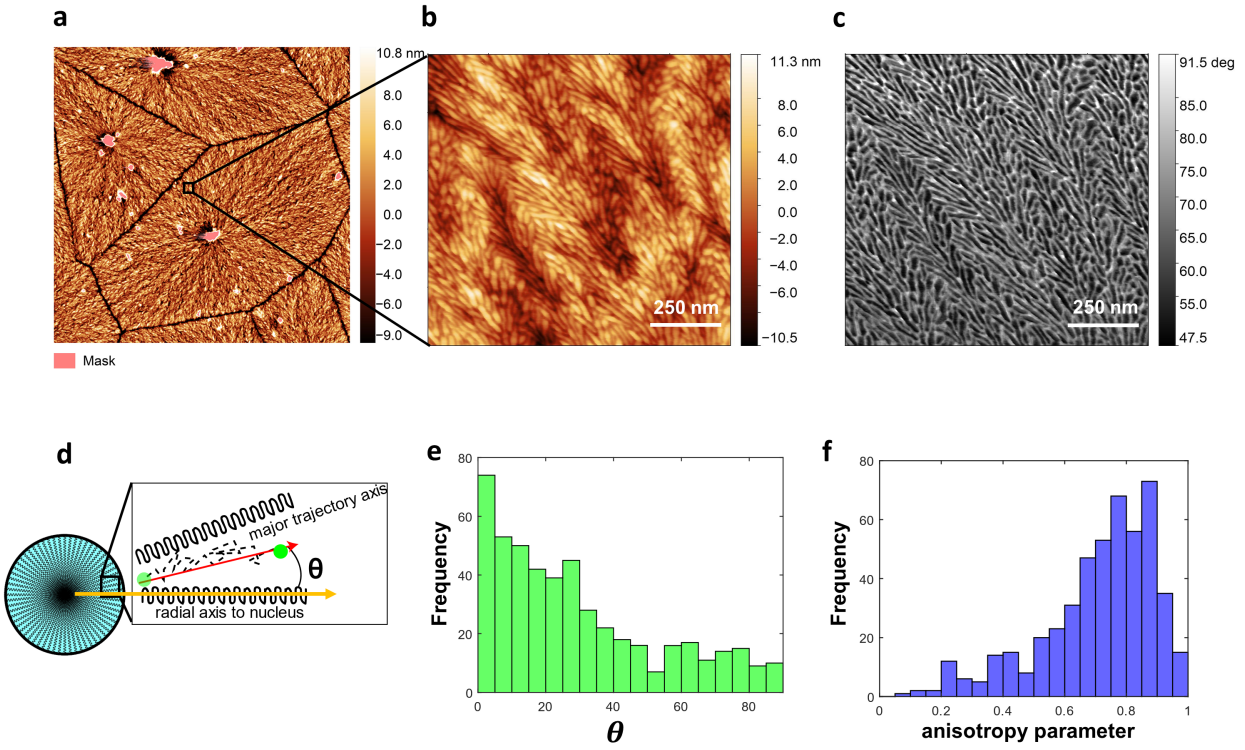


Figure 3.26: 1 mM LiOTf co-doped PEO thin films with spherulitic morphology. (a) 25 × 25 $\mu$m$^2$ tapping-mode AFM height image. (b) 1 × 1 $\mu$m$^2$height image of the boxed region within (a). (c) Phase map for the same 1 × 1 $\mu$m$^2$ field-of-view as in (b). (d) A schematic of the angle a trajectory's major axis forms relative to line formed between the trajectory's average position and the spherulite nucleus. (e) The distribution of values corresponding to the angle defined by (d). (f) The distribution of anisotropy parameters for probe trajectories measured within spherulitic PEO thin films.

the drawback of compromised mechanical strength. Rather than an exclusively negative property for transport, if aligned and ordered, crystalline domains could serve as channel boundaries to deterministically guide dopant transport, a concept that has only recently begun to be explored[142, 144]. In fact, Li and co-workers demonstrated that manufacturing single-crystalline plates of PEO can be used to anisotropically improve conductivity between plates [145]. We show here that spontaneously formed crystalline structures in an as-cast film also anisotropically guide dopants over substantial length scales. This phenomenon bears analogies to what occurs in block copolymer assemblies, where one block is mechanically strong and impermeable to dopant transport, which has also been demonstrated with SPT studies[176]. Whereas block copolymer applications make use of two different polymer

components that must be carefully synthesized, here we suggest the possibility to take advantage of a single-component polymer with two different structural phases to achieve the same goal. To fully harness the potential of such an approach with a semicrystalline polymer, one could envision leveraging methods of controlled polymer or small organic molecule crystal growth[197, 198] and taking inspiration from pre-existing strategies used for the directed self-assembly of block copolymers[133, 199, 200].

## 3.5 Conclusion

Instead of relying on bulk approaches, we have directly measured strong correlations between nanoscale mobile probe dynamics obtained by SPT and the nanoscale microstructure of PEO thin films obtained by AFM. Specifically, we confirmed by direct measurement that particle, and potentially molecular, motion occurs preferentially, if not exclusively, in amorphous regions of the semicrystalline microstructure. The single-particle tracking that we employed affords not only these spatial correlations but also provides access to statistical distributions of the parameters associated with probe motion. Our correlated SPT and AFM phase imaging strategy could be readily adapted to study other semicrystalline polymers in order to learn how various crystalline and amorphous phases dictate transport in polymers known to have different melting or glass transition temperatures or other bulk properties. Future experiments could be performed to track ionic species or species sensitive to ions[201], comparing the resulting dynamics to those measured with our hydrophobic fluorescent aggregates in this study. Differences between experiments employing charged and neutral probes could yield key insights to enable the deconvolution of size and charge in polymer–ion interactions important for ion diffusion in a solid-state electrolyte.

The strategies presented here could also be of great use in the study of impurity migration within materials composed of polymers quite different from the polymer electrolyte, for example, in plastics whose properties depend critically on eliminating impurities but where elimination strategies are neither systematic nor effective. Finally, our findings provide design principles to guide the current efforts for controlled crystalline domain growth in semicrystalline polymers. By arranging and aligning crystallites in an organized manner, the diffusion of dopants could be deterministically guided by bounded repeating arrays of crystalline and amorphous material[142]. This strategy would provide the necessary mechanical strength for device incorporation without compromising the transport of ions, drugs, and other dopants.

# Chapter 4

# TRUSTED microscopy: An ultrafast transformation of STED microscopy to probe nanoscale exciton migration

## 4.1 Introduction

In light harvesting materials and many semiconductors, the ability of light induced excitations to efficiently migrate through a material is critical for optimal energy conversion, yet, often, material imperfections or heterogeneities impede such transport. Correlating material morphology with its energetic landscape and transport functionality therefore necessitates optical resolution on both spatial scales relevant to material heterogeneities (nm - $\mu$m) and temporal scales (ps – ns) relevant to transport in the vicinity of such heterogeneities. More generally, the ability to precisely measure excitation migration, even when it is comparatively small, will lead to better informing design principles for systems used for exciton transport - perhaps most readily in their earliest stages of development.

Towards this end, our group developed a novel means to track excitons in materials using a one-of-a-kind microscopy. STED, or stimulated emission depletion microscopy[202], is a super-resolution microscopy and time-resolved ultrafast STED, or TRUSTED, is an ultrafast transformation of this super-resolution technique capable of spatiotemporally resolving exciton migration in optoelectronically active materials[116]. This chapter will provide an overview of the fundamentals of STED microscopy (Section 4.2), explain how our own imaging system operates (Section 4.3), and will then introduce TRUSTED (Section 4.4). As I am part of the second generation of TRUSTED experimentalists, I will conclude by emphasizing new challenges that came to light via my experiences applying TRUSTED to various materials with more complex photophysics. TRUSTED results on quantum dot superlattices (QDSLs), which serve as a focal point of my work with the approach are the topic of the following chapter.

## 4.2 STED super-resolution microscopy

Stimulated emission depletion (STED) microscopy is a super-resolution fluorescence imaging technique, which was a part of the suite of super-resolution methodologies awarded the 2014 Nobel Prize in Chemistry. Hell and co-workers developed and refined the technique [202, 203] to yield remarkable resolution enhancement, profoundly enriching the amount of information one can gain from fluorescence imaging in biological and non-biological contexts alike.

Briefly, STED microscopy achieves super-resolution in the far-field by coupling two coaligned light sources through a scanning microscope objective - the first is a traditional Gaussian excitation beam and the second is an annular (I prefer to say, "donut") shaped depletion beam, also referred to as the 'STED pulse.' The excitation beam generates an excitation profile that represents the diffraction limited focal intensity distribution. The depletion beam is tuned in wavelength to de-excite, or "quench," chromophores via stimulated emission. Photons emitted from the sample as a result of stimulated emission are rejected via fluorescence filters and, in the case of pulsed laser beams, detector timing. At sufficiently high intensities, the depletion beam can saturate the stimulated emission transition, relegating the chromophores solely to their ground state (i.e. "off state"). Because the focal intensity distribution is donut shaped, with an effective "zero"-intensity point in the center of the beam profile, the depletion beam's quenching efficiency radially decreases away from the central null. Chromophore excitations located on the periphery of the excitation profile are more readily quenched and fluorescent photons are only collected from the fluorescent region around the depletion beam's null. The volume of the effective fluorescent region after the action of the depletion beam therefore depends on the beam intensity. Figure 4.1 demonstrates a simple simulation of the resolving power of STED for two different depletion beam intensities.

STED is quite a different means to achieve super-resolution than techniques that rely on stochastic photoswitching of fluorophores between bright and dark states with subsequent super-localization image analysis, like PALM, PAINT, or STORM. Here, the excitation profile, or microscope point-spread function, is physically narrowed in real time with no post-processing necessary[1]. One advantage of STED microscopy is that it can achieve super-resolution in systems without requiring spatial or temporal sparsity of fluorophores for post-processing, though a related disadvantage of STED is its far more stringent requirements of the chromophore's photophysics and consequent narrower scope of effective probes.

[1]This is not strictly true if the depletion beam generates a certain amount of fluorescence from the sample, either via 2-photon or direct excitation. STED fluorophores are typically those with properties that avoid this issue. This will be discussed in more detail later in Section 4.3.4.

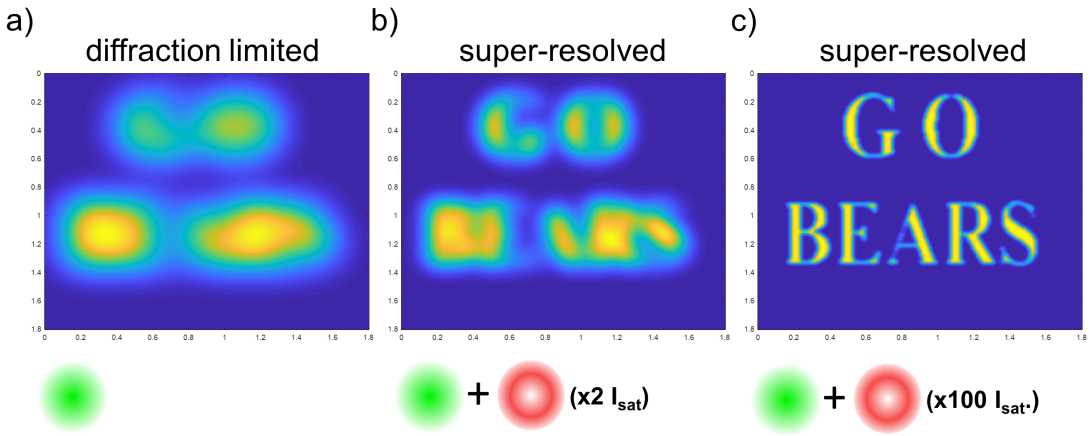


Figure 4.1: Simulation of resolution enhancement via STED on a collection of closely spaced point emitters. (a) Diffraction limited image generated with only the excitation beam. (b) Super-resolved image generated from the combined action of the excitation and depletion beams. (c) Super-resolved image, but with a higher intensity depletion beam. $I_{sat}$ is the saturation intensity, or the intensity of the STED beam at which 50% of excitations are quenched to the ground state. The field of view in each image is 1.8×1.8 microns.

## 4.3 Key ingredients of STED microscopy

This section will describe in more detail the conditions necessary to achieve STED resolution enhancement. Note that the following discussion will be framed using *pulsed* laser sources as the context, but it is similarly possible to achieve super-resolution with CW sources for the excitation and STED lasers.

### 4.3.1 Nonlinear saturation of optical transitions

The conditions required to achieve stimulated emission in fluorescent materials is very analogous to those in laser systems. It's helpful to consider the target chromophore to be a pseudo four level system, schematically shown in Figure 4.2. We first excite the system from an electronic ground state ($g_0$) to an electronic excited state surface. Because the excited state geometry that minimizes the system energy along the excited state surface is in a different nuclear configuration than the ground state, the transition with the strongest oscillator strength corresponds to a higher lying vibrational energy level within the excited electronic surface ($e_1$) (e.g. Franck-Condon overlap). Shortly after promotion from $g_0$ to $e_1$, the system will vibrationally relax along the excited state surface to a lower vibrational level, $e_0$. The radiative transition couples from $e_0$ to a higher lying vibrational level along the ground state surface, $g_1$, which will be driven via the STED pulse to achieve stimulated emission. The energy difference between the transitions from $g_0$ to $e_1$ and $e_0$ to $g_1$ is the Stokes shift.

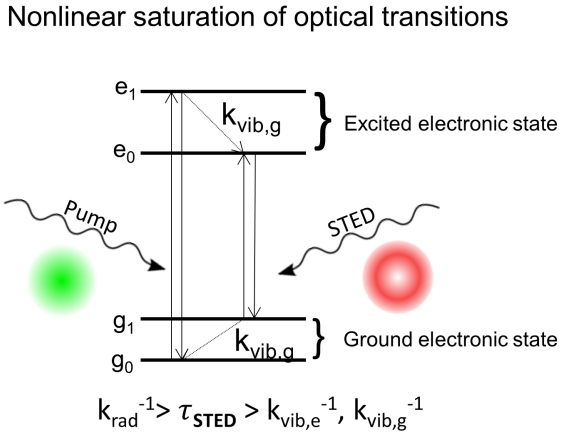


Figure 4.2: 4-level energy diagram of a hypothetical chromophore amenable to stimulated emission depletion.

Here, an equilibrium is established between the $e_0$ and $g_1$ states, and in order to achieve

stimulated emission with greater than 50% efficiency we require a population inversion (like in lasers). The population inversion is guaranteed by the rapid vibrational relaxation along the ground state surface to the lowest lying level, $g_0$.

The rate equations to describe this process in space and time are:

$$\begin{aligned}
\frac{\partial N_{e_1}(r,t)}{\partial t} &= k_{\text{pump}}(r,t)N_{g_0}(r,t) - k_{vib,e}N_{e_1}(r,t) \\
\frac{\partial N_{e_0}(r,t)}{\partial t} &= k_{vib,e}N_{e_1}(r,t) - k_{\text{STED}}(r,t)N_{e_0}(r,t) + k_{\text{STED}}(r,t)N_{g_0}(r,t) - k_{rad}N_{e_0}(r,t) \\
\frac{\partial N_{g_1}(r,t)}{\partial t} &= -k_{vib,g}N_{g_1}(r,t) + k_{\text{STED}}(r,t)N_{e_0}(r,t) - k_{\text{STED}}(r,t)N_{g_1}(r,t) + k_{rad}N_{e_0}(r,t) \\
\frac{\partial N_{g_0}(r,t)}{\partial t} &= -k_{\text{pump}}(r,t)N_{g_0}(r,t) + k_{vib,g}N_{g_1}(r,t),
\end{aligned} \tag{4.1}$$

where $k_{vib,e}$ and $k_{vib,g}$ are the rate constants for vibrational relaxation along the excited and ground state surfaces, respectively, $k_{rad}$ is rate constant for radiative relaxation, and $N_{g_0}$, $N_{g_1}$, $N_{e_0}$, $N_{e_1}$ are the density of excitations within the denoted states. $k_{\text{pump}}$ and $k_{\text{STED}}$ have space and time dependence owing to the focal intensity distribution($I_{\text{pulse}}(r)$) and time duration ($\tau_{pulse}$) of the pump and STED pulses, respectively, which are described as:

$$\begin{aligned}
k_{\text{pump}}(r,t) &\propto I_{\text{pump}}(r)e^{-t^2/(2\tau^2_{\text{pump}})} \\
k_{\text{STED}}(r,t) &\propto I_{\text{STED}}(r)e^{-t^2/(2\tau^2_{\text{STED}})},
\end{aligned} \tag{4.2}$$

$\tau_{\text{pump}}$ is sufficiently short ($< 1$ ps) that the excitation process promoting $g_0$ to $e_1$ is effectively impulsive given the timescales under consideration. The duration the STED pulse, $\tau_{\text{STED}}$, used in the experiment should consider $k_{vib,g}$ and $k_{vib,e}$, as, in order to most efficiently quench excitations via stimulated emission, the action of the STED pulse should occur over the entire duration of the excited and ground state vibrational relaxation. In other words, efficient depletion requires $\tau_{\text{STED}} > k^{-1}_{vib,g}, k^{-1}_{vib,e}$. One strategy is to offset in time the STED pulse from the pump pulse to allow the system to vibrationally relax along the electronic excited state surface per $k_{vib,e}$, but the consideration for $k_{vib,g}$ still stands. And of course, the STED pulse should be shorter in duration than the radiative lifetime, $k_{rad}$, of the chromophore, as, otherwise the sample will be able to emit photons before or concurrent with the action of the STED pulse.

Provided the conditions prescribed by the above rate equations are met, we note that the transition from $e_0$ to $g_1$ is *saturable*, meaning we can achieve $N_{e_0} = 0$ with sufficiently high $k_{\text{STED}}$ (determined by the intensity of the STED pulses, $I_{\text{STED}}(r)$). This nonlinear saturation, in combination with the donut-shaped structured transverse mode of the STED pulse, is what enables narrowing the excitation distribution to sub-diffraction limited volumes!

### 4.3.2 Donut-shaped transverse mode of STED beam

Stimulated emission depletion of the excited state population of a target chromophore can occur with any arbitrary beam mode, but in order for this to be useful for imaging the beam mode needs to be structured in a particular manner. One way to achieve resolution enhancement is to use a donut shaped beam mode, which enables quenching of the periphery of the excitation distribution but still allows excitations remaining in the center to fluoresce.

One way to achieve a donut-shaped beam mode is to control the spatially distributed phase of the light field via the use of a phase mask. A phase mask can be generated using a spatial light modulator or more simply using a vortex phase plate optic, which has a special polymer coating with azimuthally-dependent thickness. The thickness of the polymer introduces a relative phase delay between 0 to $2\pi$. This is what is known as a helical phase ramp, which is graphically shown in Figure 4.3.

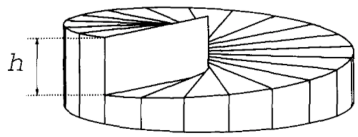


Figure 4.3: Schematic of a helical phase ramp. Figure adapted with permission from Ref [204].

Pupil function simulations of the beam mode imaged on a hypothetical isotropic point emitter are a useful way to visually understand the effect of the phase contribution on the resulting beam profile. A pupil function is the 2-dimensional Fourier transform of the image of an isotropic point source. The point-spread function amplitude is thus related to the pupil function via the following relationship:

$$PSF_A(x,y) = A\int_{-\infty}^{\infty}\int_{-\infty}^{\infty} P(f_x,f_y)\exp[-i2\pi(f_x x + f_y y)]df_x df_y \tag{4.3}$$

where $x$,$y$ are the spatial coordinates and $f_x$, $f_y$ are the frequency coordinates. $P(f_x, f_y)$ is the pupil function, which has both real (amplitude) and complex (phase) parts. Note that what we image is the modulus of the PSF amplitude, $|PSF_A(x,y)|^2$. We numerically simulate the point spread functions using the Fast Fourier Transform (FFT) capabilites in MATLAB, constructing grids of any arbitrary amplitude and phase distribution.

Figure 4.4 provides two examples of different phase delay patterns and their resulting microscope point-spread functions for a given wavelength and numerical aperture, assuming the same 2D Gaussian amplitude distribution. If the phase pattern is a helical ramp, with the phase smoothly varying from 0 to $2\pi$ as shown in the Fig 4.4a, then the beam profile results in a characteristic donut shape. One way to rationalize this is to consider the very center of the phase delay distribution as a singularity, where all phases coexist simultaneously

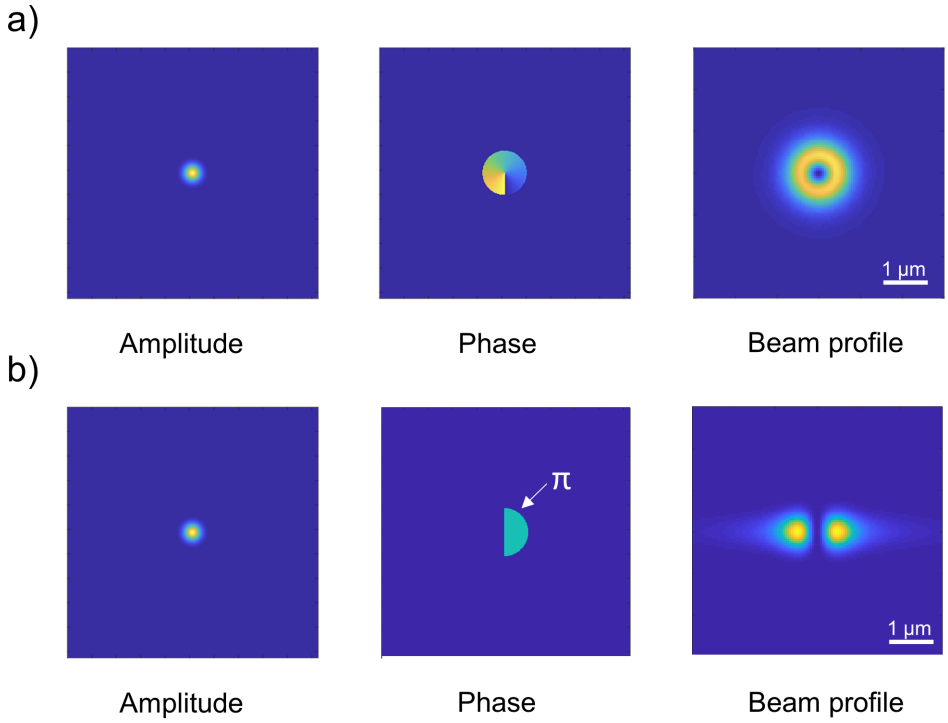


Figure 4.4: Pupil function simulations of beam profils for a given amplitdue and phase distribution. (a) A Gaussian amplitude distribution with a phase distribution that varies azimuthally from 0 to $2\pi$ results in a donut shaped beam profile. (b) A Gaussian amplitude distribution with a phase distribution that is a 0 to $\pi$ mismatch in the center results in a double-lobe beam profile.

(in practice this isn't really possible owing to finite discretization of SLM grids or optics), and as a consequence the only solution to Maxwell's equations is for the PSF amplitude to be zero in this position. Similarly, if there is a 0 to $\pi$ phase mismatch in the phase pattern, like the binary phase pattern shown in Fig 4.4b, this also generates a condition where the amplitude of the PSF must be zero. Note that the beam profile in Fig 4.4b can be considered for so-called "1D" STED, where the depletion field confines the fluorescence from the target chromophore along one axis. The use of such binary phase masks has recently demonstrated great utility in new algorithmic approaches in improving STED image quality in aberration sensing[205] and tomographic image reconstruction[206].

In practice, achieving a STED beam mode where the intensity at the center of the donut (i.e. null) is *exactly* zero is next-to-impossible, and care must be taken to try to minimize the intensity to levels below at least 1%. The greater the relative intensity of the null, the more excitations at the center of the distribution will be quenched, resulting in fewer fluorescent photons and an overall lower signal-to-noise ratio in super-resolved images. Shown in Figure

4.5 are data and fits to one dimensional line cuts of the microscope point spread functions of the pump and STED pulses in our own set-up, imaged via scattering off of a 80 nm gold nanoparticle. The null is estimated at ∼0.6% of the maximum intensity of the STED pulse, which is sufficiently low for imaging purposes.

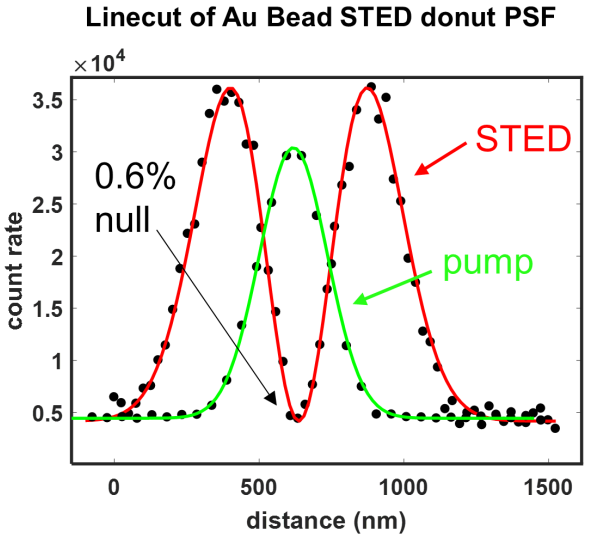


Figure 4.5: Linecut of the pump and STED beam PSFs superimposed on one another. Black data represent relative the intensity values of the individual pixels, and the green and red curves represent fits to the pump and STED PSFs, respectively. Note that the scaling of the profiles is only for clarity of overlap.

### 4.3.3 Resolution scaling in STED microscopy

The concepts of the nonlinear saturation of the optical transition driven via stimulated emission combined with the donut shape of the STED beam mode determine the resolution scaling in STED microscopy.

Harke and co-workers[203] developed a formalism to describe how the geometry of the STED donut and the rate of stimulated emission results in a resolution enhancement that scales with the intensity of the STED pulse as $\frac{1}{\sqrt{I_{STED}}}$. The metric used to evaluate an imaged feature's resolution is the full width at half maximum (FWHM) of a Gaussian fit to the feature PSF.

The rate constant of stimulated emission at any point in space and time is equivalent to the stimulated emission cross section weighted by the intensity of the STED pulse

$$k_{\mathrm{STED}} = \sigma_{SE} I_{\mathrm{STED}}, \tag{4.4}$$

where $\sigma_{SE}$ is the stimulated emission cross-section of a given chromophore. The probability of stimulated emission event occurring is therefore:

$$\eta(I_{\mathrm{STED}}) = e^{-\sigma_{SE} I_{\mathrm{STED}}}. \tag{4.5}$$

Here it is useful to define a parameter known as the saturation intensity, $I_{sat}$, which is the STED intensity at which 50% of the population is quenched via stimulated emission.

$$\eta(I_{sat}) = e^{-\sigma_{SE} I_{sat}} = 0.5. \tag{4.6}$$

This saturation intensity definition allows us to replace the $\sigma_{SE}$ in Equation 4.5 with $\sigma_{SE} = \ln(2)/I_{sat}$

To determine the probability of a stimulated emission event occurring as a function of space, we consider an approximate focal intensity distribution of the STED pulse, $I_{STED}(x)$, that is within the nearest vicinity of the pump distribution:

$$\eta(x) \simeq \exp\left(-\ln(2)\frac{I_{\mathrm{STED}}(x)}{I_{sat}}\right), \tag{4.7}$$

Formally, a STED pulse can be described radially as:

$$I_{\mathrm{STED}}(r) = r^2 e^{-r^2/2\sigma^2} \tag{4.8}$$

so similarly, along one dimension is defined as:

$$I_{\mathrm{STED}}(x) = x^2 e^{-x^2/2\sigma^2} \tag{4.9}$$

but for the purposes of this derivation, it is useful to consider only the radial portion of the STED pulse that encompasses the diffraction limited pump distribution, where $I_{STED}(x)$ can be approximated as a parabola:

$$I_{\mathrm{STED}}(x) \simeq 4 I_{\mathrm{STED}} a^2 x^2 \tag{4.10}$$

where $a$ describes the steepness of the approximated parabola.

The combined actions of the pump and STED pulses yields a new effective point-spread function:

$$PSF_{eff}(x) = PSF_c(x)\eta(x) \tag{4.11}$$

where the original confocal point spread function of the pump in isolation, $PSF_c(x)$, is well approximated by a Gaussian.

$$PSF_c(x) \simeq e^{-x^2/2\sigma^2} = e^{-x^2 4\ln(2)/FWHM_c^2}. \tag{4.12}$$

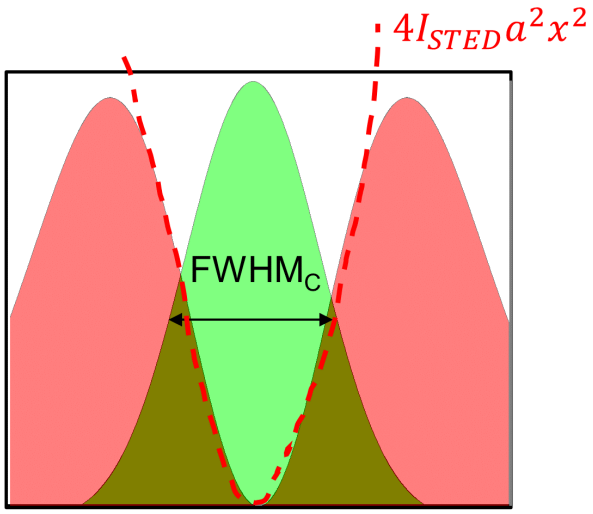


Figure 4.6: Schematic of one-dimensional linecuts of pump and STED PSFs annotated with parameters used in deriving Equation 4.14. FWHM$_c$ is the FWHM of the pump (confocal), and the hand-draw red dashed line outlines the parabola used as an estimate for the inner part of the STED distribution, which corresponds to $4I_{\mathrm{STED}}a^2x^2$

Figure 4.6 schematically demonstrates the overlay of one dimensional renderings of the PSFs resulting from a pump (green) and STED (red) pulse.The FWHM of the the confocal PSF resulting from pump excitation, $FWHM_c$, is a proxy for the resolution without the action of the STED pulse and is an initial condition. The dashed handdrawn red line tracing

out a parabola from the interior part of the STED pulse is of the form described in equation 4.10.

Considering all of the factors for equation 4.11:

$$PSF_{eff}(x) \simeq \exp\left(-4\ln(2)\frac{x^2}{\left(FWHM_c^2 + \frac{1}{a^2\frac{I_{STED}}{I_{sat}}}\right)}\right). \tag{4.13}$$

and solving for the effective FWHM,

$$FWHM_{eff} = \frac{FWHM_c}{\sqrt{1 + FWHM_c^2 a^2 \frac{I_{STED}}{I_{sat}}}}. \tag{4.14}$$

Equation 4.14 is a powerful statement, as it suggests that one can predict the resulting resolution with the action of the STED pulse provided we know the saturation intensity and steepness of the interior of the STED donut. Furthermore, equation 4.14 is often approximated in a more simple form assuming $FWHM_c^2 a^2 \approx 1$:

$$FWHM_{eff} \approx \frac{FWHM_c}{\sqrt{1 + \frac{I_{STED}}{I_{sat}}}}. \tag{4.15}$$

The resolution scaling we've arrived at indeed depends on $\frac{1}{\sqrt{I_{\mathrm{STED}}}}$, and moreover would suggest we can achieve infinitesimal resolution provided we have a large enough $I_{\mathrm{STED}}$. In practice, various limitations preclude this possibility and will be discussed in later sections. The effect of the saturation intensity, and how it impacts the final resolution, is schematically represented in Figure 4.7. One dimensional linecuts through a STED pulse profile demonstrate that at higher intensities more of the STED pulse's spatial profile exceeds the saturation intensity, resulting in a smaller detection region.

To see the resolution scaling in action, Figure 4.8 compiles an example image series of super-resolving dewetted clumps of CdSe/CdS core-shell quantum dots. Every image was collected with the same pump power (measured outside of the microscope) but with a different STED pulse power, listed in microwatts in the top right corner in each image. Visually inspecting the images demonstrates the features become smaller as the intensity of the STED pulse is increased. Even a relatively modest STED power of 25 $\mu$W allows us to verify that the rather large bright feature in the top left of the 0 $\mu$W image FOV is actually two closely spaces clumps of QDs. We observe fairly dramatic differences between the lower STED powers, but as we increase the STED power beyond 250 $\mu$W the resolution enhancement becomes less obvious.

More quantitative verification of equation 4.15 can be demonstrated by fitting linecuts to extract an approximate FWHM of a feature at each STED power. Overlaid on the image in Figure 4.8 measured at a STED power of 100 $\mu$W are colored lines, which represent the line cuts used for a fitting procedure in each of the images. The corresponding FWHM from the

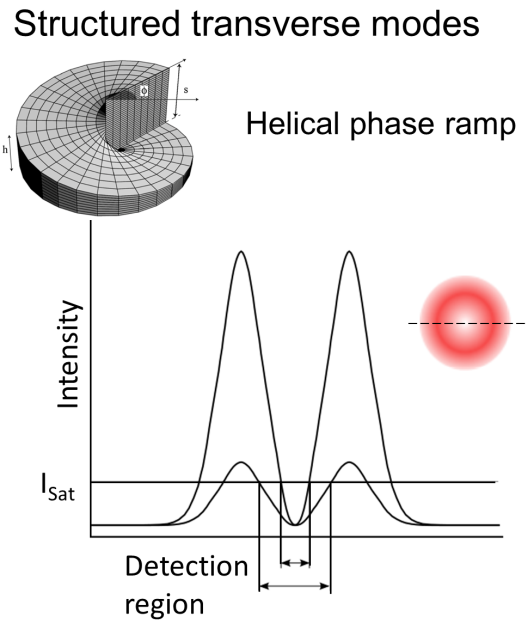


Figure 4.7: Schematic of a one dimensional linecut across a STED donut PSF at two different intensities. The higher intensity linecut results in a greater amount of the linecut intensity distribution exceeding $I_{\mathrm{sat}}$, which results in a smaller detection region.

linecut fits, assuming a simple Gaussian function, plotted against the power of the STED pulse for the 4 linecuts, is shown in Figure 4.9. The data are fit well by equation 4.15, and the $I_{\mathrm{sat}}$ values resulting from each of the fits are close to one another, within error. The resolution appears to "bottom out" between 100 and 200 nm, depending on the feature, whereas the initial FWHM were at least twice as large in each case.

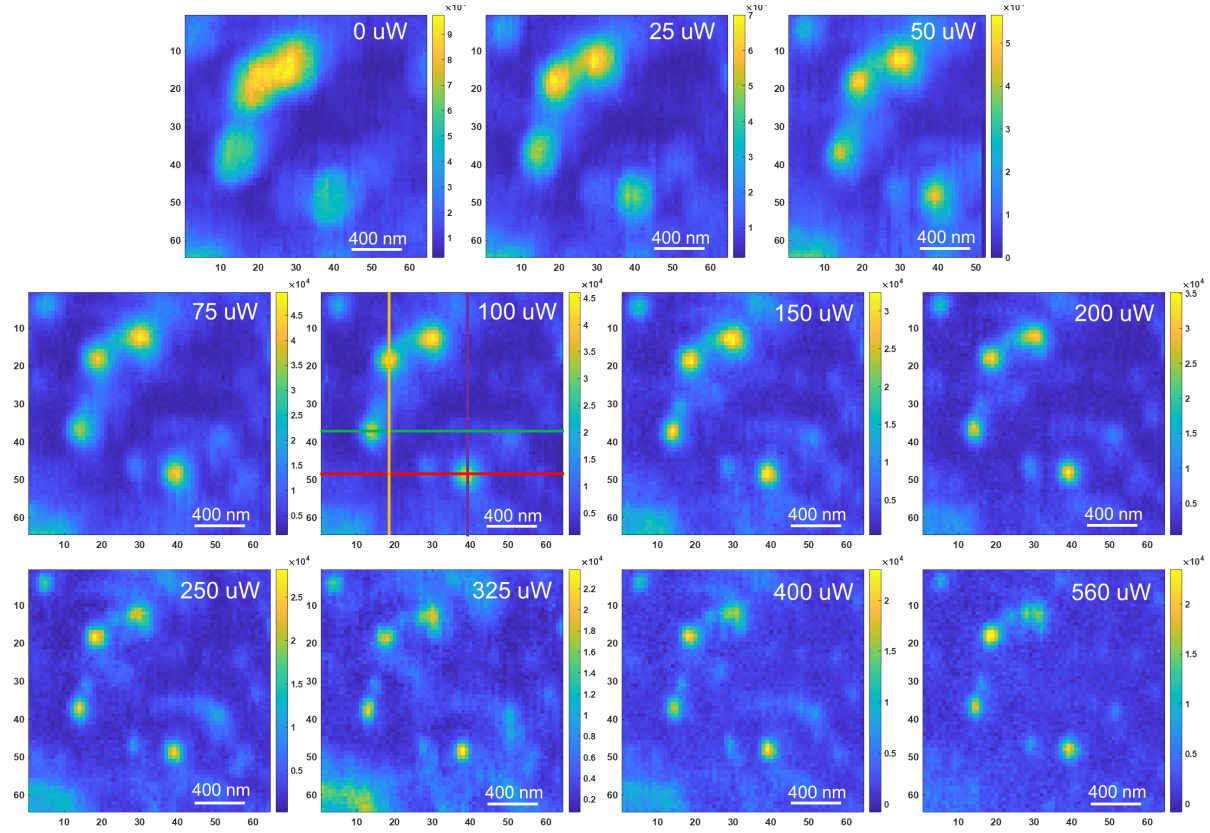


Figure 4.8: Series of modulated excitation STED images of CdSe/CdS quantum dot clumps collected with varying STED powers. The pump wavelength was 540 nm and power was 1 nW for all images. The STED powers are listed in each image in the upper right. The colored lines in the image corresponding to 100 $\mu$W STED are the linecuts used to estimate various features' FWHM in every image, the data of which is shown in Figure 4.9.

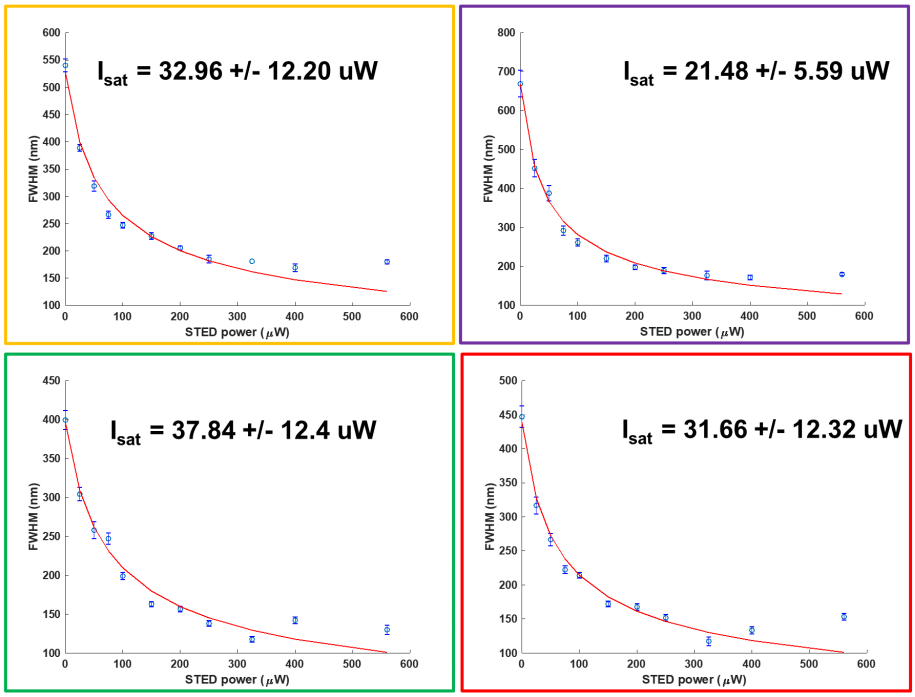


Figure 4.9: FWHM vs STED power trends corresponding to 4 different linecuts analyzed for each image in the series shown in Figure 4.8. The color of the box matches the color of the corresponding linecut. Each data point is a FWHM extracted from a Gaussian fit of the linecut. In each dataset, the red curve represents a fit using equation 4.15, and the $I_{sat}$ extracted from each fit is listed.

### 4.3.4 Requirements for STED chromophores

STED microscopy's super-resolving capabilities are intimately connected to the photophysics of the chromophores that serve as the probes used in imaging. Even in systems that are ostensibly optimized for use in STED microscopy, care must be taken to avoid sample damage or imaging artifacts that are invariably a consequence of the extremely high STED pulse intensities necessary for efficient stimulated emission. For reference, the typical pump and STED pulse powers employed in our measurements with a 200 kHz repetition rate are 1 - 10 nW and 10 - 150 $\mu$W at the sample plane , respectively, so the STED pulses are orders of magnitude higher in intensity. Here we'll briefly summarize the ideal photophysical properties of chromophores to be used with STED and their implications for applying STED to the non-traditional systems targeted with TRUSTED.

#### Absorption and emission spectra

The ideal chromophore is one in which the STED pulse exclusively drives stimulated emission without directly exciting the sample. Absorption of the STED pulse results in potentially destructive heat build-up from the chromophore's non-radiative relaxation and promotes deleterious effects for image contrast if the chromophore radiatively relaxes, effectively generating an unwanted background signal. This process, which we'll refer to as STED-induced fluorescence, is a critical concern for the later discussion of TRUSTED. In fact, absorption of the STED pulse could outcompete the desired stimulated emission, necessitating even higher STED intensities to achieve significant resolution enhancement and further exacerbating heat build-up and poor image quality. The high intensities mean that spectrally overlapping the STED pulse with the chromophore absorption, even where chromophores very weakly absorb, poses challenges.

To avoid this complication, chromophores chosen for STED are those with large Stokes shifts between their absorption and emission profiles [207]. In addition, the tails of the absorption spectra should not extend deeply into the emission spectra. The extent of the Stokes shift determines the optimal wavelength and bandwidth of the STED pulse, where less absorption/emission overlap enables a STED wavelength with greater oscillator strength with the transition corresponding to stimulated emission. Figure 4.10 schematically represents such a concept, where the greater Stokes shift in Fig 4.10b over Fig 4.10a results in placement of the STED pulse closer to the emission resonance.

#### Two photon absorption

Another concern related to the spectral characteristics of chromophores to be used with STED is their potential for two photon absorption. Two photon absorption is nonlinear and scales with the square of the pulse intensity. Despite the STED pulse being energetically displaced from a resonant transition, the high intensity could lead to a two photon absorption event whereby the energy of two photons corresponding to the STED wavelength leads to chromophore excitation [208]. For example, if the STED pulse is placed at 800 nm to overlap

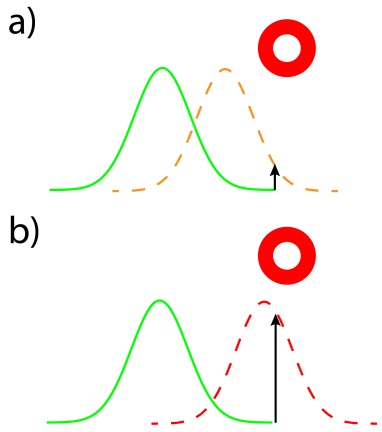


Figure 4.10: Schematic of the Stokes shift between a chromophore's absorption and emission spectrum and its consequence for STED. (a) A relatively small Stokes shift, so the STED pulse is placed towards the tail of the emission spectrum. (b) A relatively large Stokes shift, so the STED pulse can be placed closer to resonance.

with the emission profile, but the sample also strongly absorbs at 400 nm, the two photon absorption event could present non-trivial competition to stimulated emission. For this reason, one may wish to avoid chromophores with relatively broad absorption spectra.

### Chromophore excited state characteristics

Beyond their steady-state spectral properties, the excited state behavior of chromophores is of paramount concern for STED. Excited state pathways that compete with the transition driven by stimulated emission will reduce the super-resolving ability of STED. For example, excited state absorption induced by the STED pulse, where the chromophore is promoted to an even higher lying excited state, could be a competitive pathway. If the system undergoes intersystem crossing from a singlet excitation to an optically forbidden triplet, then the stimulated emission efficiency can also suffer.

As discussed previously, the rates of vibrational relaxation, within both the excited and ground electronic surfaces, are critically important for efficient stimulated emission. The excited state vibrational relaxation is ideally quick, as this process supplies the initial state that the STED pulse will drive. Similarly, because the STED pulse creates an equilibrium between the ground and excited states, the ground state vibrational relaxation must be rapid in order to "siphon" excitations out of the quenched state populated by the STED pulse. This enables a population inversion for greater than 50% quenching efficiency. For this reason and others, STED pulses are typically stretched in time to 100s of ps or even a few ns to fully capture this ground state vibrational relaxation.

### Chromophore photostability

Perhaps one of the most challenging aspects of applying STED microscopy to new systems of chromophores (successfully, at least) is ensuring that the high pulse intensities do not damage the target sample in question. As resolution scales with the STED pulse intensity, the resolution can in principle become infinitesimally small provided the laser power can reach high enough. In practice, the damage threshold of a chromophore is often what places a ceiling on the achievable resolution. Extremely robust materials, like fluorescent color-centers (nitrogen-vacancies) in diamond have demonstrated resolution on the order of ∼6 nm [209], which represents one of the best examples of STED resolution enhancement.

Many conjugated organic compounds, like staple fluorophores used in imaging experiments, are susceptible to oxidation by reactive oxygen species (ROS). After photo-excitation, energy transfer between the fluorophore and triplet oxygen can lead to a more reactive singlet oxygen species. ROS can subsequently disrupt the $\pi$-bonding network of a fluorophore via oxidation reactions and photo-bleach the compound. STED-induced fluorescence only contributes to this issue, but the use of oxygen scavengers[210] or imaging the sample under inert nitrogen environments[211, 212] can help with this.

Perhaps the most common cause of sample damage in our experiments is thermal damage. Absorption of the STED pulse creates additional thermal buildup in a material beyond the resonant pump excitation, and if the material in question possesses a thermal conductivity too low to efficiently remove the local heat build-up, the sample can undergo bleaching and even worse material deformation, like melting. Figure 4.11 shows an example of a brightfield image of a flake of a fluorescent covalent organic framework (COF) that suffered thermal damage as a consequence of the STED beam. Unfortunately for this system, even using STED powers to achieve just 40% quenching efficiency resulted in too much thermal build-up causing irreversible burning and warping of the material. Raster scanning the sample position to reduce a given sample spot's exposure to the laser beams can help with this issue, provided the change in position is a distance somewhat greater than the size of the STED pulse (∼1 micron).

Another consideration for sample stability is the potential for ionization via the high intensity STED pulses, or laser ablation. The ionization event leads to further ionization within the material and instigates the formation of a plasma, which rapidly removes material. This requires very high peak powers, but it has been demonstrated in our own set-up - if we accidentally allow too high of a STED power through the objective while imaging our gold nanoparticles for beam mode verification, the gold bead will "explode" and disintegrate into vanishingly small fragments.

### Implications for STED microscopy with optoelectronically coupled chromophores

The STED set-up we use for both imaging and time-resolved measurements was designed with the intention to study samples wherein exciton migration occurs. The individual build-

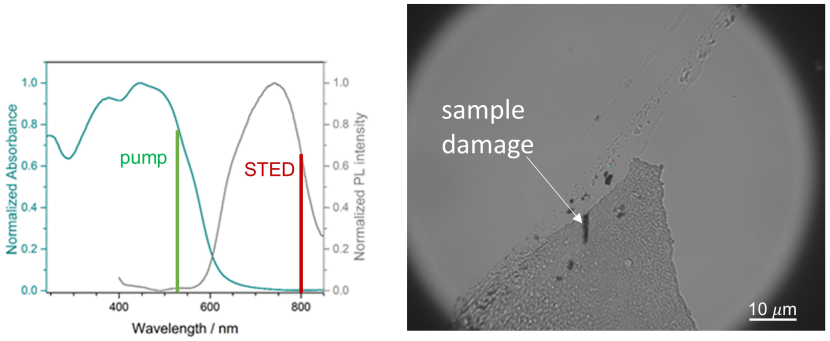


Figure 4.11: COF sample as well as absorption and emission spectra prepared by Niklas Keller of the Bein group (Ludwig-Maximilians-Universität München). Exposure to the STED beam results in the black burn marks on the COF flake in the brightfield image.

ing blocks of such materials are often chromophores that electronically couple to their neighbors to facilitate the exchange of excitation energy. These samples are a rather unique focus for STED microscopy, because the chromophores that participate in stimulated emission also compose the material of interest, which is unlike biological imaging where STED dyes are used as labelling agents to report on the underlying biological structure. In a way, the "labelling" density of our systems are substantially higher than a conventional STED microscopy measurement, as chromophores need to be packed within very close distances (e.g. $< 10$ nm) for energy transport.

The chromophore requirements that we detailed above are not always compatible with the photophysics necessary for efficient transport of excitons in materials. For example, chromophores possessing a large Stokes shift, which is ideal for STED, typically preclude long-range energy transport in systems where the operative mechanism depends on the spectral overlap of constituent chromophores (e.g. FRET). In fact, fluorescent molecules that can self-assemble into higher order electronically coupled aggregates can yield spectra that have an overall *smaller* Stokes shift than the monomer spectra, often in the form of J-aggregates [213–215]. While such J-aggregates might make an excellent model system for excitation transport, their reduced Stokes shift poses complications for STED. Alternatively, molecular dye systems can also aggregate into so-called H-aggregates, which often have dramatically increased Stokes shifts relative to the monomer species. The excitations in such systems, however, are typically non-radiative and difficult to detect with a fluorescence-based readout. Figure 4.12 provides a schematic of these kinds of aggregates and representative spectra for a Cyanine dye, a common dye used in imaging and FRET studies alike [213].

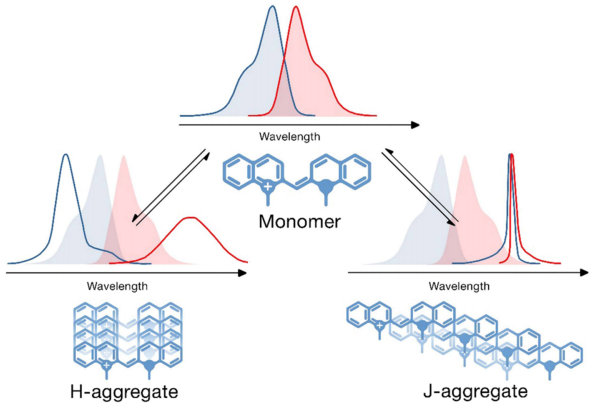


Figure 4.12: Schematic demonstrating how the coupling between monomers of a Cyanine dye molecule may result in H- or J-aggregates. Figure adapted with permission from Ref [213].

### 4.3.5 TRUSTED: Optical Table layout

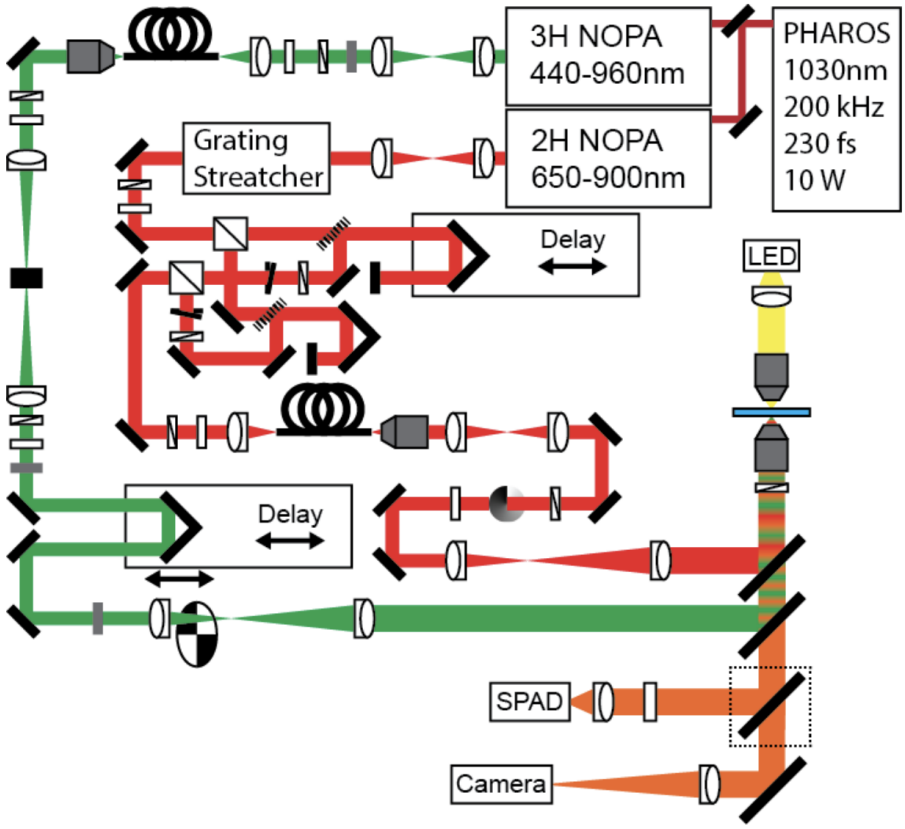


Figure 4.13: Schematic of the STED/TRUSTED optical table layout. Figure adapted with permission from the Supplementary Information of Ref [116].

A brief description of the optical system used for this chapter follows, as depicted in Figure 4.13. For a more complete description, see pages 78-81 of Sam Penwell's thesis[216].

Regeneratively amplified laser pulses at 1030 nm and 200 kHZ repetition rate are coupled into two commercial non-collinear optical parameteric amplifiers (NOPA). One NOPA uses the second harmonic generation of the 1030 nm as its pump and serves as the laser source for our STED path, while the pump path is from a NOPA that uses the third harmonic generation of the 1030 nm as its pump.

The pump beam is coupled to a single-mode fiber to ensure a high quality Gaussian beam mode. After the fiber, the pump is sent through a rotatable half-waveplate and then a fixed polarizer combination for power attenuation control. The beam is then sent down an optomechanical delay line to control the relative arrival of the pump relative to STED1. The pump is then sent through a telescope to increase/decrease the beam size, with a chopper

wheel placed in between the lenses roughly at the pump beam focus. After the telescope, the pump beam is coupled into the microscope objective via a dichroic longpass mirror, where the beam is of a diameter that overfills the back aperture of the microscope objective.

The STED beam is sent through a commercial grating stretcher to increase its duration to ∼120 ps. Next, the STED beam is split by a polarizing beam splitter cube, which generates an arm for STED1 and an arm for STED2. The STED2 path is coupled to an optomechanical delay stage, to control the arrival of STED2 relative to STED1, and sent through a rotatable half waveplate, followed by a fixed polarizer for power attenuation control. The STED1 path is similarly sent through its own half waveplate and polarizer. The STED1 and STED2 beams are recombined through a second polarizing beam splitter cube, and the recombined beam is then coupled through a single-mode fiber. The fiber is a crucial element towards ensuring that the beam modes of the STED1 and STED2 pulses are identical and possess minimal wavefront distortion. The STED beam is then expanded in size via a telescope to match the size of the vortex phase mask, the optic responsible for generating the donut shape. After the phase mask, the beam is further expanded via another telescope to overfill the back aperture of the microscope objective, and is coupled into the objective through a dichroic shortpass mirror.

Both the pump and STED beams are sent through a quarter waveplate just before entering the microscope objective. Fluorescence from the sample is filtered through both the dichroic mirrors used for the pump and STED beams. A removable mirror enables coupling the sample fluorescence to our SPAD detector. Atop of the sample stage is a second objective with a white light LED. We use this objetive and light source to image the sample plane in brightfield to assist with finding regions of interest on a sample-containing substrate. The white light is coupled to a Thorlabs CMOS camera by removing the mirror just before the SPAD.

### 4.3.6 Modulated excitation removes contributions from STED-induced fluorescence

Our goal to study systems of electronically coupled chromophores with efficient energy transport places us in a position where STED-induced fluorescence is a very high probability. Our target exciton population is that which is created by the pump and then a given portion of said population is subsequently quenched by the action of the STED pulse. This target exciton population can intermingle with excitons created by the STED pulse. Because these STED induced excitons will be present regardless of whether the pump has excited the sample or not, by measuring the sample fluorescence with *only* the STED pulse, and then measuring the sample fluorescence with the combined action of pump and STED pulses, we can isolate the target exciton population by subtracting the two signals from one another. This is similar in spirit to the lock-in detection employed in other ultrafast spectroscopies where changes in the target signal are small and ride atop a comparatively large background (though to be clear, here we are not using lock-in detection).

Herein, we employ a modulated excitation scheme to remove contributions from STED-induced fluorescence to our target signal. Developed previously by our group[217], modulated excitation demonstrated a significant improvement in the image contrast for super-resolving nanoparticles formed from a conjugated polymer (poly 2,5,2,5-tetrahexyloxy- 8,7-dicyano-di-p-phenylene vinylene , or CN-PPV). An optical chopper wheel placed in the pump path chops at a 500 Hz frequency, creating a pulse train sequence with "pump on" and "pump off" contributions. The chopper's frequency signal is synced with the computer responsible for processing the data acquisition from the detector. Each pixel of a differential image is the difference of two measurements: the average "pump on" and the average "pump off" signals. We perform this measurement pixel by pixel, with the 500 Hz chopper, to better average out the noise than simply measuring an entire image with "pump on" and then an entire "pump off" image and subtracting them. Examples of similar STED-induced fluorescence filtering can be achieved by measuring a line of pixels with the pump on and a line of pixels with the pump off[218], but these imaging systems employ much higher repetition rate laser systems (e.g. 80 MHz) than our 200 kHz system, and in my experience it's necessary to perform the subtraction pixel by pixel for quality of image rendering.

Figure 4.14 provides an overview of the modulation scheme and an example of modulated excitation imaging of CdSe/CdS quantum dot clumps. Fig 4.14a shows the chopper and the corresponding pump + STED ("pump on") and STED only ("pump off") conditions. Fig 4.14b shows two different examples of the subtraction from the two different signals, denoted by shapes that are found overlaid on the corresponding pixels in the modulated channel image in Fig 4.14c. In one situation, denoted by the star, the pump + STED signal has a higher intensity than the STED only signal, and subtraction of the two channels yields the true pump signal. In the other situation, denoted by the diamond, the pump + STED and STED only signals are the same, so the subtraction yields a 0 intensity pixel, revealing there was no pump contribution to the fluorescence signal in this location.‘

In Fig 4.14c we observe the efficacy of modulated excitation imaging. The pump only

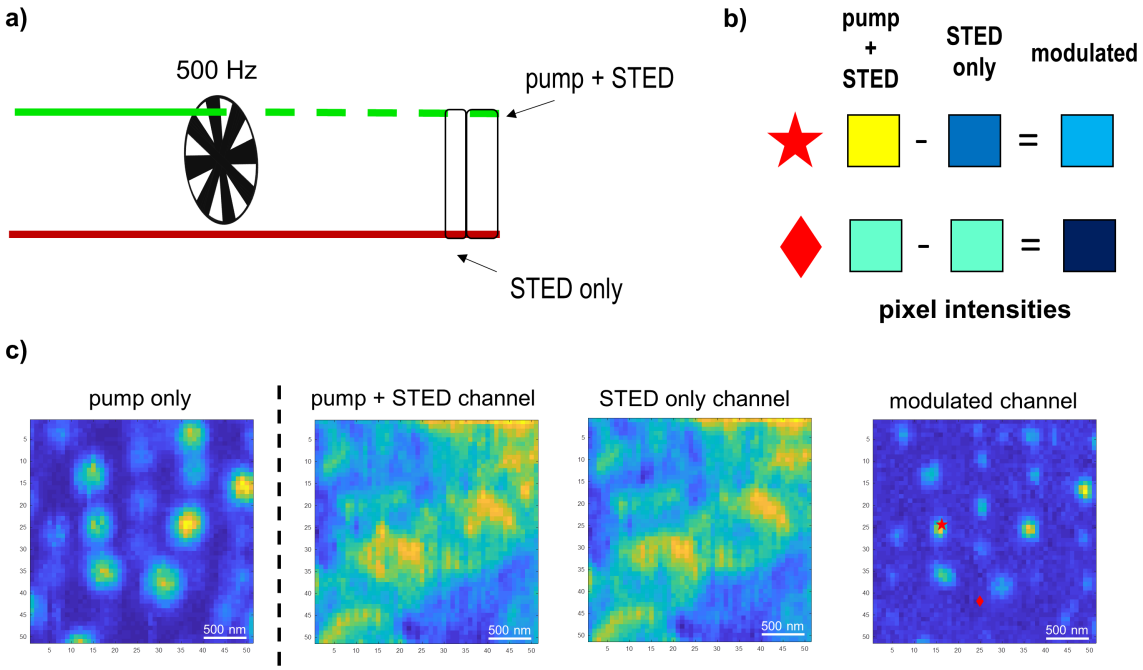


Figure 4.14: Overview of modulated excitation STED imaging. (a) A chopper wheel in the pump path intermittently blocks the pump, leading to the pump+STED and STED only sequences. (b) Examples of the subtraction between pump + STED and STED only channel pixels that result in the modulated channel pixel. The pixel colors correspond to the false-color representing to the intensity in the images in (c). These examples are taken from the modulated channel image in (c) and are annotated by the star and diamond shapes. (c) From left to right are images of different nature but of the same sample region: A pump only diffraction limited image, a pump + STED channel image, a STED only channel image, and finally a modulated channel image. The false-color corresponds to the intensity, with blue representing the lowest intensity; yellow, the highest.

image on the left represents a diffraction limited rendering of CdSe/CdS quantum dot clumps (individual particles did not possess a strong enough signal). The next two images to the right are the signal channels corresponding to pump + STED and STED only, respectively. The STED-induced signal is so severe in this case that it nearly swamps out the target signal in the pump + STED channel, and we can actually see the shapes of the STED donuts outlined in the STED only channel fairly clearly. But, as each pixel of these two images were

generated, their difference is also recorded and constructs the modulated channel image shown on the right. Comparing the pump only image and the modulated channel image, we observe clear resolution enhancement.

### SPAD detector pile-up correction

One important consideration related to the subtraction of STED-induced signal is the susceptibility of avalanche diodes, like our single-photon avalanche diode (SPAD), to non-linearity in their response to sample emission. Because the detector relies on an "avalanche" of charge upon detection of a single-photon, the detector will actually turn off for a period of time to recover its charge, and we allow a period of 300 ns for this recovery for all experiments. The period of time the detector turns off is referred to as the "dead time," and it is the reason many time-correlated single-photon correlation (TCSPC) measurements are conducted with signal count rates below 10% of the excitation source repetition rate[219]. At high laser intensities, if the sample were to emit two photons for one laser pulse, the photon that arrives later in time would be rejected. This artifact would make it appear as though the sample has a shorter radiative lifetime, among other issues. This condition sets an upper bound on the count rate we can physically observe, which is our 200 kHz laser repetition rate, because there can be no more than a single photon detected per excitation pulse in our system.

To characterize this non-linearity present in our detector, we measure the scattering signal from a glass coverslip at a series of carefully measured laser powers (we used the STED laser to do this, but we could have equally used the pump laser). The laser powers we use are sufficiently low that the scattering intensity should scale linearly with laser power. Figure 4.15 plots the experimentally measured count rate on the detector as a function of laser power, shown in grey. Also plotted in red are data linearly extrapolated from the lowest few powers. We note that at count rates near and above 20 kHz, we begin to deviate from the expected linear trend.

This measurement of this so called pile-up effect is important because we can use it as a way to re-calibrate the data in post-processing, which is helpful for imaging, and crucially so for time-resolved measurements of exciton migration. Furthermore, when comparing the results of our measurement in 2021 to those from 2015, we found that the range of the linear response had shrunk fairly significantly. Previously, the detector readout would follow a linear trend at count rates up to 70 kHz, whereas now the threshold is closer to 20 kHz. We believe the SPAD's age and amount of time it was continuously on (we would collect data for days at a time) would diminish the linear response range. We did purchase a new SPAD, but reinstallation might require adapting the older Labview software to a newer version, and the presumed time required for troubleshooting was not within my budget of remaining time at Berkeley.

In post-processing data, we apply corrections based on interpolations between the measured count rate and linearly extrapolated count rate to reconcile the detector non-linearity in the pump + STED and STED only channels. This enables us to extract the true value for our target exciton population. Our confidence in this correction scales inversely with the

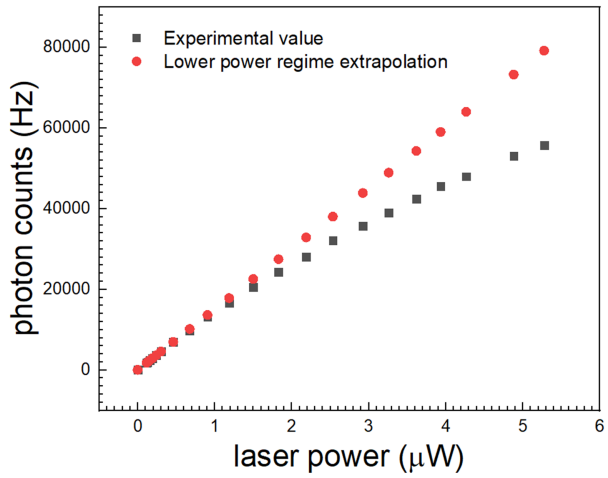


Figure 4.15: Pile-up effect measurement using scattered laser light, with both experimental data (grey) and data determined from a linear extrapolation of the lowest few powers (red).

count rate, so conservatively, we try to keep the pump + STED count rate below 40 kHz for our experiments.

This 40 kHz value, or our "pile-up correction limit," has consequences for our experimental signal-to-noise ratio. Figure 4.16 is a schematic representing why large STED-induced signal poses an issue with the pile-up correction limit. Fig 4.16a represents signal collected from the sample with only the action of the pump. The pump + STED channel and target channel read the same number of counts due to no counts being present in the STED only channel. In Fig 4.16b, we now add the action of the STED pulse. The STED pulse causes quenching of the target population created by the pump, but also generates counts, which are registered in the both the pump + STED and STED only channels. In order to achieve more quenching (i.e. better resolution enhancement), Fig 4.16c shows an increase in the STED power, resulting in more quenching of the target population but also greater counts in the pump + STED and STED only channels. The count rate of the pump + STED channel exceeds the pile-up correction limit, so to address this we insert a neutral density filter in front of the detector to sufficiently lower the count rate, seen in Fig 4.16d. While the pump + STED channel is now safely below the pile-up correction limit, the signal in our target channel is now quite small, due to both the quenching action of the STED pulse and the neutral density filter.

Had we realized this issue sooner when working with the STED set-up and understood that our quantum dot samples, the focus of Chapter 5, bear relatively large STED-induced

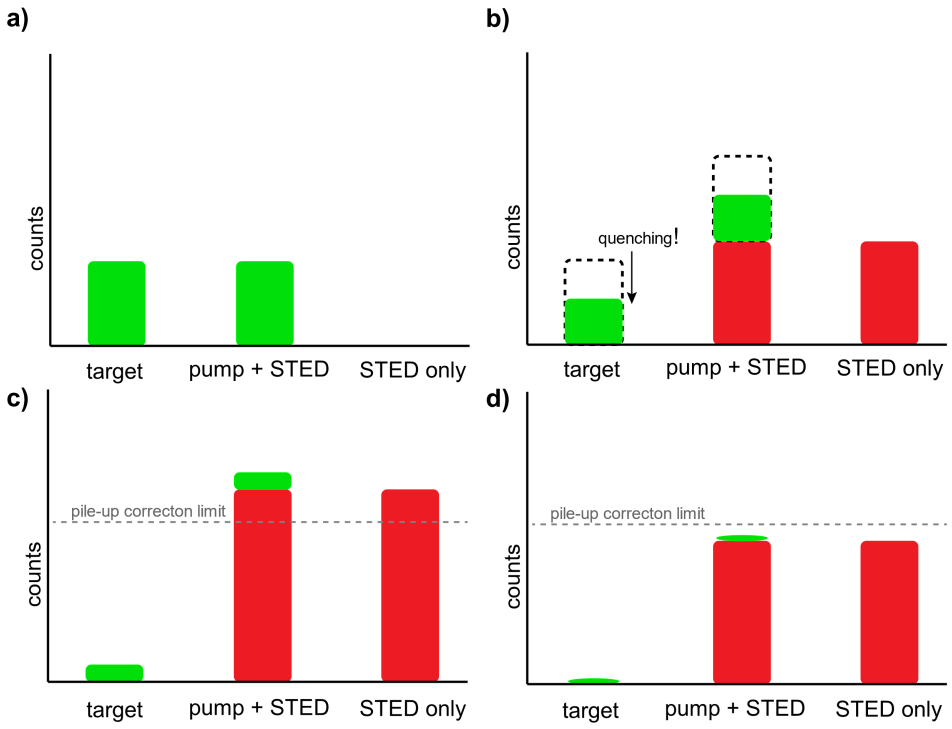


Figure 4.16: Schematic overview of modulated excitation with consideration for the pile-up correction limit. The target channel is the difference between the pump + STED and STED only channels. (a) Channel readings with only the action of the pump. (b) Channel readings with the action of the pump and STED. The target population is lowered due to quenching, indicated by the smaller green bar in the dashed outline. (c) Channel readings with the action of the pump and higher intensity STED. The pump + STED channel counts now exceed the pile-up correction limit. (d) Channel readings for the same intensities of pump and STED as (c), but with a neutral density filter applied to the detector.

signals, replacing the SPAD would have been a worthwhile investment of time from the start. Should someone take over this instrument in the future, I strongly encourage them to do so.

**Examples of modulated excitation STED imaging**

Figures 4.17 - 4.19 below provide some examples of using modulated STED imaging to achieve resolution enhancement in systems composed of densely packed chromophores. These systems are examples of where STED or other structured illumination super-resolution techniques are necessary to achieve resolution enhancement. Techniques that rely on photoswitching of individual chromophores and then reconstituting a super-resolved image in post-processing would ultimately not work here, as the individual chromophores that constitute these structures are not spatially or temporally distinct from one another.

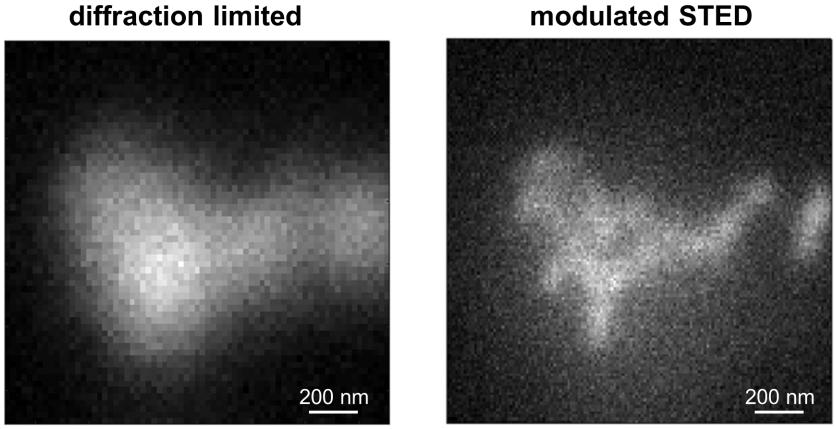


Figure 4.17: CN-PPV nanoparticles super-resolved with modulated excitation STED imaging. These particles were prepared in the same manner as they were in 2015 with this set-up(Ref [217]), and we used this as a sample to ensure everything was working properly after a few years of inactivity.

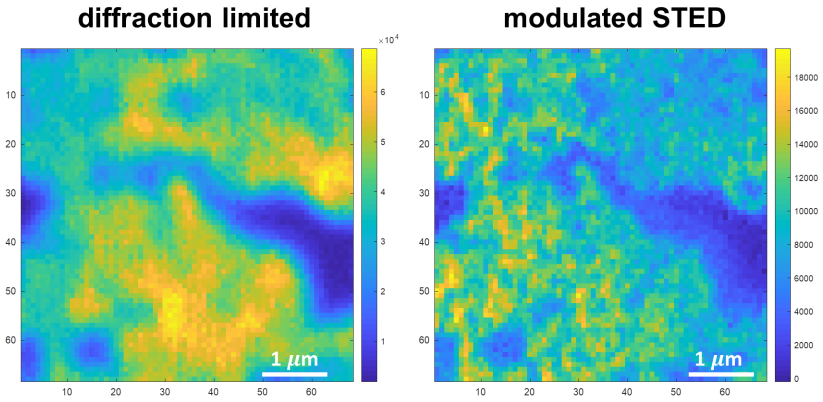


Figure 4.18: Resolution enhancement of impartially formed CdSe/CdS quantum dot superlattice film. These quantum dots are 22 nm in diameter, with an emission peak at ∼700 nm. The defects/vacancy of material is much more obvious in the modulated STED image. This is personally my favorite STED image I've collected.

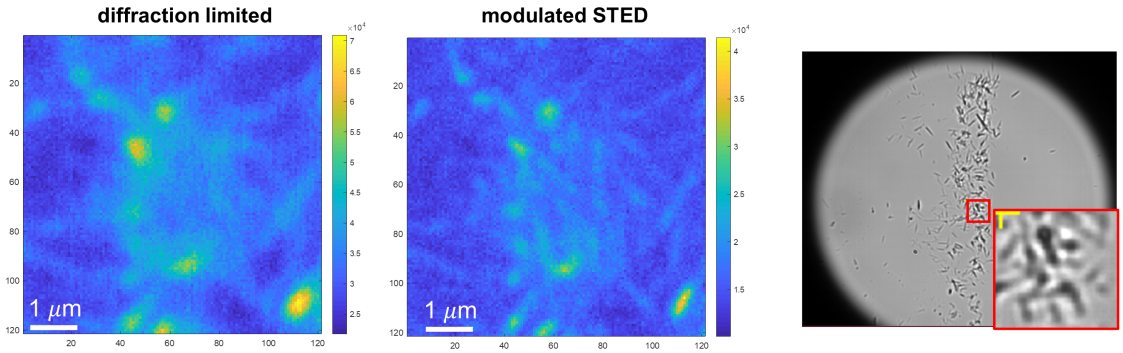


Figure 4.19: Resolution enhancement of microcrystals formed via precipitation of ATTO 590 fluorescent dye. Atto 590 is actually a stellar STED dye, but when it crashes out of solution in aggregates/microcrystals, its relative brightness decreases fairly significantly. Still, although faint, we were able to achieve resolution enhancement in a congested bundle of ATTO 590 microcrystals, when comparing the diffraction limited image (left most) and modulated excitation STED image (center). The right image is a brightfield optical image taken in the same microscope as these microcrystals. Unfortunately, I was unable to reproduce these crystals in future sample preparations.

## 4.4 Time-resolved ultrafast STED, or TRUSTED, microscopy

As mentioned in various instances within our discussion of STED microscopy, our own STED set-up was designed with the intention to monitor the migration of excitons in materials. To do so, it required a significant reworking to transform the microscopy to an ultrafast spectroscopy capable of probing exciton migration on relevant nm length and ps time scales. This development was achieved by Sam Penwell, Lucas Ginsberg, and Naomi Ginsberg, and one particular (though certainly not exclusive) fruit of their work was measuring an exciton diffusion length of 16 $\pm$ 2 nm in CN-PPV conjugated polymer films, a remarkably sensitive result[116]. One can refer Sam Penwell's thesis[216] for details of this experiment. Below I'll provide the general concept of TRUSTED, the various nuances I learned over my time with the instrument, and the samples we tried to investigate using this method.

### 4.4.1 TRUSTED: General Concept

TRUSTED uses pulsed lasers for the pump and STED beams, and couples a second STED pulse (STED2) with identical characteristics to the first STED pulse (STED1), yielding an overall 3 pulse sequence. The pump pulse excites the sample and immediately the STED1 pulse will narrow the distribution, yielding a sub-diffraction limited exciton volume. In the material of interest, excitons will sample the space available to them via diffusion, which will cause this initial sub-diffraction limited volume of excitons to expand outward. At a controllable time delay, the STED2 pulse is introduced, which quenches excitons that have migrated across the optical quenching boundary imposed by the STED2 pulse. After the action the STED2 pulse, we turn our detector on via its gated-detection capability (see Section 4.4.2 below) and collect sample fluorescence. Figure 4.20 schematically represents this pulse sequence and the corresponding changes to the exciton profile.

The key that enables sensitivity to migration is the introduction of the STED2 pulse at controllable times after the action of STED1. As the time between STED1 and STED2 increases, the exciton distribution has more time to spatially expand due to diffusion. This leads to greater fractions of the exciton profile overlapping with the STED2 quenching boundary. Thus, we would expect to collect fewer fluorescent photons at longer time delays between STED1 and STED2 because more of the excitons traverse the quenching boundary. By recording the fluorescence of the excitons remaining after the action of STED2 at various time delays, we can generate a plot like that shown in Figure 4.21. We note the data points trend downward as the time delay between STED1 and STED2 increases, where the data represent fluorescence signal converted to the fraction of excitons remaining. Encoded in the slope of the fit to the data is the diffusivity of the excitons - a steeper slope represents a higher diffusivity as more excitons were able to cross the STED2 quenching boundary in a given period of time. Provided we know the lifetime of the excitons in question, converting the diffusivity to a diffusion length is a straightforward calculation via the definition:

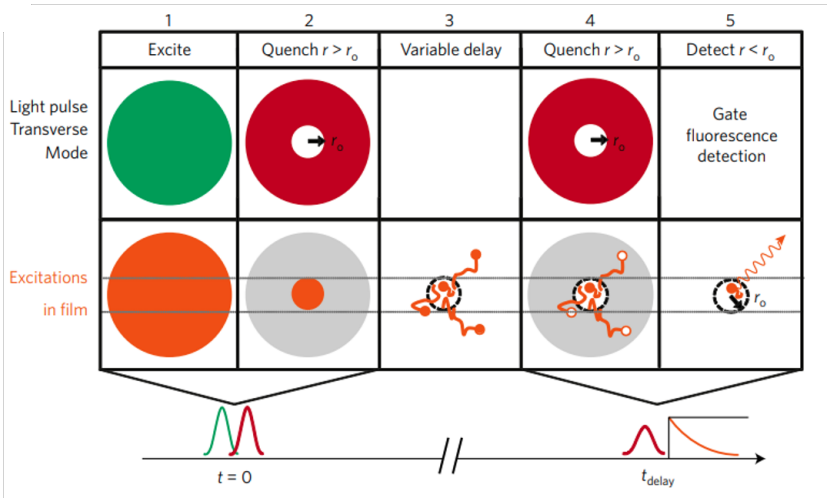


Figure 4.20: Schematic of TRUSTED pulse sequence and corresponding excitation profile in film. Figure adapted with permission from Ref [116].

$$L_D = \sqrt{D\tau}. \tag{4.16}$$

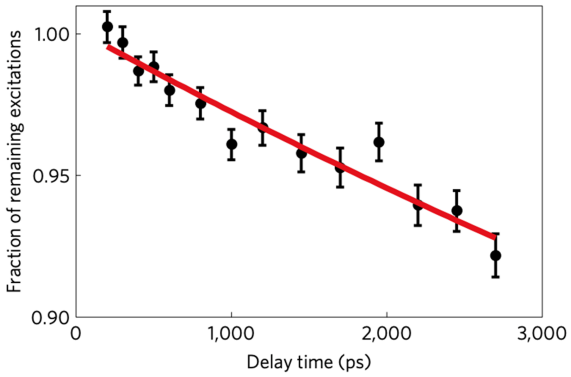


Figure 4.21: Example TRUSTED data that reveals the exciton migration length in CN-PPV thin films. Figure adapted with permission from Ref [116].

### 4.4.2 TRUSTED: Migration Signal Isolation

In order to isolate the signal presented in Figure 4.21, a fairly nuanced normalization scheme is required, the development of which was a non-trivial endeavor for the predecessors of TRUSTED. This normalization scheme, as well as the various control measurements, merits discussion here as it highlights the care required to be confident that our TRUSTED observable is indeed due to migration, as opposed to other sample photophysics. As will become apparent, our experience trying to apply TRUSTED to various samples with photophysics that differs substantially from the CN-PPV films on which this normalization scheme was first developed, demonstrate that the originally developed scheme, if used blindly, can erroneously suggest an exciton diffusivity that is too high or even present when it should not be in a given sample.

#### Gated detection

The SPAD detector is a state-of-the-art fast-gated detector[220], which allows us to control the time that the detector "turns on" relative to the arrival of our STED2 pulse. The detector is triggered by the laser system, and we can program an offset time (i.e., "gate-offset") relative to this trigger. This SPAD in particular has the capability to turn on remarkably fast, with a $< 200$ ps rise time. The ability for the detector to follow the STED2 pulse at each time-delay is important, as this allows us to reject photons emitted from the sample before interaction with the STED2 pulse.

We define the quenching efficiency of the STED pulse as:

$$\text{quenching efficiency} = 1 - \frac{[\text{modulated counts with pump + STED}]}{[\text{counts with pump only}]}. \tag{4.17}$$

where recall from Section 4.3.6 the modulated counts are those in which the STED only counts are subtracted from the pump+STED counts to yield the true pump-only counts. In order to maximize the quenching efficiency of a sample, the STED pulse should arrive shortly after the pump pulse (to account for vibrational relaxation). Introducing the STED pulse at much later times will allow photons to be emitted from the sample, per its radiative lifetime, and lead to a reduced quenching ratio. To emphasize this, Figure 4.22 is an example dataset measuring the modulated signal intensity vs the time delay between pump and STED pulses. The sample in question is a crystal formed via precipitation of ATTO 590, a common STED dye. At negative time delays, when the STED pulse arrives before the pump, there is no signal reduction because stimulated emission cannot occur. At $\sim$200 ps time delay, we observe the greatest reduction in the signal counts. At time delays longer than 200 ps, the count rate steadily increases, because more excitons are relaxing and emitting from the sample before the STED pulse has a chance to quench them. If we were to measure the efficiency per equation 4.17 at each time delay, then the value would be decreasing in time for time delays longer than 200 ps. But, if we were able to redefine what the pump-only counts were at each time delay in a way that ignores the signal prior to the action of the

STED pulse, we would notice that the efficiency would remain constant as function of time delay.

We therefore gate the detector on only after the time delay corresponding to the arrival of the STED pulse, and calculate the quenching efficiency by normalizing the time-delay trace to the time-delay trace of the pump only signal (by blocking the STED pulse) using the same detector gating time relative to the STED2 arrive time (with a fixed offset). Although the overall count rate decreases as we wait longer and longer to turn the detector on, the quenching efficiency will not change as a function of STED time delay. Essentially, the variable detector gate enables us to normalize the signal with and without the action of the STED pulse at each time delay, which removes the effect of the sample's lifetime!

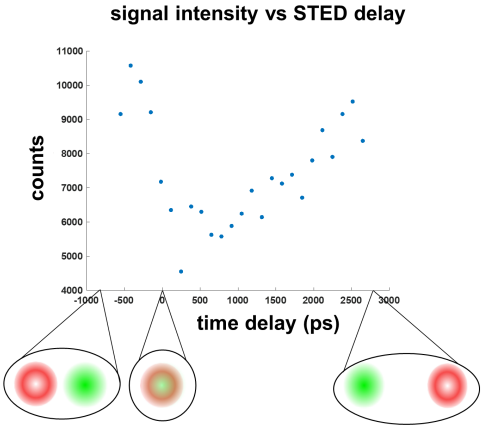


Figure 4.22: Plot of signal intensity vs. time delay between pump and STED pulse. Data collected from ATTO 590 microcrystals. Various time-delays are annotated with a graphic representing the overlap between pump and STED pulses in time. The maximum quenching efficiency, corresponding to the data point at a 250 ps time delay, is 65%.

In addition to this gating procedure, we also perform a series of measurements that involve blocking one or both STED pulses to ensure proper normalization. Here, we describe these 4 individual measurements and how they are used to verify the migration observable in TRUSTED.

### pump-only

In this measurement, fluorescence signal collected from the sample induced by the pump is measured with both STED1 and STED2 blocked. We measure the modulated pump only signal at each would-be STED2 time delay, because we still need a record of the decreasing

pump only signal as we turn the detector on at progressively later times. The overall trend in the pump only signal as function of detector gate (i.e. time delay) should reflect the exciton lifetime of the sample. This measurement is agnostic to exciton transport.

**pump + STED1**

This measurement is similar in spirit to the pump only measurement, except that we measure the modulated pump signal with the action of STED1. Neither the pump nor STED1 arrival time changes throughout the course of the measurement, and so measuring the modulated pump + STED1 signal at each would-be STED2 delay serves to account for the lifetime of the excitons that survive STED1. In other words, this provides a lifetime trace whose initial condition is the sub-diffraction exciton distribution created by the combination of pump + STED1, and the modulation serves to reject fluorescence occurring due to the undesired absorption of the STED pulse. In principle, the data we measure here *should* follow the exact same trend as the pump only data but with a constant offset due to the quenching action of STED1. However, if for whatever reason, the dynamics of the system change due to the action of STED1, this measurement should reflect that and allow us to account for it.

Furthermore, because the rate of signal change due to shifting the detector gate is nominally the same here as in the pump only measurement, the quenching efficiency recorded at each time delay should be the same. That is, the 1 - [modulated pump+STED1]/[modulated pump] should be constant as a function of time delay. Cases in which this is not true (within error), serve as a red flag that the TRUSTED observable may not reliably report diffusion. I will discuss instances of this in Section 4.6. The pump + STED1 measurement is similarly agnostic to exciton transport.

**pump + STED1 + STED2**

Here, both STED beams are unblocked and the combination of pump, STED1, and STED2 is where the "magic happens," so to speak. This combination of pulses enables sensitivity to exciton migration and, in principle, this sensitivity can be controlled via the intensities of STED1 and STED2. Using more intense STED1 will result in a more narrow sub-diffraction limited initial exciton distribution. This more narrow initial condition makes relative changes to the spatial profile of excitons due to diffusion more obvious (see also Section 4.5.1). There are of course other considerations for higher STED intensities, like sample damage, STED-induced fluorescence, and non-linear interactions between our target exciton population and excitons inadvertently created by the STED pulse.

In order to achieve the data presented in Figure 4.21, we normalize the signal at each time delay for the pump + STED1 + STED2 combination by the corresponding pump + STED1 signal. Because the change in the pump + STED1 signal should nominally just be a consequence of the lifetime of the target exciton population, this allows us to isolate the change in our signal due strictly to the action of the STED2 pulse. We call this ratio of

the measurements the "normalized detection volume fluorescence," or NDVF. Also, when we refer to "TRUSTED data," we are referring to this ratio:

$$\text{NDVF} = \frac{[\text{pump + STED1 + STED2}]}{[\text{pump + STED1}]} \tag{4.18}$$

Keep in mind, as well, that in each permutation of the 3 pulses being on or off, we are always modulating the pump via our chopper (as detailed in Section 4.3.6) to remove contributions to the signal from STED-induced fluorescence and to isolate our target exciton population.

**pump + STED2**

This pulse combination involves blocking the STED1 pulse, and it is an important control measure to ensure that our interpretation of the migration observable is valid. In many circumstances, we might expect this signal, normalized to the pump-only signal, to be constant in time. One potential concern with this technique is, however, that changes in the signal as a function of the time when STED2 is introduced may be due to changes in its relative quenching efficiency, for example as the exciton distribution redshifts, irrespective of exciton diffusion. In principle, introducing the STED2 pulse at later time delays will similarly quench a greater number of excitons due to their diffusion within the optical quenching boundary imposed STED2. But, because when we block STED1 we do not narrow the distribution of excitons created by the pump, changes in the *relative* spatial profile of the diffraction limited exciton distribution due to diffusion are less significant.

Therefore, the relative signal change over time of $\frac{[\text{pump + STED2}]}{[\text{pump only}]}$ should be strictly smaller than the relative change over time of $\frac{[\text{pump + STED1 + STED2}]}{[\text{pump + STED 1}]}$.

For example, in the investigation of exciton migration in CN-PPV from Ref [116], the TRUSTED data demonstrated a ∼4% change in the NDVF, while the pump + STED2 data showed no change in the NDVF within error. This not only confirms that there are negligible changes to the STED2 pulse's quenching efficiency as a function of time delay, but also illustrates the power of using a sub-diffraction limited initial condition. The initial FWHM in the pump + STED2 condition was ∼280 nm, while the initial FWHM with pump + STED1 + STED2 was ∼85 nm. Using this super-resolved initial distribution rendered the relative change in the spatial evolution of the excitons much more obvious, such that the exciton diffusivity could actually even be measured.

By contrast, in Chapter 5 I will show an example in which the $\frac{[\text{pump + STED2}]}{[\text{pump only}]}$ does change in time, allowing us to use this control measurement in another important way.

**Visualizing signal changes**

To assist in visualizing the effects of the above pulse combinations on the readout for a TRUSTED measurement, Figure 4.23 demonstrates simulations of the integrated signal vs time for three different STED2 time delays. The green trace represents a pump only measurement. It is decaying in time according the exciton's radiative lifetime (in this simulation, 7 ns). The red trace represents a pump + STED 1 measurement. The integrated signal has an initial drop corresponding to the quenching efficiency of STED1. The signal then proceeds to decay at the same rate as the pump only trace. The blue trace represents the pump + STED2 measurement. The signal decays according to the pump only trace, until the arrival time of the STED2 pulse which instigated a drop corresponding to the quenching efficiency of STED2. Subsequently, the signal once again decays per the exciton lifetime. The STED2 time delay is increasing from left to right. Finally, the black trace represents the pump + STED1 + STED2 measurement. There is an initial signal drop present due to the quenching action of STED1 in all three time delays, and at each time delay there is an additional signal drop due to the quenching action of STED2. In each of the three figures, the detector gate is signified by the light grey line 250 ps after the action of the STED2 pulse. For these simulations, the collection duration is only 1 ns (for computational reasons), but for our experiments the it is often 30 - 100 ns in duration.

It is worth pointing out that as we introduce the STED2 pulse at later times, we can just ever so begin to see that the blue trace (pump + STED2) is a bit lower than the red trace (pump + STED1). These simulations also propagate diffusion, so the slightly lower signal in the blue trace is due to more excitons diffusing into the STED2 quenching boundary.

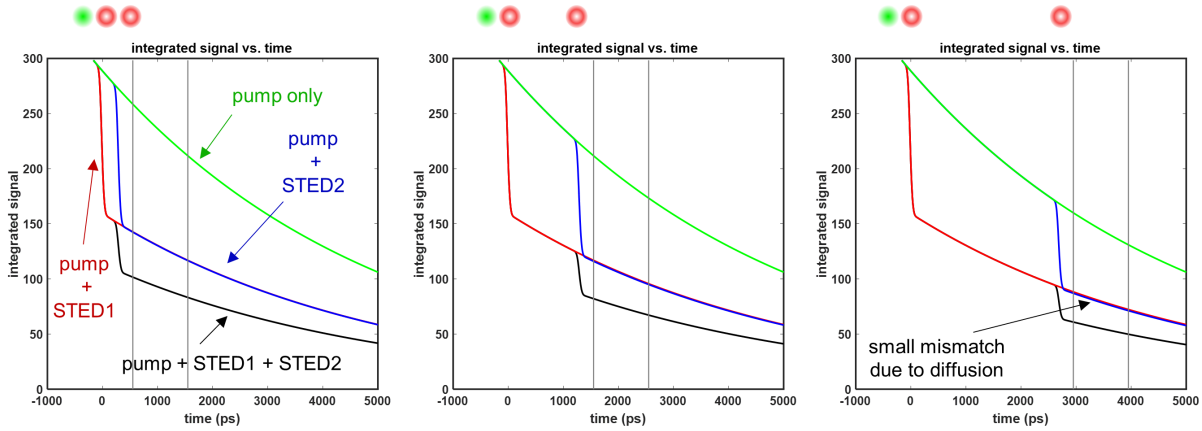


Figure 4.23: Simulations of the integrated signal vs time of the exciton profile in each of the 4 pulse configurations: pump only (green trace), pump + STED1 (red trace), pump + STED2 (blue trace), and pump + STED1 + STED2 (black trace). The thin grey lines represent the detector gate start and finish used in the simulation. The three different plots correspond to three different time delays between STED1 and STED2, with the time delay increasing from left to right.

### 4.4.3 TRUSTED data fitting

The procedure to fit TRUSTED data utilizes a custom fitting function developed previously by Sam Penwell[116]. The fitting function is based on a model of the experiment, and requires 3 inputs: the diffraction limited standard deviation of the pump intensity distribution from measuring its PSF, the standard deviation of the STED pulse intensity distribution from measuring its PSF, and the estimated FWHM of the target exciton population after the combined action of the pump and STED1. We assume the pump intensity distribution is a Gaussian, and the STED pulse distribution is that described by equation 4.8. Figure 4.24 from Ref [116] is a schematic of the key steps involved in the fitting procedure to extract a diffusivity. The first step, (panel a) is to determine the $I_{STED}$ to be propagated throughout the modelled experiment. The actual value of $I_{STED}$ is arbitrary, and it is used as a scaling factor used to determine the appropriate rate of stimulated emission that will narrow the FWHM of the exciton distribution from the diffraction limited pump PSF to the FWHM after the action of STED1. The kinetics of this first step are those outlined in equation 4.1, with the exception that we do not consider the radiative rate ($k_{rel}$) as that is accounted for in the data via normalization. We assume the rates of vibrational relaxation along the ground and excited states is sufficiently fast that there is no signficant repopulatin of the excited state via the STED pulse.

Once the value of $I_{STED}$ is determined, we propagate an exciton distribution that is Gaussian shaped with the specified super-resolved FWHM forward in time via diffusion. At each time delay, the action of the STED2 pulse using the $I_{STED}$ determined earlier is applied. Then, the normalized detection volume fluorescence (NDVF) is calculated by taking the ratio of the exciton population after vs before the action of STED2. This is schematically represented in Fig 4.24b. Both the diffusion of the exciton population and the action of the STED pulses can be described analytically, which renders the simulation more amenable to a fitting scheme in which we may need to iteratively simulate the dynamics many times.

This scheme is then incorporated into a least squares fitting procedure, varying the free parameters until the simulated trace of the NDVF vs time delay best matches the experimental data. One free parameter is the diffusion coefficient, which can either be constant for a strictly diffusive fit or time-dependent and more generally described by a power law ($D(t) = D_o t^{\alpha-1}$, where $\alpha < 1$ represents subdiffusive behavior and $\alpha > 1$ represents superdiffusive behavior). The other free parameter is a constant offset applied to the data to correct the initial value for any imperfection in the experimental pulse profiles.

The uncertainty in the diffusivity extracted from this fitting procedure takes into account the uncertainty of the free parameters, the experimental error, and the fitting residuals using an adapted procedure[221]. (For those seeking a more thorough explanation of this, see the supplementary information of Ref [116] or Ref [216]).

The above treatment assumes that the super-resolved exciton population is Gaussian, which is generally a good approximation if the STED beam mode is donut-shaped. If more exotic transverse modes were used for the depletion beam, then the initial distribution of excitons may be one that does not possess an analytical solution to the diffusion equation.

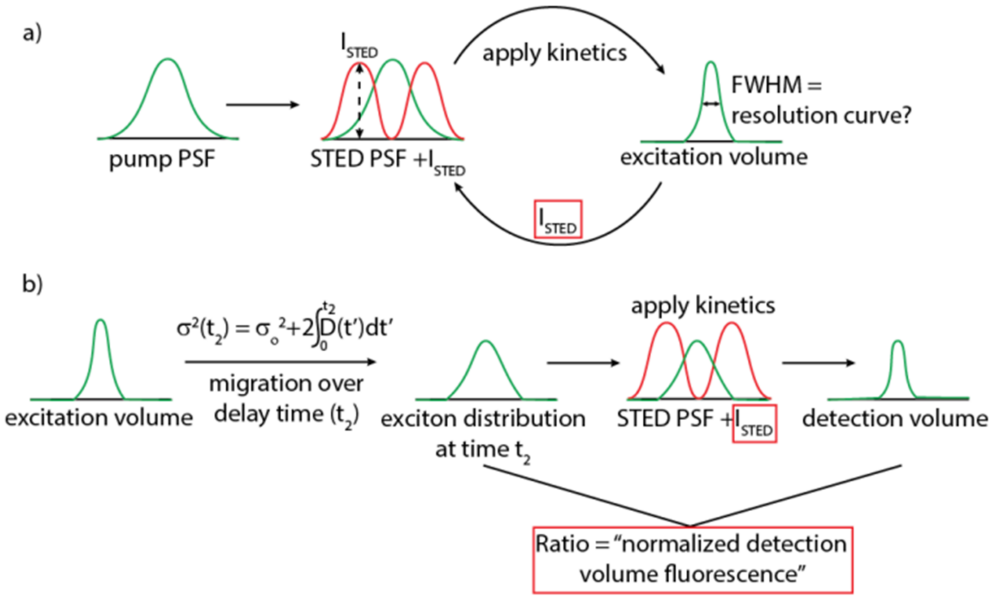


Figure 4.24: Graphical overview of the model used in the TRUSTED data fitting procedure. (a) The fit will scale $I_{STED}$ until the FWHM matches that of the input corresponding to the FWHM of the exciton distribution that remains after the action of pump and STED1. (b) The exciton distribution is then propagated via diffusion and at each STED2 time delay a STED pulse with the same $I_{STED}$ as that determined in (a) is used. The normalized detection volume fluorescence is calculated as the ratio of the integrated exciton volume after and before STED2. Figure adapted with permission from Ref [116].

This would pose an issue for the current fitting procedure, as numerically simulating the diffusion of the exciton population would be very computationally taxing in a least squares fitting scheme.

Typically, the greatest source of uncertainty in the extracted diffusivity lies in the estimation of a particular input parameter: the initial FWHM following the action of STED1. As discussed in Section 4.4.2, for the same diffusivity, a more narrow initial exciton profile will lead to greater relative changes in the NDVF vs time delay curve (i.e., a steeper slope). We therefore perform a measurement on nanoscale fragments of the investigated material, which determines the STED resolution at a series of STED powers. We fit this measurement to the functional form from equation 4.15, examples of which are shown in Figure 4.9. The uncertainty in the fit-generated FWHM at the STED power we use for TRUSTED often determines the lower and upper bound for the diffusivity extracted from fitting TRUSTED data.

## 4.5 Advantages and challenges of TRUSTED

TRUSTED is not the only time-resolved microscopy capable of probing exciton transport in materials[16]. For example, ultrafast transient absorption microscopy (TAM)[222, 223], stroboscopic scattering (stroboSCAT) [117], and time-resolved photoluminescence imaging (TRPL) [39, 224] are a selection of other techniques with the ability to monitor the spatiotemporal evolution of energy carriers. I say energy carriers, because techniques that employ scattering or absorption can also probe non-excitonic species. In light of these and other rapidly emerging techniques with the capabilites to measure exciton transport in materials, it warrants a discussion of what TRUSTED may be able to uniquely offer and similarly what remains challenging for TRUSTED's more general application.

### 4.5.1 Potential advantages of TRUSTED

#### Super-resolution

In principle, techniques that use an optical excitation source to generate energy carriers rely on monitoring a *diffraction limited* distribution. One powerful promise of TRUSTED is its unique ability to controllably narrow the initial distributions of excitons significantly below the diffraction limit (see Section 4.4.1). Let's assume that the exciton profile obeys simple diffusion, then the distribution of excitons $\phi(r,t)$ can be described by the diffusion equation:

$$\frac{\partial\phi(r,t)}{\partial t} = D\nabla^2\phi(r,t), \tag{4.19}$$

where D is the diffusion coefficient. Let's assume that the initial distribution, $\phi(r,t)$ is Gaussian and matches the focal intensity distribution of the excitation source. In many techniques that image the distribution of energy carriers at various points in time after excitation, the standard deviation of a Gaussian fit to the imaged carrier distribution is recorded. The mean - squared displacement, or MSD in one-dimension is typically defined as:

$$\sigma^2(t) - \sigma^2(t_0) = 2D(t - t_0). \tag{4.20}$$

For a given diffusion coefficient, relative changes in the width of the Gaussian profile will be more subtle the larger the initial Gaussian width is. For particularly small diffusivities (e.g. $10^{-4}\text{cm}^2/\text{s}$), a diffraction limited distribution (e.g. $\sim$200 - 300 nm FWHM) will demonstrate only very subtle changes over the lifetime fo the excitation. By narrowing the initial distribution significantly, relative changes in the profile become more obvious. The Laplacian term in equation 4.19 is responsible for this - steeper gradients will erase themselves more quickly. Figure 4.25 plots the results of simulating diffusion for two Gaussian distributions of different initial FWHM one is diffraction limited, and the other is super-resolved, but the same diffusion coefficient.

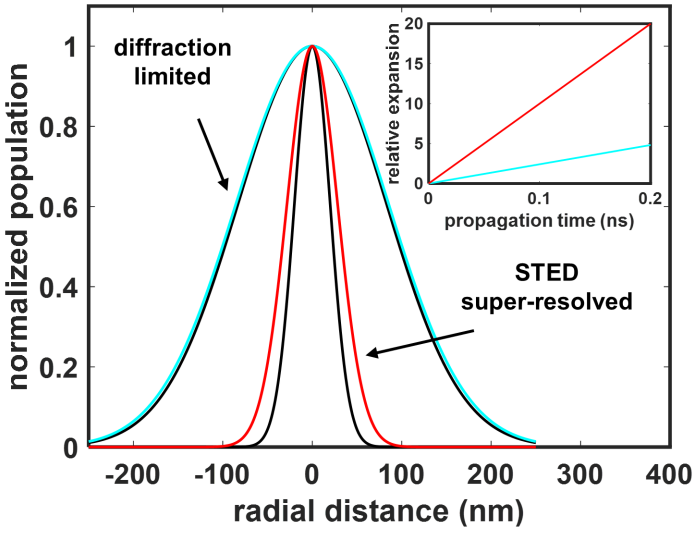


Figure 4.25: Simple simulation of 1D diffusion for a diffraction limited and super-resolved Gaussian with the same diffusion coefficient. The wider black Gaussian evolves to the cyan curve after diffusion over a given time; the narrower Gaussian, the red curve. The inset in the top right represents the relative expansion of the Gaussian width vs time for the diffraction limited (cyan) and super-resolved (red) cases.

We note that that the larger, diffraction-limited Gaussian evolves to the cyan curve in a given time period, while the more narrow STED super-resolved black curve evolves to the red curve within the same amount of time, given an identical diffusivity. Visually, the change in the normalized distribution appears more obvious in the super-resolved case. If we plot the relative expansion width vs time (inset in the top right), we see that the slope of the super-resolved case is steeper than the diffraction limited case. This ability to more sensitively measure migration is, of course, predicated on the assumption that the signal-to-noise ratio of the readout of the remaining exciton distribution after the action of the STED pulse is sufficient.

Another potential advantage of super-resolution is the ability to characterize exciton transport heterogeneity on length scales significantly below the optical diffraction limit (e.g. from ∼250 nm to ∼20 - 40 nm). For instance, grains in polycrystalline perovskite films are often on ∼100 nm length scales[225–227] and the ability to characterize transport within and at the boundary between individual grains in these and other polycrystalline materials would provide invaluable mechanistic insight. Diffraction limited approaches would be restricted to averaging dynamics over multiple grains and their interfaces.

Figure 4.26 is a schematic depicting a “dream” TRUSTED measurement. Suppose that

there is nanoscale heterogeneity present that is obfuscated by a diffraction limited excitation spot size. If we were to measure energy transport with a diffraction limited distribution, we would average the dynamics corresponding to the underlying structure. But, if we were able to super-resolve this structure, not only would we have a better idea of the distribution of material at the relevant nanoscale, but we could selectively probe these regions with TRUSTED to more accurately capture local transport dynamics and more explicitly relate a material's transport properties to its structure.

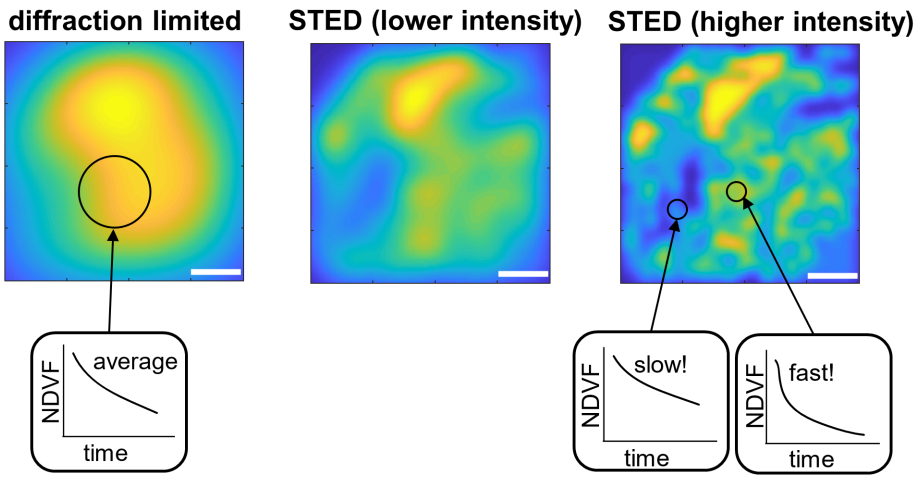


Figure 4.26: Schematic representing the "dream" of a TRUSTED measurement capable of both super-resolving a sample's structure well below the diffraction limit and characterizing transport at various spots in this landscape, something impossible to do in the diffraction limited case. The simulated "material" is composed of a 40x40 grid of point emitters spaced 20 nm apart with random removal sites to generate the heterogeneity. Each emitter in the diffraction limited case contributes a Gaussian intensity distribution of the same amplitude and a FWHM of 200 nm. The FWHM shrinks to 80 nm and 40 nm in the lower and higher intensity STED images, respectively. Scale bars are 200 nm.

Unfortunately, a sample corresponding to this dream scenario never presented itself to me over my time with TRUSTED, which is described in the challenges section.

### Fluorescence based readout

Fluorescence is often referred to as a "background free" measurement, which enables the use of sufficiently low excitation densities to study exciton dynamics in what we refer to as a linear excitation regime. In transient absorption based measurements, changes to the absorption

spectrum sometime require substantial excitation densities in order to become measurable, and as such the dynamics reported by these signatures may be a consequence of non-linear interactions between the sample and the light source or even excitations interacting with one another (e.g. exciton-exciton annihilation).

Similarly, fluorescence/photoluminescence only occurs when an electron and hole radiatively recombine. This provides confidence that changes in our fluorescence signal are a reflection of exciton dynamics. This can arguably be an advantage when absorption/reflection based approaches have multiple convolved contributions in their readout[117, 228], such as excitons, charge carriers, heat, etc. While this sensitivity to only excitons can be advantageous in certain contexts, it similarly limits the scope of samples TRUSTED can study to only those with bright excitons.

### 4.5.2 Challenges for TRUSTED

#### Ideal samples need to satisfy numerous conditions

In order to achieve the "dream scenario" of leveraging the super-resolved excitation spot size outlined in Figure 4.26, a number of conditions must be satisfied. Samples ideal for TRUSTED should possess:

- the relevant photophysics for efficient stimulated emission (see Section 4.3.4)
- the durability to withstand high intensity STED pulses for good super-resolution
- electronic coupling amongst chromophores in the material amenable for exciton transport
- a sufficiently long exciton lifetime (e.g. $> 1$ ns)
- an emission spectrum red enough to access with our STED pulse (720 - 850 nm in our apparatus)
- a sufficiently low amount of STED-induced fluorescence, either via direct or 2 photon excitation

Furthermore, the signal-to-noise ratio in this scenario would have to be substantially better than the experiments I've conducted. The changes in the normalized fluorescence signal due to migration are sometimes only a few percent, and requires at least 14-18 hours of stable data collection, averaging multiple spatial locations to obtain such data. I suspect that the detector/detection scheme would have to be improved to be able to realize this scenario, in addition to addressing the sample that criteria above.

### Current set-up limitations

There are a few challenges associated with the experiment that are related to the set-up in its current state. In principle, these challenges can be addressed with either technology upgrades or reconfiguration of the table optics.

For example, we use a commercial grating stretcher in the STED beam path in order to stretch the pulses to ∼120 ps in time. Because the intensities required for sufficient stimulated emission are high, stretching the pulses in time allows us to lower the peak intensity in an effort to not damage the sample. The stretcher is optimized for 800 nm, and the efficiency of the stretcher output decreases at both shorter and longer wavelengths of 800 nm. The NOPA responsbile for generating the STED beam in our experiment can be tuned from 650 to 900 nm, but the stretcher limits this range to 720 - 850 nm effectively for our experiments (the STED beam power is otherwise too low). We purchased the necessary optics to build a similar grating stretcher that can access bluer wavelengths more efficiently and I would recommend the next user implement this upgrade.

The time-delays between STED1 and STED2 are currently using an optomechanical delay line. This limits the dynamic range we can study to ∼3 ns. In order to study dynamics beyond the first 3 ns after the creation of excitons, one has to increase the STED2 pathlength relative to STED1, which we do for TRUSTED measurements in Chapter 5. Here, we insert a mirror in the STED2 path after the first polarizaing beam splitter cube (see Section 4.3.5) and send the beam for a 'walk' corresponding to 2 ns. This allows us to probe a dynamic range ∼1.7 - 4.8 ns after the action of the pump pulse. Such a workaround still requires multiple, separate measurements and later post-processing of the data. If there were a way to implement an electronic delay, so that STED2 could arrive at much later times than STED1 (e.g. 10 ns), this would permit characterizing dynamics more carefully in systems where the exciton lifetime is comparatively longer than organic systems, as is the case for quantum dots.

### Sample thickness

This issue is not strictly limited to TRUSTED alone. Probing 3D diffusion of carrier transport in materials is often an additional challenge for ultrafast microscopy techniques. Moreover, if the sample is much thicker than the focal depth of the microscope (e.g. ∼250 - 500 nm), then contributions to the signal from beyond the focal plane can contribute to the background. So to generally avoid the higher background, sample thicknesses are typically kept below the 100s of nm range. Such thin materials are often more fragile and susceptible to photodamage.

### Fitting model assumes isotropic transport

Our ability to extract a diffusivity is predicated on the assumption that an initial Gaussian shaped distribution is evolving in time according to a kinetic model we specify. This fails to capture more nuanced dynamics, like anisotropic transport within the material, which is often

readily available information when generating sequential images of exciton transport[229–231]. There are potentially solutions to this, like using the 1D STED beam profile (Section 4.3.2) to selectively quench excitons migrating along a given axis and then comparing to the measured diffusivity as a function of rotating the 1D STED PSF in the plane of the sample.

## 4.6 Examples of TRUSTED attempts on organic samples

This section will very briefly present a few of the samples we preliminarily investigated with TRUSTED before moving on to the Te-doped CdSe/CdS quantum dot superlattice, which is the focus of Chapter 5. These examples will demonstrate some of the challenge associated with TRUSTED and the care that must be taken when selecting samples.

### 4.6.1 Polycrystalline PDI thin films

Perylene diimide (PDI) molecules are a promising class of organic semiconductors. Simple synthetic functionalizations of a PDI molecule's imide position enables tuning the slip angle formed between individual PDIs in a crystalline solid and thus results in control over the nature and degree of intermolecular orbital overlap. Previous work by the Roberts group using a prototypical series of PDIs demonstrated that the singlet-fission rate can be optimized by inducing a particular slip distance (∼3 Å) along the long axis of the PDI molecule[24]. Although not sensitive to optically forbidden triplet species, we sought to use TRUSTED to measure the diffusivity of singlet excitons in such films to complement investigations of singlet-fission. PDI configurations optimal for producing triplet excitons via singlet-fission may not necessarily be optimal for transport of excited state species, so understanding structural paradigms that sufficiently balance both is critical. Figure 4.27 is a schematic representing how the electronic properties of PDI films can be tuned via the short and long axis slipping angles as well as the interchromophore distance between PDI molecules.

Our collaborator in the Roberts group at UT Austin, Cam Li, prepared polycrystalline films of a novel PDI derivative, also synthesized by the Roberts group. Unfortunately, attempts to super-resolve small, isolated fragments of the PDI films with even modest STED pulse energies were unfruitful due to sample bleaching. We found that the photobleaching due to the STED beam was less severe when applied to a film that contiguously spanned 100s of microns. This may suggest that heat deposited by the STED pulse can more efficiently diffuse away in the case of a film, but with small islands the heat build-up is more locally concentrated.

Although we did not obtain a resolution measurement after the action of pump and STED1, and therefore did not know the FWHM of the initial exciton distribution in our measurements, we attempted TRUSTED measurements to verify if the data we obtain could conceivably represent exciton migration. Figure 4.28 represents a series of TRUSTED measurements acquired with different detector gate-on times relative to STED2. Recall from

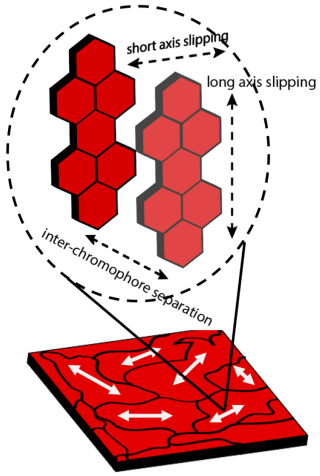


Figure 4.27: Schematic rendering of a PDI film, where the film's properties are determined by the short and long axis slip angles, as well as the interchromophore distance, of the constituent PDI molecules.

Section 4.4.2 that we can turn our detector on at a specific time relative to the arrival of STED2 at each time delay. Because the lifetime is relatively short in this sample, $< 2$ ns, we initially used a detector gate-on time of 0.5 ns after the arrival of STED2 to maximize the signal detection. The TRUSTED data, shown in the top row, initially seems promising as there is an overall downward trend in the NDVF as a function of time-delay. Inspection of the pump + STED2 and pump + STED1 measurements, however, reveal concerns. As discussed, in Section 4.4.2, the pump + STED1 data should nominally be constant with time-delay, and in cases where it is not there is concern that the exciton lifetime is not adequately accounted for. Furthermore, the data in the pump + STED2 measurement appear to be trending downward at an almost equivalent rate as the data in the TRUSTED dataset. If the change in the TRUSTED data were due strictly to migration, then the pump + STED2 data may only change by a smaller magnitude to corroborate this.

Peculiarly, we note that as we increase the detector gate-on time (right 3 columns of Fig 4.28), there appear to be systematic changes in the trends of each TRUSTED, pump + STED1, and pump + STED2 measurement. As the gate-on time increases from 0.5 to 1 ns, the downward trends in the 3 datasets become less prominent, but from 1 ns to 1.5 ns we observe the data at later time delays actually begin to increase relative to early times. This is particularly so in the pump + STED1 measurement. From 1.5 to 2 ns, we note

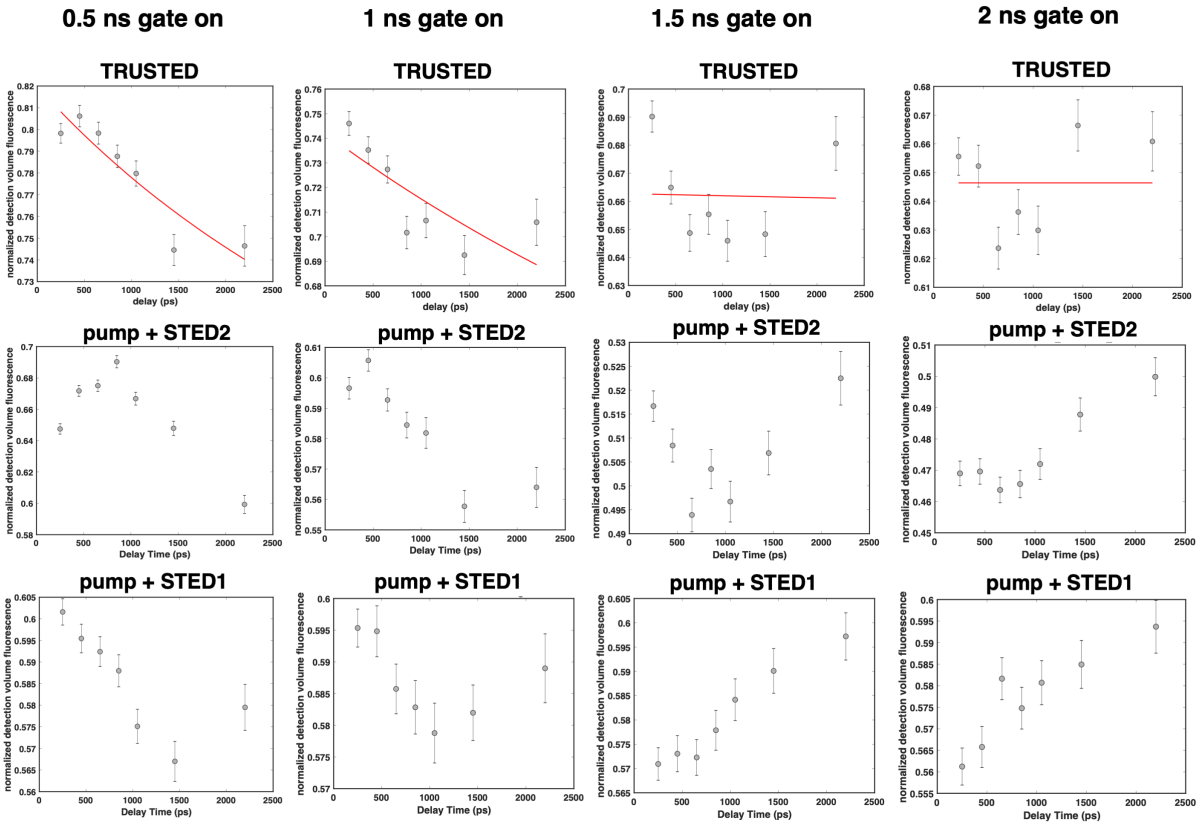


Figure 4.28: TRUSTED, pump + STED1, and pump + STED2 datasets of a PDI film at various detector gate on times. Each experiment with a different detector gate on time was conducted with the same pump and STED pulse characteristics - spectra, power, and PSF. The red traces in the TRUSTED data are fits assuming an arbitrary FWHM - we are unable to extract an actual diffusivity from these data.

that a trend in the TRUSTED data becomes less prominent, and both the pump + STED2 and pump + STED1 measurements trend upwards. (Note, the data become systematically noisier as we increase the gate-on time, as we're progressively rejecting a greater number of emitted photons).

Clearly, there are complicating photophysics present in this PDI film that render interpreting exciton migration challenging. One speculation regarding the varying TRUSTED trends is that there are multiple excited state species present with different lifetimes, but they vary in their response to the STED pulses. In other words, the quenching efficiencies of each excited state species are different, and as we change the detector gate-on time, we

bias our detection more towards the species with the longer lifetime.

#### Numerical simulations of TRUSTED experiment

To obtain a qualitative handle on the effect of having two different excitation species present in TRUSTED, we turn to numerical simulations of our TRUSTED experiment. The simulation assumes the distribution of excitons created by the pump pulse is composed with two different species. One species possesses a lifetime of 500 ps, contributes 60% amplitude to the distribution, and cannot be quenched via STED. The other species has a lifetime of 2000 ps, contributes 40% amplitude to the distribution, and can be quenched via STED. Figure 4.29 summarizes the simulation results for a given STED pulse power at 0.25 ns and 2 ns gate-on times. We simulate the experiment in both the case where excitons may diffuse with some diffusivity (filled data) and the case where excitons are stationary (open data).

The simulation results emphasize a few key concepts. One is that the magnitude of the change in the data points is different between the two different gate-on times (note that the axis ranges are smaller in the 2 ns gate on condition). Second, even in the case with no diffusion, we observe a downward trend in the TRUSTED and pump+STED2 curves! The time-dependent change in the data values corresponding to no diffusion become less prominent in the 2 ns gate-on condition, but this still raises the point that if our system is composed of multiple excitations with unique stimulated emission cross-sections, the TRUSTED data are not a strict reflection of migration. In fact, when comparing these simulations to our TRUSTED measurements in Figure 4.28, we note that as we increase the gate on time, the downward trends in the data become less prominent between 0.5 and 1 ns. The simulations do not, however, capture the emergence of the upward trending data at longer gate-on times, which may be the result of a third excitation species or other photophysics.

### 4.6.2 P3HT polymer films

P3HT (Poly(3-hexylthiophene-2,5-diyl) is a well studied polymer in the field of organic semiconductors. It has demonstrated high exciton and charge mobilities[232, 233] and, as a semicrystalline polymer, it exhibits different properties in the amorphous and crystalline state[3, 234]. In fact, one of the proposed future directions for TRUSTED after its first demonstration with CN-PPV was to investigate regio-regular (more crystalline) and regio-random (more amorphous) P3HT films to further understand how the different structural order and energetic landscapes lead to higher exction diffusion lengths in regio-regular P3HT[116].

To begin, we first tested whether disordered fibers of regio-regular P3HT that has been crashed out from solution (pipetting a small volume of the dissolved polymer into water, in which P3HT is insoluble) were amenable to our STED imaging set-up. Figure 4.30 is a darkfield image of such P3HT fibers of varying lengths.

We then proceeded to image these fiber-like structures with a 2 nW pump (540 nm) and 50 uW (760 nm) STED beam (powers measured at the sample plane), an example of

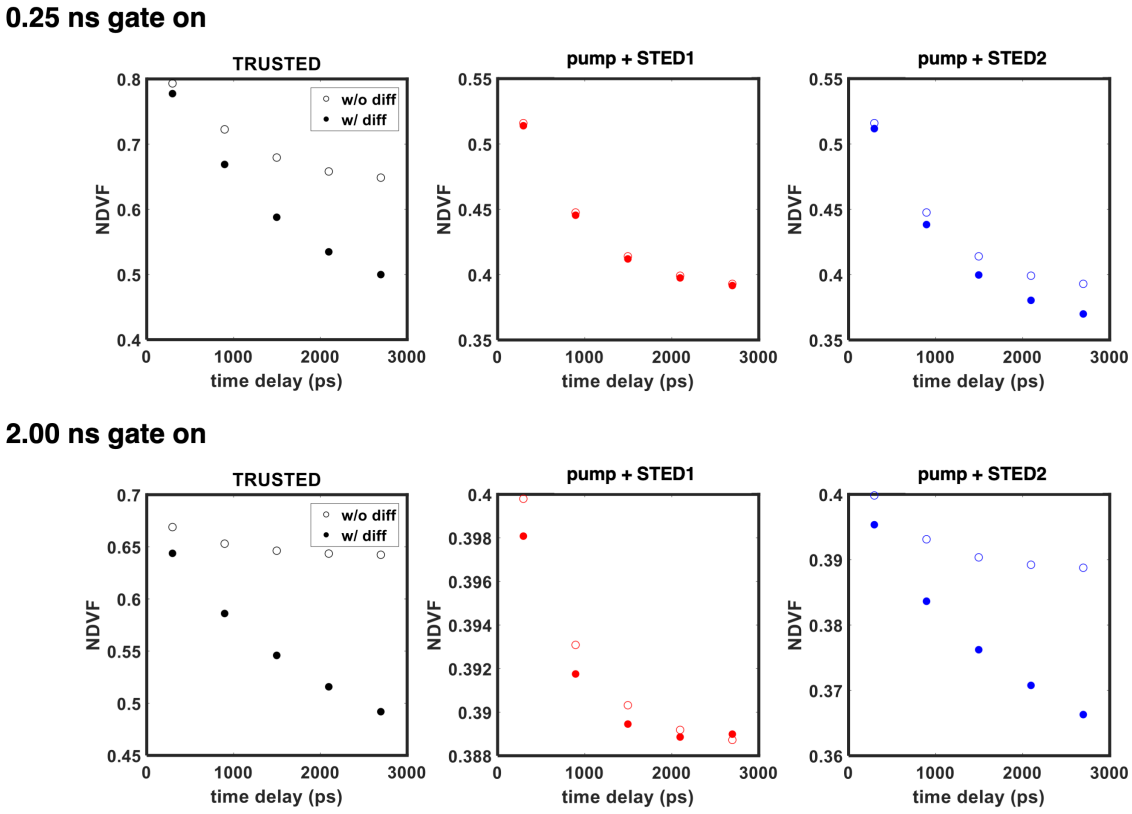


Figure 4.29: Numerical simulations of the TRUSTED experiment with a distribution of excitations composed of two different species. One species contributes 60% to the distribution amplitude, has a lifetime of 500 ps, and cannot be quenched by the STED pulse. The other species contributes 40% to the distribution amplitude, has a lifetime of 2000 ps, and can be quenched by the STED pulse. Simulations generate data corresponding to the TRUSTED, pump + STED1, and pump + STED2 measurement assuming the excitons can diffuse with some constant diffusivity (filled points) as well as assuming the excitons are stationary (empty points). We perform these simulations for a detector gate on time of 0.25 ns (top row) and 2.0 ns (bottom row).

which is shown in Figure 4.31. Visually, it seems as though the features in the modulated excitation STED image are relatively thinner than in the diffraction limited case, but these images are not ideal for quantitative resolution assessment given the relatively large pixel size (100 nm). Unfortunately, this size of a field of view (5x5 microns$^2$) and pixel size were the best conditions we found for modulated excitation imaging. Attempts to zoom-in and

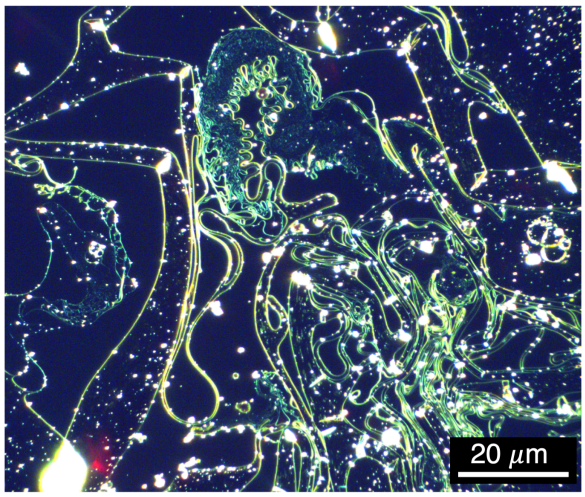


Figure 4.30: Darkfield image of regio-regular P3HT fibers deposited on a glass substrate.

measure the resolution using finer pixel sizes led to irreversible sample warping under the STED pulse before image acquisition could be completed.

Despite being unable to use nanoscale regio-regular P3HT objects as resolution targets, we tried TRUSTED with spincoated films to see if we could observe migration. The results were surprising and admittedly confusing. Strikingly, under the action of the STED pulses, the fluorescence from the spatial locations we investigated appeared to increase relative to before we began an overnight TRUSTED measurement. Figure 4.32 is a fluorescence image of the sample taken after the TRUSTED measurement, where one can actually see enhanced fluorescence signal in the shape of the STED donut PSF in each of the investigated spots within the film. Also, the tracks of the Piezo stage movement pattern we program to sample spot-to-spot are imprinted. My speculation is that the STED pulse thermally annealed out either the local crystallinity or residual solvent, both of which could lead to removal of excitonic trap states.

The data corresponding to this experiment did not yield a clear migration observable. The TRUSTED data set appears flat within the experimental noise. But more concerning is the systematic trend in the pump + STED1 and pump + STED2 trends. The increase at each time delay of the NDVF of pump + STED1 suggests the lifetime is not appropriately accounted for in the measurement, which is perhaps unsurprising given how short P3HT's lifetime is (∼600 ps) relative to our time resolution (∼120 ps). The increasing pump + STED2 could be a related issue to the lifetime, or this could suggest some time-dependent

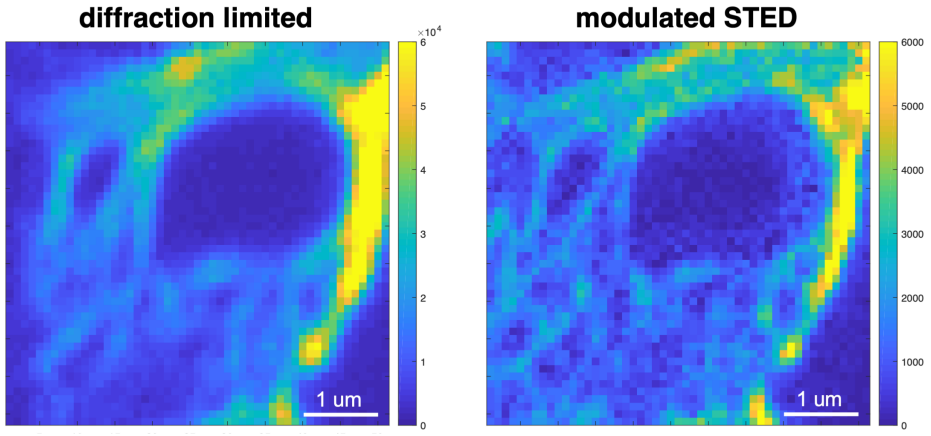


Figure 4.31: Diffraction limited (left) and modulated excitation STED (right) images of regio-regular P3HT fibers.

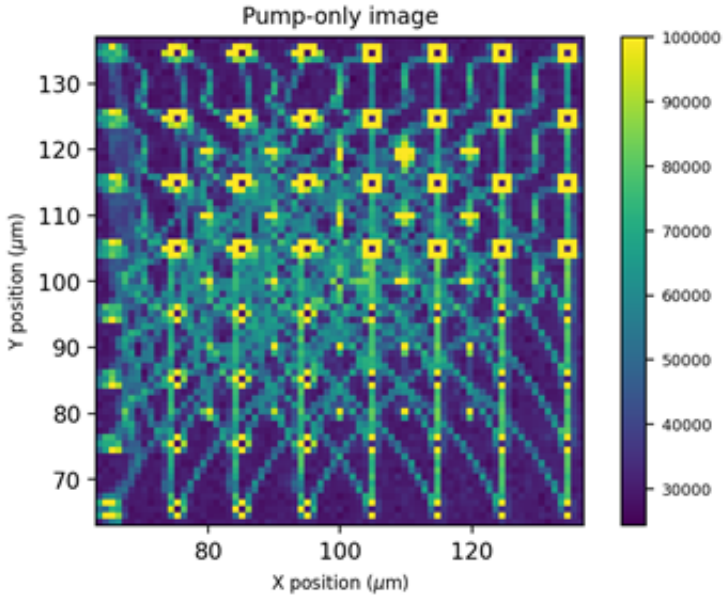


Figure 4.32: Pump only fluorescence image of a spincoated regio-regular P3HT film after a TRUSTED measurement.

quenching efficiency, where as we introduce STED2 at later times its ability to quench P3HT excitons is reduced, owing to the spectral evolution in the sample.

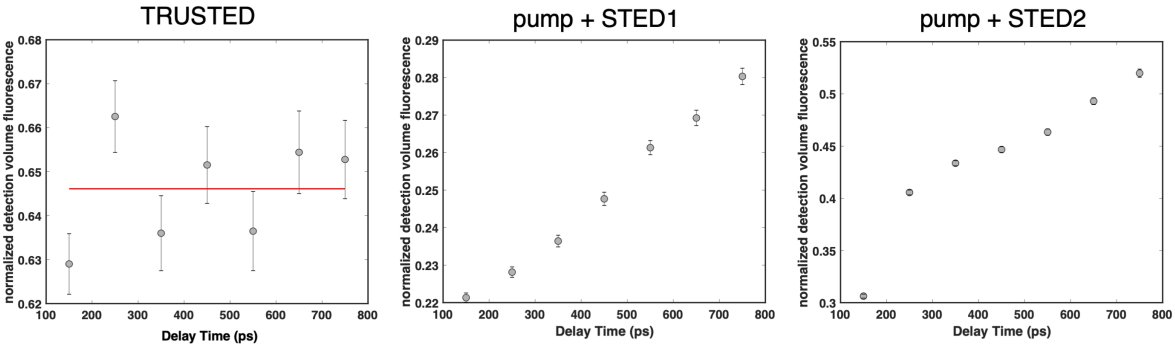


Figure 4.33: TRUSTED, pump + STED1, and pump + STED2 datasets for a P3HT spin-coated film.

## 4.7 Conclusion

STED microscopy is a potent super-resolution imaging technique that takes advantage of both the nonlinear saturation of the stimulated emission of chromophores from their excited to ground state as well as a donut-shaped transverse beam mode. Applying STED microscopy to systems of electronically coupled chromophores bears challenges that, to some degree, can be overcome with modulated excitation, as demonstrated with conjugated polymers, quantum dots, and fluorescent dye crystals. TRUSTED brings STED super-resolution imaging into the ultrafast frontier, and leverages the optical quenching boundaries of STED pulses to spatiotemporally monitor exciton migration. The super-resolving capabilities of TRUSTED make it sensitive even to very small diffusivities, but there are certain challenges in applying this approach to any given material with electronically coupled chromophores. TRUSTED involves a number of pulse sequence permutations that help determine whether our data exclusively represent exciton diffusivity or not, and this proved useful in deducing that systems bearing complex photophysics, like P3HT and polycrystalline PDI films, will require adapting the current TRUSTED approach in order to isolate signatures of exciton migration. We did, however, find success in applying TRUSTED to measure exciton migra-

tion in Tellurium doped CdSe/CdS quantum dot superlattice monolayers, which is the focal point of the following chapter.

# Chapter 5

# Characterizing Non-equilibrium Exciton Transport in Te-doped CdSe/CdS Quantum Dot Superlattice Monolayers

The content presented in this chapter is, at the time of this writing, still an ongoing investigation. The hypotheses, analyses, and speculations of the accumulated data presented herein reflect our current assessment of the project but are potentially subject to change. This work is a highly collaborative endeavor. **Rongfeng Yuan** and I worked together with the TRUSTED apparatus and each performed various spectroscopic characterizations of the samples and as well as simulations. **Rafaela Brinn** (Alivisatos group) synthesized all quantum dots, prepared the superlattice films, and performed various characterizations of the quantum dot quality and superlattice formation.

## 5.1 Introduction

Colloidal Quantum dot (QD) nanocrystals are highly tunable building blocks for next generation solid-state devices, like displays[235–237], lasers[238], or solar cells[239–245]. By virtue of changing their size, the emission spectra of QD nanocrystals can be tuned owing to the quantum confinement nature of the exciton, aptly analogous to the particle in a box model. Exciton transport is a critical process for the function of many solid QD devices, albeit in different ways. For example, light harvesting architectures are designed with the intention for long range exciton migration for efficient charge collection. Yet, QD solids in display applications ideally have little-to-no exciton transport to prevent photoluminescence losses, where bluer emitting QDs will transfer their energy to redder emitting acceptors prior to emission (or even transfer to quenching sites)[237]. Thus, strategies that afford control over exciton migration improve our ability to tailor QDs for specific applications.

QD solids are typically prepared by dropcasting or some other solvent evaporation techniques, but such methods often result in spatially disordered QD films. Another important consideration in preparing ordered QD solids is nanocrystal size polydispersity, which affects both the energetic and spatial disorder. Provided their size distribution is sufficiently narrow, colloidal quantum dots can readily assemble into crystalline superlattices[246]. Superlattices are sometimes referred to as "artificial solids" because the nanocrystals take the place of a hypothetical atom in a traditional crystalline lattice. Superlattice systems have been developed and leveraged extensively over the past 20 years because of their predisposition as excellent model systems to explore material properties, like thermal and electronic transport [247]. In this study, the high degree of spatial order present in superlattices provides a platform to isolate the effects of energetic disorder on exciton transport, which is traditionally coupled to spatial disorder owing to the relationship between QD size and bandgap.

A commonly sought design principle for QD solids is a so-called energy "gradient," which spatially arranges QDs such that their bandgap energies go from high-to-low as a function of a given spatial coordinate. Such a design promotes directional exciton transport, as transfer from higher to lower bandgap QDs is favored. These gradients can be formed through layer by layer deposition of films composed of QDs of different sizes[248–251], but using different sized QDs renders preserving the high degree of spatial order present in superlattices challenging. Towards this end, isovalent atomic doping of QDs enables control over their optoelectronic properties[30, 31, 252–254], without perturbing the nanocrystal's size and shape, and, consequentially, their arrangement with respect to other nanocrystals in a QD solid. The role midgap states (that result from dopants) play in charge transport has been explored in the context of QD solids [245, 255], but herein we seek to understand the role isovalent atomic dopants play in modulating exciton migration.

In this study, we measure the exciton transport dynamics in Tellurium-doped CdSe/CdS (CdSe:Te/CdS) core-shell quantum dot superlattices (QDSL) using a combination of transient microscopy (TRUSTED, described in Chapter 4) and time-resolved emission spectroscopy (TRES), which allows us to characterize the spatial and spectral evolution of exciton transport, respectively. We complement these measurements with single-particle emission spectroscopy of both doped and undoped particles to explicitly characterize the intrinsic and inhomogeneous spectral contributions. We find evidence for non-equilibrium exciton transport within CdSe:Te/CdS superlattice monolayers, and our results suggest that excitons in doped systems that can participate in energy transfer possess competitive diffusivities within the earliest timescales of their non-equilibrium transport. Our study suggests better control over the distribution of dopants among QDs will prove necessary in order to minimize energy loss. Furthermore, more precise doping levels could enable systems with well-defined energy gradients to take advantage of the observed high initial diffusivities in excitons' non-equilibrium transport from higher to lower site energies.

## 5.2 Background: QD Material Properties and Sample Characterization

### 5.2.1 Core-shell quantum dots and band engineering

Core-shell quantum dot architectures have been extensively explored owing to their rich optoelectronic properties. One can exquisitely tune the band structure of a given QD via the selection of core and shell materials[256–259]. Additional control over the QD's band energies is determined by the relative and absolute sizes of core and shell material[260]. Depending on the relative energy levels of the core and shell materials' valence and conduction bands, the electron and hole wavefunctions of an exciton may sample different regions of the QD's space. Core-shell QDs can be classified as: Type I, where both the valence and conduction band of the core material are lower in energy than the shell material, strongly localizing both electron and hole wavefunctions to the core, Inverse Type I, where the shell material has lower energy valence and conduction bands than the core, leading to localization of electron and hole to shell, and Type II, where the valence band of the core material is at a lower energy than that of the shell but the conduction band of the shell material is at a lower energy than core, leading to localization of the hole to the core but localization of the electron to the shell. Finally, in a quasi-Type II band alignment, the valence band of the core material is at a lower energy than that of the shell, but the conduction bands of the core and shell material are energetically close enough such that the material mismatch poses a small-to-negligible barrier for the electron wavefunction. Thus, the electron can be delocalized across the extent of both core and shell.

Figure 5.1, from Ref [258], shows the relative energy differences between the valence and conduction bands of CdS, CdSe, and CdTe materials resulting from first-principle calculations. CdSe/CdS core-shell quantum dots are an example of a quasi-Type II band structure and have a wide array of applications, such as imaging[261, 262], lasing[238], solar cells[263], and more. CdSe/CdS QDs have demonstrated enhanced photostability and exceptional brightness, with recent measurements demonstrating they can reach near unity photoluminescence quantum yields[9]. The hole wavefunction is strongly localized to the CdSe core, while the electron wavefunction is delocalized over the extent of the CdSe core and CdS shell, schematically represented in Figure 5.2.

### 5.2.2 Isovalent Te doping lowers the bandgap energy of CdSe/CdS QDs

In addition to the selection of core and shell materials, atomic doping of QDs enables further control over their optoelectronic properties[30, 31, 252–254]. Dopants enable the transformation of a nanocrsytal's optoelectronic properties without perturbing the nanocrystal's size, shape, or arrangement to other nanocrystals in a QD solid. This is a potentially powerful design tool as traditionally in order to achieve specific optical characteristics, such as PL

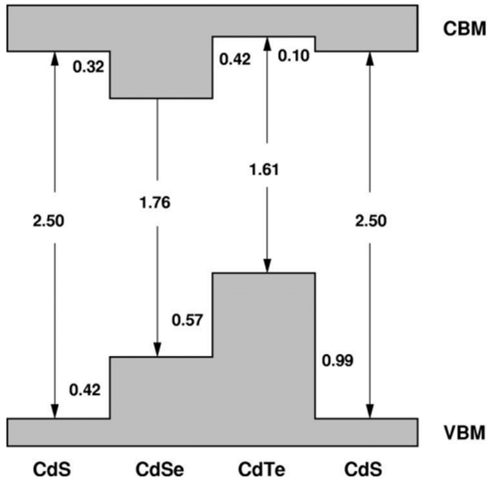


Figure 5.1: Energy differences (in eV) between valence and conduction bands of CdS, CdSe, and CdTe materials as well as their respective offsets from one another. Reprinted from ref [258] with permission.

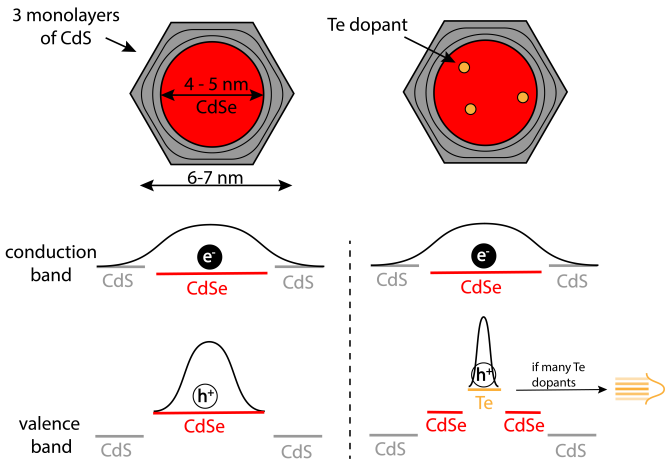


Figure 5.2: Schematic overview of CdSe/CdS core-shell quantum dots and their band structure with and without Te dopants. Without Te, the hole wavefunction is localized to the CdSe core, while the electron is delocalized out to the shell. With Te, the hole wavefunction is further localized to the Te dopants, resulting in a smaller bandgap energy, and provided there are many Te dopants, a density of Te dopant states may form.

spectra, one has to change the size of the nanocrystals in question. This chapter focuses on the role Te dopants play in modulating the exciton transport properties of Te-doped

CdSe/CdS QD superlattices, in particular.

Isovalent doping of CdSe matrices with Te leads to a pronounced redshift and broadening in the emission profile of the nanocrystal[32, 264]. We hypothesize that the Te dopants are incorporated into the CdSe/CdS band structure such that the effective bandgap energy is decreased. While much of the literature concerning Tellurium doping of CdSe proposes that Te dopants are hole trap sites that introduce midgap states, this is inconsistent with the spectra we measure, presumably because Te should couple to the Cd atoms within the CdSe matrix. Te dopants effectively lower the energy of the valence band[32]. The timescale of hole transfer from CdSe to Te is typically less than 1 ps[265], which, for the purposes of our fluorescence-based measurements, is effectively instantaneous. Figure 5.2 schematically represents the changes to the CdSe/CdS energy diagram upon addition of Te dopants. One hypothesis put forth by Franzl et. al. is that upon addition of multiple Te dopants a density of states can be formed[264], and as each Te incorporated into the band structure will slightly differ in relative energy, this can lead to substantial broadening of an individual QD's emission spectrum.

### 5.2.3 CdSe:Te/CdS QDs

Te-doped CdSe/CdS core-shell quantum dots, synthesized by our collaborator **Rafaela Brinn** in the Alivisatos group at Berkeley, were prepared using a previously reported protocol. The nanocrystals are synthesized colloidally with 5% (as well as 2 and 7%) Te doping stoichiometrically added during the seeded growth synthesis of wurtzite CdSe and grown ∼4 - 5 nm in diameter. Layer-by-layer shell growth is then performed resulting in a thin 3 monolayer CdS shell, ∼1 - 2 nm thick, grown around the CdSe:Te core, yielding nanoparticles ∼6-7 nm in diameter. Finally, the nanocystal surfaces are passivated with a combination of oleic acid and oleylamine ligands for stability.

The shapes of the nanocrystals, once the CdS shell growth is complete, are similar to a hexagonal prism. The nanocrystal in the $XY$ plane has an approximate diameter of 7-8 nm while a 4-5 nm diameter in the $Z$ plane. Figure 5.3 shows a schematic representation of these nanocrystals in 3D. Note that this is a cartoon representation to help visualize the constituent components of the QD, but there is actually NO free volume between the CdSe core and CdS shell interface. The hexagonal prism shape of these nanocrystals could facilitate the ordered packing requisite of superlattice formation, and furthermore increases the relative surface area interactions between adjacent QDs.

### 5.2.4 Steady-state absorption and emission spectra of CdSe/CdS and CdSe:Te/CdS QDs

Steady state absorption and emission spectra verify the successful incorporation of the Te dopants within the CdSe matrix, shown in Figures 5.5 and 5.4. The absorption spectra of undoped CdSe/CdS and doped CdSe:Te/CdS systems are shown as solid curves and their PL

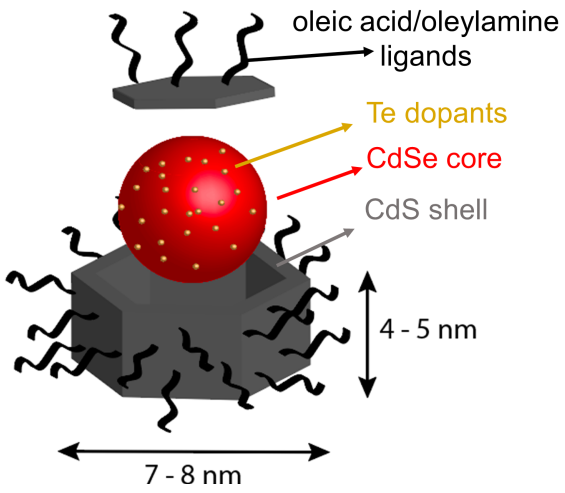


Figure 5.3: Schematic of the 3D shape of our CdSe:Te/CdS quantum dots.

emission are shown as dashed curves. The absorption spectra are scaled to aid in comparison, and the emission spectra are normalized to their peak emission intensity.

It is important to mention here that the 2% and 7% Te-doped systems were developed at a later date using a newly synthesized batch of nanocrystals. While we include the spectral characterization of the 2% and 7% systems to provide a sense of the effects of the Te-doping concentration in our system, we have some concerns about the relative quality of superlattice formation using characterization discussed in the following section. Figure 5.4 presents the same absorption and emission spectra as presented in Figure 5.5, but with only the undoped and 5% doped systems for clarity, as the 5% doped system is our primary sample focus for transport measurements.

The undoped QD solution PL emission peaks at ∼632 nm, and the doped emission profiles peak at ∼646 nm, ∼632 nm, and ∼648 nm for the 2, 5, and 7 % Te doping, respectively. In addition to the redshift of the emission profiles of the doped QDs, the width of the doped emission spectra are substantially wider. The FWHM of the undoped CdSe/CdS QDs in solution is ∼21 nm (∼65 meV), and for the doped profiles, ∼53 nm (∼155 meV), ∼92 nm (∼280 meV), and ∼100 nm (∼284 meV) for the 2, 5, and 7 % Te doping, respectively.

When measured in the superlattice solid-state, the PL emission of all 4 systems redshift. The undoped QDSL PL emission peaks at ∼634 nm, and the doped emission profiles peak at ∼645 nm, 646 nm, and 670 nm for 2, 5, and 7 % Te doping, respectively. The FWHM of the undoped QDSL emission profile is ∼24 nm (∼72 meV), and for the doped profiles, ∼56 nm (∼159 meV), 86 nm (∼247 meV), and 96 nm (∼264 meV) for 2, 5, and 7 % Te doping, respectively. We observe that although the emission peak changes very little between the 2

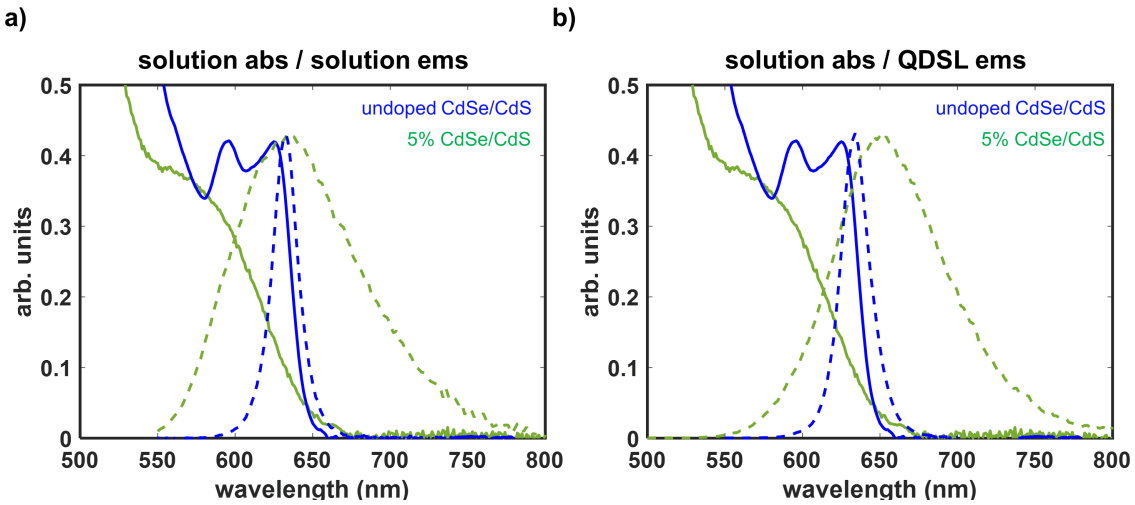


Figure 5.4: Steady state absorption and emission spectra of just undoped and 5% doped systems. (a) Solution absorption and solution emission. (b) Solution absorption and superlattice emission.

and 5% Te doping conditions, there is a substantial change in the breadth of the emission profile. Note that this comparison is made cautiously given the different nanocrystal batch synthesis.

The absorption spectra are also dramatically altered with varying Te dopant concentration. We note a blueshift of the first excitation peaks in the absorption spectra between the undoped, at ∼625 nm, and the 2% doped, at ∼613 nm. The well-defined absorbance peaks present in the undoped and 2% systems are comparatively "smeared" in the 5 and 7%, rendering the assignment of first excitation peaks less obvious. If we fit the absorption profile of the 5 and 7% spectra with the a sum of 2 Gaussians, one to capture the redder shoulder and one to capture the absorption progression in the blue, we obtain a peak of ∼586 nm for the first excitation peak of both 5 and 7% doping. By defining the apparent Stokes shift as the energy difference between the first excitation peak in the absorption spectrum and the emission peak in the QD solution PL profile, then we observe a Stokes shift of approximately 9 nm (28 meV) for the undoped system, and approximately 42 nm (103 meV), 46 nm (153 meV), and 62 nm (202meV) for the 2, 5, and 7% systems.

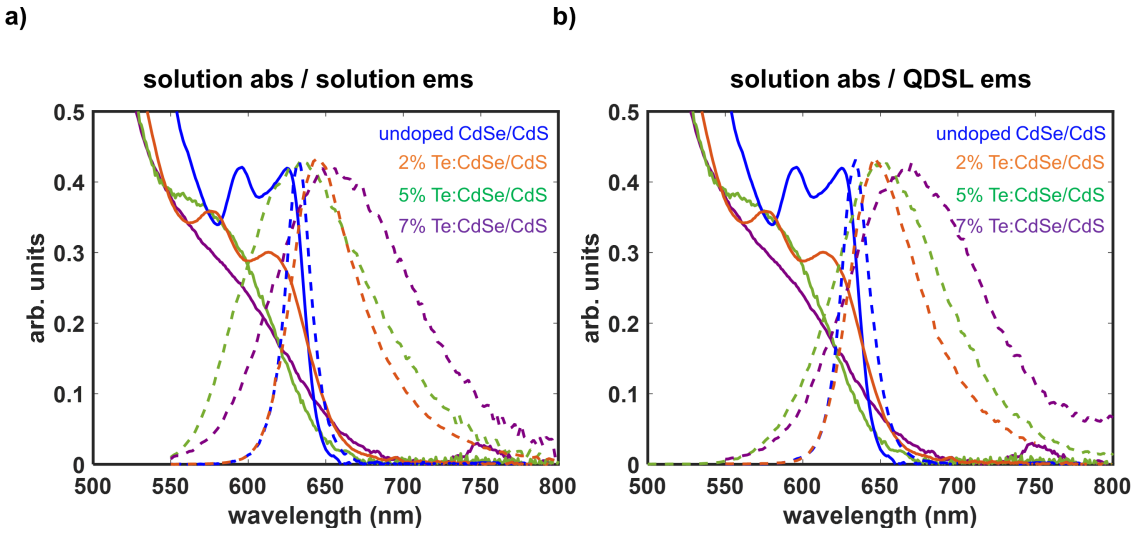


Figure 5.5: Steady state absorption and emission spectra of undoped and 2, 5, and 7 % Te-doped CdSe/CdS QDs. (a) Absorption and emission spectra of all 4 systems, collected in hexanes solution. (b) The same solution absorption spectra as (a), but the emission spectra are collected from the superlattices of all 4 systems.

### 5.2.5 Te-doped CdSe/CdS QDs form highly ordered superlattices

Once synthesized, CdSe:Te/CdS QDs are self-assembled into a highly ordered hexagonal superlattice structure using a liquid subphase method[266, 267]. Briefly, the QDs are soluble in a non-polar solution phase floating atop of a polar solvent in a Teflon well. As the non-polar solvent evaporates, the QDs gradually merge closer to one another due to the reduction in the non-polar solvent free volume, and eventually this leads to ordering in a close-packed hexagonal superlattice film. Films may then be "scooped" out of the Teflon well onto a desired substrate, such as a TEM grid or glass microscope coverslip.

Verification of quality superlattice formation is conducted through a few key imaging characterization tools.

#### TEM

Transmission electron microscopy (TEM) enables imaging each individual nanoparticle in a superlattice monolayer. Figure 5.6 is a representative TEM image from a superlattice of 5 % doped CdSe:Te/CdS QDs, where there is notable long-range (∼500 nm) ordering of QDs.

Figure 5.7b shows an image where each QD of the imaged superlattice is false colored by the magnitude of the single particle hexagonal bond order parameter ($|\Psi_{6,j}|$) generated by

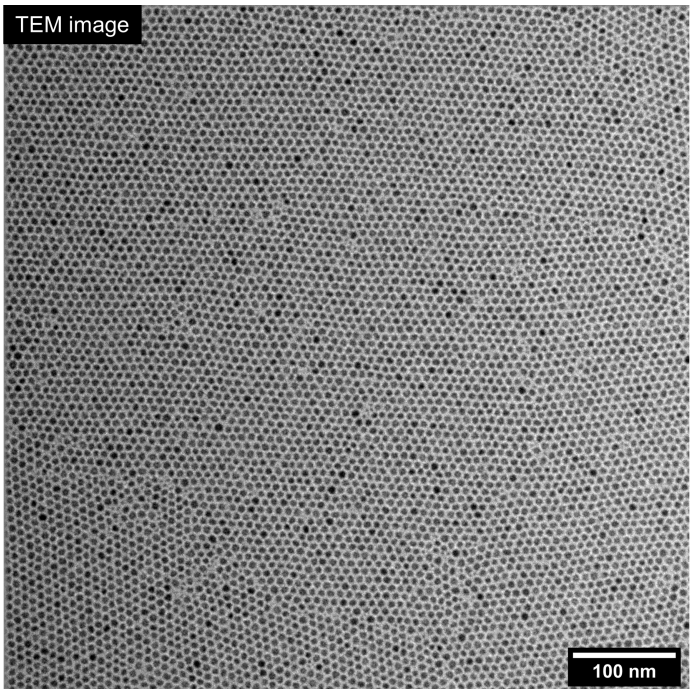


Figure 5.6: TEM image of 5% doped CdSe:Te/CdS QDSL. Image collected by **Rafaela Brinn**.

an analysis involving the following definition:

$$\Psi_{6,j} = \frac{1}{N_{nn}} \sum_{k=1}^{N_{nn}} e^{6i\theta_{j,k}} \tag{5.1}$$

where $N_{nn}$ is the number of neighboring particles, and $\theta_{j,k}$ is the angle between the bond vector connecting particle $j$ and particle $k$. $|\Psi_{6,j}|$ for each particle ranges from 0 (blue) to 1 (yellow) and specifies the local order of the particles within the superlattice monolayer. Visually, one can see large grains of high order present within the superlattice in addition to sparse regions of comparative disorder, reminiscent of grain boundaries.

In addition to more quantitatively establishing the relative order of the superlattice from the representative TEM image, we can also gain a sense of the center-to-center particle separation by histogramming the distribution of calculated center-to-center distances for all neighboring particle pairs (Figure 5.7c). The mean and median interparticle center-to-center distance is 8.9 nm, with a standard deviation of 0.7 nm. Subtle size polydispersity amongst the QDs or the sparser disordered regions within the lattice could contribute to the width of the distribution.

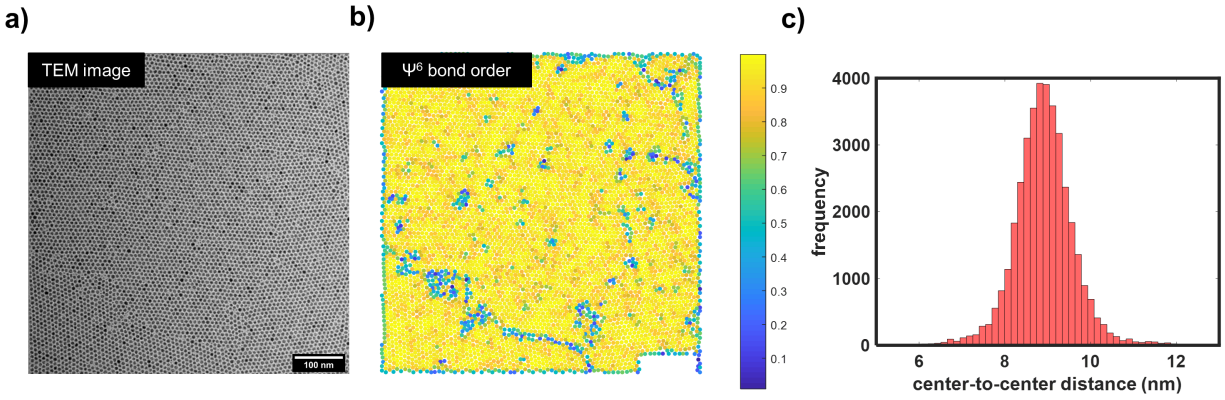


Figure 5.7: TEM image analysis for relative order and center-to-center distance. (a) TEM image of 5% doped CdSe:Te/CdS QDSL. (b) Hexagonal bond order parameter, $|\Psi_{6,j}|$, analysis of QDs in the TEM imaged superlattice. (c) Center-to-center distance distribution of all closest neighbor pairs of QDs.

### AFM

AFM height mapping is useful in determining whether the large area superlattice structures we investigate are monolayers, bilayers, or higher order thicknesses. Figure 5.8 is a representative AFM height map of a piece of superlattice film. The central, relatively featureless surface is approximately 6-7 nm in height and agrees well with the estimated 5 nm height of our CdSe:Te/CdS QDs (inclusive of the ligand layer). The additional lighter contrast features adorning the periphery of the superlattice fragment represent smaller subregions of bilayers, with an approximate height of 12-13 nm. The lightest contrast features are larger scale structures, possibly thicker disordered aggregates of QD material.

### Brightfield optical microscopy

Atop of the sample stage in the STED microscope is a second object with a white light LED for widefield illumination that allows us to more quickly select desired sample regions as well as to aid in focusing. The transmitted white light is then coupled into a ThorLabs CMOS camera, enabling us in real time to image the sample in a brightfield configuration.

Figure 5.9 shows an example image of a region of predominantly CdSe:Te/CdS monolayer superlattice (left) and a region of predominantly CdSe:Te/CdS superlattice bilayers (right). In both cases, owing to the 10s of nm thickness, we often have to sligthly defocus the image in order to more easily see the superlattice fragments.

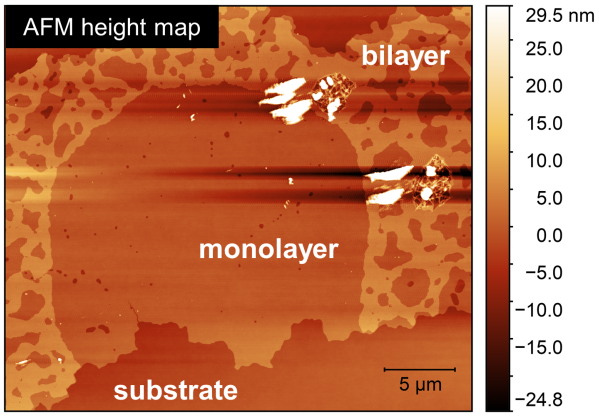


Figure 5.8: AFM height image of a CdSe:Te/CdS superlattice fragment. Labeled in the image are regions of monolayer and bilayer superlattice formation.

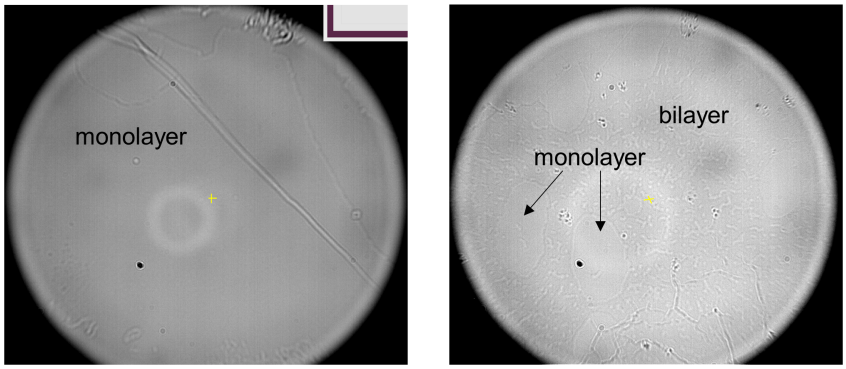


Figure 5.9: Brightfield images of CdSe:Te/CdS fragments.

### Photoluminescence imaging

Before performing TRUSTED measurements on a given superlattice fragment, we collect a photoluminescence image to determine which spatial coordinates correspond to areas that are indeed monolayers. Figure 5.10 is one such image. The bottom of the image, where the counts are close to 0, represents bare substrate with an absence of photoluminescent material. The lighter blue material between 20,000 to 40,000 counts represents a superlattice monolayer, which makes up the majority of the imaged structure. Sparse, higher PL intensity

areas represent portions of the superlattice fragment with additional layers of QDs and are avoided in TRUSTED measurements.

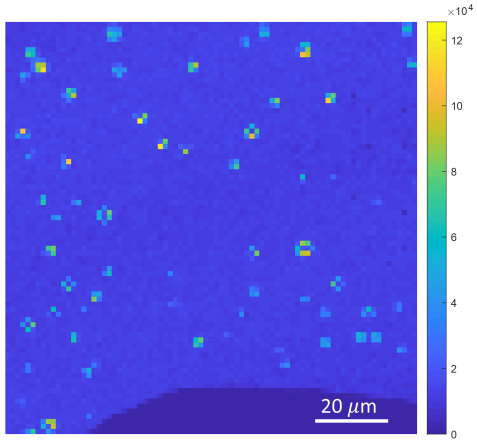


Figure 5.10: Photoluminescence image of a predominantly monolayer fragment of CdSe:Te/CdS superlattice. Sparse higher intensity regions are impartially formed bilayer or multilayer structures.

## 5.3 Measurements of Energy Transport

### 5.3.1 Time-resolved emission spectroscopy (TRES)

Time-resolved emission spectroscopy (TRES) is a simple extension of time-resolved fluorescence spectroscopy. Operationally, one collects a fluorescence/photoluminescence lifetime trace of a sample at each specified spectral component within its emission spectrum using the same laser fluence and integration time for all traces. By combining each of these traces, we effectively achieve the time-dependence of the emission spectrum, where at each time measured after excitation the sample spectrum is reported. This simple, yet powerful, technique reveals much more comprehensive information about a system's spectral properties than steady-state measurements alone. For instance, if there are two different molecular species within a solution that have overlapping spectra but different radiative lifetimes, their individual spectra may be decoupled using a global fitting scheme. For our purposes, TRES provides an opportunity to more readily characterize the spectral heterogeneity present in our QD superlattices and, provided there is spectral heterogeneity, verify if there are signatures of energy transport within the system.

If we follow the emission peak as a function of time after excitation, we find that our QDs suspended in hexanes solvent show a minor dynamic redshift ($\sim$ 50 meV at most, in the case of the 7% Te doped sample), but when organized into a solid superlattice structure, the dynamic redshift is substantial, greater than $\sim$ 50 meV for all Te doping concentrations over the course of the 60 ns shown in Figure 5.11. As a reminder, the 2% and 7% samples are from a different batch of nanocrystals, precluding making quantitative comparisons between their time-resolved emission traces and those of the undoped and 5% samples. Figure 5.12 shows both the solution and superlattice emission peak as a function of time for the undoped CdSe/CdS system.

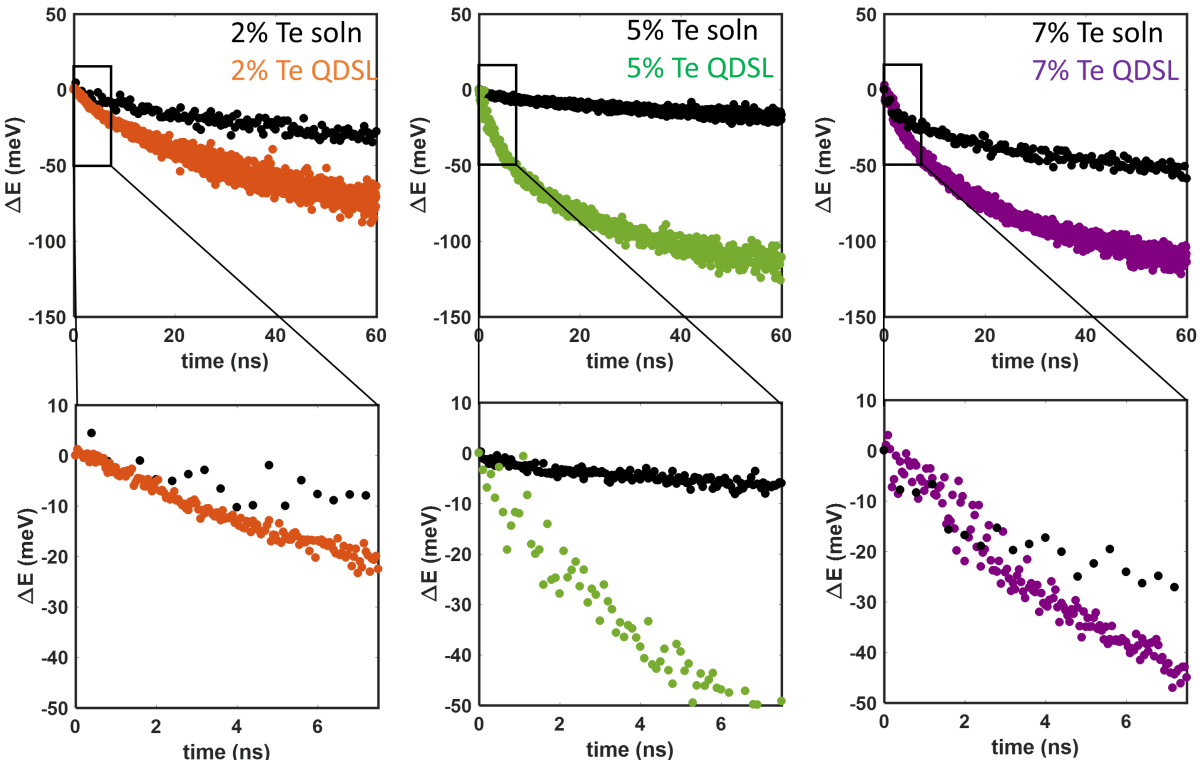


Figure 5.11: Time-resolved emission (TRES) of 2, 5, and 7 % Te doping of CdSe/CdS QDs in solution (black data) and in superlattice (colored data).

A pronounced redshift observed when the QDs are arranged in a close-packed solid is typically attributed to energy transfer[39, 250, 268–270], where spectral inhomogeneity present in the ensemble (due to variation in QD size, surface defects, doping, etc.) results in a distribution of higher and lower energy "sites" within the superlattice. As the photoexcitations approach equilibrium in the excited state manifold, the excitation energy will progress "downhill" via energy transfer from higher to lower energy sites and consequentially redshift

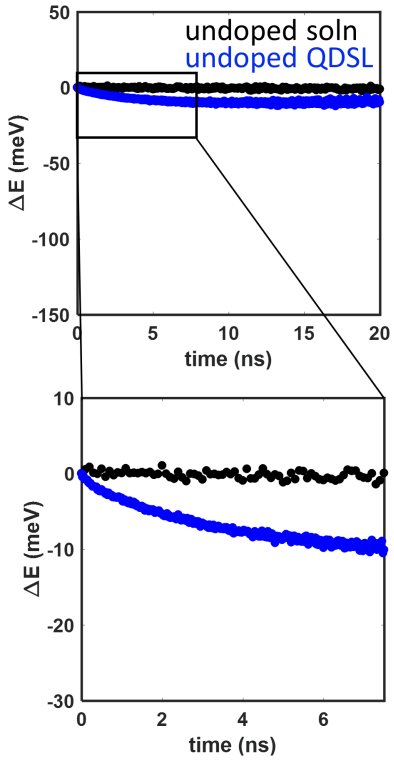


Figure 5.12: Time-resolved emission (TRES) of undoped CdSe/CdS QDs in solution (black data) and in superlattice (blue data).

the emission profile. Figure 5.13 schematically represents two scenarios: a QD superlattice with a perfectly homogeneous spectral landscape such that there is no observable change in the emission profile as a function of time, and another where spectral inhomogeneity in the superlattice leads to a time-dependent shift in the emission profile towards the redder energies.

We speculate that the subtle redshift over the course of 60 ns present in the QD solution observations is due to variability in the relative doping density among QDs and small aggregates of QDs. As individual QDs are in close enough contact with one another in small aggrgates, higher-to-lower site energy transfer could still take place. If the variability in the amount of dopants among QDs is substantial, there could be a distribution of much bluer and much redder QDs.

If we assume the density of site energies follows a Gaussian distribution of states, then from these time-resolved emission traces one can estimate the inhomogeneous broadening components from the following expression, provided the energy relaxation in the system

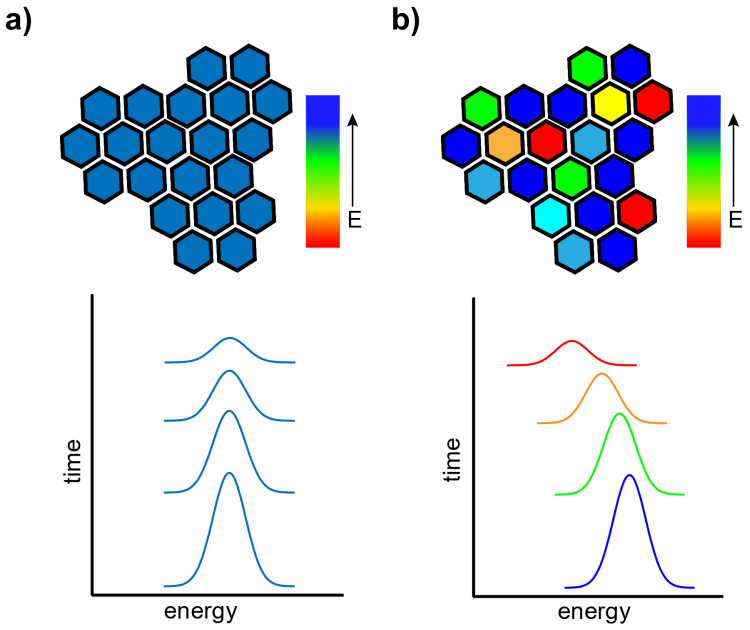


Figure 5.13: Schematic representing the spectral evolution as a function of time for two different energetic landscapes. (a) A perfectly homogeneous energy landscape results in no changes to the emission spectrum as a function of time. (b) An inhomogeneous energy landscape results in the emission spectrum progressively becoming redder as a function of time as energy progresses downhill.

follows Boltzmann statistics and is within a "hopping" regime[271]:

$$\Delta E = \Delta E_{\infty}[1 - e^{-k_{\Delta E}t}], \tag{5.2}$$

where $k_{\Delta E}$ is the rate constant corresponding to the rate of energy change in the system and $\Delta E_{\infty}$ represents the equilibration energy, which can be related to the inhomogeneous broadening via:

$$\Delta E_{\infty} = \frac{-\sigma_{ih}^2}{k_B T} \tag{5.3}$$

where $\sigma_{ih}$ is the inhomogeneous broadening component of the spectral linewidth. Bässler demonstrates that Equation 5.3 is a result of assuming an excitation reaches an "equilibrium" amongst lattice sites within its lifetime, where the equilibration energy is the expectation value of the system energy using a Gaussian multiplicity of states ($e^{-E^2/2\sigma_{ih}^2}$):

$$\langle \Delta E_{\infty} \rangle = \frac{\int_{-\infty}^{\infty} E(e^{-E^2/2\sigma_{ih}^2})(e^{-E/k_B T})dE}{\int_{-\infty}^{\infty} (e^{-E^2/2\sigma_{ih}^2})(e^{-E/k_B T})dE} \tag{5.4}$$

Note that the above treatment is only strictly valid if we assume the exciton transfer rate has an energy dependence that follows a Boltzmann distribution[272], which is very unlikely, but still provides a sense of the relative disorder in the energetic landscape of our QD superlattices[39]. A more appropriate treatment would explicitly account for the correct model of energy transfer that describes exciton transport in QD superlattices, but as will be discussed in detail later, such a model is presently still in development for our system (Section 5.6).

Next, assuming both the homogeneous ($\sigma_{homo}$) and inhomogenous($\sigma_{ih}$) components of the steady-state emission spectrum adopt Gaussian lineshapes, then determining the homogeneous broadening component is a straightforward deconvolution:

$$\sigma_{homo} = \sqrt{\sigma_{ss}^2 - \sigma_{ih}^2} \tag{5.5}$$

where $\sigma_{ss}$ is the standard deviation of the steady state emisson spectrum in energy.

For our 5% doped samples, this deconvolution leads to an estimate of ∼97 meV for $\sigma_{homo}$. (Note, this is likely an overestimate of the homogeneous component, as Ref [272] shows that Boltzmann statistics understimate the inhomogeneity).

Comparing the relative $k_{\Delta E}^{-1}$ values extracted from fits of the QD superlattice traces from the first 10 ns, we find for the undoped system $k_{\Delta E}^{-1}$ is ∼3.2 ns, and for the doped systems we extract ∼8.4 ns, ∼6.7 ns, and ∼7.0 ns for the 2, 5, and 7% doping, respectively. Figure 5.14 shows the peak energy change traces of the 4 QDSL systems and a blow up of the first 10 ns to aid in comparison. The magnitude of the peak energy change is much smaller in the undoped case than in the doped cases, but this is largely due to the much more narrow ensemble emission linewidth. If we normalize each of the TRES traces by the amplitude of the decay fit, shown in the right panels of Fig. 5.14, the relative rates of energy decay become more clear (note for the undoped case, we consider the value at 10 ns to be the amplitude, as the data becomes quite noisy at longer timescales. This is because the undoped particles have a much shorter lifetime than the doped particles).

Assuming the mechanism of excitation energy transport is the same across each of these 4 systems would suggest that excitation diffusivity is greater in the undoped superlattice than in the doped systems, as the $k_{\Delta E}^{-1}$ is ∼2× smaller for the undoped than the 5% doped sample. Extracting a diffusion coefficient, $D$, from this analysis would require an explicit model of energy transport, but $D$ should in principle be proportional to the rate of energy decay, $k_{\Delta E}^{-1}$ [39, 272]. Among the doped systems, the relative diffusivity would be highest in the 5% case and lowest in the 2% case (though again, these relative differences could be due in part to the different nanocrystal batches of the 5% and the 2%/7%) .

TRES of each of our 4 systems demonstrates that when arranged in a superlattice solid, there is a much more pronounced time-dependent redshift of the emission spectrum than when the QDs are suspended in solution, which is *strongly* indicative of energy transport, as higher energy excitons are able to sample lower energy sites by virtue of the spatial proximity afforded by the superlattice structure. Moreover, the mean exciton energy decreasing

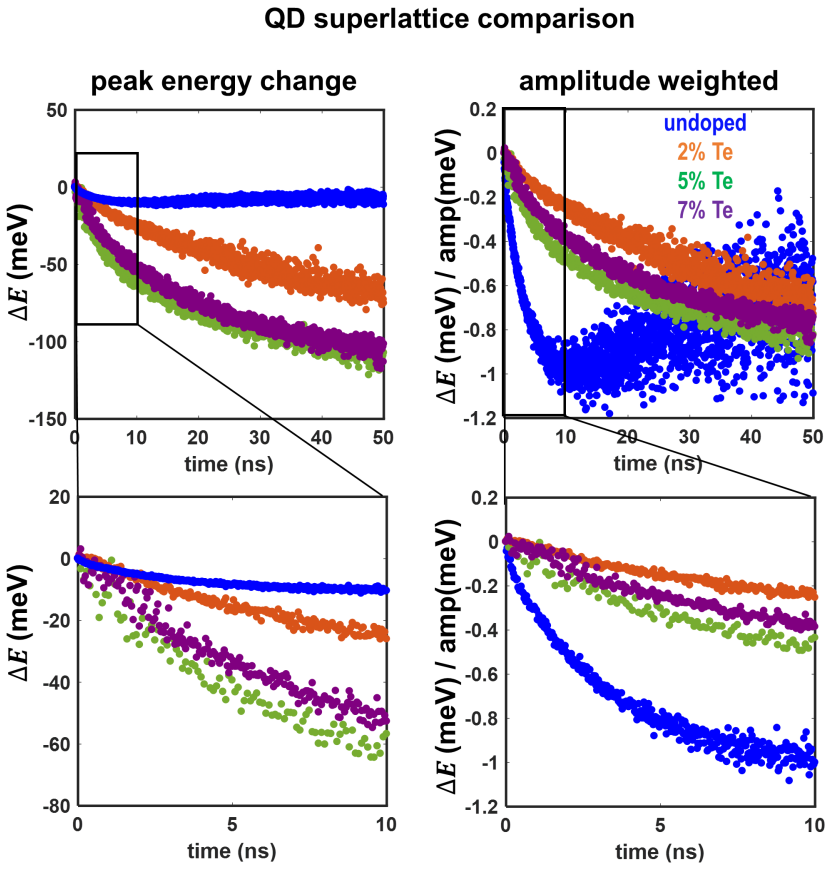


Figure 5.14: Plots of the change in energy of the peak emission for superlattices of all 4 doping conditions. The left plots show the absolute changes in energy of all 4 superlattices with a zoom-in of the first 10 ns. The right plot shows each trace divided by the amplitude of the decay to more readily observe the time-rate of energy decay in each system.

as a function of time suggests transport within the earliest timescales is occurring out of equilibrium.

### 5.3.2 TRUSTED measurements of exciton diffusivity

To more directly probe the diffusivity of excitons in CdSe:Te/CdS QDSL monolayers, we use TRUSTED to monitor the spatial evolution of an exciton profile via optical quenching boundaries, and we describe extensively in the previous chapter. We performed these measurements on 5% CdSe:Te/CdS QDSL monolayers. Our pump (excitation) source is centered at 550 nm with a 20 nm bandwidth and a 5 nW power at the sample plane to gen-

erate a distribution of excitons. This power corresponds to an exciton density of $\sim 7.7 \times 10^{-5}$ excitations/nm$^3$. Our STED pulses are centered at 740 nm with a 16 nm bandwidth and a 25 $\mu$W power at the sample plane. We collect emission from the sample in the 687.5 to 712.5 nm wavelength range.

Figure 5.15a provides a schematic of exciton migration in a QDSL monolayer, recapitulating the notion that at longer times a greater number of excitons will migrate within the quenching boundary imposed by the second STED pulse in our TRUSTED experiment. Fig 5.15b represents the aggregated data from multiple TRUSTED datasets collected over a 4.8 ns dynamic range. TRUSTED data are plotted as the value of the normalized detection volume fluorescence (described in Section 4.4.2) vs time delay with a fit that assumes a constant diffusivity. Fig 5.15c represents the same data plot but with a fit to a time-dependent diffusivity model of the form $D(t) = D_o e^{-k_d t} + D_c$.

If we assume a constant diffusivity, we obtain a diffusivity of $2.7 \pm 0.3$ x10$^{-3}$ cm$^2$/s. For a time dependent diffusivity, we obtain $4.4 \pm 2.7$ x10$^{-3}$ cm$^2$/s for $D_o$, $1.7 \pm 1.2$ x10$^{-3}$ cm$^2$/s for $D_c$, and $0.0008 \pm 0.0011$ ps$^{-1}$ for $k_d$. These fits respectively result in an exciton diffusion length of 35 $\pm$ 1.5 nm and 35 $\pm$ 4.3 nm over the first 4.8 ns of exciton evolution. If we assume that the diffusivities extracted from these fits hold for the 14 ns exciton lifetime, then the diffusion lengths would correspond to 60 $\pm$ 3 nm and 52 $\pm$ 12 nm, respectively.

Although the uncertainty in the fitting parameters resulting from the time-dependent diffusivity fit are substantially larger (which is unsurprising given there are 3 parameters instead of 1), we believe such a fit is warranted given the time-dependent change in the rate of the energy decay present in Figure 5.11. As excitons equilibrate from higher to lower energy sites over their lifetime, the density of acceptor sites is gradually reduced and a concomitant reduction in the diffusivity is expected. Akselrod et al. observed very similar changes in the time-resolved emission of disordered QD films and were able to rationalize their observed sub-diffusive exciton transport from spatially-resolved measurements by explicitly accounting for this downhill energy change[39].

We also used TRUSTED to measure exciton diffusivities in the 2 and 7% Te-doped QDSL monolayers. The 2% and 7% data are presented in Figure 5.16. The TRUSTED data for each sample are shown, assuming a constant diffusivity model, and we obtain diffusivities of $1.3 \pm 0.2$ and $1.3 \pm 0.5 \times 10^{-3}$ cm$^2$/s for the 2% and 7% doped samples, respectively. We did not attempt a fit to the data with a time-dependent diffusivity model given the relatively small change in the normalized detection volume fluorescence. The relatively larger error in the 7% data is a consequence of the lower photoluminescence quantum yield of the 7% QDSL monolayers. As mentioned in Section 5.2.4, we are hesitant to make a direct comparison between the 5% dataset and the 2% and 7% data given we suspect batch-to-batch variability in the nanocrystal preparation. As such, differences between the dynamics in these systems may not be exclusively due to changes in the Te doping concentration, but we include the 2% and 7% data for posterity.

Finally, although we attempted to measure the undoped CdSe/CdS QDSL system with TRUSTED, we found that the emission spectrum was too blue for us to access in the current configuration of our set-up. In fact, the one motivation behind using CdSe:Te/CdS was

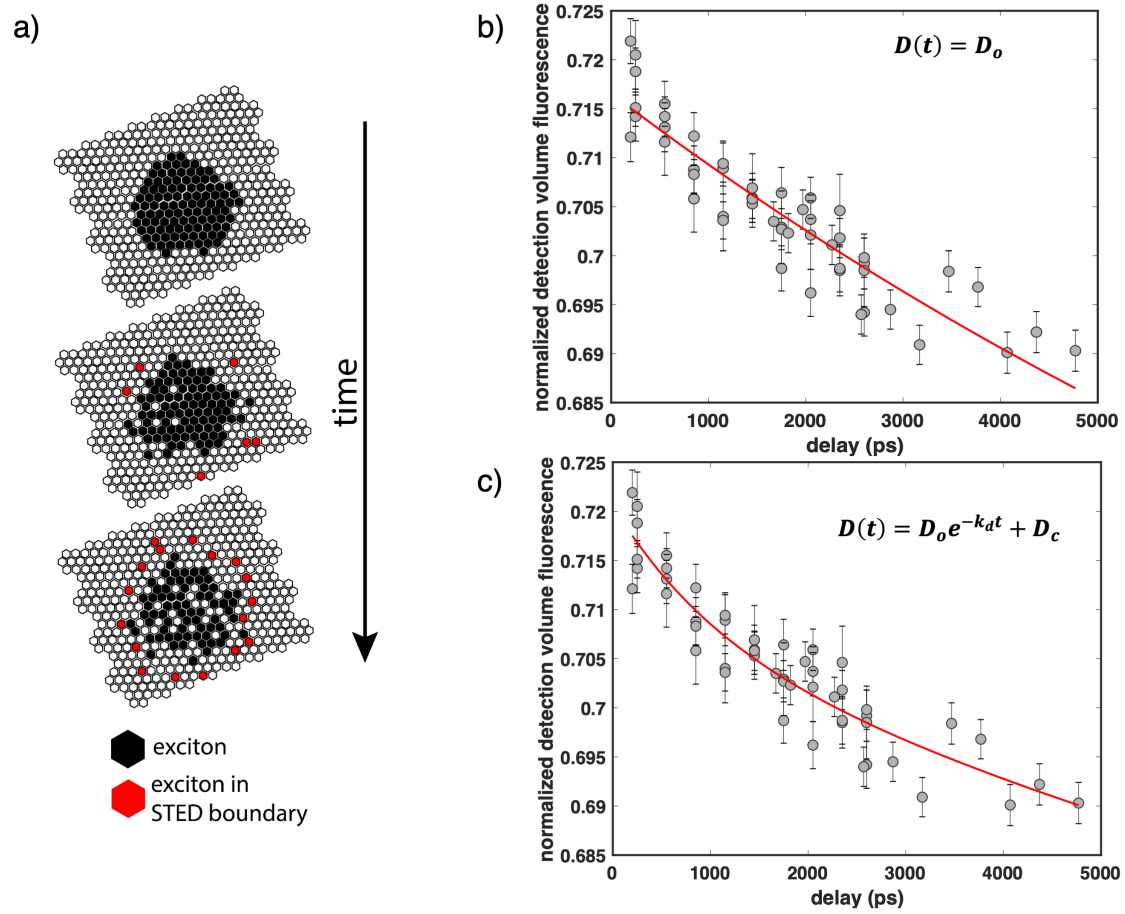


Figure 5.15: TRUSTED measurements of CdSe:Te/CdS superlattice monolayers. (a) Schematic demonstrating excitons (black hexagons) propagating in a QDSL monolayer. At later times, more excitons have migrated into the quenching boundary imposed by the STED2 pulse (red hexagons). (b) TRUSTED dataset of the normalized detection volume fluorescence vs time-delay with a constant diffusivity fit collected from a 5% doped CdSe:Te/CdS QDSL monolayer. (c) TRUSTED data identical to (b), but with a fit assuming a time-dependent diffusivity of the form $D(t) = D_o e^{-k_d t} + D_c$.

because the system possesses red enough emission for us to access with our STED pulse, while maintaining smaller center-to-center distances that are substantially smaller than larger undoped CdSe/CdS in order to facilitate longer-range transport.

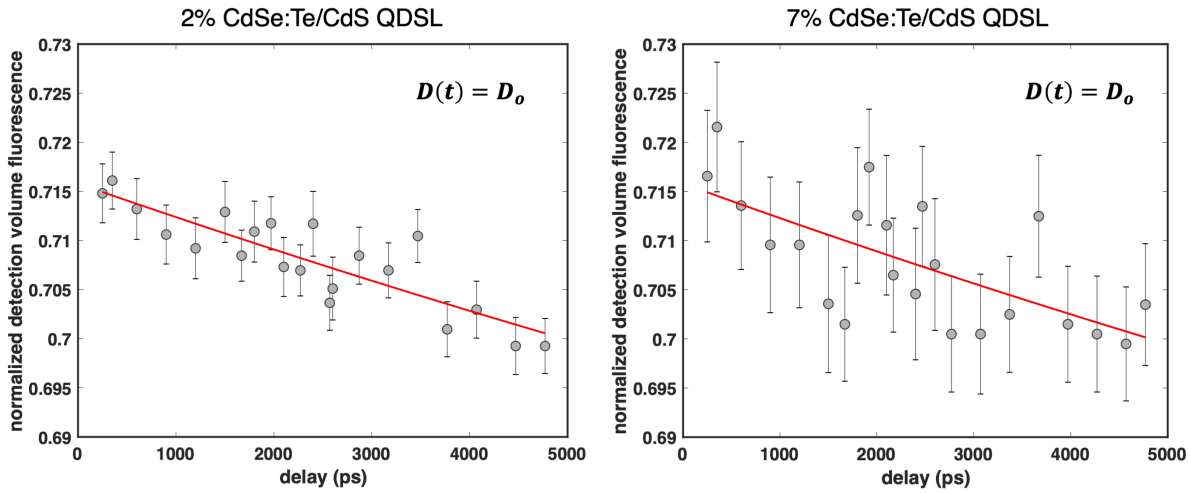


Figure 5.16: TRUSTED measurements of CdSe:Te/CdS superlattice monolayers for the 2% (left) and 7% (right) Te-doping.

### Placing a bound on the FWHM uncertainty of the initial distribution

As discussed in Section 4.4.3, the fitting scheme used to extract a diffusivity requires as an input parameter the FWHM of the exciton distribution after the action of STED1. We determined this value by imaging a sub-diffraction limited sized fragment of a 5% CdSe:Te/CdS superlattice at a series of different STED powers. Figure 5.17 presents a plot of the FWHM vs STED power (measured at the sample plane), where the FWHM are the result of fitting a line-cut of the imaged fragment using a Gaussian. The STED power we employ in our TRUSTED measurements is 25 $\mu$W at the sample plane (at 200 kHz repetition rate and $\sim$120 ps pulse duration). We fit the data using equation 4.15 (red curve) and generate a $2\sigma$ error in the fit by taking into account both the variance in the fitting as well as the uncertainty in the data, which is the uncertainty to the linecut fits used to extract the FWHM from the imaged QDSL fragment (red shaded region). According to Fig 5.17, at a 25 $\mu$W STED power we assume our resolution to be 220 nm, with an upper and lower bound of 230 and 215 nm, respectively.

Fitting the TRUSTED datasets with these upper and lower bounds of the FWHM estimate, with both the constant diffusivity and time-dependent diffusivity fit, yields the results presented in Table 5.1:

Table 5.1 demonstrates that in all cases, the diffusivity extracted from our TRUSTED measurement is on the order of $10^{-3}$ cm$^2$/s. With regards to the time-dependent diffusivity

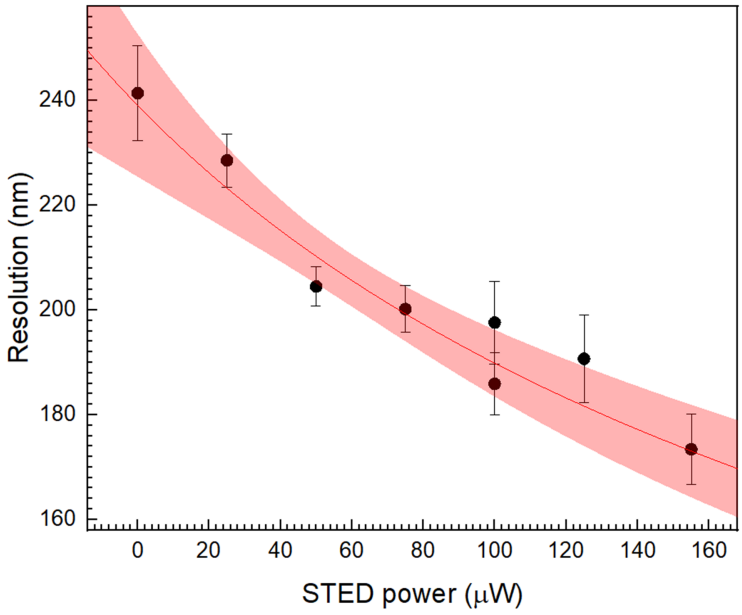


Figure 5.17: Resolution vs STED power of an isolated 5% CdSe:Te/CdS QDSL fragment. The red curve is the result of a fit to eqn 4.15, and the pink shaded region represents the $2\sigma$ range of the error of the fit weighted by the uncertainty in the data. Plot rendered by **Rongfeng Yuan**.

model, we note that the time-constant of the decay is nearly identical across our three initial FWHM guesses, and the ratio of $(D_o + D_c)$ to $D_c$ ranges between 3.3 and 3.9. As $D_c$ is the hypothetical diffusivity at equilibrium (i.e. as time approaches infinity), the diffusivity can conceivably decay by a factor between 3.3 and 3.9, provided an exciton lives long enough to reach equilibrium. Though, given the uncertainty in the fitting parameters, and the fact that we are not measuring the full 14 ns exciton lifetime, this is a rough estimate.

## 5.4 Direct measurement of energy inhomogeneity via single-particle emission spectroscopy

Single-particle emission spectroscopy, where individual QDs and their corresponding emission spectra can be measured, provides information regarding both the intrinsic linewidths (homogeneous broadening) as well as the spectral heterogeneity present within the distribution of measured individual QDs (inhomogeneous broadening). In other words, single-particle spectroscopy more readily decouples the inhomogeneous contribution to the bulk spectrum,

Table 5.1: TRUSTED fitting results with upper and lower uncertainty of initial FWHM

| FWHM(nm) | $D_o$ (x$10^{-3}$ cm$^2$/s) | $D_c$ (x$10^{-3}$ cm$^2$/s) | $k_d$ (ps$^{-1}$) | model |
|---|---|---|---|---|
| 215 | $4.0 \pm 2.4$ | $1.4 \pm 1.0$ | $0.0008 \pm 0.0010$ | $D_o e^{-k_d t} + D_c$ |
| 220 | $4.4 \pm 2.7$ | $1.7 \pm 1.2$ | $0.0008 \pm 0.0011$ | $D_o e^{-k_d t} + D_c$ |
| 230 | $5.5 \pm 3.8$ | $2.4 \pm 1.5$ | $0.0009 \pm 0.0012$ | $D_o e^{-k_d t} + D_c$ |
| 215 | $2.3 \pm 0.2$ | - | - | $D_o$ |
| 220 | $2.7 \pm 0.3$ | - | - | $D_o$ |
| 230 | $3.7 \pm 0.3$ | - | - | $D_o$ |

and further does not require assuming particular characteristics about the nature of energy relaxation of our system, unlike the treatment involving time-resolved emission spectroscopy (section 5.3.1). To achieve this, we collaborated with the Xu group here at Berkeley (just like in Chapter 3!) in order to spectrally resolve our 5% Te doped QDs as well as our undoped QDs.

Spectrally-resolved single-particle measurements were performed using previously established methods[190, 191] on a widefield fluorescence microscope. Solutions of QDs in hexanes were diluted to single-particle concentrations (e.g. $\sim$100 pM) and deposited on a cleaned microscope slide and quickly encapsulated with a coverslip using Cytoseal to prevent evaporation. The fluorescence from the sample is split between two channels and registered simultaneously: one channel provides a widefield image of the emitters while the other channel has a prism inserted into the Fourier plane of two lenses prior to the detector. The prism disperses the fluorescence, and therefore individual particle emission is spread across multiple pixels of the camera, encoding the emission spectrum. The intensity levels reported by the widefield image are used to confirm that the observed emitters are indeed single QDs and not multiple QDs within a given diffraction limited volume.

Figure 5.18 summarizes several important findings from the single QD emission measurements made on undoped and 5% Te-doped CdSe/CdS QDs. First, we note that the averaged single-particle emission spectrum is substantially broadened in the case of the 5% Te-doped, compared to the undoped CdSe/CdS QDs (Fig 5.18a), which is consistent with our steady-state emission spectra (Fig 5.4). Distributions of the wavelength corresponding to the peak emission of each measured QD (Fig 5.18b) as well as the distribution of the FWHM of each measured QD spectrum (Fig 5.18c) show a substantially larger spread in the case of the Te-doped QDs relative to the undoped QDs. The median wavelength from the distribution of wavelengths corresponding to the emission peak is 640 nm with a standard deviation of 25 nm for the doped case, while the undoped distribution has a median wavelength of 634 nm with a standard deviation of 4 nm. The distribution of emission spectra FWHM has a median value of 58 nm with a standard deviation of 17 nm for the doped case and a median value of 32 nm with a standard deviation of 2 nm for the undoped case.

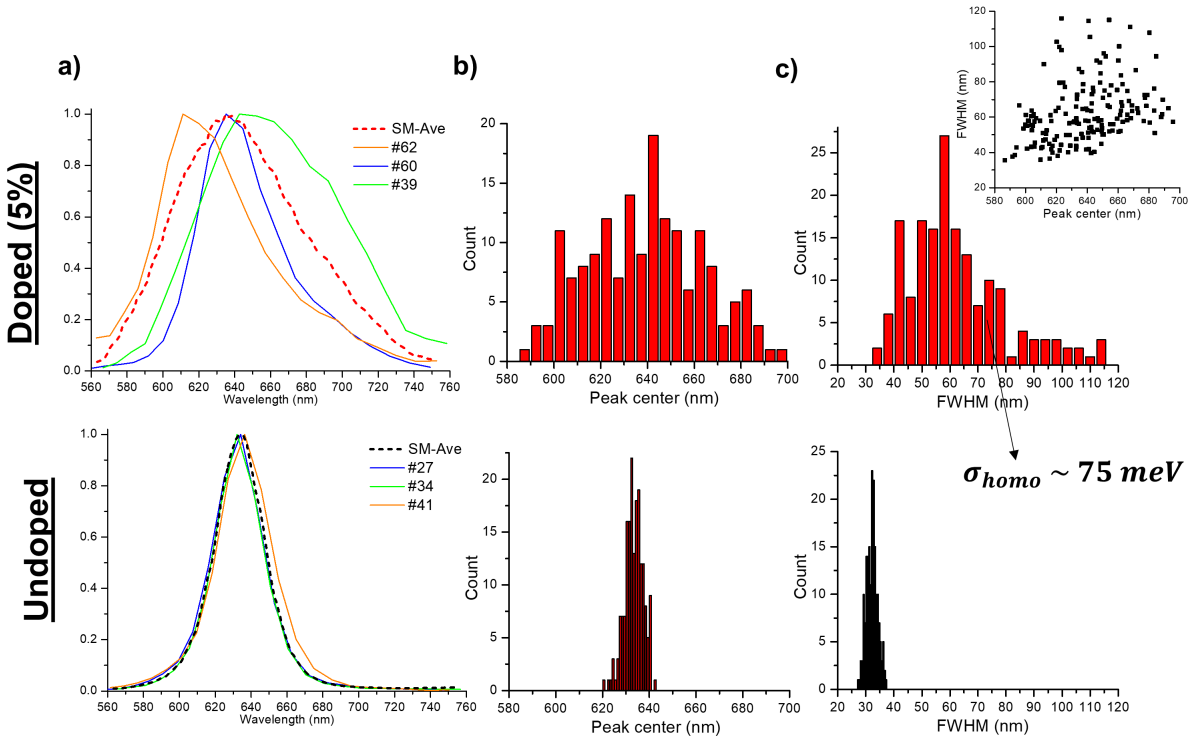


Figure 5.18: Single-particle emission characterization of both 5% doped CdSe:Te/CdS QDs and undoped CdSe/CdS QDs in hexanes solvent. (a) Example single-particle spectra (solid-colored curves) as well as the average of all collected single-particle spectra (dashed curves). (b) Distributions of the peak wavelengths of the individual particle spectra in both doped and undoped cases. (c) The distribution of estimated FWHM from Gaussian fits to the individual particle spectra in both doped and undoped cases. The inset in the top right is the plot of each particle spectra's FWHM vs it peak wavelength value for the 5% CdSe:Te/CdS system.

This would suggest that the process of Te doping CdSe/CdS QDs introduces spectral inhomogeneity, and the most likely cause is variability in the number of Te dopants in a given QD. One known possible contribution to spectral inhomogeneity in QDs is size polydispersity[273–275], but as the doped QDs were prepared using CdSe cores from the same batch as the undoped particles, the comparatively narrow peak emission distribution in the undoped particles would suggest size polydispersity is unable to account for the breadth of the distributions found in the case of the doped particles. Furthermore, the distribution of center-to-center distances in Figure 5.7 reinforces the notion that the size polydispersity of the CdSe:Te/CdS system is relatively narrow.

Although Te-doping appears to contribute more spectral inhomogeneity to the ensem-

ble of CdSe/CdS QDs, we also note that individual CdSe:Te/CdS QDs have substantially broader intrinsic linewidths than undoped CdSe/CdS QDs, given the median FWHM of the individual spectra shifts from 32 to 58 nm. In addition, plotting the individual particle spectra FWHM against their peak emission wavelength (inset of Fig 5.18c) demonstrates a correlation: as the emission becomes redder it commensurately becomes broader. Such related emission redshift and broadening of individual particle spectra has been observed in other, low temperature, single-particle emission measurements of Te-doped CdSe/ZnS core-shell QDs[264]. The relative increase in the homogeneous linewidth could help mitigate the reduction in spectral overlap due to the corresponding heterogeneity in emission spectra peaks.

If we assume the median peak emission wavelength and median spectrum FWHM is the most representative individual particle spectrum, the homogeneous component of our Te-doped QD ensemble is $\sigma_{homo} \sim 75$ meV. This is notably smaller than the 97 meV estimate we extracted for $\sigma_{homo}$ using time-resolved emission spectroscopy. In all likelihood, the single-particle emission estimate for the homogeneous broadening is more representative of the actual system's photophysics because, as discussed previously in Section 5.3.1, assuming that the rate of site energy decrease follows Boltzmann statistics often leads to an underestimate of system inhomogeneity (and therefore an overestimate of homogeneity) when analyzing TRES data of dynamic redshifts in solid-state samples[272].

## 5.5 Towards reconciling measures of exciton transport with possible models of energy transfer

Taken together, both the TRES and TRUSTED measurements would suggest we are observing non-equilibrium exciton transport, where, as the mean exciton energy of the system relaxes via exciton diffusion among lattice sites, there is a presumed ∼3.4 fold reduction in the diffusivity over the course of 4.8 ns. Of course, such a reduction in the diffusivity is extracted from TRUSTED data that is collected over only 4.8 ns, as compared to the exciton lifetime (∼14 ns), so this is a rough estimate. While the nature of the transport being non-equilibrium seems rational, the measured diffusivities on the order of $\sim 10^{-3}$ cm$^2$/s are peculiarly high. We therefore dedicate a substantial portion of this chapter to discuss this relatively high diffusivity, but at the time of this writing we are still developing our understanding.

### 5.5.1 FRET inadequately supports our observed exciton diffusivities

The mechanism by which energy is transported between a pair of QDs or densely packed QD arrays is generally thought to be divided into two classes: FRET dipole-dipole coupling or electron/charge transfer. Note that there is a massive body of research on this topic.

For example, Hildebrandt et. al. provide a highly comprehensive review of QDs as energy transfer donor and/or acceptors in a biological labeling context, citing over 1000 studies in their review article alone[276]. Peculiarly, even in systems where electron/charge transfer is exceedingly unlikely, FRET does not appear able to universally describe energy transport in QD solids, as there are a number of experimentally measured diffusivities that are higher than FRET would reasonably predict. Our own experimentally measured diffusivity on the order of $\sim 10^{-3}$ cm$^2$/s is significantly greater than a FRET model would predict, and therefore merits an in-depth discussion.

FRET is an often-invoked mechanism for energy transport in QD solids, particularly if the surfaces of individual QDs are capped with long insulating alkyl ligands (such as the oleic acid and oleylamine ligands used in this study) that preclude charge tunneling. Many studies have suggested that energy transfer between QDs and organic acceptors[277–280], and between smaller and larger QDs[281, 282], can be modelled well with FRET. For example, FRET predicts that the energy transfer rate between a donor and acceptor should scale as $(1/r)^6$, and indeed experimental work, like that involving CdSe/ZnS QD donors and Cy3 molecular acceptors[283, 284], demonstrate this scaling.

Despite the numerous reports that suggest FRET is an apt descriptor of the energy transfer mechanism between QDs as well as between QDs and molecular acceptors, there are also a number of reports that find FRET underestimates the experimentally observed rate of energy transfer[39, 269, 285, 286]. Some studies suggest the use of the point-dipole approximation is inappropriate with closely-packed QDs, given their comparatively larger size than molecular systems[285, 287], which we will address. Even accounting for the larger size of QDs, it remains unclear if the mechanism of energy transport in our CdSe:Te/CdS system is actually FRET but just requires a correction and/or more accurate estimates of system parameters, or if the mechanism is entirely different.

### Estimates of the CdSe:Te/CdS Förster radius

Revisiting the equations describing the rate of energy transfer in a FRET framework, the rate constant is:

$$k_{\text{FRET}} = \frac{1}{\tau_D}\left(\frac{R_o}{R}\right)^6 \tag{5.6}$$

where $\tau_D$ is the radiative lifetime of the donor chromophore, $R$ is the distance between the centers of the point transition dipoles used to approximate the spatial extent of the electronic transition densities corresponding to the ground-to-excited state transitions, and $R_o$ is the "FRET radius", which is the distance at which the energy transfer rate is 50% efficient. $R_o$ packages up many terms, and is defined as:

$$R_o^6 = \frac{9\log(10)\Phi_D\kappa^2}{128\pi^5\eta^4}\int \sigma_A(\lambda)\overline{F_D}\lambda^4 d\lambda, \tag{5.7}$$

where $\Phi_D$ is the fluorescence (photoluminescence) quantum yield of the donor chromophore, $\eta$ is the index of refraction of the medium, $\kappa^2$ is the dipole-dipole orientation factor (see

Chapter 2), $\sigma_A(\lambda)$ is the wavelength-dependent absorptivity of the acceptor chromophore species, and $\overline{F_D}$ is the fluorescence emission spectrum normalized by its area. Note that $\int \sigma_A(\lambda)\overline{F_D}\lambda^4 d\lambda$ is referred to as the spectral overlap integral and often denoted as $J$. ($J$ is typically presented in units of $M^{-1}$ $cm^{-1}$, and converting to the more useful unit of $nm^{-1}$ requires a $10^{17}$ conversion factor).

For our CdSe:Te/CdS homo-FRET (i.e. energy transfer between identical chromophores) system, we establish estimates of the various parameters used to determine $R_o$. For $\Phi_D$ we use 23% as an estimate, from a measurement performed by **Rafaela Brinn** shown in Figure 5.19. For the index of refraction, we assume $\eta$ to be between 1.8 - 2.0 based on Dement et. al.'s investigation of CdSe/CdS QD thin films[288].

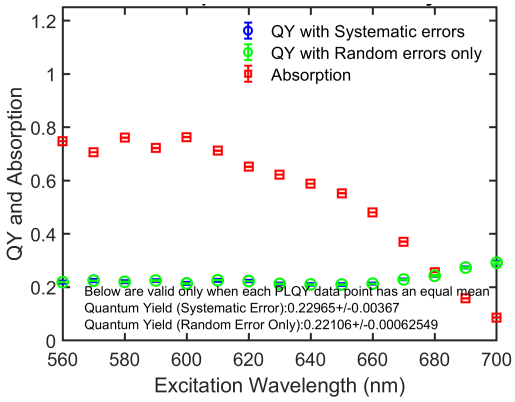


Figure 5.19: PLQY are measured at various excitation wavelengths for the 5% CdSe:Te/CdS system, shown as green data. Data collected and plotted by **Rafaela Brinn**

The last two parameters, the spectral overlap integral and $\kappa^2$, are potentially the greatest sources of uncertainty. For $\kappa^2$, a conservative estimate is typically to assume that the transition dipole moments of all chromophores in the ensemble are isotropically distributed, such that $\langle\kappa^2\rangle = 2/3$. In a highly ordered superlattice, however, the orientation of QD transition dipole moments could very well be locked in place, yielding more optimal configurations than 2/3 for $\langle\kappa^2\rangle$. Our ability to accurately estimate the spectral overlap integral is contingent on knowing the absorptivity of the quantum dot superlattice, which is not necessarily the same as the QDs in solution and would require more sophisticated experiments to extract.

The absorption spectrum is collected from a stock solution of CdSe:Te/CdS QDs with a 45 mg/mL concentration that is diluted 100-fold. Based on Striolo et. al.'s measurements using membrane osmometry as a benchmark for correlating CdSe nanocrystal diameter with molecular weight[289], and taking into account the relative amounts of Cd, Se, S, and Te in our system, we crudely estimate the molecular weight of our CdSe:Te/CdS nanocrystals to fall in between 600 and 1200 kg/mol. Figure 5.20a plots heatmaps of estimated $R_o$ values by varying both the molecular weight (absorptivity) of the 5% CdSe:Te/CdS ($y$-axis) and the $\kappa^2$ parameter ($x$-axis). The top panel presents the estimates of $R_o$ using varying molecular

weight estimates, and the bottom panel is identical but the molecular weight values are converted to corresponding absorptivity values. For comparison, panel b) shows heatmaps of $R_o$ estimates using the steady-state parameters for the undoped system.

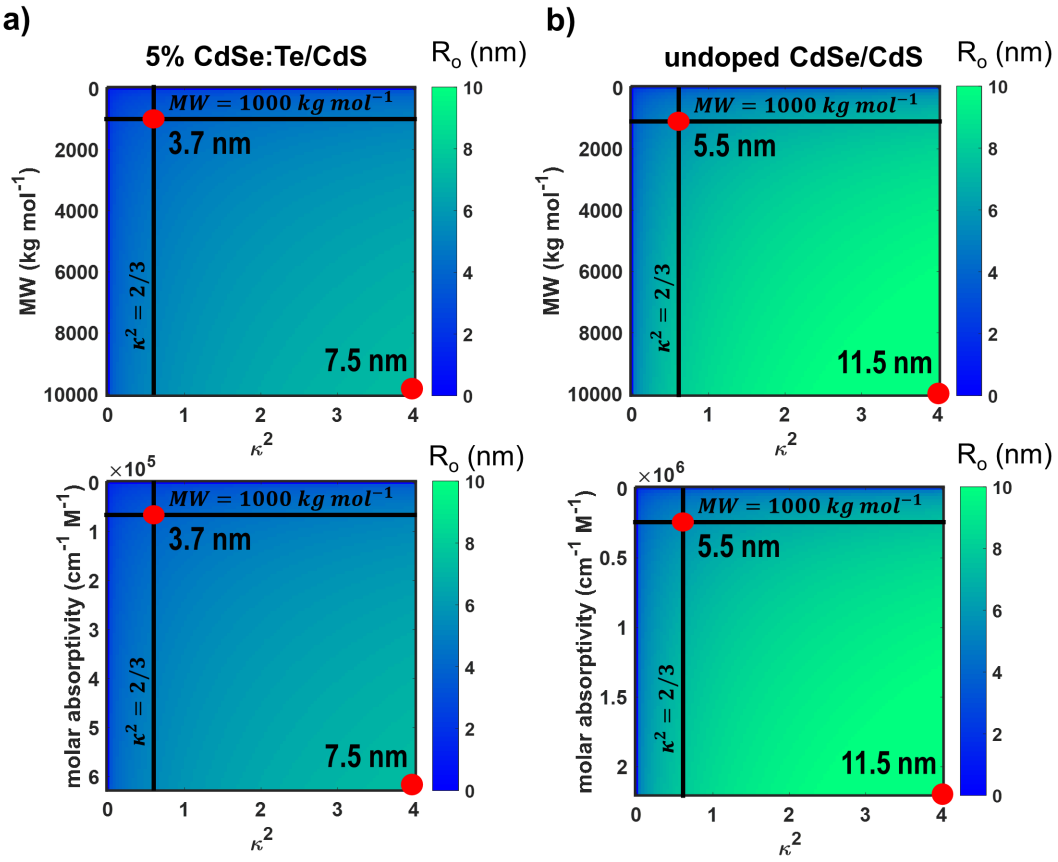


Figure 5.20: Heatmaps of the estimated $R_o$ parameter for a range of values for $\kappa^2$ and the molecular weight/absorptivity, using available steady-state parameters. (a) Heatmap of the estimated $R_o$ parameter for the 5% CdSe:Te/CdS system shown with units of molecular weight (top) and absorptivity (bottom). (b) Heatmaps of the estimated $R_o$ parameter for the undoped CdSe/CdS system.

The red dot located at the intersection of the two solid black lines in each of the heat map plots corresponds to an $R_o$ estimate of 3.7 nm and is conceivable given our known parameters, assuming the CdSe:Te/CdS nanocrystals possess a molecular weight of 1000 kg/mol and that we have isotropically distributed transition dipole orientations for a $\kappa^2$ of 2/3. If we were to assume we had the benefit of the extremes of this plot, wherein we assume the CdSe:Te/CdS

molecular weight is 10x higher and that there is a perfect dipole orientation factor of $\kappa^2$ of 4, then $R_o$ would be 7.5 nm. In the undoped CdSe/CdS case, these $R_o$ estimates would be 5.5 nm and 11.5 nm, respectively.

Immediately, these plots suggest that within a FRET framework the addition of Te-dopants reduces the $R_o$ parameter of our system, which is unsurprising given the steady-state spectra shown in Figure 5.4 reveal a marked reduction in the spectral overlap of the solution absorption and superlattice emission when comparing the undoped and 5% CdSe:Te/CdS cases.

### Monte Carlo Simulations of energy transport

We turn to kinetic Monte Carlo simulations of exciton transport both to verify the extent excitons can spatially sample a superlattice grid as well as determine the requisite $R_o$ value to recapitulate our experimentally measured diffusivities. In order to more readily emulate our system, we use the TEM image shown in Figure 5.6 to generate our grid of QDs. In the most simple simulation, we only consider a hypothetical rate of energy transfer, $k_{\text{FRET}} = \frac{1}{\tau_D}\left(\frac{R_o}{R}\right)^6$, with a $\tau_D$ and $R_o$ of our choosing. The QD center-to-center distance between nearest neighbor pairs is determined by the the simulated excitation's position on the grid. The probability of an energy transfer event over time is:

$$\frac{\partial P(t)}{\partial t} = k_{\text{hop}} \tag{5.8}$$

and therefore the distribution function of the probability that an energy transfer event, or "hop," occurs within the system is defined as:

$$P(t) = k_{\text{hop}} e^{-k_{\text{hop}} t} \tag{5.9}$$

To capture this in simulations we generate a random number uniformly distributed between [0, 1], $U$, and invert the probability distribution function to evaluate the time at which any event happens[290] such that:

$$\int_0^{t_{\text{hop}}} P(t) = U, \text{and} \tag{5.10}$$

$$t_{\text{hop}} = -ln(1-U)/k_{\text{hop}} \tag{5.11}$$

For a given excitation, a $t_{\text{hop}}$ is evaluated for each of the nearest neighbor sites and the neighbor yielding the smallest $t_{\text{hop}}$ is chosen as the excitation's new location. This evaluation repeats until the sum total of an excitation's hop times exceed the specified simulation time window, $t_{\text{sim}}$.

$$\sum_{i=1}^{N_{\text{hop}}} t_{\text{hop},i} \leq t_{\text{sim}} \tag{5.12}$$

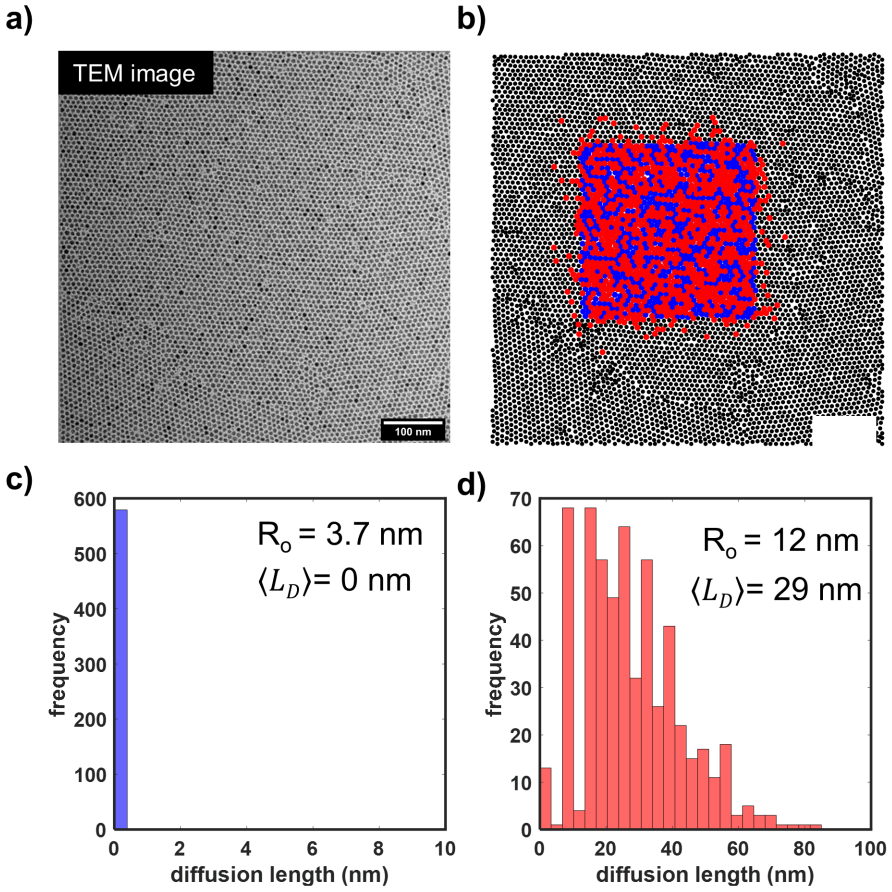


Figure 5.21: Overview of simple kinetic Monte Carlo simulations of exciton FRET hopping. (a) TEM image of QDSL. (b) Grid of QDs (black dots) used for simulation generated via localization analysis of QDs from the TEM image in (a). The simulation grid is the same size as the TEM image. The blue points in the shape of a square are the initial locations of trajectories, and the red points represent the final locations. (c) Distribution of diffusion lengths resulting from trajectories of simulation with a $R_o$ of 3.7 nm. (d) Distribution of diffusion lengths resulting from trajectories of simulation with a $R_o$ of 12 nm.

From here, we can report a distribution of diffusion lengths by calculating the distance between the initial and final grid locations of each trajectory. Figure 5.21b shows the simulation grid determined via particle localization of the TEM image in Fig 5.21a. The initial and final locations of trajectories are grid locations colored in blue and red, respectively. We do not employ periodic boundary conditions here, but for all values of $R_o$ simulated–even for 12 nm–excitation trajectories never reach the border of the grid based off the TEM image within the 4.8 ns simulation time. For these simulations we assume the lifetime of an

excitation is 14 ns (which we determined from a separate TCSPC lifetime measurement of the 5% CdSe:Te/CdS superlattice on our STED microscope), and we only run the simulation for 4.8 ns, which is our observation window for our TRUSTED measurements. If we use the $R_o$ estimate of 3.7 nm from Figure 5.20, then the average diffusion length ($L_D$) is 0 nm because no hopping event occurs, shown in Fig 5.21c. In fact, only by dramatically increasing the value of $R_o$ to 12 nm do we begin to achieve an average $L_D$ value of 29 nm that is consistent with our ∼35 nm TRUSTED measurements (Fig 5.21d). These findings are not altogether unsurprising given the average center-to-center distance between QDs is 8.9 nm, and FRET energy transfer is very sensitive to interchromophore distance owing to the $(1/r)^6$ dependence.

Unfortunately, even taking potentially aphysical liberty with our estimates of the system's absorptivity and $\kappa^2$, the $R_o$ parameter reaches 7.5 nm at best (Figure 5.20). Of course, these simulations reduce describing the whole system to only two parameters, $\tau_D$ and $R_o$, and more refined simulations would allow for variability amongst the $R_o$ values for each pairwise interaction. For example, if spectral inhomogeneity among the constituent QDs was taken into account, then $R_o$ would adjust for each pairwise interaction due to differing spectral overlaps. Moreover, we experimentally verified inhomogeneity to be present in our system, both through single-particle measurements of the inhomogeneity as well as the TRES data in Figure 5.11 demonstrating a substantial dynamic redshift.

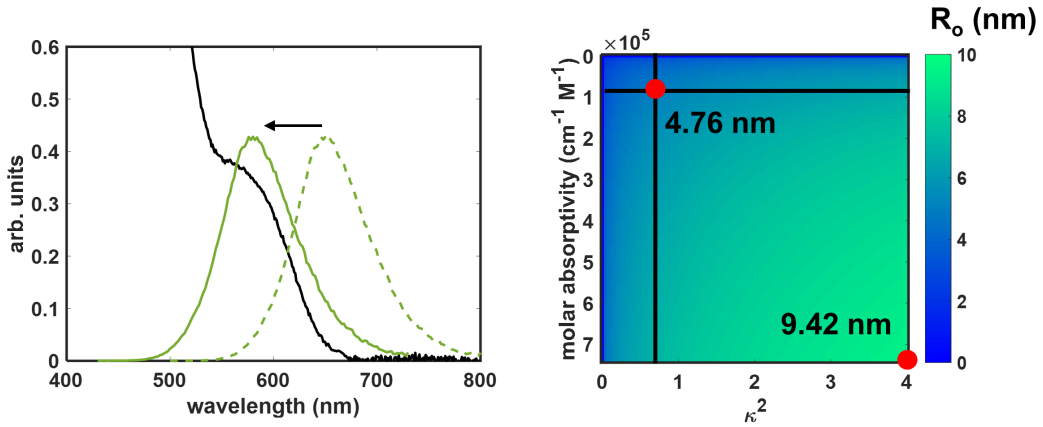


Figure 5.22: The $R_o$ parameter heatmap for a range of values for $\kappa^2$ and the molar absorptivity assuming the emission spectrum is 70 nm blueshifted.

Figure 5.22 provides $R_o$ estimates across a range of absorptivities and $\kappa^2$ values, assuming the entire emission spectrum were 70 nm bluer. We find that the conservative and extreme estimates of absorptivity and $\kappa^2$ yield $R_o = 4.76$ nm and 9.42 nm, respectively. Thus, even artifically altering the spectral overlap by blueshifting the emission spectrum to eliminate

the 70 nm Stokes shift estimated from Figure 5.4, is not sufficient to reconcile with our TRUSTED measurement.

The point-dipole approximated FRET model clearly fails to support our measured diffusivity. Confronted with such a discrepancy, rationalizing the diffusivity extracted from our TRUSTED measurements can take a few approaches: 1) a substantial correction to the FRET model, 2) a different model for energy transport, or 3) identifying ways TRUSTED might overestimate the exciton diffusivity.

### 5.5.2 Corrections to the point-dipole approximation

A point-dipole approximation is typically invoked to render calculations and estimates of energy transfer more feasible than if we had to account for the full charge density of donor and acceptor chromophores. Strictly speaking, the potential term to describe donor-acceptor interactions is a Coulomb potential:

$$V = \sum_{ij} \frac{q_i q_j}{|r_i - r_j|} \tag{5.13}$$

where $q_i$, $q_j$ and $r_i$, $r_j$ are the charges and positions of all the nuclei and electrons in the donor ($i$) and acceptor ($j$) chromophores, respectively. By reworking the potential term as a dipole-dipole interaction, and estimating the entire charge distribution of a chromophore to be summarized as a dipole, we get a comparatively simpler potential interaction term. Tokmakoff provides a nice overview of this from his "Time Dependent Quantum Mechanics and Spectroscopy" notes, and the following equations are from this source for the sake of discussion[291]. The interaction potential term now becomes:

$$V = \frac{3(\overline{\mu}^A \cdot \hat{r})(\overline{\mu}^D \cdot \hat{r}) - \overline{\mu}^A \cdot \overline{\mu}^D}{\overline{r}^3} \tag{5.14}$$

where the donor ($D$) and acceptor ($A$) dipole terms are defined as:

$$\overline{\mu}^D = \sum_i q_i^D (r_i^D - r_0^D) \tag{5.15}$$

$$\overline{\mu}^A = \sum_j q_j^A (r_j^A - r_0^A) \tag{5.16}$$

The rate of energy transfer is proportional to the transition matrix element squared per Fermi's Golden Rule, $|V|^2$, which is where the $(1/r)^6$ dependence of FRET is realized.

The point-dipole approximation is usually valid if the separation between donor and acceptor chromophores is significantly larger than the size of the chromophores in question. Molecular fluorophores typically possess hydrodynamic radii $< 1$ nm, and so in common FRET measurements where fluorophores are placed distances 3 - 10 nm apart (e.g. molecular ruler experiments of biological systems), the point-dipole approximation is sufficient.

Quantum dots on the other hand are much larger chromophores, with diameters traditionally larger > 2 nm. Zheng et al. demonstrated that approximating the interaction potential between two QDs with distributions of dipole moments, rather than single (point) dipoles defined at the centers of QDs, can provide an important correction to FRET[287] when the surface-to-surface distance is small.

If one were to use a zeroth-order Bessel distribution of transition dipole moments bounded by the the spatial extend of the QD, the distance dependence of the interaction potential term then becomes:

$$V(r_{cc}) = \int_{r_1,\theta_1,\phi_1} \int_{r_2,\theta_2,\phi_2} \frac{1}{(|\vec{r_1} - \vec{r_2}|)^3} D(r_1)D(r_2)sin(\phi_1)r_1^2 sin(\phi_2)r_2^2 \\ dr_1 d\theta_1 d\phi_1 dr_2 d\theta_2 d\phi_2 \quad (5.17)$$

where $r_{cc}$ is the center-to-center distance, defined as the difference between $\vec{r_1}$ and $\vec{r_2}$ (which are the coordinates of hypothetical dipoles), and $D(r)$ are the dipole moment densities the individual QDs. The dipole moment densities are defined as:

$$D(r) = \frac{\pi}{8R^3} \frac{sin(\frac{\pi r}{R})}{\frac{\pi r}{R}} \quad (5.18)$$

where $R$ is the radius of the QD. Note the notation and expressions for Equations 5.17 and 5.18 are slightly different than Ref [287] to be more explicit.

By evaluating Equation 5.17 using a distribution as defined in Equation 5.18 versus a delta function representing a point-dipole at the center of a QD, and plotting the ratio of $|V(r_{cc})|^2$, one can create a plot like that shown in Figure 5.23. Considering a pair of QDs with diameters 2.3 and 3.7 nm, for center-to-center distances sufficiently large (e.g. > 10 nm), the Bessel function distribution and delta function distribution recover very similar values. But at center-to-center distances < 10 nm, using a Bessel distribution of dipoles yields a higher $|V(r_{cc})|^2$ value. The inset in the top right of Fig 5.23 demonstrates that the ratio between using a Bessel distribution over a delta function.

Equation 5.17 does not have an analytical solution, and must be solved numerically. Zheng et al.'s approach was to numerically evaluate the integral deterministically via 20 segments along each coordinate. Although this leads to a precise result, it requires $20^6$ computations for each $r_{cc}$ to be evaluated. As I am unaware of the algorithm used in Ref [287] and my computer memory was insufficient, I used Monte Carlo Integration instead to evaluate Equation 5.17 in order to collapse the 6-dimensional calculation to a more feasible single dimension.

### Monte Carlo integration to estimate FRET distance term correction

For each of the parameters, $r_1$, $\theta_1$, $\phi_1$, $r_2$, $\theta_2$, $\phi_2$, we generate a random number uniformly distributed along the bounds of integration, then evaluate the integrand at these randomly

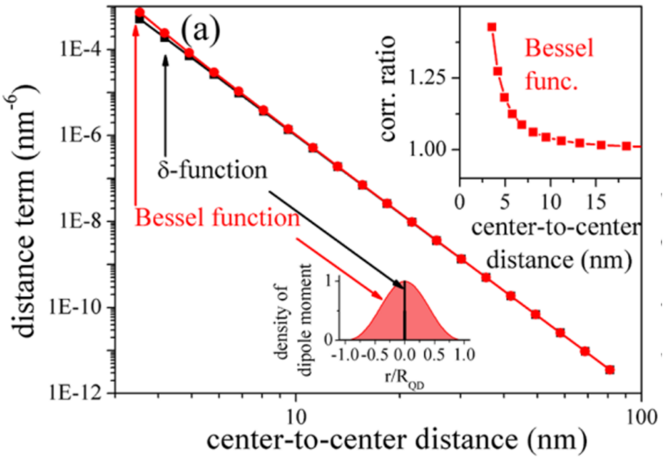


Figure 5.23: Calculation of the distance term used in FRET for a Bessel function distribution of dipoles (red) and a delta function distribution of dipoles (black) as function of the center-to-center distance between QDs. The ratio of the Bessel function to the delta function data are plotted in the upper right inset for the center-to-center distances up to 20 nm. Adapted from Ref [287] with permission.

generated coordinates with $dr_1$, $d\theta_1$, $d\phi_1$, $dr_2$, $d\theta_2$, $d\phi_2$ all estimated as $\frac{1}{b-a}$, where $a$ and $b$ represent the lower and upper bounds of integration along a given coordinate. This process is repeated $N$ times, and the sum of these evaluations is weighted against $1/N$ for normalization. The error in such an approach scales as $1/\sqrt{N}$, so provided we use large enough sampling statistics we can achieve close to exact results. As a quality check, using the parameters of Zheng et al.'s system of a QD pair composed of 2.3 and 3.7 nm diameter QDs, the Monte Carlo integration estimate of the Bessel distribution vs delta function distribution is shown in Figure 5.24. The correction ratio appears to match well to the inset from Ref [287] shown in Figure 5.23.

Now turning to our system - using the 7 nm QD diameter along the $XY$ plane, as illustrated in Figure 5.3, we simulate a Bessel distribution of dipole moments for a sphere of radius 3.5 nm and compute the distance term of the interaction potential for varying $R_{cc}$. Figure 5.25 shows our estimates of the correction ratio to a delta function, and at a 9 nm $R_{cc}$ we see that a Bessel distribution of dipole moments is a correction ratio of ∼1.3. Using this treatment suggests to divide the center-to-center distances used in calculating the FRET rates by 1.3 (or in other words multiply $R_o$ by 1.3).

The QDs are hexagonal prisms, so in principle there exists comparatively more interactions between close parts of the QDs than in the spherical pair case. To provide an upper bound, simulations assuming the QDs are cubes with 7 nm side length are computed. We

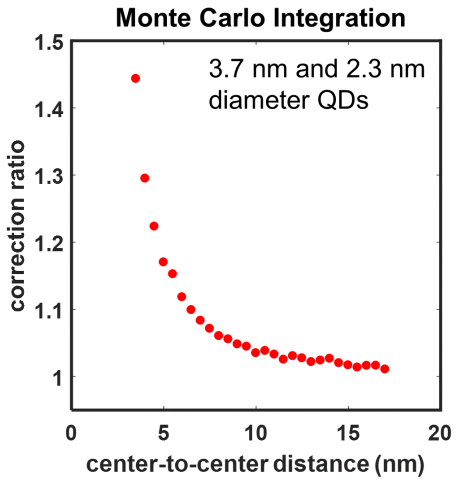


Figure 5.24: Monte Carlo integration results of correction ratio of the distance term between a Bessel distribution of dipoles and a delta function of dipoles for a series of center-to-center distances, using the same diameter of QDs from Ref [287].

find that cubes yield a trend with overall higher correction ratio values, and at 9 nm $R_{cc}$ the correction suggests we should divide the center-to-center distances in FRET calculations by a factor of 1.4. This is interesting beyond our system, as it suggests as a design principle that particular nanocrystal shapes could more readily facilitate energy transfer in solid-state arrays within a FRET framework, like cubic shaped nanoparticles. In fact, this is hypothesized to be among one of the reasons why cubic shaped perovskite nanocrystal (PNC) arrays have demonstrated remarkable diffusion lengths [292], where the interparticle distance is assumed to be the ligand layer only.

Reducing the conventional center-to-center distance used in calculating the FRET energy transfer rate by a factor between 1.3 to 1.4 is a non-trivial adjustment, and the above treatment serves to demonstrate an important consideration for energy transport amongst relatively large chromophores within a FRET framework. Despite how accounting for these geometrical considerations narrows the discrepancy between our observed and expected exciton migration, we would require for a factor closer to 2 to 3. Considering a distribution of transition dipole moments instead of a point-dipole is therefore not sufficient on its own to use FRET to describe our results.

### 5.5.3 Other considerations within the FRET framework

Mork et al. extensively explore the ways in which applying Förster theory to solid QD films using common assumptions can lead to underestimates of the energy transfer rate and suggest

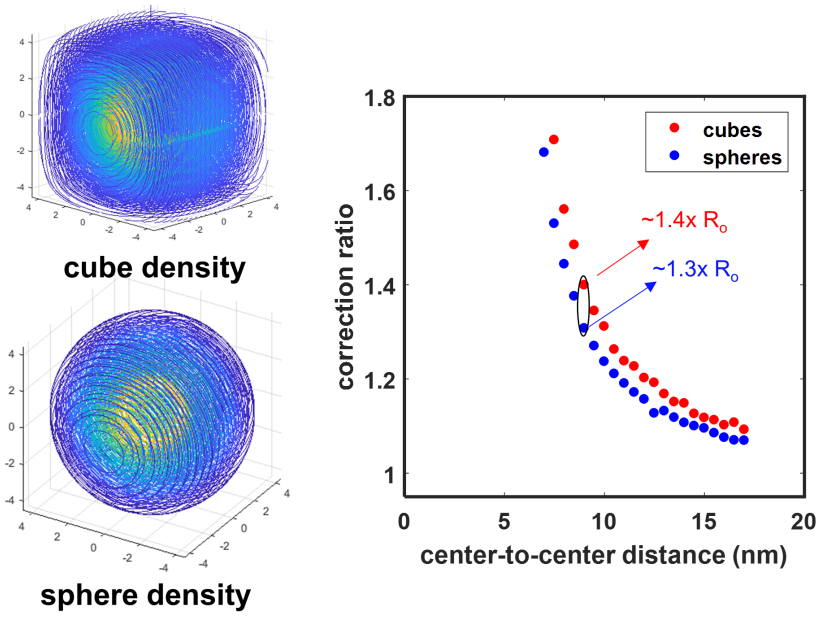


Figure 5.25: Monte Carlo integration calculation of the correction ratio between a Bessel distribution of dipoles and a delta function distribution of dipoles for QDs of 7 nm diameter. Calculations were performed for spherical (blue data) and cubic (red data) shaped distributions.

potential sources of discrepancy between experiment and theory [269]. In their system of blended donor/acceptor QD films, where the donors are smaller QDs (emit bluer) and the acceptors are larger QDs, assessment of the energy transfer rate via photoluminescence lifetime measurements would suggest $R_o$ values of $9 \pm 2$ nm and $8 \pm 1$ nm for configurations with short and long ligands, respectively. The theoretical estimates of $R_o$, however, were 5.2 nm and 5.1 nm, respectively.

As discussed previously, when QDs are packed in solid assemblies the dipole orientation could have more optimal alignment due to the static configuration prohibiting QD translation or reorientation. Mork et al. comment that this could certainly be the case for their film system, but more optimal dipole orientation alone will not account for their discrepancy between theory and experiment. This is recapitulated in our own exploration of the dipole orientation in previous sections.

With regard to the nature of the electronic coupling, Mork et al. suggested that higher order dipole-multipole interactions, which are neglected in FRET theory, could provide a non-trivial boost to the theoretically estimated transfer rate. Baer and Rabani demonstrated that accounting for an additional dipole-quadrupole interaction can increase simulated FRET rates of a model system when the surface-to-surface distance between QDs is sufficiently small relative to the average diameter of a QD pair[293]. In our system, the surface-to-

surface distance is ∼1.5 nm due to interdigitation of the oleic acid/oleylamine ligands, which represents ∼20% of the QD diameter and ∼17% of the center-to-center distance.

One other potential adjustment to the theoretical estimate of the FRET rate in QD films Mork et al. put forth is related to underestimates of the film absorptivity. The work of Geiragat et al. suggests that in films of CdSe nanocrystals with 6 - 7 nm diameters, the absorptivity can be nearly 4x greater in films than in solution [294]. We ostensibly explored what such an enhancement would do to the rates of our energy transfer in Figure 5.20, where if we assume a 4x higher absorptivity than our conservative estimate from both the solution absorption spectrum and estimate of the CdSe:Te/CdS molecular weight, then our $R_o$ can range from 4.75 to 6.35 nm assuming a range of $\langle\kappa^2\rangle$ between 0.66 to 4.

### 5.5.4 Other mechanisms of energy transport

A substantial portion of the discussion thus far has focused on FRET, or more generally dipole-dipole interactions, as the potential mechanism for energy transport because this is historically the framework thought to best describe QDs with long organic ligands. Here, we will briefly address other possible mechanisms of energy transport.

#### Charge tunneling

Charge tunneling is the process whereby the wavefunction of either the electron or hole species can propagate through the insulating potential barrier imposed by the organic ligands, enabling the exchange of electron or hole species between adjacent QDs. For the CdSe:Te/CdS system, hole tunneling is unlikely given the hole wavefunction is strongly localized to the Te dopants and would furthermore have to tunnel through the CdS shell and ligand barrier. For the purposes of this discussion, let us assume only electrons may tunnel.

The tunneling probability, as a function of the barrier distance, $d$, for an electron from a QD to an acceptor can be described as the following [295–297]:

$$k_{i,j}(d) = k_o e^{-\beta d} \begin{cases} \exp(-\frac{E_j - E_i}{k_B T}) & \text{if } E_j > E_i \\ 1 & \text{if } E_j \leq E_i \end{cases} \tag{5.19}$$

where $k_{i,j}$ is the rate constant for transfer from the donor, $i$, to an acceptor, $j$, $k_o$ is the barrierless rate constant, and $\beta$ is the wavefunction decay factor through the barrier reported in units of length$^{-1}$. If the energy level of the acceptor is of a higher energy than the donor, then we have an additional Boltzmann term to account for this energy discrepancy. If the energy level of the acceptor is the less than or equal to the donor, then we ignore this penalty. For the sake of this argument, we assume that the QDs are isoenergetic with one another, such that we only consider the rate to be $k_o e^{-\beta d}$.

In principle, all 3 parameters in our probability equation for charge tunneling, $k_o$, $\beta$, and $d$ are somewhat unknown. For long (e.g. 18 carbon unit) organic ligands, the value of $\beta$ is presumed to be relatively large, on the order of ∼1 Å$^{-1}$ [296]. There are studies

involving electron transfer from CdSe QDs connected to $TiO_2$ via methylene bridges that report $\beta \sim 0.8$Å$^{-1}$ [21, 298] or even as low as $\beta \sim 0.35$Å$^{-1}$ [298] under the special circumstance that the ligand shell collapses (i.e. not all the methylene units are in a *trans-* conformation). This is to say, there is some variability in the $\beta$ value. For the barrier distance, $d$, we assume that the oleic acid/oleylamine ligands somewhat interdigitate, and so rather than the full ligand length (∼2.0 nm) we believe $d$ to be $\sim$ 1.5 nm. Finally, $k_o$ is not a parameter we would know a priori for the electron exchange between our particular QDs.

To address these unknowns, we can calculate a range of potential values that $k_o$, $\beta$, and d would correspond to in order to match our experimentally observed diffusion rate. From the simple kinetic Monte Carlo simulations used in Figure 5.21, we learned we need an $R_o$ of 12 nm to roughly match our TRUSTED results, which corresponds to a hopping rate of $k_{\text{FRET}} = 4.29 \times 10^8$ s$^{-1}$. Figure 5.26 plots the value of $\log(k_o)$ vs $\beta$ that yields an energy transfer rate predicted by FRET, which in turn matches our TRUSTED results. We perform this calculation to match FRET rates predicted for $R_o$ values of 11 and 13 nm, as well, for posterity. The different colored curves in each plot represent different values of $d$ used in the calculation.

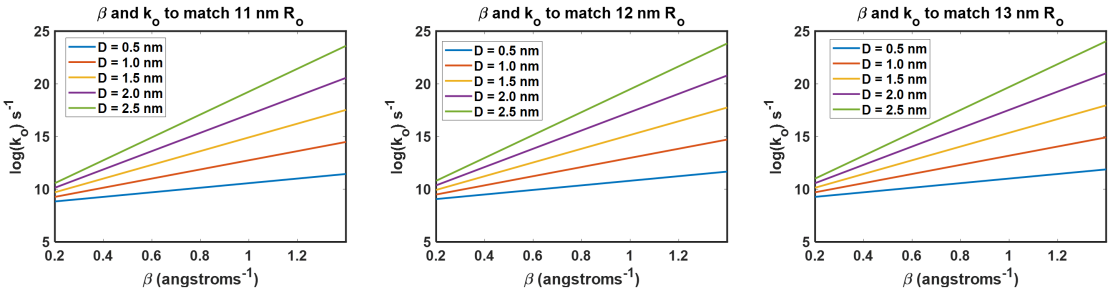


Figure 5.26: Calculations of the $k_o$ and $\beta$ parameter values required to match the hopping rate predicted by FRET for $R_o$ values of 11, 12, and 13 nm. Different colored curves in each plot represent a different tunneling barrier distance, $d$.

If we were to assume that we have a $\beta$ of 0.8Å$^{-1}$ and a $d$ of 1.5 nm, then we would require a $k_o$ value on the order of $10^{13}$ - $10^{14}$ s$^{-1}$. Such a rate constant is very large, especially when compared to values reported by Hines et al. for the transport of electrons from organic ligand capped CdSe QDs to a $TiO_2$ metal oxide acceptor[299], which are on the order of $10^8$ - $10^9$. The fact that seemingly reasonable values of $\beta$ and $d$ require a $k_o$ value 4 - 5 orders of magnitude larger than those in comparable systems would suggest tunneling is just as or

even more unlikely than FRET.

Furthermore, in order for charge tunneling to actually manifest in our measurement, it would require non-geminate electron and hole recombination, as TRUSTED and TRES are fluorescence based read-outs. We would have to carefully consider if this is possible, and, furthermore whether we can drive stimulated emission via the non-geminate recombination of electron and hole to quench such species.

The large potential barriers imposed by the organic ligand layer similarly preclude the possibility of exciton delocalization as the mechanism for transport. If the excitonic wave-function were able to sample spatial extents greater than a single QD, in principle such an exciton delocalization, or coherence, length would enable longer range transport. While large diffusion lengths have been observed in systems bearing such exciton delocalization[300, 301], this possibility is quite unlikely in this system.

### Photon recycling

Photon recycling is the process by which a photon emitted by a sample is reabsorbed by the same sample in question, albeit at a different location. This can in principle contribute to remarkably large diffusion lengths, as the emitted photon moves at the speed of light, and has been demonstrated as a non-trivial factor in the $> 1$ $\mu$m diffusion lengths in perovskite nanocrystal films[302] and the incredible observation that in lead-iodide perovskites emission can occur distances $> 50$ $\mu$m away from the excitation source[303]. There is some current debate, however, as to the extent photon recycling can contribute to the observed lateral transport of carriers, particularly using pulsed excitation sources[304].

For our particular system, we have a few obstacles for efficient photon recycling. The first is the morphology of the material. QDSL monolayers only enable observable transport to occur within the plane of the sample. We have no reason to suspect that the emission is strictly within the sample plane, and so assume that the emission occurs isotropically, though it could be waveguided. As such, from a strictly geometric perspective, the probability of a reabsorption event decreases at further distances from the emission site. Figure 5.27 is a cartoon schematic demonstrating that in order to crudely determine the probability of a reabsoprtion event occurring, a disk slice of the same thickness as the monolayer ($\sim$5 - 7 nm) must be integrated relative to the volume of the sphere representing the isotropic emission distribution. The relative volume of the slice decreases as the radius of the emission sphere increases.

The other obstacle for efficient photon recycling is the quantum yield (QY) of our system. In a photon recycling scheme, the probability of each emission event is weighted by the QY. This is why systems meant for luminescent solar concentrators (LSCs) require very high (e.g. $> 99\%$) QY[9], as their performance scales logarithmically. Given the QY of our CdSe:Te/CdS system in solution is only 23% (see Fig 5.19), the probability of any given excitation trajectory possessing multiple hops seems unlikely. Yet, only a small fraction (on the order of a few percent) of excitons would need to participate in photon recycling to manifest a higher average diffusivity like that observed in our measurements.

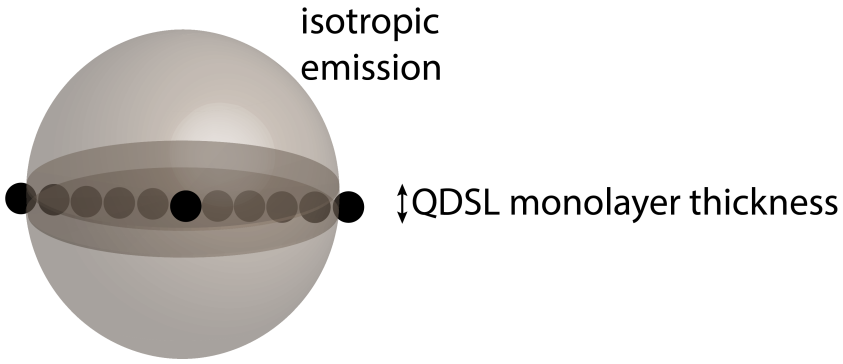


Figure 5.27: Schematic of the overlap between the QDSL monolayer and the isotropic emission distribution for photon recycling.

### 5.5.5 TRUSTED control measures

So far the approach to reconciling our experimentally extracted diffusivity with theoretical descriptions of energy transport has been predicated on the assumption that our TRUSTED measurements are a faithful reporter of exciton diffusivity. In order to substantiate our confidence in the measurement, a few key control measurements were required to rule out potential non-diffusion related contributions to our signal, which as a reminder is a readout based on the remaining fluorescence after the action of the second STED pulse.

#### Exciton-exciton annihilation or Auger-Meitner recombination

Density-dependent contributions to the non-radiative decay of the exciton population, such as exciton-exciton annihilation or Auger-Meitner recombination, could be mistaken for migration due to relative changes in the spatial profile leading to more pronounced overlap with the STED pulse. An initially Gaussian shaped distribution of excitons may progressively adopt more of a "flat top" shape, as the density in the center of the distribution is high enough such that multi particle interactions and their subsequent non-radiative recombination events can occur until the density is sufficiently low. Provided the timescales associated with such a change to the exciton profile are within our observation window (e.g. 200 to 4800 ps) this could lead to a time-dependent change in the quenching action of the second STED pulse.

To address this, we collected the photoluminescence from 25 different spatial locations on a 5% CdSe:Te/CdS monolayer at several pump powers. We plot the average of the collected photoluminescence counts from the different spatial locations as a function of pump power measured at the sample in Figure 5.28. We fit a linear trend to the lowest 5 powers and extrapolate across the entire range of pump powers measured. At powers higher than 5 nW, we note that the average photluminescence counts begin to deviate significantly from the expected trend, which is a characteristic sign of Auger recombination or exciton-exciton anni-

hilation. TRUSTED measurements conducted at 2 nW and 5 nW powers, which correspond to excitation densities of $\sim 3.1\times10^{-5}$ excitations/nm$^3$ and $\sim 7.7\times10^{-5}$ excitations/nm$^3$, respectively, indicated as arrows in Fig 5.28 yielded similar diffusivities within error of one another, suggesting we are operating within a linear excitation regime. Note the data shown in Fig 5.28 has taken into account the pile-up non-linearity of the SPAD detector discussed in Section 4.3.6.

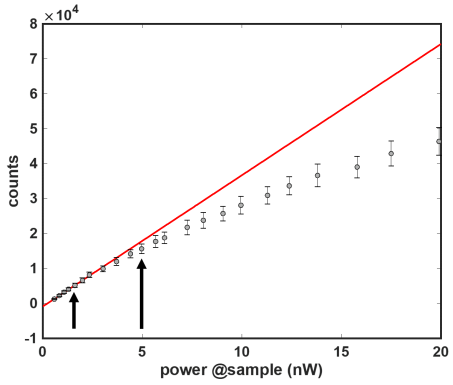


Figure 5.28: Photoluminescence counts vs pump power measured at the sample plane. The red curve is a linear fit determine by the lowest 5 power data points. The black arrows indicate 2 and 5 nW excitation, which are the two powers used in TRUSTED.

### Time-dependent quenching efficiency

Another potential transient change in the TRUSTED experimental conditions that could lead to the mistaken assignment of a migration observable is a time-dependent change in the quenching efficiency of the second STED pulse, based on when it is introduced to the target exciton profile. Our observable represents a change of the exciton population on the order of only a few percent, so even subtle changes in the quenching efficiency need to be accounted for. For a given intensity, the STED pulse's ability to quench excitons via stimulated emission through a normal fluorescent/photoluminescent pathway depends on the oscillator strength at the spectral frequency of the STED pulse. If changes in the sample's photophysics on timescales between 100s of ps to a few ns lead to greater oscillator strength with the STED pulse, then we would expect more efficient quenching as the second STED pulse is introduced at later times.

The STED pulse is typically tuned to be spectrally overlapped with the redder edge of a sample's emission profile in order to avoid complications due to direct and two-photon absorption. If the sample's emission profile were to redshift as a function of time after excitation, then the spectral overlap between sample emission and STED pulse (i.e. oscillator

strength) can be enhanced. In our CdSe:Te/CdS superlattice, we see clear evidence of a dynamic redshift occuring on timescales commensurate with our TRUSTED observation window. Although our hypothesis is that this redshift is due to exciton migration within the superlattice, the concomitant change in the spectra and consequent change in quenching efficiency via the second STED pulse can lead to an overestimate of the exciton diffusivity via TRUSTED.

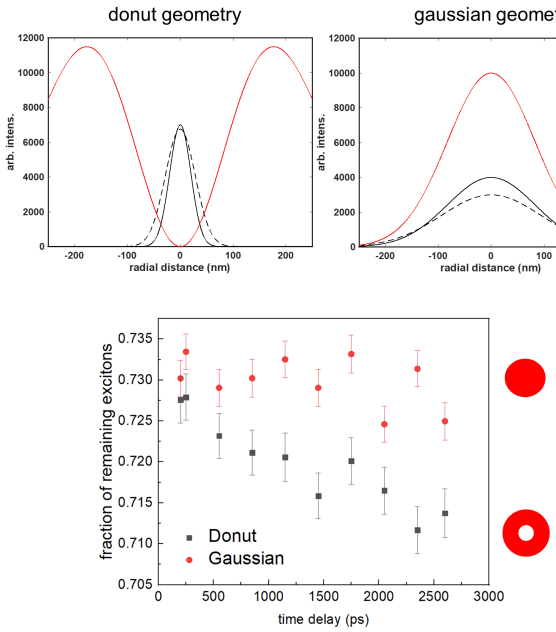


Figure 5.29: Summary of using a Gaussian shaped STED pulse as a control measure. 1D linecuts of a donut and Gaussian shaped STED pulse are overlain with simulations of the target exciton profile diffusion (top). TRUSTED data corresponding to measurements with a Gaussian shaped STED pulse (red data) and a donut shaped STED pulse (black data) are overlain togeter (bottom).

In order to address whether time-dependent quenching changes are present in our experiment, we employ a control measurement with Gaussian shaped STED pulses. TRUSTED's sensitivity to migration is due to increased overlap between the exciton profile and the optical quenching boundary imposed by the donut-shaped STED pulse as the excitons sample the space available to them. If the STED pulse were a Gaussian with a FWHM significantly larger than the target exciton population, then a change in the exciton profile due to diffusion would not necessarily register as a change in the amount of quenched excitons because the depletion field envelopes the entire distribution. Figure 5.29 schematically represents these two scenarios, where the initial exciton profile is a 1D solid black curve and evolves to

the dashed curve due to diffusion. In the donut geometry case, where the 1D STED pulse is represented as a red curve, the exciton profile's tails more substantively overlap with the STED pulse after diffusion. In the case of the Gaussian geometry, the subtle exciton profile evolution due to diffusion shows much of the same overlap with the STED pulse as the initial distribution. Therefore, if we do observe a substantial change in the amount of quenched excitons as a function of time, it is unlikely to be due to diffusion. Rather, it is more likely due to time-dependent changes in the quenching efficiency of the STED pulse.

TRUSTED datasets from two different experiments, one with donut shaped STED pulses and one with Gaussian shaped STED pulses, are shown in Figure 5.29. We find that in the case of the donut geometry STED pulse, there is a decrease in the fraction of remaining excitons on the order ∼1.5%, whereas in the case of the Gaussian geometry there is a decay of ∼0.25%, which is within the error of our measurement. It is worth noting that the intensity distribution is more concentrated spatially in the Gaussian geometry. To reconcile this difference, we attenuate the Gaussian STED pulse intensity to ensure that the quenching efficiency matches that of the donut shaped STED pulse.

This experiment is reassuring, as it suggests that the shape of the quenching boundary is responsible for generating our signal, which leads us to the conclusion that time-dependent changes in the quenching efficiency of the STED pulse are negligible within the error of our measurement.

## 5.6 Reconciling the non-equilibrium transport reported by TRUSTED and TRES

In an effort to reconcile the non-equilibrium transport reported both by our spatial measurement via TRUSTED and spectral measurement via TRES, we turn to kinetic Monte Carlo (KMC) simulations that take into account a more complete description of dipole-dipole coupling beyond the typical near-field Förster theory. As a reminder, this analysis is current at the time of this writing, and it may continue to evolve as we refine our understanding and exploration of the system photophysics. The below analysis was carried out by my colleague, **Rongfeng Yuan**.

To refine the KMC simulations, we use the results from the single-particle emission measurements of 5% CdSe:Te/CdS QDs (Section 5.4), where we determined the homogeneous linewidth of $\sigma_{\text{homo}}$ ∼75 meV. To account for the heterogeneity present in the ensemble of QDs in a QDSL, we randomly draw emission peaks (i.e. bandgap energies) from the single-particle peak emission distribution shown in Figure 5.18b of the 5% doped CdSe:Te/CdS particles for each individual QD in the simulated grid. With these conditions we propagate trajectories using a treatment similar to that outlined previously (Section 5.5.1). By incorporating spectral heterogeneity, these simulations are not only more physically representative of the investigated system, but, also enable tracking changes to the mean exciton energy over all time points in the simulation, which would have been trivial assuming all QDs are isoenergetic

as in Section 5.5.1.

Figure 5.30 presents the change in the emission peak energy from TRES (green data, also shown in Figure 5.11) as well as the change in the mean exciton energy from KMC simulations involving two different rates of energy transfer. The simulation parameters are adjusted such that the average diffusivity of the simulated trajectories matches the diffusivity reported by TRUSTED (e.g. between 1.7 and 4.4 $\times 10^{-3}$ cm$^2$/s) in each case. One simulation uses the typical FRET equation and the distance dependence for the energy transfer rate is proportional strictly to $R^{-6}$ (black curve), as expected for near-field energy transfer. The other simulation (red curve) involves a more complete description of dipole-dipole coupling [305], which contains higher order terms beyond the near field, which represent three different distance-dependent regimes: $R^{-6}$ (near-field), $R^{-4}$ (intermediate), and $R^{-2}$ (far-field). The equation used for this particular energy transfer description in the simulations is a modified version of the equation presented in Ref [305]:

$$k_{\mathrm{ET}} = \frac{1}{\tau_D}\left(\frac{R_o}{R}\right)^6 \left(3 + (kR)^2 + \gamma(kR)^4\right) e^{-R/l} \tag{5.20}$$

where $k$ is the reduced wavelength of the sample's emission ($2\pi/\lambda$, $\sim$0.01 nm), $\tau_{\mathrm{D}}$ is the donor lifetime, and $R_o$ is the FRET radius. In addition, $\gamma$ is a phenomenological parameter introduced to control the relative contribution of the $R^{-2}$ term. Finally, the exponential term, $e^{-R/l}$ accounts for the possibility of re-absorption in the material, where $l$ represents the characteristic transmission length estimated from the the film's absorptivity. We take $l$ to be $\sim$ 1000 nm.

The simulations reveal that using a mechanism for energy transport with only near field considerations ($R^{-6}$) and an average exciton diffusivity that matches TRUSTED (using an $R_o \sim 14$ nm) will result in a rate of change of the mean exciton energy that is much faster than TRES reports. If the mechanism of energy transport follows that described by Equation 5.20, a rate of change of the mean exciton energy for simulated trajectories possessing an average diffusivity matching TRUSTED may also match TRES, provided we use a value of $\gamma$ of 14 and a $R_o \sim 8.8$ nm. One possible interpretation of this $\gamma$ parameter is that it represents far field contributions from waveguiding, where a subset of photons emitted from a given point in the film experience total internal reflection and continue to propagate within the plane of the QDSL monolayer. Regardless of the actual mechanism, these simulations critically reveal that a portion of the exciton transfers must occur between QDs separated by distances greater than nearest-neighbors ($\sim$8.9 nm). The requisite $R_o$ to match the diffusivity reported by TRUSTED is overall lower in the more complete dipole-dipole coupling treatment than in the FRET treatment, which leads to a slower rate of the mean exciton energy decay. Despite the challenges discussed for efficient photon recycling (Section 5.5.4), which is the physical manifestation of the $R^{-2}$ term's contribution to the energy transfer rate, the simulations reveal that only 2-3% of exciton transfers need be a result of such far field interactions. To be clear, though, in each KMC simulation from Figure 5.30 we require $R_o$ values that still exceed the estimates born out of the analysis in Section 5.5.1, even upon using the more

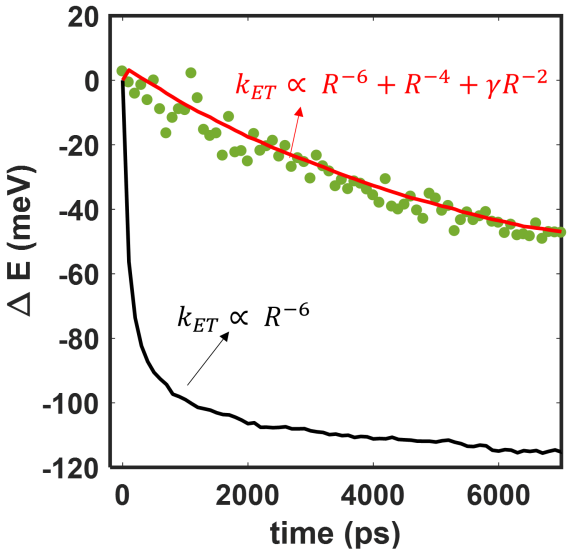


Figure 5.30: KMC simulations of the change of the mean exciton energy vs time to reconcile diffusivity measured from TRUSTED with rate of energy decay measured from TRES.

complete dipole-dipole coupling description case.

## 5.7 Preliminary Conclusion

Thus far, we have studied non-equilibrium exciton transport in Tellurium doped CdSe/CdS quantum dot superlattice monolayers, both spatially with TRUSTED and spectrally with TRES. Te doping CdSe/CdS QDs enhances the inhomogeneous and homogeneous linewidth, as well as the Stokes shift, which we more directly characterize via single-particle emission. Despite the larger intrinsic linewidth, the greater degree of inhomogeneity and larger Stokes shift likely results in slower exciton transport in doped superlattices than those composed of undoped particles, based on the rate of energy decay from TRES.

Although this presumably lower exciton diffusivity is a consequence of the introduction of dopants, TRUSTED reveals that this diffusivity is still on the order of $10^{-3}$ cm$^2$/s after the first 4.8 ns of creation. Such a diffusivity dramatically exceeds what conventional models of energy transport would predict for this system. FRET is historically the mechanism invoked to describe transport in organic-ligand decorated QD solids, but as discussed in detail in Section 5.5.1, we require either a significant series of corrections to a FRET model, or that we have underestimated parameters used in estimating the transport, or both. This may speak to the more general observation that transport in quantum dot solids is still lacking a comprehensive mechanistic description. The answer to such a question is beyond the scope

of the current work, and although we do speculate about possible transport mechanisms, we can more readily discuss the consequences of the dopants introducing a greater degree of heterogeneity to the energetic landscape.

Through a judicious combination of single-particle emission spectroscopy, which more directly probes inhomogeneity amongst the QD ensemble, TRES, which reveals the magnitude and rate at which energy decays in the system, and TRUSTED, which spatially resolves the transport on relevant nanometer length scales, we more comprehensively characterize the effects of Te dopants on exciton transport in CdSe:Te/CdS superlattices. We suspect the larger intrinsic linewidth caused by Te dopants could serve to buffer, to an extent, the higher degree of spectral inhomogeneity. Still, our findings suggest that synthetic protocols which provide better control over the distribution of dopants amongst QDs will need to be developed in order to minimize the energy loss within the system, which is evident from TRES. Our TRUSTED results, when modelled with time-dependent diffusivity, suggest that the exciton diffusivity will continuously decrease until it has reached equilibrium, and by 4.8 ns will have decreased by a factor $\sim$3.4. Yet, the fact that doping doesn't completely suppress transport also suggests that, provided the doping levels are precise enough, stacked superlattices of nanocrystals with varying doping levels could be a viable design for long distance energy gradients. Such a design should alleviate disorder introduced by the spatial mismatch of arrays of different sized QDs.

Remaining questions involve reconciling the rate of energy decay in the system reported by TRES with the diffusivity extracted from TRUSTED. We find thus far that using a FRET model with the requisite $R_o$ to match the diffusivity reported by TRUSTED leads to a rate of energy decay that is much faster than TRES reports. As of now, it would appear that in order to achieve a rate of energy decay that is sufficiently slow to match TRES but a diffusivity that is sufficiently high to match TRUSTED we need to allow for exciton hopping to occur at distances greater than the nearest neighbors. At present, we hypothesize that a small subset of excitons participate in photon recycling, which is facilitated to a certain degree by waveguiding within the plane of the QDSL monolayer.

# Chapter 6

# Concluding Remarks

This dissertation has presented several different characterizations of the various ways in which the underlying structure of heterogeneous materials manifests in their resulting dynamics. Chapter 1 provided the necessary background, covering the motivation behind studying solution processable materials, the relevant chromophore and/or semiconductor photophysics, as well as an overview of diffusion, which is a dynamical phenomenon at the heart of the motivation (either explicitly or implicitly) behind each of the studied projects. Similarly, an introduction to fluorescence microscopy was provided to supplement Chapters 3,4,5 which all rely on the technique.

Chapter 2 described ultrafast transient absorption (TA) measurements characterizing the excited state evolution of a biomimetic light harvesting complex with a series of chromophore-protein chemical linking groups that vary in their length and rigidity. We find changing the linkers enables control over the degree of coupling between SRB and its protein/solvent environment on the cpTMV light harvesting platform. The findings here suggest using chemical linking groups to more readily position a chromophore in the vicinity of relatively dense amino acid residue regions can lead to a dramatic slowing of its excited state evolution. We suggest such a retardation of the excited state relaxation can in principle be employed by natural systems to more readily exchange excitation energy among other choromphores within a light harvesting network.

Chapter 3 involved correlative widefield single-particle tracking and AFM phase imaging to explicitly determine the extent polymer crystallites in electrolytic thin films of poly(ethylene oxide) (PEO) influence neutral probe transport. Critically, we note that although adjacent crystallites with nanoscale spacing anisotropically constrain the motion of the fluorescent probe species, the crystallites do not perturb the intrinsic diffusivity of the probes. Only by characterizing *both* the crystalline/amorphous polymer phase distribution and particle motion at the relevant nanoscale could we establish such a manifest structure-function relationship. Moreover, this study suggest crystallites, if controlled, could enable deterministic mass transport along well-defined amorphous channels.

Chapter 4 introduced our group's ultrafast transformation of stimulated emission depletion (STED) microscopy, referred to as time resolved ultrafast STED (TRUSTED). This

description was first supplemented with an overview of STED microscopy and the implementations developed in order to use STED microscopy with electronically coupled materials. In order to use TRUSTED to measure exciton migration, care must be taken to reconcile sample photophysics with sample-STED pulse interactions. To this end we provided a few examples where systems bearing rich photophysics will require adapting the current TRUSTED approach in order to isolate signatures of exciton migration.

Finally, chapter 5 discussed an ongoing investigation, at the time of this writing, of exciton migration within Tellurium doped CdSe/CdS quantum dot superlattice (QDSL) monolayers. Here we used the TRUSTED method from Chapter 4 to spatiotemporally resolve exciton migration after the first 4.8 ns of photoexcitation, and complemented this measurement with time-resolved emission spectroscopy (TRES) and single-particle emission spectroscopy. TRES revealed the mean exciton energy decays as a function of time after photoexcitation, and suggested the energetic heterogeneity introduced by the Tellurium dopants, which we directly characterized via single-particle emission, leads to non-equilibrium exciton transport. The exciton diffusivity we measured, however, is higher than conventional models of energy transport would suggest, and furthermore using such models we find ourselves incapable of reconciling the time-rate of energy decay measured via TRES with the exciton diffusivity measured via TRUSTED. To this end, we tentatively suggest that a small fraction of excitons participate in photon recycling and that such far-field interactions give rise to higher apparent exciton diffusivities.

Taken together, these studies emphasize that in order to characterize dynamics in materials that are influenced by material heterogeneity, no single tool nor method alone is capable of addressing all systems on their relevant length and time scales. This thesis combines and leverages several state-of-the-art spectroscopies and microscopies to explore material dynamics ranging from 10s of femtoseconds to minutes and material length scales ranging from 10s of nanometers to 100s of microns. It is my hope that this work serves as inspiration to become familiar with, combine, or develop new tools to tackle pressing questions regarding the intricate structure-function relationships of next generation materials.

# Bibliography


(1) Cui, Y.; Wan, J.; Ye, Y.; Liu, K.; Chou, L.-Y.; Cui, Y. *Nano Letters* **2020**, *20*, 1686–1692.

(2) Kim, D. H.; Oh, D. Y.; Park, K. H.; Choi, Y. E.; Nam, Y. J.; Lee, H. A.; Lee, S.-M.; Jung, Y. S. *Nano Letters* **2017**, *17*, Publisher: American Chemical Society, 3013–3020.

(3) Noriega, R.; Rivnay, J.; Vandewal, K.; Koch, F. P. V.; Stingelin, N.; Smith, P.; Toney, M. F.; Salleo, A. *Nature Materials* **2013**, *12*, Number: 11 Publisher: Nature Publishing Group, 1038–1044.

(4) Tan, P.; Wang, H.; Xiao, F.; Lu, X.; Shang, W.; Deng, X.; Song, H.; Xu, Z.; Cao, J.; Gan, T.; Wang, B.; Zhou, X. *Nature Communications* **2022**, *13*, Number: 1 Publisher: Nature Publishing Group, 358.

(5) Someya, T.; Bao, Z.; Malliaras, G. G. *Nature* **2016**, *540*, Number: 7633 Publisher: Nature Publishing Group, 379–385.

(6) Allard, S.; Forster, M.; Souharce, B.; Thiem, H.; Scherf, U. *Angewandte Chemie International Edition* **2008**, *47*, 4070–4098.

(7) Coropceanu, V.; Cornil, J.; da Silva Filho, D. A.; Olivier, Y.; Silbey, R.; Brédas, J.-L. *Chemical Reviews* **2007**, *107*, Publisher: American Chemical Society, 926–952.

(8) Coropceanu, I. et al. *Science* **2022**, *375*, Publisher: American Association for the Advancement of Science, 1422–1426.

(9) Hanifi, D. A.; Bronstein, N. D.; Koscher, B. A.; Nett, Z.; Swabeck, J. K.; Takano, K.; Schwartzberg, A. M.; Maserati, L.; Vandewal, K.; van de Burgt, Y.; Salleo, A.; Alivisatos, A. P. *Science* **2019**, *363*, Publisher: American Association for the Advancement of Science, 1199–1202.

(10) Miller, R. A.; Presley, A. D.; Francis, M. B. *Journal of the American Chemical Society* **2007**, *129*, Publisher: American Chemical Society, 3104–3109.

(11) Xue, Z.; He, D.; Xie, X. *J. Mater. Chem. A* **2015**, *3*, 19218–19253.

(12) Choudhury, S.; Stalin, S.; Vu, D.; Warren, A.; Deng, Y.; Biswal, P.; Archer, L. A. *Nature Communications* **2019**, *10*, Number: 1 Publisher: Nature Publishing Group, 4398.

(13) Keum, C.; Murawski, C.; Archer, E.; Kwon, S.; Mischok, A.; Gather, M. C. *Nature Communications* **2020**, *11*, Number: 1 Publisher: Nature Publishing Group, 6250.

(14) Li, J.; Tang, W.; Wang, Q.; Sun, W.; Zhang, Q.; Guo, X.; Wang, X.; Yan, F. *Materials Science and Engineering: R: Reports* **2018**, *127*, 1–36.

(15) Moon, H.; Lee, C.; Lee, W.; Kim, J.; Chae, H. *Advanced Materials* **2019**, *31*, _eprint: https://onlinelibrary.wiley.com/doi/pdf/10.1002/adma.201804294, 1804294.

(16) Ginsberg, N. S.; Tisdale, W. A. *Annual Review of Physical Chemistry* **2020**, *71*, 1–30.

(17) Nozik, A. J.; Beard, M. C.; Luther, J. M.; Law, M.; Ellingson, R. J.; Johnson, J. C. *Chemical Reviews* **2010**, *110*, Publisher: American Chemical Society, 6873–6890.

(18) West, B. A.; Womick, J. M.; McNeil, L. E.; Tan, K. J.; Moran, A. M. *The Journal of Physical Chemistry C* **2010**, *114*, Publisher: American Chemical Society, 10580–10591.

(19) Peterson, M. D.; Cass, L. C.; Harris, R. D.; Edme, K.; Sung, K.; Weiss, E. A. *Annual Review of Physical Chemistry* **2014**, *65*, _eprint: https://doi.org/10.1146/annurev-physchem-040513-103649, 317–339.

(20) Noriega, R.; Finley, D. T.; Haberstroh, J.; Geissler, P. L.; Francis, M. B.; Ginsberg, N. S. *The Journal of Physical Chemistry B* **2015**, *119*, Publisher: American Chemical Society, 6963–6973.

(21) Wang, H.; McNellis, E. R.; Kinge, S.; Bonn, M.; Cánovas, E. *Nano Letters* **2013**, *13*, Publisher: American Chemical Society, 5311–5315.

(22) Cha, H.; Wheeler, S.; Holliday, S.; Dimitrov, S. D.; Wadsworth, A.; Lee, H. H.; Baran, D.; McCulloch, I.; Durrant, J. R. *Advanced Functional Materials* **2018**, *28*, _eprint: https://onlinelibrary.wiley.com/doi/pdf/10.1002/adfm.201704389, 1704389.

(23) Grancini, G.; Maiuri, M.; Fazzi, D.; Petrozza, A.; Egelhaaf, H.-J.; Brida, D.; Cerullo, G.; Lanzani, G. *Nature Materials* **2013**, *12*, Number: 1 Publisher: Nature Publishing Group, 29–33.

(24) Le, A. K.; Bender, J. A.; Arias, D. H.; Cotton, D. E.; Johnson, J. C.; Roberts, S. T. *Journal of the American Chemical Society* **2018**, *140*, Publisher: American Chemical Society, 814–826.

(25) Berezin, M. Y.; Achilefu, S. *Chemical Reviews* **2010**, *110*, Publisher: American Chemical Society, 2641–2684.

(26) Morello, G.; De Giorgi, M.; Kudera, S.; Manna, L.; Cingolani, R.; Anni, M. *The Journal of Physical Chemistry C* **2007**, *111*, Publisher: American Chemical Society, 5846–5849.

(27) Grabolle, M.; Ziegler, J.; Merkulov, A.; Nann, T.; Resch-Genger, U. *Annals of the New York Academy of Sciences* **2008**, *1130*, 235–241.

(28) Lakowicz, J. R., *Principles of Fluorescence Spectroscopy*; Springer Science & Business Media: 2007.

(29) F. Haneef, H.; M. Zeidell, A.; D. Jurchescu, O. *Journal of Materials Chemistry C* **2020**, *8*, Publisher: Royal Society of Chemistry, 759–787.

(30) Wu, P.; Yan, X.-P. *Chemical Society Reviews* **2013**, *42*, Publisher: Royal Society of Chemistry, 5489–5521.

(31) Beaulac, R.; Schneider, L.; Archer, P. I.; Bacher, G.; Gamelin, D. R. *Science* **2009**, *325*, Publisher: American Association for the Advancement of Science, 973–976.

(32) Avidan, A.; Oron, D. *Nano Letters* **2008**, *8*, Publisher: American Chemical Society, 2384–2387.

(33) Yuste, R. *Nature Methods* **2005**, *2*, Number: 12 Publisher: Nature Publishing Group, 902–904.

(34) Lichtman, J. W.; Conchello, J.-A. *Nature Methods* **2005**, *2*, Number: 12 Publisher: Nature Publishing Group, 910–919.

(35) Childress, L.; Gurudev Dutt, M. V.; Taylor, J. M.; Zibrov, A. S.; Jelezko, F.; Wrachtrup, J.; Hemmer, P. R.; Lukin, M. D. *Science* **2006**, *314*, Publisher: American Association for the Advancement of Science, 281–285.

(36) Shaik, A. B. D.-j.-w.-i.; Palla, P. *Scientific Reports* **2021**, *11*, Number: 1 Publisher: Nature Publishing Group, 12285.

(37) Werner, C.; Sauer, M.; Geis, C. *Chemical Reviews* **2021**, *121*, Publisher: American Chemical Society, 11971–12015.

(38) Xu, K.; Zhong, G.; Zhuang, X. *Science* **2013**, *339*, Publisher: American Association for the Advancement of Science, 452–456.

(39) Akselrod, G. M.; Prins, F.; Poulikakos, L. V.; Lee, E. M. Y.; Weidman, M. C.; Mork, A. J.; Willard, A. P.; Bulović, V.; Tisdale, W. A. *Nano Letters* **2014**, DOI: 10.1021/nl501190s.

(40) Robbins, M.; Hadwen, B. *IEEE Transactions on Electron Devices* **2003**, *50*, Conference Name: IEEE Transactions on Electron Devices, 1227–1232.

(41) Chen, R.; Wu, R.; Zhang, G.; Gao, Y.; Xiao, L.; Jia, S. *Sensors* **2014**, *14*, Number: 2 Publisher: Multidisciplinary Digital Publishing Institute, 2449–2467.

(42) Thiele, J. C.; Helmerich, D. A.; Oleksiievets, N.; Tsukanov, R.; Butkevich, E.; Sauer, M.; Nevskyi, O.; Enderlein, J. *ACS Nano* **2020**, *14*, Publisher: American Chemical Society, 14190–14200.

(43) Sarder, P.; Maji, D.; Achilefu, S. *Bioconjugate Chemistry* **2015**, *26*, Publisher: American Chemical Society, 963–974.

(44) Abbe, E. *Archiv für Mikroskopische Anatomie* **1873**, *9*, 413–468.

(45) Axelrod, D. *Journal of Biomedical Optics* **2001**, *6*, Publisher: SPIE, 6–13.

(46) Scholes, G. D.; Fleming, G. R.; Olaya-Castro, A.; van Grondelle, R. *Nature Chemistry* **2011**, *3*, Number: 10 Publisher: Nature Publishing Group, 763–774.

(47) Pujals, S.; Feiner-Gracia, N.; Delcanale, P.; Voets, I.; Albertazzi, L. *Nature Reviews Chemistry* **2019**, *3*, Number: 2 Publisher: Nature Publishing Group, 68–84.

(48) Möckl, L.; Lamb, D. C.; Bräuchle, C. *Angewandte Chemie International Edition* **2014**, *53*, _eprint: https://onlinelibrary.wiley.com/doi/pdf/10.1002/anie.201410265, 13972–13977.

(49) Cardellini, J.; Balestri, A.; Montis, C.; Berti, D. *Pharmaceutics* **2021**, *13*, 861.

(50) Berg, H. C., *Random Walks in Biology: New and Expanded Edition*, Publication Title: Random Walks in Biology; Princeton University Press: 1992.

(51) Pinsky, M. A.; Karlin, S. In *An Introduction to Stochastic Modeling (Fourth Edition)*, Pinsky, M. A., Karlin, S., Eds.; Academic Press: Boston, 2011, pp 391–446.

(52) Kubo, R. *Reports on Progress in Physics* **1966**, *29*, Publisher: IOP Publishing, 255–284.

(53) Chmyrov, V.; Spielmann, T.; Hevekerl, H.; Widengren, J. *Analytical Chemistry* **2015**, *87*, Publisher: American Chemical Society, 5690–5697.

(54) Xiang, L.; Chen, K.; Yan, R.; Li, W.; Xu, K. *Nature Methods* **2020**, *17*, Number: 5 Publisher: Nature Publishing Group, 524–530.

(55) Chambers, J. E.; Kubánková, M.; Huber, R. G.; López-Duarte, I.; Avezov, E.; Bond, P. J.; Marciniak, S. J.; Kuimova, M. K. *ACS Nano* **2018**, *12*, 4398–4407.

(56) Michels, L.; Gorelova, V.; Harnvanichvech, Y.; Borst, J. W.; Albada, B.; Weijers, D.; Sprakel, J. *Proceedings of the National Academy of Sciences* **2020**, *117*, Publisher: Proceedings of the National Academy of Sciences, 18110–18118.

(57) Fassioli, F.; Dinshaw, R.; Arpin, P. C.; Scholes, G. D. *Journal of The Royal Society Interface* **2014**, *11*, Publisher: Royal Society, 20130901.

(58) Caruso, F.; Chin, A. W.; Datta, A.; Huelga, S. F.; Plenio, M. B. *The Journal of Chemical Physics* **2009**, *131*, Publisher: American Institute of Physics, 105106.

(59) Roszak, A. W.; Howard, T. D.; Southall, J.; Gardiner, A. T.; Law, C. J.; Isaacs, N. W.; Cogdell, R. J. *Science* **2003**, *302*, Publisher: American Association for the Advancement of Science, 1969–1972.

(60) Blankenship, R. E. In *Molecular Mechanisms of Photosynthesis*; John Wiley & Sons, Ltd: 2002, pp 1–10.

(61) Herek, J. L.; Fraser, N. J.; Pullerits, T.; Martinsson, P.; Polívka, T.; Scheer, H.; Cogdell, R. J.; Sundström, V. *Biophysical Journal* **2000**, *78*, 2590–2596.

(62) Magdaong, N. M.; LaFountain, A. M.; Greco, J. A.; Gardiner, A. T.; Carey, A.-M.; Cogdell, R. J.; Gibson, G. N.; Birge, R. R.; Frank, H. A. *The Journal of Physical Chemistry B* **2014**, *118*, Publisher: American Chemical Society, 11172–11189.

(63) Cohen-Ofri, I.; van Gastel, M.; Grzyb, J.; Brandis, A.; Pinkas, I.; Lubitz, W.; Noy, D. *Journal of the American Chemical Society* **2011**, *133*, Publisher: American Chemical Society, 9526–9535.

(64) Gust, D.; Moore, T. A.; Moore, A. L. *Accounts of Chemical Research* **2001**, *34*, Publisher: American Chemical Society, 40–48.

(65) Peng, H.-Q.; Niu, L.-Y.; Chen, Y.-Z.; Wu, L.-Z.; Tung, C.-H.; Yang, Q.-Z. *Chemical Reviews* **2015**, *115*, 7502–7542.

(66) Nam, Y. S.; Shin, T.; Park, H.; Magyar, A. P.; Choi, K.; Fantner, G.; Nelson, K. A.; Belcher, A. M. *Journal of the American Chemical Society* **2010**, *132*, Publisher: American Chemical Society, 1462–1463.

(67) Springer, J. W.; Parkes-Loach, P. S.; Reddy, K. R.; Krayer, M.; Jiao, J.; Lee, G. M.; Niedzwiedzki, D. M.; Harris, M. A.; Kirmaier, C.; Bocian, D. F.; Lindsey, J. S.; Holten, D.; Loach, P. A. *Journal of the American Chemical Society* **2012**, *134*, Publisher: American Chemical Society, 4589–4599.

(68) Park, H. et al. *Nature Materials* **2016**, *15*, Number: 2 Publisher: Nature Publishing Group, 211–216.

(69) Utschig, L. M.; Soltau, S. R.; Tiede, D. M. *Current Opinion in Chemical Biology* **2015**, *25*, 1–8.

(70) Farid, T. A. et al. *Nature Chemical Biology* **2013**, *9*, Number: 12 Publisher: Nature Publishing Group, 826–833.

(71) Endo, M.; Fujitsuka, M.; Majima, T. *Chemistry – A European Journal* **2007**, *13*, _eprint: https://onlinelibrary.wiley.com/doi/pdf/10.1002/chem.200700895, 8660–8666.

(72) Renger, T. *Photosynthesis Research* **2009**, *102*, 471–485.

(73) Lee, H.; Cheng, Y.-C.; Fleming, G. R. *Science* **2007**, *316*, Publisher: American Association for the Advancement of Science, 1462–1465.

(74) Arpino, J. A. J.; Czapinska, H.; Piasecka, A.; Edwards, W. R.; Barker, P.; Gajda, M. J.; Bochtler, M.; Jones, D. D. *Journal of the American Chemical Society* **2012**, *134*, Publisher: American Chemical Society, 13632–13640.

(75) Sarovar, M.; Whaley, K. B. *New Journal of Physics* **2013**, *15*, Publisher: IOP Publishing, 013030.

(76) Grondelle, R. v.; Novoderezhkin, V. I. *Physical Chemistry Chemical Physics* **2006**, *8*, Publisher: The Royal Society of Chemistry, 793–807.

(77) Renger, T.; May, V.; Kühn, O. *Physics Reports* **2001**, *343*, 137–254.

(78) McDermott, G.; Prince, S. M.; Freer, A. A.; Hawthornthwaite-Lawless, A. M.; Papiz, M. Z.; Cogdell, R. J.; Isaacs, N. W. *Nature* **1995**, *374*, Number: 6522 Publisher: Nature Publishing Group, 517–521.

(79) Jordan, P.; Fromme, P.; Witt, H. T.; Klukas, O.; Saenger, W.; Krauß, N. *Nature* **2001**, *411*, Number: 6840 Publisher: Nature Publishing Group, 909–917.

(80) Liu, Z.; Yan, H.; Wang, K.; Kuang, T.; Zhang, J.; Gui, L.; An, X.; Chang, W. *Nature* **2004**, *428*, Number: 6980 Publisher: Nature Publishing Group, 287–292.

(81) Hu, X.; Ritz, T.; Damjanović, A.; Autenrieth, F.; Schulten, K. *Quarterly Reviews of Biophysics* **2002**, *35*, Publisher: Cambridge University Press, 1–62.

(82) Dedeo, M. T.; Duderstadt, K. E.; Berger, J. M.; Francis, M. B. *Nano Letters* **2010**, *10*, Publisher: American Chemical Society, 181–186.

(83) Wen, A. M.; Steinmetz, N. F. *Chemical Society Reviews* **2016**, *45*, Publisher: The Royal Society of Chemistry, 4074–4126.

(84) Ma, Y.-Z.; Miller, R. A.; Fleming, G. R.; Francis, M. B. *The Journal of Physical Chemistry B* **2008**, *112*, Publisher: American Chemical Society, 6887–6892.

(85) Maiuri, M.; Garavelli, M.; Cerullo, G. *Journal of the American Chemical Society* **2020**, *142*, Publisher: American Chemical Society, 3–15.

(86) Berera, R.; van Grondelle, R.; Kennis, J. T. M. *Photosynthesis Research* **2009**, *101*, 105–118.

(87) Wang, L.; McCleese, C.; Kovalsky, A.; Zhao, Y.; Burda, C. *Journal of the American Chemical Society* **2014**, *136*, Publisher: American Chemical Society, 12205–12208.

(88) Cabanillas-Gonzalez, J.; Grancini, G.; Lanzani, G. *Advanced Materials* **2011**, *23*, _eprint: https://onlinelibrary.wiley.com/doi/pdf/10.1002/adma.201102015, 5468–5485.

(89) Corp, K. L.; Schlenker, C. W. *Journal of the American Chemical Society* **2017**, *139*, Publisher: American Chemical Society, 7904–7912.

(90) Wu, K.; Zhu, H.; Liu, Z.; Rodríguez-Córdoba, W.; Lian, T. *Journal of the American Chemical Society* **2012**, *134*, Publisher: American Chemical Society, 10337–10340.

(91) Attar, A. R.; Bhattacherjee, A.; Pemmaraju, C. D.; Schnorr, K.; Closser, K. D.; Prendergast, D.; Leone, S. R. *Science* **2017**, *356*, Publisher: American Association for the Advancement of Science, 54–59.

(92) Beck, A. R.; Neumark, D. M.; Leone, S. R. *Chemical Physics Letters* **2015**, *624*, 119–130.

(93) Manzoni, C.; Cerullo, G. *Journal of Optics* **2016**, *18*, 103501.

(94) Van Stokkum, I. H. M.; Larsen, D. S.; van Grondelle, R. *Biochimica et Biophysica Acta (BBA) - Bioenergetics* **2004**, *1657*, 82–104.

(95) Sabatini, R. P.; Mark, M. F.; Mark, D. J.; Kryman, M. W.; Hill, J. E.; Brennessel, W. W.; Detty, M. R.; Eisenberg, R.; McCamant, D. W. *Photochemical & Photobiological Sciences* **2016**, *15*, Publisher: The Royal Society of Chemistry, 1417–1432.

(96) Grabowski, Z. R.; Rotkiewicz, K.; Rettig, W. *Chemical Reviews* **2003**, *103*, 3899–4032.

(97) Savarese, M.; Aliberti, A.; De Santo, I.; Battista, E.; Causa, F.; Netti, P. A.; Rega, N. *The Journal of Physical Chemistry A* **2012**, *116*, Publisher: American Chemical Society, 7491–7497.

(98) Savarese, M.; Raucci, U.; Adamo, C.; Netti, P. A.; Ciofini, I.; Rega, N. *Physical Chemistry Chemical Physics* **2014**, *16*, Publisher: The Royal Society of Chemistry, 20681–20688.

(99) Zhang, X.-F.; Zhang, Y.; Liu, L. *Journal of Luminescence* **2014**, *145*, 448–453.

(100) Fedoseeva, M.; Letrun, R.; Vauthey, E. *The Journal of Physical Chemistry B* **2014**, *118*, Publisher: American Chemical Society, 5184–5193.

(101) Best, R. B.; Hofmann, H.; Nettels, D.; Schuler, B. *Biophysical Journal* **2015**, *108*, 2721–2731.

(102) Laage, D.; Elsaesser, T.; Hynes, J. T. *Chemical Reviews* **2017**, *117*, Publisher: American Chemical Society, 10694–10725.

(103) Jordanides, X. J.; Lang, M. J.; Song, X.; Fleming, G. R. *The Journal of Physical Chemistry B* **1999**, *103*, Publisher: American Chemical Society, 7995–8005.

(104) Pal, S. K.; Zewail, A. H. *Chemical Reviews* **2004**, *104*, Publisher: American Chemical Society, 2099–2124.

(105) Bagchi, B. *Chemical Reviews* **2005**, *105*, Publisher: American Chemical Society, 3197–3219.

(106) Nilsson, L.; Halle, B. *Proceedings of the National Academy of Sciences* **2005**, *102*, Publisher: National Academy of Sciences Section: Biological Sciences, 13867–13872.

(107) Li, T.; Hassanali, A. A.; Kao, Y.-T.; Zhong, D.; Singer, S. J. *Journal of the American Chemical Society* **2007**, *129*, Publisher: American Chemical Society, 3376–3382.

(108) Furse, K. E.; Corcelli, S. A. *Journal of the American Chemical Society* **2008**, *130*, Publisher: American Chemical Society, 13103–13109.

(109) Yang, M.; Szyc, Ł.; Elsaesser, T. *The Journal of Physical Chemistry B* **2011**, *115*, Publisher: American Chemical Society, 13093–13100.

(110) Sterpone, F.; Stirnemann, G.; Laage, D. *Journal of the American Chemical Society* **2012**, *134*, Publisher: American Chemical Society, 4116–4119.

(111) King, J. T.; Arthur, E. J.; Brooks, C. L.; Kubarych, K. J. *The Journal of Physical Chemistry B* **2012**, *116*, Publisher: American Chemical Society, 5604–5611.

(112) Halle, B.; Nilsson, L. *The Journal of Physical Chemistry B* **2009**, *113*, Publisher: American Chemical Society, 8210–8213.

(113) Furse, K. E.; Corcelli, S. A. *Journal of the American Chemical Society* **2011**, *133*, Publisher: American Chemical Society, 720–723.

(114) Bakulin, A. A.; Pshenichnikov, M. S.; Bakker, H. J.; Petersen, C. *The Journal of Physical Chemistry A* **2011**, *115*, Publisher: American Chemical Society, 1821–1829.

(115) Tronrud, D. E.; Wen, J.; Gay, L.; Blankenship, R. E. *Photosynthesis Research* **2009**, *100*, 79–87.

(116) Penwell, S. B.; Ginsberg, L. D. S.; Noriega, R.; Ginsberg, N. S. *Nature Materials* **2017**, *16*, 1136–1141.

(117) Delor, M.; Weaver, H. L.; Yu, Q.; Ginsberg, N. S. *Nature Materials* **2020**, *19*, Number: 1 Publisher: Nature Publishing Group, 56–62.

(118) Wahadoszamen, M.; Margalit, I.; Ara, A. M.; van Grondelle, R.; Noy, D. *Nature Communications* **2014**, *5*, Number: 1 Publisher: Nature Publishing Group, 5287.

(119) Scholes, G. D. et al. *Nature* **2017**, *543*, Number: 7647 Publisher: Nature Publishing Group, 647–656.

(120) Fuller, F. D.; Pan, J.; Gelzinis, A.; Butkus, V.; Senlik, S. S.; Wilcox, D. E.; Yocum, C. F.; Valkunas, L.; Abramavicius, D.; Ogilvie, J. P. *Nature Chemistry* **2014**, *6*, Number: 8 Publisher: Nature Publishing Group, 706–711.

(121) Ghosh, S.; Bishop, M. M.; Roscioli, J. D.; LaFountain, A. M.; Frank, H. A.; Beck, W. F. *The Journal of Physical Chemistry Letters* **2017**, *8*, Publisher: American Chemical Society, 463–469.

(122) *Brydson's Plastics Materials*, 8th Edition; Gilbert, M., Ed.; Butterworth-Heinemann: 2017.

(123) Bartczak, Z.; Argon, A.; Cohen, R.; Weinberg, M. *Polymer* **1999**, *40*, 2331–2346.

(124) Mollinger, S. A.; Krajina, B. A.; Noriega, R.; Salleo, A.; Spakowitz, A. J. *ACS Macro Letters* **2015**, *4*, 708–712.

(125) Pandey, A.; Toda, A.; Rastogi, S. *Macromolecules* **2011**, *44*, 8042–8055.

(126) Jabbari-Farouji, S.; Rottler, J.; Lame, O.; Makke, A.; Perez, M.; Barrat, J.-L. *ACS Macro Letters* **2015**, *4*, 147–150.

(127) Zhou, J.; Turner, S. A.; Brosnan, S. M.; Li, Q.; Carrillo, J.-M. Y.; Nykypanchuk, D.; Gang, O.; Ashby, V. S.; Dobrynin, A. V.; Sheiko, S. S. *Macromolecules* **2014**, *47*, 1768–1776.

(128) Toolan, D. T. W.; Pullan, N.; Harvey, M. J.; Topham, P. D.; Howse, J. R. *Advanced Materials* **2013**, *25*, 7033–7037.

(129) Sauer, B. B.; Hsiao, B. S. *Polymer* **1995**, *36*, 2553–2558.

(130) Rastogi, S.; Lippits, D. R.; Peters, G. W. M.; Graf, R.; Yao, Y.; Spiess, H. W. *Nature Materials* **2005**, *4*, 635–641.

(131) Balani, K.; Verma, V.; Agarwal, A.; Narayan, R. In *Biosurfaces*; John Wiley & Sons, Ltd: 2015, pp 329–344.

(132) Flory, P. J. *Journal of the American Chemical Society* **1962**, *84*, 2857–2867.

(133) Song, Y.; Feng, W.; Liu, K.; Yang, P.; Zhang, W.; Zhang, X. **2013**, *29*, 3853–3857.

(134) Paul J. Flory; Do Yeung Yoon *Nature* **1978**, *272*, 226–229.

(135) Zelikin, A. N. *ACS Nano* **2010**, *4*, 2494–2509.

(136) Crist, B.; Schultz, J. M. *Progress in Polymer Science* **2016**, *56*, 1–63.

(137) Dingler, C.; Dirnberger, K.; Ludwigs, S. *Macromolecular Rapid Communications* **2019**, *40*, Publisher: John Wiley & Sons, Ltd, 1800601.

(138) Li, C. Y.; Cheng, S. Z. D. In *Encyclopedia of Polymer Science and Technology*; John Wiley & Sons, Ltd: 2002.

(139) Goodenough, J. B.; Kim, Y. *Chemistry of Materials* **2010**, *22*, Publisher: American Chemical Society, 587–603.

(140) Robitaille, C. D.; Fauteux, D. *Journal of The Electrochemical Society* **1986**, *133*, 315–325.

(141) Stolwijk, N. A.; Wiencierz, M.; Heddier, C.; Kösters, J. *The Journal of Physical Chemistry B* **2012**, *116*, 3065–3074.

(142) Park, M. J. *Molecular Systems Design and Engineering* **2019**, *4*, Publisher: Royal Society of Chemistry, 239–251.

(143) Croce, F.; Appetecchi, G. B.; Persi, L.; Scrosati, B. *Nature* **1998**, *394*, 456–458.

(144) Li, X.; Cheng, S.; Zheng, Y.; Li, C. Y. *Molecular Systems Design & Engineering* **2019**, *4*, Publisher: The Royal Society of Chemistry, 793–803.

(145) Cheng, S.; Smith, D. M.; Li, C. Y. *Macromolecules* **2014**, *47*, Publisher: American Chemical Society, 3978–3986.

(146) Golodnitsky, D.; Strauss, E.; Peled, E.; Greenbaum, S. *Journal of The Electrochemical Society* **2015**, *162*, A2551–A2566.

(147) Sun, J.; Liao, X.; Minor, A. M.; Balsara, N. P.; Zuckermann, R. N. *Journal of the American Chemical Society* **2014**, *136*, 14990–14997.

(148) Fullerton-Shirey, S. K.; Maranas, J. K. *Macromolecules* **2009**, *42*, Publisher: American Chemical Society, 2142–2156.

(149) Minier, M.; Berthier, C.; Gorecki, W. *Journal de Physique* **1984**, *45*, 739–744.

(150) Rhodes, C. P.; Frech, R. *Macromolecules* **2001**, *34*, Publisher: American Chemical Society, 2660–2666.

(151) Stoeva, Z.; Martin-Litas, I.; Staunton, E.; Andreev, Y. G.; Bruce, P. G. *Journal of the American Chemical Society* **2003**, *125*, Publisher: American Chemical Society, 4619–4626.

(152) Gadjourova, Z.; Martín y Marero, D.; Andersen, K. H.; Andreev, Y. G.; Bruce, P. G. *Chemistry of Materials* **2001**, *13*, Publisher: American Chemical Society, 1282–1285.

(153) Zardalidis, G.; Ioannou, E.; Pispas, S.; Floudas, G. *Macromolecules* **2013**, *46*, Publisher: American Chemical Society, 2705–2714.

(154) Vallée, A.; Besner, S.; Prud'Homme, J. *Electrochimica Acta* **1992**, *37*, 1579–1583.

(155) Blumich, B.; Blümler, P. *Die Makromolekulare Chemie* **1993**, *194*, 2133–2161.

(156) McKenzie, I.; Harada, M.; Kiefl, R. F.; Levy, C. D. P.; MacFarlane, W. A.; Morris, G. D.; Ogata, S.-I.; Pearson, M. R.; Sugiyama, J. *Journal of the American Chemical Society* **2014**, *136*, Publisher: American Chemical Society, 7833–7836.

(157) Klett, M.; Giesecke, M.; Nyman, A.; Hallberg, F.; Lindström, R. W.; Lindbergh, G.; Furó, I. *Journal of the American Chemical Society* **2012**, *134*, Publisher: American Chemical Society, 14654–14657.

(158) Frech, R.; Chintapalli, S.; Bruce, P. G.; Vincent, C. A. *Macromolecules* **1999**, *32*, Publisher: American Chemical Society, 808–813.

(159) Money, B. K.; Swenson, J. *Macromolecules* **2013**, *46*, 6949–6954.

(160) Abbrent, S.; Greenbaum, S. *Current Opinion in Colloid & Interface Science* **2013**, *18*, 228–244.

(161) Bondia, P.; Casado, S.; Flors, C. In *Methods in Molecular Biology*, ISSN: 10643745; Humana Press Inc.: 2017; Vol. 1663, pp 105–113.

(162) Beuwer, M. A.; Knopper, M. F.; Albertazzi, L.; van der Zwaag, D.; Ellenbroek, W. G.; Meijer, E. W.; Prins, M. W. J.; Zijlstra, P. *Polymer Chemistry* **2016**, *7*, Publisher: Royal Society of Chemistry, 7260–7268.

(163) Cosentino, M.; Canale, C.; Bianchini, P.; Diaspro, A. *Science Advances* **2019**, *5*, Publisher: American Association for the Advancement of Science, eaav8062.

(164) Müller, D. J.; Dumitru, A. C.; Lo Giudice, C.; Gaub, H. E.; Hinterdorfer, P.; Hummer, G.; De Yoreo, J. J.; Dufrêne, Y. F.; Alsteens, D. *Chemical Reviews* **2021**, *121*, Publisher: American Chemical Society, 11701–11725.

(165) Tamayo, J.; Garcıa, R. *Applied Physics Letters* **1997**, *71*, 2394–2396.

(166) Gil, A.; Colchero, J.; Luna, M.; Gómez-Herrero, J.; Baró, A. M. *Langmuir* **2000**, *16*, 5086–5092.

(167) Stark, M.; Möller, C.; Müller, D. J.; Guckenberger, R. *Biophysical Journal* **2001**, *80*, 3009–3018.

(168) Garcıa, R. In *Amplitude Modulation Atomic Force Microscopy*; John Wiley & Sons, Ltd: 2010, pp 91–101.

(169) Shen, H.; Tauzin, L. J.; Baiyasi, R.; Wang, W.; Moringo, N.; Shuang, B.; Landes, C. F. *Chemical Reviews* **2017**, *117*, 7331–7376.

(170) Kusumi, A.; Tsunoyama, T. A.; Hirosawa, K. M.; Kasai, R. S.; Fujiwara, T. K. *Nature Chemical Biology* **2014**, *10*, 524–532.

(171) Haas, B. L.; Matson, J. S.; DiRita, V. J.; Biteen, J. S. *Molecular Microbiology* **2015**, *96*, _eprint: https://onlinelibrary.wiley.com/doi/pdf/10.1111/mmi.12834, 4–13.

(172) Flier, B. M. I.; Baier, M. C.; Huber, J.; Müllen, K.; Mecking, S.; Zumbusch, A.; Wöll, D. *Journal of the American Chemical Society* **2012**, *134*, 480–488.

(173) Bhattacharya, S.; Sharma, D. K.; Saurabh, S.; De, S.; Sain, A.; Nandi, A.; Chowdhury, A. *The Journal of Physical Chemistry B* **2013**, *117*, Publisher: American Chemical Society, 7771–7782.

(174) Kastantin, M.; Keller, T. F.; Jandt, K. D.; Schwartz, D. K. *Advanced Functional Materials* **2012**, *22*, 2617–2623.

(175) Chen, R.; Li, L.; Zhao, J. *Langmuir* **2010**, *26*, 5951–5956.

(176) Tran-Ba, K.-H.; Higgins, D. A.; Ito, T. *Analytical Chemistry* **2015**, *87*, Publisher: American Chemical Society, 5802–5809.

(177) Skaug, M. J.; Mabry, J. N.; Schwartz, D. K. *Journal of the American Chemical Society* **2014**, *136*, Publisher: American Chemical Society, 1327–1332.

(178) Moerner, W. E.; Orrit, M. *Science* **1999**, *283*, 1670–1676.

(179) Liao, Y.; Yang, S. K.; Koh, K.; Matzger, A. J.; Biteen, J. S. *Nano Lett* **2012**, *12*, 3085.

(180) Huang, B.; Bates, M.; Zhuang, X. *Annual Review of Biochemistry* **2009**, *78*, _eprint: https://doi.org/10.1146/annurev.biochem.77.061906.092014, 993–1016.

(181) Shroff, H.; Hess, S. T.; Betzig, E.; Hess, H. F.; Patterson, G. H.; Lippincott-Schwartz, J.; Davidson, M. W. ZEISS Microscopy Online Campus — Practical Aspects of Photoactivated Localization Microscopy (PALM).

(182) Edelstein, A. D.; Tsuchida, M. A.; Amodaj, N.; Pinkard, H.; Vale, R. D.; Stuurman, N. *Journal of Biological Methods* **2014**, *1*, e10.

(183) Schindelin, J. et al. *Nature Methods* **2012**, *9*, 676–682.

(184) Chenouard, N. et al. *Nature Methods* **2014**, *11*, Number: 3 Publisher: Nature Publishing Group, 281–289.

(185) Marzantowicz, M.; Krok, F.; Dygas, J. R.; Florjańczyk, Z.; Zygadło-Monikowska, E. *Solid State Ionics* **2008**, *179*, 1670–1678.

(186) Corrent, S.; Hahn, P.; Pohlers, G.; Connolly, T. J.; Scaiano, J. C.; Fornés, V.; García, H. **1998**, *102*, Publisher: American Chemical Society, 5852–5858.

(187) Scaiano, J. C.; Laferriere, M.; Ivan, M. G.; Taylor, G. N. **2003**, *36*, Publisher: American Chemical Society, 6692–6694.

(188) Fery-Forgues, S.; El-Ayoubi, R.; Lamère, J.-F. *Journal of Fluorescence* **2008**, *18*, Publisher: Springer US, 619–624.

(189) Ghosh, P.; Das, T.; Maity, A.; Mondal, S.; Purkayastha, P. *RSC Adv.* **2015**, *5*, 4214–4218.

(190) Yan, R.; Moon, S.; Kenny, S. J.; Xu, K. *Accounts of Chemical Research* **2018**, *51*, 697–705.

(191) Zhang, Z.; Kenny, S. J.; Hauser, M.; Li, W.; Xu, K. *Nature Methods* **2015**, *12*, 935–938.

(192) Li, L.; Chan, C.-M.; Yeung, K. L.; Li, J.-X.; Ng, K.-M.; Lei, Y. **2001**, *34*, 316–325.

(193) Pearce, R.; Vancso, G. J. **1997**, *30*, Publisher: American Chemical Society, 5843–5848.

(194) Beekmans, L.; van der Meer, D.; Vancso, G. *Polymer* **2002**, *43*, Publisher: Elsevier, 1887–1895.

(195) Lei, Y.-G.; Chan, C.-M.; Li, J.-X.; Ng, K.-M.; Wang, Y.; Jiang, Y.; Li, L. **2002**, *35*, Publisher: American Chemical Society, 6751–6753.

(196) McCulloch, I.; Heeney, M.; Bailey, C.; Genevicius, K.; MacDonald, I.; Shkunov, M.; Sparrowe, D.; Tierney, S.; Wagner, R.; Zhang, W.; Chabinyc, M. L.; Kline, R. J.; McGehee, M. D.; Toney, M. F. *Nature Materials* **2006**, *5*, 328–333.

(197) Hu, Z.; Baralia, G.; Bayot, V.; Gohy, J.-F.; Jonas, A. M. *Nano Letters* **2005**, *5*, 1738–1743.

(198) Bangsund, J. S.; Fielitz, T. R.; Steiner, T. J.; Shi, K.; Van Sambeek, J. R.; Clark, C. P.; Holmes, R. J. *Nature Materials* **2019**, *18*, Number: 7 Publisher: Nature Publishing Group, 725–731.

(199) Raybin, J.; Ren, J.; Chen, X.; Gronheid, R.; Nealey, P. F.; Sibener, S. J. *Nano Letters* **2017**, *17*, 7717–7723.

(200) Mai, Y.; Eisenberg, A. *Chemical Society Reviews* **2012**, *41*, 5969–5985.

(201) Padilla, N. A.; Rea, M. T.; Foy, M.; Upadhyay, S. P.; Desrochers, K. A.; Derus, T.; Knapper, K. A.; Hunter, N. H.; Wood, S.; Hinton, D. A.; Cavell, A. C.; Masias, A. G.; Goldsmith, R. H. *ACS Sensors* **2017**, *2*, Publisher: American Chemical Society, 903–908.

(202) Hell, S. W.; Wichmann, J. *Optics Letters* **1994**, *19*, Publisher: Optica Publishing Group, 780–782.

(203) Harke, B.; Keller, J.; Ullal, C. K.; Westphal, V.; Schönle, A.; Hell, S. W. *Optics Express* **2008**, *16*, Publisher: Optica Publishing Group, 4154–4162.

(204) Beijersbergen, M. W.; Coerwinkel, R. P. C.; Kristensen, M.; Woerdman, J. P. *Optics Communications* **1994**, *112*, 321–327.

(205) Klauss, A.; Conrad, F.; Hille, C. *Scientific Reports* **2017**, *7*, 15699.

(206) Krüger, J.-R.; Keller-Findeisen, J.; Geisler, C.; Egner, A.; Egner, A. *Biomedical Optics Express* **2020**, *11*, Publisher: Optica Publishing Group, 3139–3163.

(207) Müller, T.; Schumann, C.; Kraegeloh, A. *ChemPhysChem* **2012**, *13*, 1986–2000.

(208) Bianchini, P.; Harke, B.; Galiani, S.; Vicidomini, G.; Diaspro, A. *Proceedings of the National Academy of Sciences* **2012**, *109*, Publisher: Proceedings of the National Academy of Sciences, 6390–6393.

(209) Rittweger, E.; Han, K. Y.; Irvine, S. E.; Eggeling, C.; Hell, S. W. *Nature Photonics* **2009**, *3*, Number: 3 Publisher: Nature Publishing Group, 144–147.

(210) Aitken, C. E.; Marshall, R. A.; Puglisi, J. D. *Biophysical Journal* **2008**, *94*, 1826–1835.

(211) Byers, G. W.; Gross, S.; Henrichs, P. M. *Photochemistry and Photobiology* **1976**, *23*, _eprint: https://onlinelibrary.wiley.com/doi/pdf/10.1111/j.1751-1097.1976.tb06768.x, 37–43.

(212) Kwon, J.; Elgawish, M. S.; Shim, S.-H. *Advanced Science* **2022**, *9*, 2101817.

(213) Bricks, J. L.; Slominskii, Y. L.; Panas, I. D.; Demchenko, A. P. *Methods and Applications in Fluorescence* **2017**, *6*, Publisher: IOP Publishing, 012001.

(214) Brixner, T.; Hildner, R.; Köhler, J.; Lambert, C.; Würthner, F. *Advanced Energy Materials* **2017**, *7*, 1700236.

(215) Cai, K.; Xie, J.; Zhao, D. *Journal of the American Chemical Society* **2014**, *136*, Publisher: American Chemical Society, 28–31.

(216) Penwell, S. B. Spatially Resolving Dynamics and Nanoscale Migration of Excitons in Organic Semiconductors Using Transient Absorption Imaging and STED Microscopy, Ph.D. Thesis, University of California, Berkeley, 2016.

(217) Penwell, S. B.; Ginsberg, L. D. S.; Ginsberg, N. S. *The Journal of Physical Chemistry Letters* **2015**, *6*, Publisher: American Chemical Society, 2767–2772.

(218) Hanne, J.; Falk, H. J.; Görlitz, F.; Hoyer, P.; Engelhardt, J.; Sahl, S. J.; Hell, S. W. *Nature Communications* **2015**, *6*, Number: 1 Publisher: Nature Publishing Group, 7127.

(219) Bruschini, C.; Homulle, H.; Antolovic, I. M.; Burri, S.; Charbon, E. *Light: Science & Applications* **2019**, *8*, Number: 1 Publisher: Nature Publishing Group, 87.

(220) Renna, M.; Ruggeri, A.; Sanzaro, M.; Villa, F.; Zappa, F.; Tosi, A. *IEEE Photonics Journal* **2020**, *12*, Conference Name: IEEE Photonics Journal, 1–12.

(221) Rivnay, J.; Noriega, R.; Kline, R. J.; Salleo, A.; Toney, M. F. *Physical Review B* **2011**, *84*, Publisher: American Physical Society, 045203.

(222) Deng, S.; Blach, D. D.; Jin, L.; Huang, L. *Advanced Energy Materials* **2020**, *10*, _eprint: https://onlinelibrary.wiley.com/doi/pdf/10.1002/aenm.201903781, 1903781.

(223) Schnedermann, C.; Sung, J.; Pandya, R.; Verma, S. D.; Chen, R. Y. S.; Gauriot, N.; Bretscher, H. M.; Kukura, P.; Rao, A. *The Journal of Physical Chemistry Letters* **2019**, *10*, Publisher: American Chemical Society, 6727–6733.

(224) Akselrod, G. M.; Deotare, P. B.; Thompson, N. J.; Lee, J.; Tisdale, W. A.; Baldo, M. A.; Menon, V. M.; Bulović, V. *Nature Communications* **2014**, *5*, Number: 1 Publisher: Nature Publishing Group, 3646.

(225) Castro-Méndez, A.-F.; Hidalgo, J.; Correa-Baena, J.-P. *Advanced Energy Materials* **2019**, *9*, 1901489.

(226) Bischak, C. G.; Hetherington, C. L.; Wu, H.; Aloni, S.; Ogletree, D. F.; Limmer, D. T.; Ginsberg, N. S. *Nano Letters* **2017**, *17*, Publisher: American Chemical Society, 1028–1033.

(227) Shao, Y.; Fang, Y.; Li, T.; Wang, Q.; Dong, Q.; Deng, Y.; Yuan, Y.; Wei, H.; Wang, M.; Gruverman, A.; Shield, J.; Huang, J. *Energy & Environmental Science* **2016**, *9*, Publisher: Royal Society of Chemistry, 1752–1759.

(228) Liu, Q.; Wei, K.; Tang, Y.; Xu, Z.; Cheng, X.; Jiang, T. *Advanced Science* **2022**, *9*, _eprint: https://onlinelibrary.wiley.com/doi/pdf/10.1002/advs.202105746, 2105746.

(229) Delor, M.; Slavney, A. H.; Wolf, N. R.; Filip, M. R.; Neaton, J. B.; Karunadasa, H. I.; Ginsberg, N. S. *ACS Energy Letters* **2020**, *5*, Publisher: American Chemical Society, 1337–1345.

(230) M. Hermes, I.; Best, A.; Winkelmann, L.; Mars, J.; M. Vorpahl, S.; Mezger, M.; Collins, L.; Butt, H.-J.; S. Ginger, D.; Koynov, K.; L. Weber, S. A. *Energy & Environmental Science* **2020**, *13*, Publisher: Royal Society of Chemistry, 4168–4177.

(231) Liao, B.; Zhao, H.; Najafi, E.; Yan, X.; Tian, H.; Tice, J.; Minnich, A. J.; Wang, H.; Zewail, A. H. *Nano Letters* **2017**, *17*, Publisher: American Chemical Society, 3675–3680.

(232) Tamai, Y.; Ohkita, H.; Benten, H.; Ito, S. *The Journal of Physical Chemistry Letters* **2015**, *6*, Publisher: American Chemical Society, 3417–3428.

(233) Dang, M. T.; Hirsch, L.; Wantz, G. *Advanced Materials* **2011**, *23*, 3597–3602.

(234) Dimitriev, O. P.; Blank, D. A.; Ganser, C.; Teichert, C. *The Journal of Physical Chemistry C* **2018**, *122*, Publisher: American Chemical Society, 17096–17109.

(235) Ho, S.-J.; Hsu, H.-C.; Yeh, C.-W.; Chen, H.-S. *ACS Applied Materials & Interfaces* **2020**, *12*, Publisher: American Chemical Society, 33346–33351.

(236) Yang, J.; Choi, M. K.; Yang, U. J.; Kim, S. Y.; Kim, Y. S.; Kim, J. H.; Kim, D.-H.; Hyeon, T. *Nano Letters* **2021**, *21*, 26–33.

(237) Guzelturk, B.; Martinez, P. L. H.; Zhang, Q.; Xiong, Q.; Sun, H.; Sun, X. W.; Govorov, A. O.; Demir, H. V. *Laser & Photonics Reviews* **2014**, *8*, 73–93.

(238) Bisschop, S.; Geiregat, P.; Aubert, T.; Hens, Z. *ACS Nano* **2018**, *12*, Publisher: American Chemical Society, 9011–9021.

(239) Kholmicheva, N.; Moroz, P.; Eckard, H.; Jensen, G.; Zamkov, M. *ACS Energy Letters* **2017**, *2*, Publisher: American Chemical Society, 154–160.

(240) Kamat, P. V. *The Journal of Physical Chemistry Letters* **2013**, *4*, Publisher: American Chemical Society, 908–918.

(241) Nabiev, I.; Rakovich, A.; Sukhanova, A.; Lukashev, E.; Zagidullin, V.; Pachenko, V.; Rakovich, Y. P.; Donegan, J. F.; Rubin, A. B.; Govorov, A. O. *Angewandte Chemie International Edition* **2010**, *49*, 7217–7221.

(242) Walker, B. J.; Bulović, V.; Bawendi, M. G. *Nano Letters* **2010**, *10*, Publisher: American Chemical Society, 3995–3999.

(243) Semonin, O. E.; Luther, J. M.; Choi, S.; Chen, H.-Y.; Gao, J.; Nozik, A. J.; Beard, M. C. *Science* **2011**, *334*, Publisher: American Association for the Advancement of Science, 1530–1533.

(244) Kodaimati, M. S.; Lian, S.; Schatz, G. C.; Weiss, E. A. *Proceedings of the National Academy of Sciences* **2018**, *115*, Publisher: Proceedings of the National Academy of Sciences, 8290–8295.

(245) Yuan, M.; Liu, M.; Sargent, E. H. *Nature Energy* **2016**, *1*, Number: 3 Publisher: Nature Publishing Group, 1–9.

(246) Shevchenko, E. V.; Talapin, D. V.; Murray, C. B.; O'Brien, S. *Journal of the American Chemical Society* **2006**, *128*, Publisher: American Chemical Society, 3620–3637.

(247) Collier, C. P.; Vossmeyer, T.; Heath, J. R. *Annual Review of Physical Chemistry* **1998**, *49*, _eprint: https://doi.org/10.1146/annurev.physchem.49.1.371, 371–404.

(248) Xu, F.; Ma, X.; Haughn, C. R.; Benavides, J.; Doty, M. F.; Cloutier, S. G. *ACS Nano* **2011**, *5*, Publisher: American Chemical Society, 9950–9957.

(249) Franzl, T.; Koktysh, D. S.; Klar, T. A.; Rogach, A. L.; Feldmann, J.; Gaponik, N. *Applied Physics Letters* **2004**, *84*, 2904–2906.

(250) Crooker, S. A.; Hollingsworth, J. A.; Tretiak, S.; Klimov, V. I. *Physical Review Letters* **2002**, *89*, 186802.

(251) Jin, X.; Sun, W.; Luo, S.; Shao, L.; Zhang, J.; Luo, X.; Wei, T.; Qin, Y.; Song, Y.; Li, Q. *Journal of Materials Chemistry A* **2015**, *3*, Publisher: Royal Society of Chemistry, 23876–23887.

(252) Mocatta, D.; Cohen, G.; Schattner, J.; Millo, O.; Rabani, E.; Banin, U. *Science* **2011**, *332*, Publisher: American Association for the Advancement of Science, 77–81.

(253) Beaulac, R.; Archer, P. I.; Ochsenbein, S. T.; Gamelin, D. R. *Advanced Functional Materials* **2008**, *18*, 3873–3891.

(254) Makkar, M.; Viswanatha, R. *RSC Advances* **2018**, *8*, Publisher: The Royal Society of Chemistry, 22103–22112.

(255) Zhitomirsky, D.; Voznyy, O.; Levina, L.; Hoogland, S.; Kemp, K. W.; Ip, A. H.; Thon, S. M.; Sargent, E. H. *Nature Communications* **2014**, *5*, Number: 1 Publisher: Nature Publishing Group, 3803.

(256) McElroy, N.; Page, R. C.; Espinbarro-Valazquez, D.; Lewis, E.; Haigh, S.; O'Brien, P.; Binks, D. J. *Thin Solid Films* **2014**, *560*, 65–70.

(257) Nandan, Y.; Mehata, M. S. *Scientific Reports* **2019**, *9*, Number: 1 Publisher: Nature Publishing Group, 2.

(258) Wei, S.-H.; Zhang, S. B.; Zunger, A. *Journal of Applied Physics* **2000**, *87*, 1304–1311.

(259) Vasudevan, D.; Gaddam, R. R.; Trinchi, A.; Cole, I. *Journal of Alloys and Compounds* **2015**, *636*, 395–404.

(260) Van Embden, J.; Jasieniak, J.; Mulvaney, P. *Journal of the American Chemical Society* **2009**, *131*, Publisher: American Chemical Society, 14299–14309.

(261) Chen, O.; Zhao, J.; Chauhan, V. P.; Cui, J.; Wong, C.; Harris, D. K.; Wei, H.; Han, H.-S.; Fukumura, D.; Jain, R. K.; Bawendi, M. G. *Nature Materials* **2013**, *12*, Number: 5 Publisher: Nature Publishing Group, 445–451.

(262) Wichner, S. M.; Mann, V. R.; Powers, A. S.; Segal, M. A.; Mir, M.; Bandaria, J. N.; DeWitt, M. A.; Darzacq, X.; Yildiz, A.; Cohen, B. E. *ACS Nano* **2017**, *11*, Publisher: American Chemical Society, 6773–6781.

(263) Huang, F.; Zhang, L.; Zhang, Q.; Hou, J.; Wang, H.; Wang, H.; Peng, S.; Liu, J.; Cao, G. *ACS Applied Materials & Interfaces* **2016**, *8*, Publisher: American Chemical Society, 34482–34489.

(264) Franzl, T.; Müller, J.; Klar, T. A.; Rogach, A. L.; Feldmann, J.; Talapin, D. V.; Weller, H. *The Journal of Physical Chemistry C* **2007**, *111*, Publisher: American Chemical Society, 2974–2979.

(265) Avidan, A.; Pinkas, I.; Oron, D. *ACS Nano* **2012**, *6*, Publisher: American Chemical Society, 3063–3069.

(266) Dong, A.; Chen, J.; Vora, P. M.; Kikkawa, J. M.; Murray, C. B. *Nature* **2010**, *466*, Number: 7305 Publisher: Nature Publishing Group, 474–477.

(267) Boles, M. A.; Engel, M.; Talapin, D. V. *Chemical Reviews* **2016**, *116*, Publisher: American Chemical Society, 11220–11289.

(268) Lunz, M.; Bradley, A. L.; Chen, W.-Y.; Gunko, Y. K. *The Journal of Physical Chemistry C* **2009**, *113*, 3084–3088.

(269) Mork, A. J.; Weidman, M. C.; Prins, F.; Tisdale, W. A. *The Journal of Physical Chemistry C* **2014**, *118*, Publisher: American Chemical Society, 13920–13928.

(270) Lee, E. M. Y.; Tisdale, W. A.; Willard, A. P. *Journal of Vacuum Science & Technology A* **2018**, *36*, Publisher: American Vacuum Society, 068501.

(271) Bässler, H. *Physica Status Solidi (b)* **1993**, *175*, 15–56.

(272) Madigan, C.; Bulović, V. *Physical Review Letters* **2006**, *96*, 046404.

(273) Ravindran, T. R.; Arora, A. K.; Balamurugan, B.; Mehta, B. R. *Nanostructured Materials* **1999**, *11*, 603–609.

(274) Gilmore, R. H.; Lee, E. M. Y.; Weidman, M. C.; Willard, A. P.; Tisdale, W. A. *Nano Letters* **2017**, *17*, Publisher: American Chemical Society, 893–901.

(275) Zhitomirsky, D.; Kramer, I. J.; Labelle, A. J.; Fischer, A.; Debnath, R.; Pan, J.; Bakr, O. M.; Sargent, E. H. *Nano Letters* **2012**, *12*, Publisher: American Chemical Society, 1007–1012.

(276) Hildebrandt, N.; Spillmann, C. M.; Algar, W. R.; Pons, T.; Stewart, M. H.; Oh, E.; Susumu, K.; Díaz, S. A.; Delehanty, J. B.; Medintz, I. L. *Chemical Reviews* **2017**, *117*, Publisher: American Chemical Society, 536–711.

(277) Willard, D. M.; Carillo, L. L.; Jung, J.; Van Orden, A. *Nano Letters* **2001**, *1*, Publisher: American Chemical Society, 469–474.

(278) Zhang, C.-Y.; Yeh, H.-C.; Kuroki, M. T.; Wang, T.-H. *Nature Materials* **2005**, *4*, Number: 11 Publisher: Nature Publishing Group, 826–831.

(279) Allan, G.; Delerue, C. *Physical Review B* **2007**, *75*, Publisher: American Physical Society, 195311.

(280) Pons, T.; Medintz, I. L.; Sapsford, K. E.; Higashiya, S.; Grimes, A. F.; English, D. S.; Mattoussi, H. *Nano Letters* **2007**, *7*, Publisher: American Chemical Society, 3157–3164.

(281) Kagan, C. R.; Murray, C. B.; Nirmal, M.; Bawendi, M. G. *Physical Review Letters* **1996**, *76*, Publisher: American Physical Society, 1517–1520.

(282) Kagan, C. R.; Murray, C. B.; Bawendi, M. G. *Physical Review B* **1996**, *54*, Publisher: American Physical Society, 8633–8643.

(283) Clapp, A. R.; Medintz, I. L.; Mauro, J. M.; Fisher, B. R.; Bawendi, M. G.; Mattoussi, H. *Journal of the American Chemical Society* **2004**, *126*, Publisher: American Chemical Society, 301–310.

(284) Clapp, A. R.; Medintz, I. L.; Mattoussi, H. *ChemPhysChem* **2006**, *7*, 47–57.

(285) Kodaimati, M. S.; Wang, C.; Chapman, C.; Schatz, G. C.; Weiss, E. A. *ACS Nano* **2017**, *11*, Publisher: American Chemical Society, 5041–5050.

(286) Kholmicheva, N.; Moroz, P.; Bastola, E.; Razgoniaeva, N.; Bocanegra, J.; Shaughnessy, M.; Porach, Z.; Khon, D.; Zamkov, M. *ACS Nano* **2015**, *9*, Publisher: American Chemical Society, 2926–2937.

(287) Zheng, K.; Žídek, K.; Abdellah, M.; Zhu, N.; Chábera, P.; Lenngren, N.; Chi, Q.; Pullerits, T. *Journal of the American Chemical Society* **2014**, *136*, Publisher: American Chemical Society, 6259–6268.

(288) Dement, D. B.; Puri, M.; Ferry, V. E. *The Journal of Physical Chemistry C* **2018**, *122*, Publisher: American Chemical Society, 21557–21568.

(289) Striolo, A.; Ward, J.; Prausnitz, J. M.; Parak, W. J.; Zanchet, D.; Gerion, D.; Milliron, D.; Alivisatos, A. P. *The Journal of Physical Chemistry B* **2002**, *106*, Publisher: American Chemical Society, 5500–5505.

(290) Bojarski, P.; Kulak, L.; Walczewska-Szewc, K.; Synak, A.; Marzullo, V. M.; Luini, A.; D'Auria, S. *The Journal of Physical Chemistry B* **2011**, *115*, 10120–10125.

(291) Tokmakoff, A. Time Dependent Quantum Mechanics and Spectroscopy, en, 2018.

(292) Penzo, E.; Loiudice, A.; Barnard, E. S.; Borys, N. J.; Jurow, M. J.; Lorenzon, M.; Rajzbaum, I.; Wong, E. K.; Liu, Y.; Schwartzberg, A. M.; Cabrini, S.; Whitelam, S.; Buonsanti, R.; Weber-Bargioni, A. *ACS Nano* **2020**, *14*, Publisher: American Chemical Society, 6999–7007.

(293) Baer, R.; Rabani, E. *The Journal of Chemical Physics* **2008**, *128*, 184710.

(294) Geiregat, P.; Justo, Y.; Abe, S.; Flamee, S.; Hens, Z. *ACS Nano* **2013**, *7*, Publisher: American Chemical Society, 987–993.

(295) Liu, Y.; Gibbs, M.; Puthussery, J.; Gaik, S.; Ihly, R.; Hillhouse, H. W.; Law, M. *Nano Letters* **2010**, *10*, Publisher: American Chemical Society, 1960–1969.

(296) Zhu, N.; Zheng, K.; Karki, K. J.; Abdellah, M.; Zhu, Q.; Carlson, S.; Haase, D.; Žídek, K.; Ulstrup, J.; Canton, S. E.; Pullerits, T.; Chi, Q. *Scientific Reports* **2015**, *5*, 9860.

(297) Zhu, H.; Yang, Y.; Wu, K.; Lian, T. *Annual Review of Physical Chemistry* **2016**, *67*, _eprint: https://doi.org/10.1146/annurev-physchem-040215-112128, 259–281.

(298) Tagliazucchi, M.; Tice, D. B.; Sweeney, C. M.; Morris-Cohen, A. J.; Weiss, E. A. *ACS Nano* **2011**, *5*, Publisher: American Chemical Society, 9907–9917.

(299) Hines, D. A.; Forrest, R. P.; Corcelli, S. A.; Kamat, P. V. *The Journal of Physical Chemistry B* **2015**, *119*, Publisher: American Chemical Society, 7439–7446.

(300) Zhu, T.; Wan, Y.; Huang, L. *Accounts of Chemical Research* **2017**, *50*, Publisher: American Chemical Society, 1725–1733.

(301) Sneyd, A. J. et al. *Science Advances* **2021**, *7*, Publisher: American Association for the Advancement of Science, eabh4232.

(302) Giovanni, D.; Righetto, M.; Zhang, Q.; Lim, J. W. M.; Ramesh, S.; Sum, T. C. *Light: Science & Applications* **2021**, *10*, Number: 1 Publisher: Nature Publishing Group, 2.

(303) Pazos-Outón, L. M.; Szumilo, M.; Lamboll, R.; Richter, J. M.; Crespo-Quesada, M.; Abdi-Jalebi, M.; Beeson, H. J.; Vrućinić, M.; Alsari, M.; Snaith, H. J.; Ehrler, B.; Friend, R. H.; Deschler, F. *Science* **2016**, *351*, Publisher: American Association for the Advancement of Science, 1430–1433.

(304) deQuilettes, D. W.; Brenes, R.; Laitz, M.; Motes, B. T.; Glazov, M. M.; Bulović, V. *ACS Photonics* **2022**, *9*, Publisher: American Chemical Society, 110–122.

(305) Jones, G. A.; Bradshaw, D. S. *Frontiers in Physics* **2019**, *7*.